№2, 2026

ISSN 2706-977X

MATERIAL AND MECHANICAL ENGINEERING TECHNOLOGY

Content

DOI 10.52209/2706-977X_2026_2_3 **IRSTI 55.03.99** **UDC 621.31**

Dynamics of the Vibration Process of a Pumping unit Taking into Account the Elastic and Dissipative Properties of the Elements of Support Devices

Mustafin A. Kh., Sadykov N. S.*, Abdullina G. G., Akhmedyanova G. K., Aigozhina D. G.
Toraighyrov university, Pavlodar, Kazakhstan
*corresponding author

Abstract. The dynamics of the vibration process of a pumping unit can be considered as independent oscillations of two separate sprung masses from the centrifugal force: the rotor on the bearings and the pump casing on the foundation supports. In the absence of special damping devices in the oscillating system, the reaction force from the rotor vibration affects the casing and the bearing supports approximately equally. However, when dampers are used in the oscillating system, they can significantly reduce transmitted force to unit supports. Such a method made it possible, in addition to the acoustic parameters of the unit, to determine the dynamic loads on the supports and to conduct a comparative assessment of the strength parameters of rolling bearings. Vibration protection of rotating machines, i. e. with a rotor, which includes an impeller with a shaft and support parts, requires a large amount of research, largely experimental in nature. At present, some of this work can be significantly reduced by using mathematical apparatus to perform calculations and model dynamic processes. The aim of the paper is to show method and model to calculate dynamics of vibration process in a pumping unit, considering elastic and dissipative properties of elements in support devices.

Keywords: damping, vibration, shock absorbers, frequency, rotor.

Introduction.

An effective method of vibration isolation is to provide the pump with elastic and dissipative connections, for example, on the pump mounting supports to the frame. The problem is that the methods of calculation and assessment of the effect of damping devices on reducing vibration emitted by pump units existing in modern literature are not accurate enough. They are performed without taking into account the inertia of oscillating masses and internal friction in the support materials. More accurate calculations can be made using nonlinear differential equations describing the processes of mass oscillation, i.e., methods of mathematical modelling of the process dynamics. The paper considers one of the main types of vibration of pump units arising due to rotor imbalance when the shaft axes are displaced. An assessment is made of the effect of operating pumps with elastic connections made of elastomeric materials on the dynamic loading of the supports. It is established that vibrations will decrease when using damping devices made of modern high-tech elastic materials in the form of elastomers. Polyurethane elastomers are produced in Austria by Getzner Werkstoffe GmbH under the Sylomer and Sylodyn brands and can be recommended for vibration isolation of pump units. The aim of the paper is to show method and model to calculate dynamics of vibration process in a pumping unit, considering elastic and dissipative properties of elements in support devices.

1. Materials and methods

Isolation of pump vibrations with shock absorbers achieves the goal when the ratio of the frequencies of forced and natural vibrations of the mechanical system,

$$\omega/\omega_a > \sqrt{2}.$$

where ω - forced frequency, ω_a - the natural frequency.

In practice, the ratio of these frequencies is taken as 2.5–5.

The transfer coefficient at low damping can be calculated by the following formula

$$\mu_t = \left| 1/1 - (\omega/\omega_a)^2 \right| \quad (1)$$

Effective vibration isolation is attained with $\mu_t = 0.125 - 0.066$. The vibration isolation (dB) of the shock-absorbing mount is defined by the reciprocal of the transmission coefficient, represented in logarithmic units:

$$\Delta L = 20\, lg|F/F_a| = 20\, lg|1 - (\omega/\omega_a)^2| \quad (2)$$

To ensure acceptable levels of noise and vibration, the effectiveness of the unit's acoustic vibration insulation ΔL should not be less than 26, for centrifugal pumps given at [1].

In the paper [2] it is demonstrated that the research of vibrations occurring on supports of the rotor shaft in the housing and in the pump mounts on the foundation can be considered as independent vibrations of two separate sprung masses. In this regard, in this work a study of two vibration variants is carried out:

1) the rotor on bearings from centrifugal force, which results from the pump and electric motor shaft axes moving parallel to the centre axis;

2) For the same reason, the foundation's pump housing is supported by centrifugal force, but without taking into account the elastic-damping properties of the bearings.

It should be noted that the assessment of vibration isolation efficiency of pumps is currently carried out using the second calculation option. However, to what extent this is justified in detailing vibration studies can be considered using the example of vibration calculations of the 2D630-125 pump. These units are used at industrial water supply pumping stations, as well as in the petrochemical industry. A parallel offset of the pump and electric motor shaft axes relative to the central axis of 0.10 mm was taken. The centrifugal force on the supports of rotor, with mass of rotor $m_r = 120\ kg$ and shaft speeds $\omega_s = 308.7 s^{-1}$ makes up

$$F_a = 120 \cdot 308,7^2 \cdot 0,1 \cdot 10^{-3} = 1145\ N \quad (3)$$

To simplify calculations, the elastic and dissipative properties of the elements of the oscillatory system are taken into account by constant coefficients. For example, the rigidity of rolling bearings, represented through the static load capacity W_0**,** can be determined by the formula [3]

$$k_n = 5350\sqrt[3]{d_r W_0 z^2 cos^2 \psi}\ , \quad (4)$$

where d_r– diameter of rolling elements;

z – number of rolling elements;

ψ – nominal contact angle.

However, it gives an overestimated value of the bearing stiffness coefficient, since it is calculated for the static loading of all rolling elements and does not take into account the uneven distribution of the load between them. The following formula is suggested in [2]

$$k_{rb} = F_0/a \quad (5)$$

As per the theory of load distribution for rolling elements in single bearing, the ball that is opposite the load's line of action experiences the most force, which as following

$$F_0 = 5\ F_a/2z, \quad (6)$$

The convergence of the axes of two spheres in contact along concave surfaces according to Hertz's theory [3]

$$a = 1,55\sqrt[3]{(F_0/E)^2 (R_1 - R_2)/2R_1 R} \quad (7)$$

Natural frequency of the system

$$\omega_a = \sqrt{2k_{rb.}/m_r} \quad (8)$$

The ratio of the frequencies of the disturbing force oscillations and the system's natural oscillations of $308.7/1053 = 0.292.\ [1 - (\omega/\omega_a)^2\ ] = 1 - 0.292^2 = 0.914$ and transfer coefficient $1/0.914 = 1.09$ not within the suggested range

$\mu_t = 0.125 - 0.066$, which characterises the low vibration isolation of bearings. To ensure isolation of rolling bearings from vibration, the frequency of the system's natural oscillations must be decreased and support compliance must be increased. This problem can be solved in one of several ways:

- structurally by installing a polyurethane elastomer bushing on the bearing seating surfaces in the pump housing;
- technologically - by spraying a polyurethane layer on the same surface;
- applying a film of composite material and dispersed metal additives [4].

The last two methods are limited by the thickness of the sprayed or applied layer δ, with an increase in which its homogeneity and strength decrease. A decrease in thickness helps to increase the rigidity k of the mounting surface and, accordingly, the frequency of the natural oscillations of the system. Figure 1 shows a diagram of installing a polyurethane bushing in a hole in the pump body for mounting a bearing in it. For instance, motorists mostly use polyurethane shock absorber bushings to repair vehicles. Main properties of polyurethane bushings are presented below:

- wear resistance;

- low friction;
- elasticity;
- operation at high pressure;
- long service life;
- resistance to oils, fuel and petroleum.

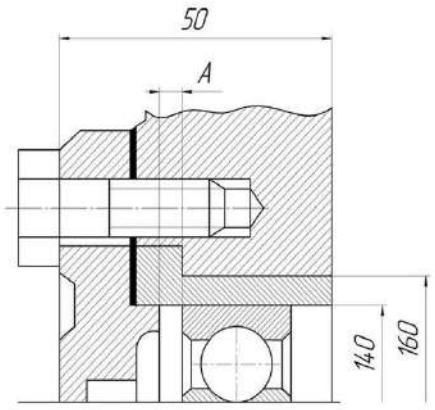

Fig. 1 – Installation of a polyurethane bushing into the hole of the 2D630-125 pump body

Rigidity coefficient of polyurethane bushing

$$k_{el.} = \mathrm{EA}/\,\delta, \tag{9}$$

where $\mathrm{A} = \pi \mathrm{B}\,(D\ +\ \delta\,)$– surface area of polyurethane bushing;
δ – polyurethane bushing thickness;
B – bearing width;
D – diameter of the bearing bushing hole.

The wall thickness of a polyurethane bushing is determined by the Bach formula

$$\delta = \frac{\mathrm{D}}{2}\left(\sqrt{\frac{[\sigma_\rho]+0.4\mathrm{P_Z}}{[\sigma_\rho]-1.3\mathrm{P_Z}}} - 1\right), \tag{10}$$

where σ_ρ – the permissible tensile stress of elastomer grade SR55, in accordance with the data of the "Getzner Werkstof" company [5] is equal to 0.061 MPa;
p_z – the pressure on the bushing's walls is calculated as F_a/A.

When connecting in series the elements of a viscoelastic system consisting of a bearing and a polyurethane bushing, the reduced stiffness

$$k_{re} = k_n k_{el}\ /\ (k_n + k_{el}). \tag{11}$$

For damped oscillations of systems with damping, the natural frequency is determined by the frequency of free oscillations ω_0

$$\omega_a = \sqrt{\ }\,\omega_a^2 - n^2, \tag{12}$$

where $n = \omega_0\psi/4\pi$– the given damping coefficient through the energy loss coefficient ψ connects the oscillation frequencies of the two systems in such a way

$$\omega_a = \omega_0\sqrt{1 - (\psi/4\pi)^2} \sim \omega_0, \tag{13}$$

where ω_0 - the frequency of free oscillations.

Due to the insignificance of the damping effects, the natural frequency of a system consisting of a more flexible support is determined by the well-known formula

$$\omega_a = \sqrt{2k_{re}/m} = \sqrt{2 \cdot 0.364 \cdot 10^6/120} = 77\ s^{-1} \quad (14)$$

The ratio of the frequencies of the oscillations of the disturbing force and the natural oscillations of the system $308.7/77 = 4$. Expression $|1 - (\omega/\omega\_a)^2| = |1 - 4^2| = 15$. Transfer coefficient $1/15 = 0{,}066$.

Based on computations

$$\Delta L = 20\ lg 1/0.066 = 26.02\ Hz, \quad (15)$$

that corresponds to the permissible level of vibration. Thus, the use of a bearing support with a flexible base in the form of a polyurethane bushing provides sufficient acoustic vibration insulation of the unit.

To assess the dynamic properties of the system, forced vibrations of the viscoelastic model shown in Figure 2 are considered. Taking into account the elastic forces *kx* and linear viscous resistance *bx*, the differential equation of motion of the mass m has the form

$$m\ddot{x} + b\dot{x} + kx = F\ sin\ \omega\ t, \quad (16)$$

or

$$m\frac{d^2x}{dt^2} + b\frac{dx}{dt} + kx = F\sin\omega t$$

where m is the mass, b is the damping coefficient, k is the stiffness, x is the displacement, F is the forcing amplitude, and ω is the forced frequency.

Through the reduced damping and mass

$$b = 2\,nm = 2m(\omega_0\psi/4\pi) = m\omega_0\psi\,/2\pi \quad (17)$$

The final expression is obtained

$$b = k_{el}\psi/2\pi\omega_0, \quad (18)$$

where ψ – coefficient of mechanical losses of the elastomer, for the previously selected elastomer brand SR55 - $\psi = 0.17$.

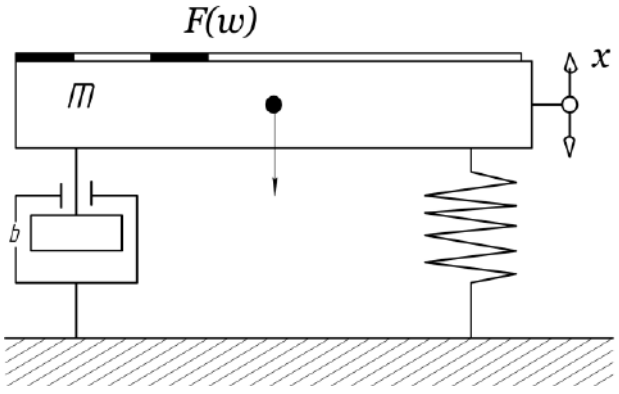

Fig. 2 - Model of a rotor on bearings in the form of a viscoelastic body

Bushing settlement from the rotor weight per support

$$x_{cm} = \frac{mg}{2k_{el}} = \frac{1200}{2} \cdot 0.364 \cdot 106 = 0.001648\ m \quad (19)$$

The differential equation of motion of the mass m, taking into account the settlement of the walls of the polyurethane bushing, takes the form

$$m\ddot{x} + b\dot{x} + k(x + \mathrm{x}_0) = F\,sin\,\omega\,t \tag{20}$$

The elastic and damping properties of the components in this model must be known in order to replicate the vibrations of the pump body on the foundation [9]. A concrete class of at least 10 (compressive strength in MPa) is required in order to construct a foundation for a 2D630-125 pumping unit. Class B 25 concrete is approved, and the pumping unit's foundation is rigid.

$$k_f = EA_f/h, \tag{22}$$

where $E = 30 \cdot 10^3$ MPa – modulus of elasticity of concrete under compression;

A_f – the foundation base's area is taken to be larger than the area of the horizontal projection of the pump;

h – the underground part's depth of the foundation, for heated rooms the minimum - 0.5 m

$$k_f = 30 \cdot 10^9 \cdot 0.33/0.5 = 20 \cdot 10^9 N/m. \tag{23}$$

System's natural frequency

$$\omega_a = \sqrt{20000 \cdot 10^6 /1350} = 3874\ s^{-1} \tag{24}$$

significantly exceeds the frequency of disturbing vibrations, that characterises system's low vibration isolation. $[1 - (\omega/\omega_a)^2\ ] = [1 - (308.7/3874)^2] = 1$. Transfer coefficient μ_t*=1.*

Stress occurring in elastomer flooring with unit weight 13500 N

$$\sigma = 13500/0{,}2232 = 60483 N/m^2 \tag{25}$$

Elastomer flooring settlement from pump weight

$$x_s = H \cdot \sigma/E, \tag{26}$$

where H – the thickness of the flooring is taken as 0.4 m;

For grade SR55 elastomer, the dynamic modulus of elasticity - 0.753 MPa

$$x_s = 0.04 \cdot 60483/0.753 \cdot 10^6 = 0.003212\ m \tag{27}$$

Rigidity of flooring under the pump sole

$$k_{el}\ = 0.753 \cdot 10^6 \cdot 0.2232/0.04\ = 4.2 \cdot 10^6 \mathrm{N/m} \tag{28}$$

Natural frequency of pump oscillation on elastomer flooring

$$\omega_a = \sqrt{4.2 \cdot 10^6/1350} = 55.67 s^{-1} \tag{29}$$

The ratio of frequencies of disturbing force's oscillations and the natural oscillations

$$308.7/55.67 = 5.54. \tag{30}$$

$$|1 - (\omega/\omega_a)^2| = |1 - 5.54^2| = |29.69|. \tag{31}$$

Transfer coefficient $1/29.69 = 0.033$. Since the rigidity of the foundation is much higher than the rigidity of the elastomer, the rigidity of the decking is taken as the design rigidity. Damping coefficient

$$b_{el} = k_{el}\psi/2\,\pi\omega = 4.2 \cdot 10^6 \cdot 0.17/6.28 \cdot 55.67 = 2042\ \mathrm{Ns/m} \tag{32}$$

2. Results and discussion

The results of calculations using known methods for calculating differential equations [6] with different values of the stiffness and damping coefficients are presented in Table 1. The calculation is based on the representation of a non-homogeneous equation through a characteristic equation, then using the method of varying constant coefficients, a general solution is found in which the dependence of the mass displacement on time is determined in analytical or graphical form.

The elastic resistance force on the supports is calculated based on the amplitude of the mass displacement, taking into account damping $R = kx + bx^{/}$. The damping rate is determined by the formula

$$x^{/} = fx, \tag{21}$$

where f – frequency of oscillation of pump rotor on supports, Hz

Table 1. Results of calculations with different values of stiffness and damping coefficients

Number of row	m, kg	k, N/m	b, Ns/m	x, m	R, N	μ_t	k_n
1	60	$65 \cdot 10^6$	-	0000096	624	0.97	0.97
2	60	$364 \cdot 10^3$	125	-0.00021	86.4	0.066	6.62
3	1350	$20 \cdot 10^9$	-	$5.85 \cdot 10^{-8}$	1170	1.0	1.0
4	1350	$4200 \cdot 10^3$	2042	-0.00002	84	0.033	13.6

The ratio of the exciting force F_a to the resistance force R is used to determine the force transfer coefficient k_n, which in oscillatory systems without damping is equal to the transfer coefficient μ_t [7], [8]. In mechanical units where devices with built-in dampers are used, these coefficients may differ significantly. In the absence of damping, the reaction in the bearings falling on one side of the rotor, $R = 624$ N, is approximately equal to half the load from the exciting force $F_a = 1145/2 = 572.5N$. The reaction in the pump casing supports $R = 1170\ N$ with a small difference - the force exciting the rotor oscillations $F_a = 1145$ N. In pumps with dampers, the above regularities are not observed. In the presence of dampers, the reaction force on the bearings is less than the exciting force falling on it by $572.5/86.4 = 6.62$ times. The reaction on the pump body supports is $1145/84 = 13.6$ times.

Conclusions

The analysis of the results of the calculation shows that., vibration of the mass without taking into account damping is of a harmonic nature (row 1 and 3 in Table 1), as well as the oscillations of the disturbing force, they have positive and negative values of the amplitudes of the cycles. The reaction forces are approximately equal to the load exciting the oscillations, i. e. $F_a \sim R$, which is possible when ratio of frequencies of disturbing and natural oscillations is insignificant because of high frequency of the latter. Considering shock absorbers' damping and static settlement, the vibration is a pulsating (row 2 and 4 in Table 1) curve, the amplitude is determined as the difference in the ordinates of the peaks: with a negative result, the direction of mass movement is against the gravity vector of the pump, i. e. aimed at weakening the initial settlement of the shock absorber.

When using a damping base under the pump body, the stress in the threaded connection during vibrations is reduced as a result of reducing the calculated external load. The article presents a method for calculating the dynamics of the vibration process of a pump unit taking into account the elastic and dissipative properties of the elements of the support devices. In the absence of special damping devices in the oscillatory system, the reaction force in the supports is equal to the load exciting the vibrations, which is possible with high rigidity and frequency of the latter. The reaction forces from the rotor vibration affect the housing and the bearing supports approximately equally. However, when using dampers in the oscillatory system, they can significantly reduce the force transmitted to the unit supports. The reaction forces on the bearings must be determined by detailing the pump model, since, as established above, they can differ significantly from the disturbing force.

References

[1] Trunova I.G. Selection and calculation of means of protection against noise and vibration: textbook. a guide to the implementation of theses, term papers and practical work for students. Nizhny Novgorod; 2012. – 116 p.
[2] Mustafin A.Kh. Popular mechanics in engineering: a monograph. Pavlodar: Toraighyrov University; 2021. – 96 p.
[3] Birger I.A. Calculations for the strength of machine parts. Handbook. M.: Mechanical Engineering; 1993. – 702 p.
[4] Mashin D.V. Theoretical aspects of improving the efficiency of restoration of housing parts of agricultural machinery with compositions based on elastomers. Vestnikmichgau. 2013;1:53-55.
[5] Mustafin A.Kh. Modeling of vibration of pumping units on supports and methods of their reduction. In : Materials of the 10th International Scientific and Technical Conference, Omsk: 2020. p. 133-134.
[6] Kashina S.G. Protection from vibration. Kazan: KISI; 2012; – 133 p.
[7] ISO 3945-2006. Mechanical vibration of large rotation machines with speed range from 10 to 200 rev/s/ Measurement and evaluation of vibration severity in situ.
[8] Ghazali M., Rahiman W. Vibration Analysis for Machine Monitoring and Diagnosis: A Systematic Review. Shock and Vibration. 2021, P. 1-25.
[9] Wan FYM. Classics in Applied Mathematics Mathematical Models and Their Analysis. California: Harper & Row; 2010. – 394 p.

Information of the authors

Mustafin Adilbek, c.t.s., professor, Toraighyrov University
e-mail: mustafin-51@mail.ru

Sadykov Nursultan, master of science, senior lecturer**,** Toraighyrov University
e-mail: sadykov.n@teachers.tou.edu.kz

Abdullina Gulnara, c.c.s., associate professor, Toraighyrov University
e-mail: abdullina.g@teachers.tou.edu.kz

Akhmedyanova Galiya, master of science, senior lecturer, Toraighyrov University
e-mail: akhmedyanova.g@teachers.tou.edu.kz

Aigozhina Dinara, master of science, senior lecturer, Toraighyrov University
e-mail: aigozhina.d@teachers.tou.edu.kz

DOI 10.52209/2706-977X_2026_2_10 **IRSTI 55.03.14** **UDC 625.096**

Analysis of Limit Loads and 3D Modeling of Removable Equipment for Rail Transporters

Balabayev O.[1], Mikhailov V.[1], Kassymzhanova A.[1], Beisembayev D.[1*], Nurullaev P.[2]
[1]Abylkas Saginov Karaganda Technical University, Karaganda, Kazakhstan
[2]Tashkent State Transport University, Tashkent, Uzbekistan
* corresponding author

Abstract. The paper analyzes critical issues related to the reliability of transporting long rail strings exceeding 800 m in length along curved sections of the railway network of the Republic of Kazakhstan using specialized rail-transport wagons. An original methodological approach is presented for the analytical determination of limit force effects arising in the detachable equipment of flat wagons when negotiating track sections with circular geometry. A detailed three-dimensional representation of the structure was created within the ANSYS computational framework to enable numerical simulation and analysis. The developed digital model was verified through a comparative analysis of theoretical and experimental data, demonstrating a high degree of accuracy (with an error margin not exceeding 5%). The results obtained allow for a more precise assessment of the structure's safety under complex geometric conditions, which is particularly relevant in the context of modernizing the country's transportation infrastructure.

Keywords: railway transport, rail carrier, rail platforms, long welded rails, limit loads, oversized cargo transportation

Introduction.

In his address to the citizens of the Republic of Kazakhstan on September 1, 2023, President Kassym-Jomart Tokayev emphasized the need to prioritize the development of the national transport and logistics system, highlighting the importance of implementing large-scale railway infrastructure projects. Among the key initiatives identified were the construction of the "Bakhty–Ayagoz" and "Darbaza–Maktaaral" railway lines, as well as the development of a railway bypass route in the Almaty region, underscoring the high relevance of the project under consideration [1].

At present, the railway sector is increasingly focused on the widespread adoption of high-speed continuous welded rail technologies, which involve the use of long rail strings. This approach significantly reduces the number of rail joints and improves the operational performance of the track structure [2–4]. Eliminating joints decreases dynamic impacts on the track, significantly reducing wheel wear on rolling stock and train resistance, which in turn lowers fuel and electricity consumption for traction [2-4].

An analysis of practices applied in northern countries demonstrates successful experience in transporting long rail strings exceeding 800 m in length using specialized rail-carrying platforms of the RS-800/3 type (Figure 1) [5, 6]. At the same time, the specific natural and geographical conditions of the Republic of Kazakhstan impose increased requirements on the reliability and safety of such transportation, particularly when rolling stock operates on track sections with curved alignment [7].

An extensive survey and critical assessment of the available scholarly literature and normative calculation procedures [7–10] has shown that, at present, no generalized analytical dependencies or validated mathematical formulations exist that can reliably characterize the force interactions between rolling stock components during the movement of continuous rail strings exceeding 800 m in length along curved track sections. Among the methods currently reported, the approach most closely aligned with the technical concept proposed in this work is the calculation scheme developed by specialists of the China Academy of Railway Sciences for the Ministry of Railways of the People's Republic of China (Beijing) [9].

In that research, a dynamic simulation model was formulated to estimate the loads generated during the transportation of rail strings with lengths of up to 100 m on curved track segments with radii not exceeding 300 m. The results of experimental validation demonstrated that the calculated dynamic responses satisfy the prescribed safety requirements for transportation. Nevertheless, the scope of applicability of this approach is confined to relatively short rail strings (up to 100 m), which makes it unsuitable for assessing the behavior and loading conditions of ultra-long rail elements during transportation.

a) b)

Fig. 1. – Transportation (a) and Laying (b) of Long Welded Rails

As a result, the development of a reliable calculation methodology, along with the verification of a numerical model realized within the ANSYS simulation platform, continues to be an open issue of substantial practical importance. This makes it necessary to employ a methodology capable of accurately determining the load effects imposed on the removable structural elements of rail-transporting flatcars as continuous welded rails longer than 800 m are conveyed along curved portions of the railway alignment.

1 Materials and Methods

Figure 2 illustrates the suggested computational method for assessing the maximum loads on the detachable components of rail transport platforms arranged in a connected formation while conveying welded rails exceeding 800 m along curved track sections.

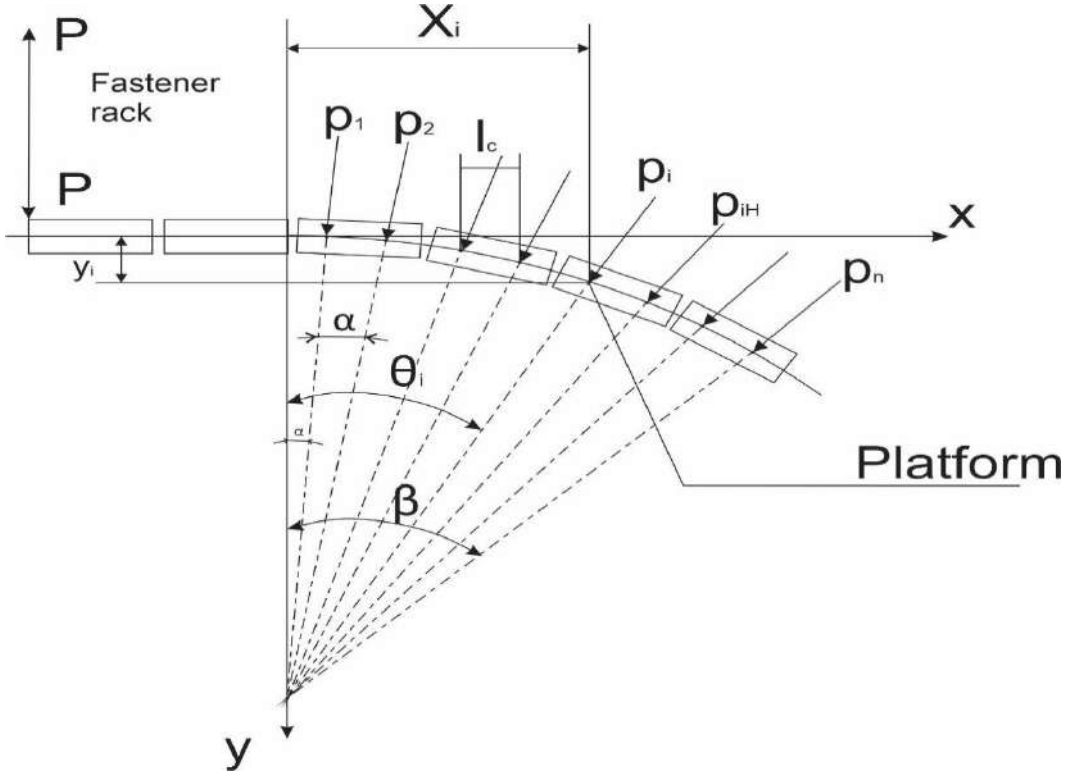

P_i – loads (support reactions) resulting from the imposed deformation of the continuous welded rail at the i-th support; l_e – distance between the supports of the fastening platform; R – curve radius; y_i – bending deformation of the long welded rails at the i-th support; α – rotation angle between adjacent supports of the fastening platform; β – total curve rotation angle; x_i – distance from the bending angle to the i-th support of the fastening platform in the curve; θ – cross-section rotation angle of the long welded rails at the i-th support.

Fig. 2. – Methodology for Evaluating Maximum Loads on Detachable Components of Coupled Rail Transport Platforms During the Conveyance of Continuous Welded Rails Exceeding 800 m Along Curved Track Sections

Obvious geometric relationships derived from the calculation scheme (Figures 2 and 3) have been observed.

$$x_i = \sum_{j=1}^{i} l_e$$
$$\theta_i = \sum_{j=1}^{i} \alpha$$

$$\Delta = l_e \cdot tg\alpha \tag{1}$$
$$\alpha = arctg\frac{l_e}{2R}$$

where **Δ** – bending or distortion of an individual segment spanning between two support points.

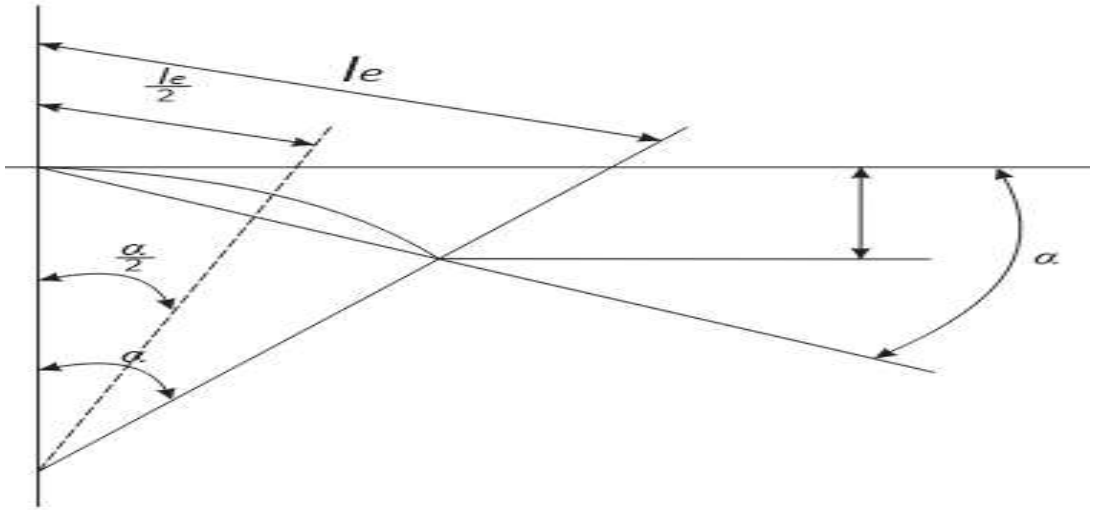

Fig. 3. – Procedure for Assessing the Bending of Continuous Welded Rails

Subsequently, the general expression for the elastic curve, formulated using the initial parameters, can be written as follows:

$$y = y_0 + \theta_Q x + \frac{M_0 x^2}{2EY} + \frac{Q_0 x^3}{6EY} + f(x), \tag{2}$$

where y_0, θ, Q_0, and M_0represent the initial values of deflection, rotation angle, transverse load, and bending moment at the reference point, respectively.

To enhance the accuracy of predicting the maximum forces acting on the removable coupling elements of flatcars during the transport of rail strings exceeding 800 m along curved track segments—and to validate the proposed computational model—comprehensive numerical analyses were conducted within the ANSYS simulation environment.

In the course of developing and executing the numerical simulations, the following methodological and investigative steps were completed:

– assessment of the principal geometric and structural characteristics of the studied components;

– evaluation of real-world operating conditions and service scenarios of the rolling stock;

– formulation of a procedure for carrying out the computational experiment;

– execution of preliminary trial calculations to verify the fidelity of the 3D simulation model by comparing numerical predictions with experimental data [11–12].

The numerical study was conducted step by step in the following sequence:

– creation of a 3D representation of the removable components of flat rail transport wagons using AutoCAD (Figure 4);

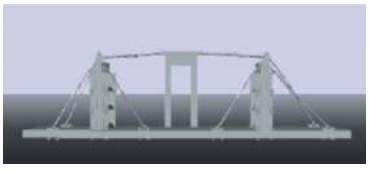
a)

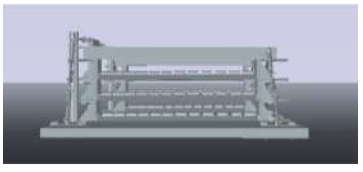
b)

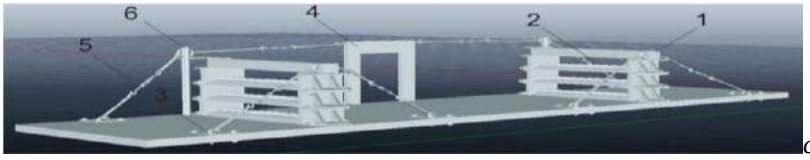

c)

Fig. 4. – 3D Model of the Removable Equipment of Rail Transport Platforms in the AutoCAD Software Environment: 1) Support post; 2) Roller supports; 3) Platform attachment; 4) Side support; 5)Turnbuckle; 6) Tension post.

– transfer of the three-dimensional geometry to the ANSYS computational environment for further analysis (Figure 5);

– identification of the structural components selected for simulation and loading during virtual testing (Figure 6a);

– the physical and mechanical properties of the materials in the computational model were defined, and a structural steel material from the built-in ANSYS library with typical mechanical properties was used (Figure 6b).;

– generation of the finite element mesh and computation of the stress–strain state taking into account all adopted assumptions and boundary conditions (Figure 6c, d);

– interpretation and systematization of the numerical analysis results (Figure 7).

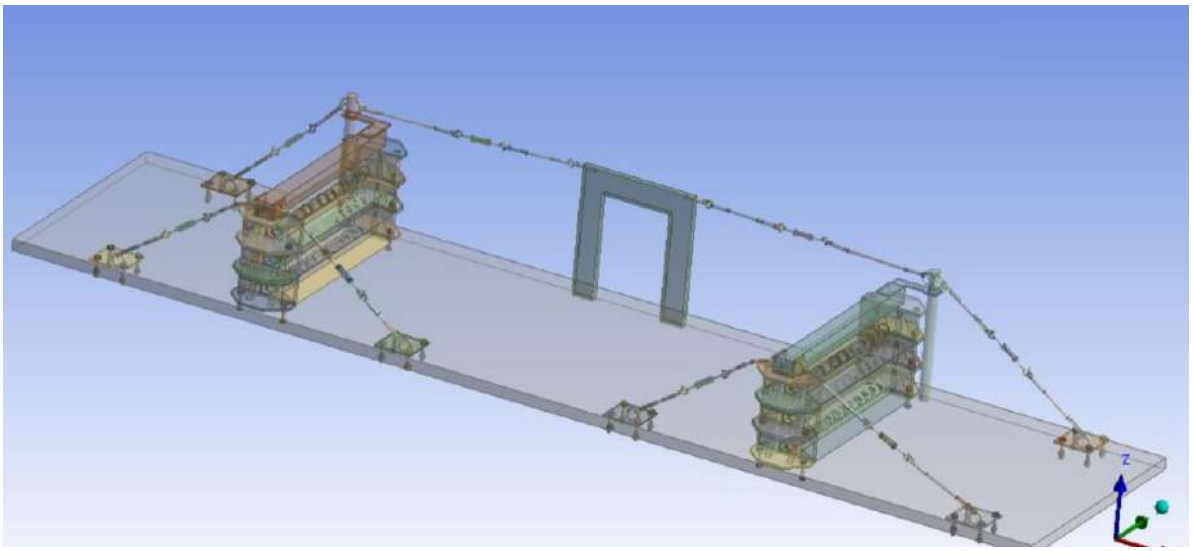

Fig. 5. – 3D Model of the Removable Equipment of Rail Transport Platforms in the ANSYS Software Environment

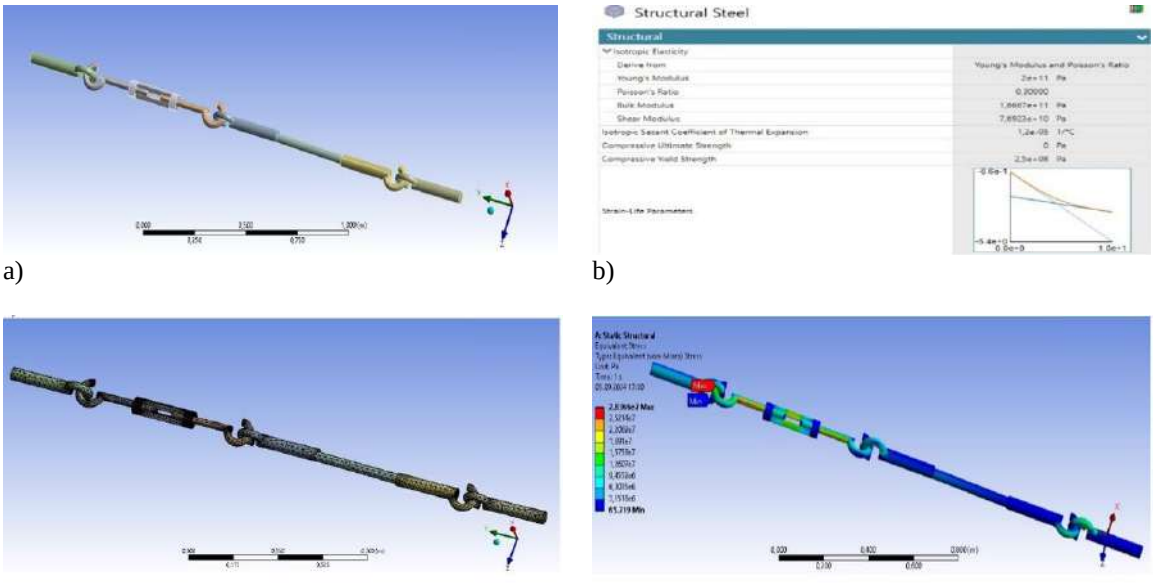

a) b)

c) d)

Fig. 6. – Preparation of a 3D Model Element of the Removable Equipment of Rail Transport Platforms in a Coupled Configuration for Simulation Testing in the ANSYS Software Environment

2. Results and discussion

Within the numerical investigation, four calculation scenarios were implemented, differing in the combinations of external loads applied to the analyzed element of the spatial model of the detachable coupling units of flat wagons (rail carriers). Upon completion of each scenario, distributions of the stress–strain state were obtained in the form of graphical stress fields, and the corresponding output parameters of the model were calculated (Figure 7a–c).

To clarify the differences between the implemented calculation scenarios, Table 1 summarizes the loading conditions in terms of the ratio of the applied tensile force to the cross-sectional area (F/S), along with the corresponding maximum equivalent stresses.

Table 1. Parameters of calculation scenarios and simulation results

Scenario	Fi/S (MPa)	Max stress σ_e (MPa)	Description
Test I	Low	28.4	Initial loading condition
Test II	Medium	85.1	Increased tensile load
Test III	High	141.8	Near allowable stress
Test IV	Critical	198.6	Exceeds allowable limit

As shown in Table 1, an increase in the applied load leads to a nonlinear growth in equivalent stresses. It should be noted that in Test IV the stress level exceeds the allowable limit of 160 MPa, indicating a potentially unsafe operating condition

Based on the calculations performed using the ANSYS software package, an experimental–computational relationship was established (Figure 5d) that describes the variation of equivalent mechanical stresses σ_{ei} (MPa) in the structural material as a function of the intensity of the applied external force, characterized by the ratio Fi/S (MPa), at a maximum allowable stress level of 160 MPa.

To identify the functional relationship between the model input parameters (Fi/S) and the corresponding structural responses (σ_{ei}), an approximating empirical equation was derived:

$$y_{\text{т}i} = a \cdot e^{bx_i} = 26{,}188 \cdot e^{0{,}311x_i} . \quad (3)$$

where x_i – influencing factors, F_i/S, MPa;

y_{ti} – output parameters, σ_{ti}, MPa.

Figure 7(d) presents a comparison between the outcomes of the numerical simulations and the analytical calculations. The evaluation indicates that the results derived from Equation (3) deviate only within the acceptable ranges defined by relevant standards, thereby validating the reliability of the employed computational methodology..

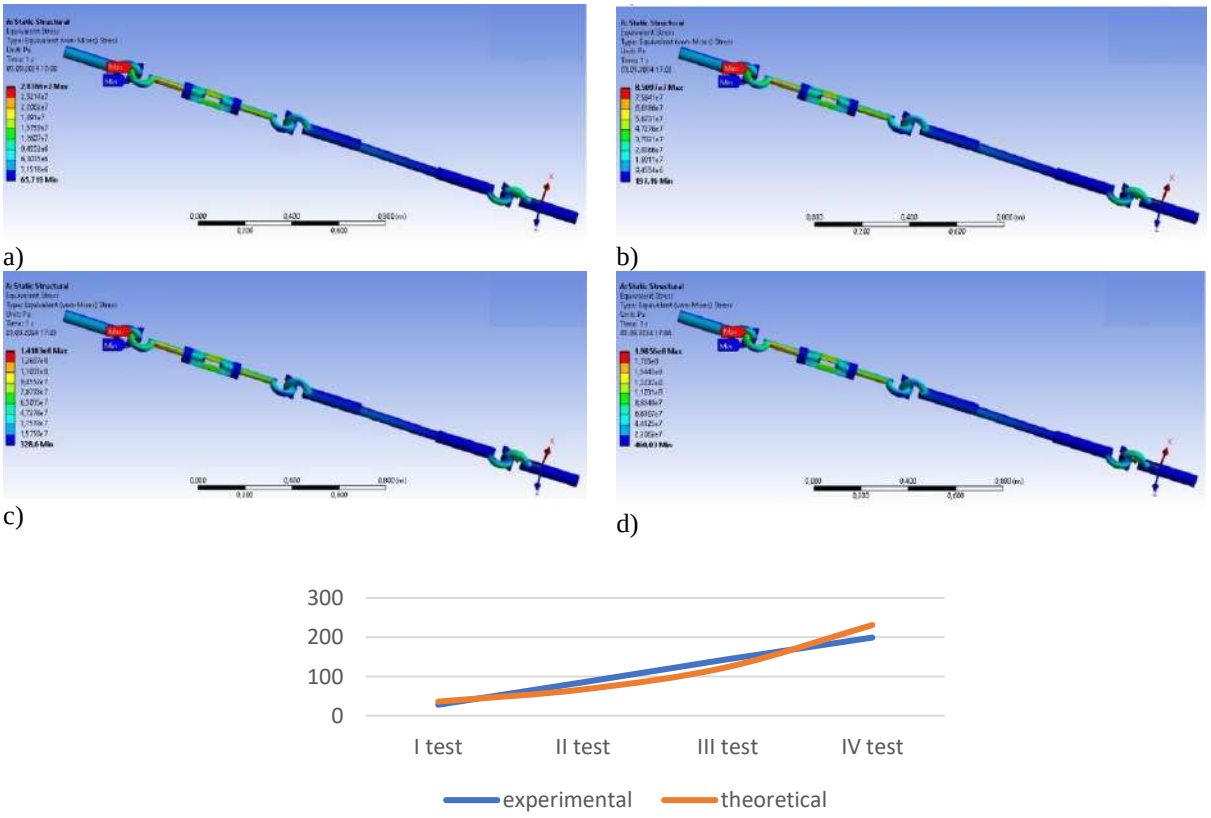

Fig. 7. – Simulation Test Results of a 3D Model Element of the Removable Equipment of Rail Transport Platforms (Rail Carriers) in the ANSYS Software Environment

The application of numerical modeling using the ANSYS software package enabled the evaluation of the maximum permissible force effects arising during the transportation of long rail strings exceeding 800 m in length along curved sections of railway track. Within a series of four computational scenarios, distributions of the stress–strain state were obtained, indicating that when the equivalent stress level does not exceed 160 MPa, the strength characteristics of the structure satisfy the established requirements.

A generalized analysis of the numerical experiment results demonstrated a high degree of agreement between the computational and analytical data, with discrepancies not exceeding 5%, which confirms the correctness and robustness of the proposed calculation model. At the same time, to further improve the accuracy of predicting limit loads, it is advisable to conduct extended simulation studies followed by the development of a specialized computational approach for determining allowable loads in the elements of detachable equipment of flat wagons (rail carriers). Implementation of this approach will enhance the reliability of safety assessments for the transportation of long rail strings (over 800 m) when negotiating circular curves on the railway network of the Republic of Kazakhstan.

Conclusions

The conducted study confirmed the feasibility of using the improved computational model and digital simulation in ANSYS to determine the maximum loads in the detachable equipment of rail transporters during the transportation of long welded rails along curved tracks. The simulation tests demonstrated a strong correlation between experimental data and theoretical calculations, which validates the reliability of the developed model. This provides a solid basis for considering the proposed methodology as an effective tool for assessing the strength and safety of structures under challenging operational conditions. The findings of this study may be utilized in engineering applications to refine design solutions, enhance the safe transport of extended welded rails, and contribute to the advancement of regulatory guidelines and technical norms within Kazakhstan’s railway sector.

References

[1] Tokayev K.K. Message of the Head of State Kassym-Jomart Tokayev to the people of Kazakhstan "Kazakhstan in the era of artificial intelligence: current challenges and their solutions through digital transformation"/ Official website of the President of the Republic of Kazakhstan Akorda, 2025. URL: https://www.akorda.kz/en/president-kassym-jomart-tokayevs-state-of-the-nation-address-to-the-people-of-kazakhstan-kazakhstan-in-the-era-of-artificial-intelligence-current-challenges-and-solutions-through-digital-transformation-1083029.

[2] Rozhkov A.B., Balabayev O.T., Nartov M.A. Development of Calculation Methods for Diesel Locomotives of Industrial Transport // Material and Mechanical Engineering Technology. – Karaganda, 2020, Vol. 2, Issue 2, pp. 21–25. URL: https://mmet.kstu.kz/download/articles/29062023033626_digest.pdf.

[3] Stoilov V., Sinapov P., Slavchev S., Maznichki V, Purgic S. Analysis of Lateral Forces for Assessment of Safety against Derailment of the Specialized Train Composition for the Transportation of Long Rails // Applied Sciences (Switzerland). URL: https://www.mdpi.com/2076-3417/14/2/860.

[4] Wikaranadhi P., Handoko Y. A. Curving Performance Analysis of a Freight Train Transporting 50-Meter-long Rail Using Multibody Dynamics Simulation //Journal of Engineering and Technological Sciences, 55(2), 2024. 189-199. URL: https://www.webofscience.com/wos/woscc/basic-search.

[5] Ju S.-H., Ro T.-I. Vibration and Derailment Analyses of Trains Moving on Curved and Can’t Rails //Appl. Sci. 2021, 11, 5106. URL: https://www.mdpi.com/2076-3417/11/11/5106.

[6] Diana G., Sabbioni E., Somaschini C., Tarsitano D., Cavicchi P., Di Mario M., Labbadia L. Full-scale derailment tests on freight wagons //Veh. Syst. Dyn. 2021, 60, 1849–1866. URL: https://www.tandfonline.com/doi/abs/10.1080/00423114.2021.1877745.

[7] Balabayev O.T., Rozhkov A.V., Askarov B.Sh., Kasymzhanova A.D., Beisembayev D.M. On the Issue of Determining Ultimate Loads During the Transportation of Long-Welded Rail Strings (800 m and longer) //Science and Technology of Kazakhstan. – Pavlodar: Toraighyrov University, 2024. – No. 2. – pp. 213-221.

[8]Wen Kexue, Ma Yukun, Li Shanpo, Zhang Changqing, Yang Guangquan. "Simulation and Experimental Research on Transporting 100 m Long Steel Rails Using Flatcars Passing Turnouts and Curves." Zhongguo Tiedao Kexue/China Railway Science (2022, Scopus percentile 33%), Volume 32, Issue 2, Pages 90-96, 2011. ISSN: 10014632. URL: https://www.scopus.com/record/display.uri?eid=2-s2.0-79955730726&origin=resultslist&sort=plf-f&src=s&sid=f221811fe2bd1b3b719886b4b41dbe53&sot=b&sdt=cl&cluster=scosubjabbr%2C%22ENGI%22%2Ct%2Bscosubtype%2C%22ar%22%2Ct&s=KEY%28long+rails%29&sl=15&sessionSearchId=f221811fe2bd1b3b719886b4b41dbe53.

[9] Kukulski J., Gołębiowski P., Makowski J., Jacyna-Gołda I., Żak J. Effective Method for Diagnosing Continuous Welded Track Condition Based on Experimental Research //Energies 2022, Volume 14, Issue 102, 2021. Article No. 28892. DOI: http://dx.doi.org/10.3390/en14102889.

[10] Petraska A., Jarasuniene A., Ciziuniene K. Routing Methodology for Heavy-Weight and Oversized Loads Carried by Rail Transport //Procedia Engineering, 2020, Volume 178, 589-596, DOI: http://dx.doi.org/10.1016/j.proeng.2017.01.114.

[11] Ibatov M.M., Balabaev O.T., Kassymzhanova A.D. Studying the Method of Loading Containers by Testing in the Software Environment // Material and Mechanical Engineering Technology. – Karaganda, 2021, Issue 4, pp. 36–39. URL: https://mmet.kstu.kz/download/articles/29062023033357_digest.pdf.

[12] Kassymzhanova A.D., Ibatov M.K., Balabaev O.T., Donenbaev B.S., Ilessaliyev D.I. Experimental Study of Maximum Stresses in the Stationary Hoist Design in the ANSYS Software Environment // Communications - Scientific Letters of the University of Žilina, 2022, Vol. 24, Issue 4, pp. B310–B318. URL: https://www.scopus.com/record/display.uri?eid=2-s2.0-85145364138&origin=recordpage.

Information of the authors

Balabayev Oyum Temirgalievich, c.t.s, professor, Abylkas Saginov Karaganda Technical University
e-mail: balabaev.ot@mail.ru

Mikhailov Valentin Feliksovich, c.t.s, docent, Abylkas Saginov Karaganda Technical University
e-mail: v.mihaylov@kstu.kz

Kassymzhanova Aidana Donenbaykyzy, PhD, acting professor, Abylkas Saginov Karaganda Technical University
e-mail: aidana_dak@mail.ru

Beisembayev Dias Madatovich, master of science, PhD student, Abylkas Saginov Karaganda Technical University
e-mail: d.beysembaev@ktu.edu.kz

Nurullaev Parakhat, master, PhD student, Tashkent State Transport University
e-mail: uer_tashiit@mail.ru

DOI 10.52209/2706-977X_2026_2_17 **IRSTI 55.22.19** **UDC 620.179.16**

Formation of Wear-Resistant Coatings by Surfacing in a Shielding Gas Environment

Kapkenova M.T. [1], Gabdyssalyk R.[1*], Kapayeva S.D. [1], Cieślik J.[2]
[1] D. Serikbayev East Kazakhstan Technical University, Ust-Kamenogorsk, Kazakhstan
[2]AGH University of Science and Technology, Krakow, Poland
*corresponding author

Abstract. This paper investigates the wear mechanisms of rotary mining cutters operating under abrasive and impact loading conditions and presents science-based approaches to improving their service life. During the study, gas metal arc welding (GMAW) hard-facing technology was applied to produce wear-resistant coatings using flux-cored wires EnDOtec DO351, EnDOtec DO332, and EnDOtec DO*11. Structural carbon steel C45, widely used in mechanical engineering, was selected as the base material. Hard-facing of experimental samples and cutting edges of rotary cutters were carried out using a CNC-controlled robotic three-axis system developed at AGH University of Science and Technology (Krakow, Poland). A comprehensive analyses, including metallographic, mechanical, and hardness were performed to determine the structural features and strength characteristics of the obtained coatings. In addition, the elemental composition of the deposited layers was analyzed using energy-dispersive spectroscopy (EDS). Microstructural analysis revealed the formation of chromium-rich carbide phases, which ensure high resistance of the coating to abrasive wear. Microhardness measurements showed that the hardness of the hard-faced layer significantly exceeds that of the base metal, reaching a maximum value of 1705 HV. The obtained results confirm the high efficiency of hard-facing technology in improving the wear resistance of rotary mining cutters and enhancing the reliability of mining machine working elements. The scientific novelty of this work lies in the comprehensive evaluation of the structural features of coatings obtained using GMAW technology and their influence on wear resistance.

Keywords: rotary mining cutter, hard-facing, wear resistance, hardness, flux-cored wire, GMAW, mechanical properties

Introduction

In the modern engineering industry, increasing the service life of machinery and equipment, especially in mining, is considered as one of the most important engineering tasks. Drilling tools and tangentially rotating ore cutting blades, operating in the conditions of an abrasive environment are subject to significant wear effects. As a result of gradual damage to the working surface, their original geometric shape changes, material consumption occurs, leading to premature failure of equipment. Such changes negatively affect the stability of the production process, increasing the cost of maintenance and replacement of parts.

The phenomenon of wear is considered a complex and multifactorial physico-mechanical process. Under abrasive action, solid mineral particles penetrate the metal surface, causing destruction of the material structure by micro-cutting and micro-bending mechanisms. In addition, as a result of dynamic impact loads, cracks are formed at the microstructure level, and their gradual increase reduces the strength of the material. In this regard, the problem of strengthening the surface and increasing the wear resistance of working bodies is of particular scientific and practical importance [1].

As one of the most effective wear-preventing solutions, melt plating technology is widely used. This method allows to form an alloy layer on the surface of the base material, with properties determined in advance, characterized by its high hardness and wear resistance. Such coatings take on the abrasive and shock effects that arise during operation and significantly slow down the destruction of the base metal. As a result, the service life of the part is extended and its reliability increases.

Gas Metal Arc Welding (GMAW) technology, implemented in a protective gas environment, is one of the most widely used methods in the smelting coating process. The main advantage of this technology is the ability to accurately adjust the parameters of heat input, due to which, the depth and structure of the melting zone are controlled. In addition, the GMAW process creates conditions for uniform and high-quality coating of surfaces of complex shapes, if combined with automated or robotic systems. This, in turn, ensures the stability of the technological process and increases the repeatability of the properties of the resulting coating.

The main goal of the research work is to increase the wear resistance of Rotary mining knives by the method of melting coating and a comprehensive assessment of the structural – phase State, as well as mechanical characteristics of the resulting coatings. To achieve this goal, in the course of experimental studies, the microstructure of the coating layers, hardness indicators and features of their distribution by thickness were determined.

The experimental part of the work consisted of several interrelated stages. At first, the base metal surface was subjected to mechanical processing and cleaned of impurities and oxide layers. After that, the melting coating process was carried out in the selected modes: parameters such as welding current, voltage, wire feed speed and protective gas consumption were optimized. In the process of coating, a layer of material was applied in layers and formed to the required thickness.

After the completion of the coating, the samples obtained were prepared for metallographic analysis: they were cut, sanded and polished. Microstructural studies were carried out using optical and electron microscopy methods, as a result of which phase changes and structural features in the composition of the coating were revealed. In addition, the distribution of mechanical properties in different areas of the coating layer was studied by measuring micro-strength. These measurements made it possible to assess the strength properties of the coating and determine the main indicators characterizing its wear resistance.

Assessment of the effectiveness of the implementation in production and the possibilities of application of the proposed technology in terms of increasing the operational resource of cutting tools and reducing operating costs in specific operating conditions of mining production.

In recent years, the international scientific community has paid special attention to the study of the microstructure and phase composition of connective coatings. In 2023 studies, Badisch and colleagues showed that the wear resistance of Chromium-based coatings directly depends on the morphology and distribution features of carbide Phases [3]. In 2024, García-León et al systematically studied the influence of welding parameters on microstructure formation and found that there is a correlation relationship between heat input energy and Carbide size. Chromium-rich powder wires contribute to the formation of abrasive wear-resistant carbide phases (Cr_7C_3, $Cr_{23}C_6$) [4]. Therefore, it is relevant to conduct research on melt coating technology.

For the machine-building industry of Kazakhstan, especially in the context of mining enterprises, increasing the wear resistance of equipment is considered one of the most urgent tasks from an economic point of view. Taking into account the peculiarities of local production, a scientifically based approach is required for the correct selection of effective packaging materials and melting coating parameters [5].

1. Materials and methods

Rotary is the identification and scientific justification of effective technological approaches aimed at increasing the wear resistance of mining knives. The object of the study was considered the laws of the influence of the technological parameters of the melting coating process and the chemical composition of wear-resistant coatings on the structural-phase State of the working surface of the Blades, the features of the microstructure, the level of micro-strength and tribological characteristics.

In the process of preparing experimental samples, structural carbon steel of grade 45, common in the mechanical engineering industry, was used as the main material (Figure 1).

Fig. 1. - The rotating performing body for rock destruction and the wear-resistant coating on the conical geometry mining knife: a) the general view of the rotating performing Body; B) the mining knife with a melt-coated coating.

The study considered Steel C45 (DIN 1.0503/ISO 683-1 1987) as the main material. This material is medium carbon structural steel and is widely used in Mechanical Engineering [6]. Table 1 presents the chemical composition of C45 steel recommended by the manufacturer.

Table 1. Chemical composition of C45 steel

Element	C	Si	Mn	P	S	Cr	Ni	Mo	Cu
Mass. %	0,42-0,50	0,15-0,35	0,50-0,80	<0,035	<0,035	<0,30	<0,30	<0,10	<0,30

The carbon equivalent (CE) lies between 0.52-0.82, depending on the calculation standard, which indicates the difficulty of welding the material.

The study looked at three different metal core powder wires from Castolin Eutectic: EnDOtec DO*351* (wire A), DO*332* (wire B) and DO*11 (wire C). All wires are designed for chrome-rich and abrasive working environments [6]. Table 2 presents the chemical composition of the wires.

Table 2. Chemical composition of powder wires

Wire	C(%)	Cr (%)	Si(%)	Mn(%)	Mo(%)	Ni(%)	Fe(%)
DO*351	4,5-5,2	26-30	0,8-1,2	0,5-1,0	0,5-1,5	<2,5	Waste
DO*332	3,8-4,5	22-26	1,0-1,8	0,8-1,5	1,0-2,0	<3,0	Waste
DO*11	5,0-5,8	28-32	0,5-1,0	<1,0	<1,0	<2,0	Waste

The diameter of all wires is 1.6 mm. Due to the metal core structure, the actual cross-section is slightly smaller and may vary in coil length [6].

The smelting coating process was carried out on robotic three-axis equipment with digital software control, located at EVH and the University of Science and technology (Poland). The unit is equipped with an additional fourth axis of rotation, which makes it possible to process complex spatial surfaces. The working area is 320 × 300 × 170 mm, and the moving speed of the melting coating head is adjustable in the range of 0.1–200 mm/s. A voltage of 22 V, A Current of 160-453 a, a coating speed of 400 mm/min and a wire feed speed of 3-10 m/min were used as technological parameters. A mixture of 82% argon and 18% carbon dioxide was used as a protective gas, and its consumption was kept at the level of 15 l/min [6].

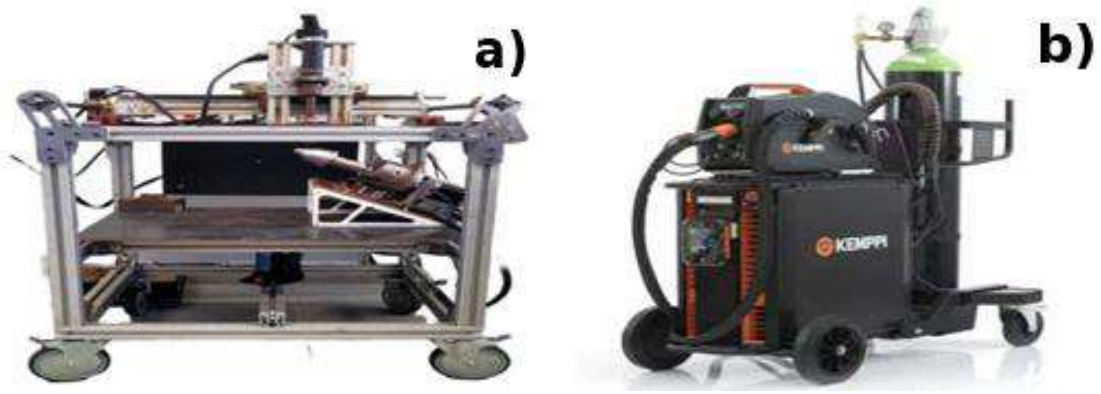

Fig. 2. - Equipment used in the smelting plating process: a) 4-axis test station for melting coating of welding joints (melting coating process); b) current source used in the research

The main technical means used in the study are presented in Figure 2. To carry out the experimental work, a four-axis test station for melting coating of welding seams was used, with the help of which all stages of the coating process were carried out in an automated mode. In addition, the Kemppi X8 semi-automatic complex was used as a source of welding current, according to which a wire feeder was introduced. This equipment is adapted for stable operation at high current values and can bring the current value up to 600 A under short-term load.

Such technical characteristics allow you to accurately control the melting coating process, including adjusting the heat input parameters. As a result, the structure of the formed coating layer becomes uniform, and conditions are created for a targeted change in its mechanical properties.

The technology of smelt plating by the GMAW method is distinguished by its versatility and wide application in production conditions. Among the main advantages of this approach are its technological simplicity, flexibility of application and relatively affordable cost of equipment.

There are two main types of the mentioned technology: MIG and MAG. The MIG (Metal Inert Gas) process is based on the protection of the welding area with inert gas, and in the MAG (Metal Active Gas) method, chemically active components are added to the protective gas composition. Inert gases usually include argon and helium or their mixtures, and carbon dioxide, oxygen, nitrogen, and hydrogen are used as active gases. In addition, various combinations of these gases are also widely used in the experiment, including formulations mixed together with argon or helium [7-8].

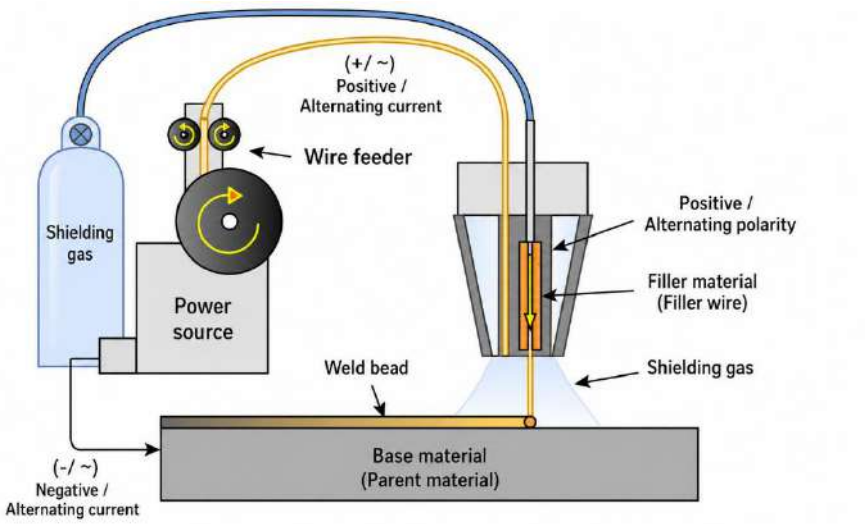

Fig. 3. - Diagram of the arc melting coating process using a melting electrode in a protective gas environment

In the course of this study, the GMAW method performed in a protective gas environment was used to implement the melting coating process, which made it possible to ensure the high quality, structural uniformity and wear resistance of the coating layer.

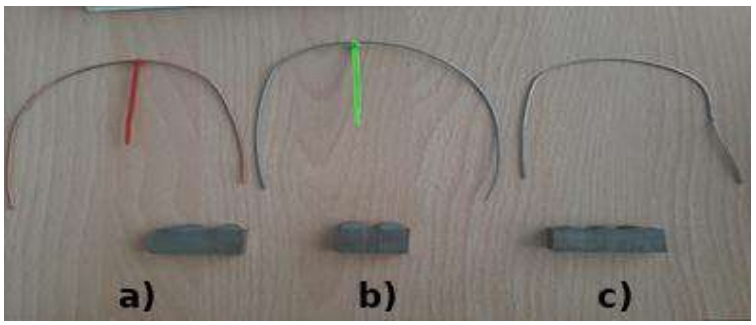

Fig. 4. - Experimental samples manufactured on the basis of EnDOtec DO351 (a), DO332 (b) and DO*11 (c) powder wires

Preparation of samples for macrostructural and hardness studies was carried out in the testing laboratory of the engineering profile "VERITAS" at D. Serikbayev ektu. As shown in Figure 4, the study examined three different brands of metal core powder wires.

The preparation of macroschliffs was carried out according to the standard metallographic methodology: coarse grinding, fine grinding, diamond polishing with slurry (9-1 microns) and treatment with 10% nitric acid.

Fig. 5. - Equipment for metallographic research: a) sample preparation device; b) optical microscope

In the work, the elemental composition of the coated layers was determined by the method of energodispersion analysis, and the micro-density was measured by the Vickers method. These studies make it possible to comprehensively

assess the structural features and mechanical properties of melt-coated coatings. Metallographic studies were carried out under the Olympus BX51 microscope (Japan) with a computing station equipped with the Mineral C7 program. In addition, the method of X – ray energodispersion microanalysis (EDX-Energy Dispersive X-Ray microanalysis) was used (Figure 5).

2. Results and discussion

The metallographic and energy-intensive studies made it possible to determine the structural features and elemental composition of the molten coating layer.

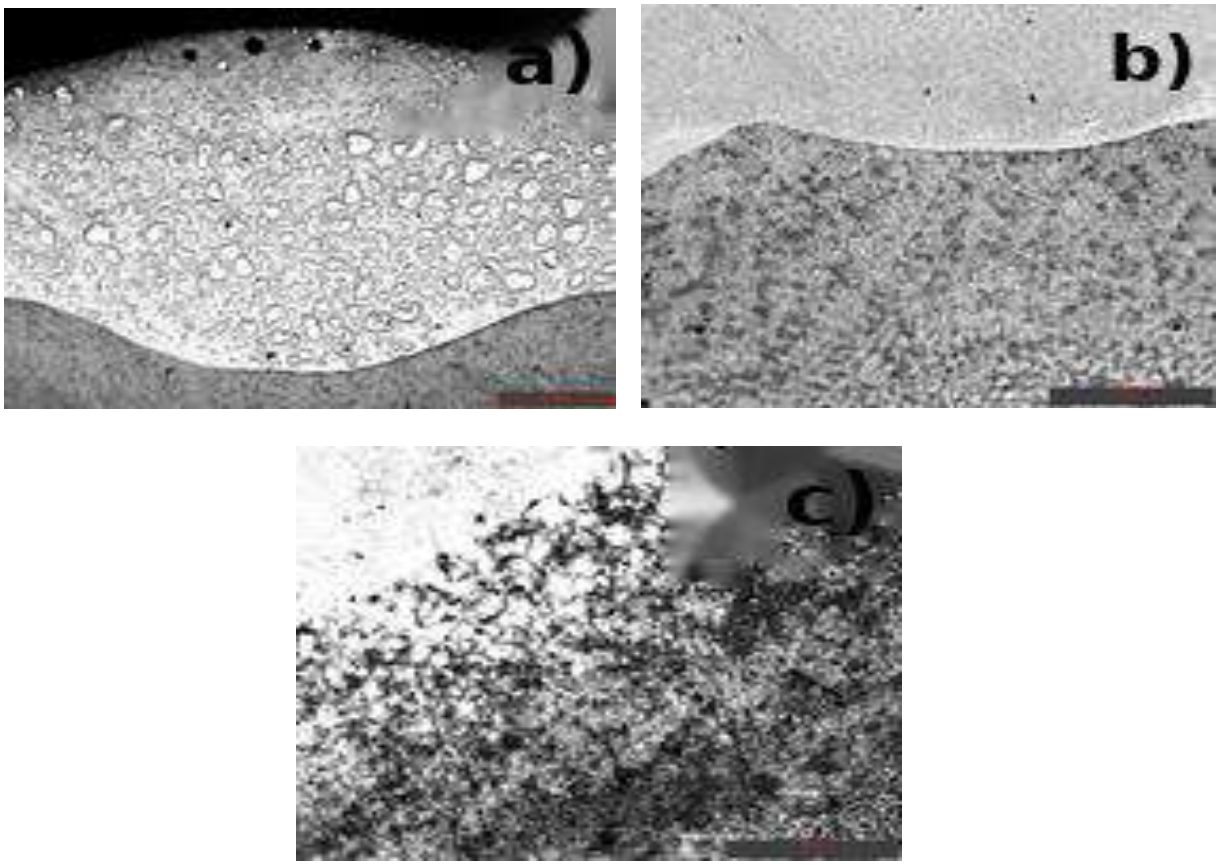

Fig. 6. - Microstructure of the molten coated layer: a) general structure of the coated layer; b) microstructure of the transition zone; c) distribution of carbide phases

The results of microstructural analysis showed that a heterogeneous structure was formed in the melt-coated layer, characterized by a uniform distribution of structural components. This structure is distinguished by a harmonious combination of Matrix and solid phases and provides high wear resistance properties of the coating [9].

Figure 6 shows the microstructure of the coating layer obtained as a result of melt coating. In part 6a of the figure, the general structure of the coated layer and the Boundary Zone with the base metal are clearly traced. In this area, it is seen that a metallurgical bond is formed between the coated layer and the base metal, which ensures the adhesive strength of the coating. Part 6b of the figure depicts the structure of the transition zone between the coated layer and the base metal. In this zone, there is a gradual change in the structure, which is associated with diffusion processes resulting from the introduction of heat and contributes to reducing the concentration of stresses. In part 6c) of the figure, solid carbide phases are clearly visible, evenly distributed throughout the Matrix. These phases are mainly chromium-rich carbides and provide high hardness and abrasion resistance of the coating. The dispersed distribution of carbide phases affects the improvement of the mechanical properties of the coating and the formation of a stable structure during Operation. The results of energodispersion X-ray microanalysis (EDX) showed that the studied coating is dominated by Iron (Fe) as the main element, as well as Silicon (Si) and a small amount of other alloying elements. It has been found that in most spectra, the iron content reaches the range of 90-98%, which proves the formation of an iron-based structure in the molten coating layer. The presence of silicon and other elements is associated with the chemical composition of the powder wire used and contributes to increasing the hardness and wear resistance of the coating [10,11, 12].

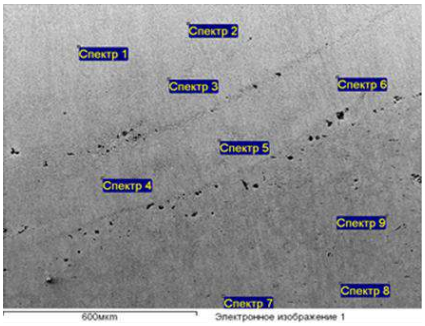

Спектр	В стат.	Si	Cr	Mn	Fe	Итог
Спектр 1	Да	1.74	5.57	0.84	91.85	100.00
Спектр 2	Да	1.88	5.52	0.72	91.88	100.00
Спектр 3	Да	1.81	6.14	1.01	91.04	100.00
Спектр 4	Да	1.51	4.12	1.00	93.37	100.00
Спектр 5	Да	1.24	4.89	0.71	93.16	100.00
Спектр 6	Да	1.48	4.52	0.73	93.27	100.00
Спектр 7	Да	0.15	0.00	0.82	99.03	100.00
Спектр 8	Да	0.17	0.00	0.83	99.00	100.00
Спектр 9	Да	0.00	0.00	0.42	99.58	100.00
Среднее		1.11	3.42	0.79	94.69	100.00
Станд. отклонение		0.78	2.63	0.17	3.48	
Макс.		1.88	6.14	1.01	99.58	
Мин.		0.00	0.00	0.42	91.04	

a)

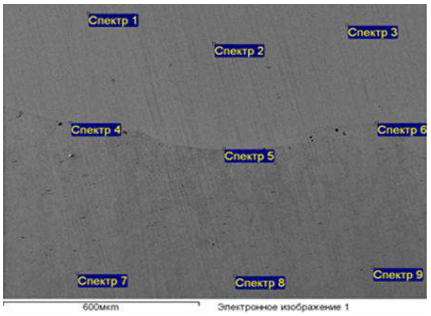

Спектр	В стат.	Si	Cr	Mn	Fe	Mo	Итог
Спектр 1	Да	0.86	31.55		63.86	3.72	100.00
Спектр 2	Да	0.79	38.63		56.95	3.63	100.00
Спектр 3	Да	1.04	22.48		74.25	2.23	100.00
Спектр 4	Да	0.63	7.30	0.53	90.83	0.71	100.00
Спектр 5	Да	0.69	13.09	0.00	84.97	1.25	100.00
Спектр 6	Да	0.76	15.16	0.00	82.72	1.36	100.00
Спектр 7	Да	0.00		2.05	97.95		100.00
Спектр 8	Да	0.34		0.49	99.17		100.00
Спектр 9	Да	0.31		0.77	98.92		100.00
Макс.		1.04	38.63	2.05	99.17	3.72	
Мин.		0.00	7.30	0.00	56.95	0.71	

b)

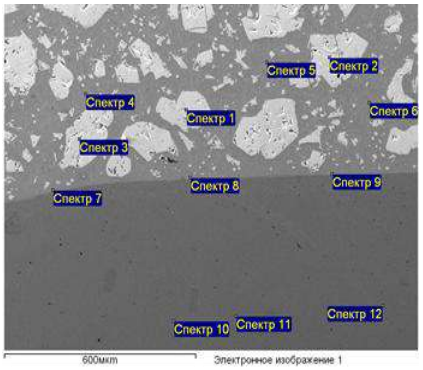

Спектр	В стат.	Si	Ti	Mn	Fe	Ni	W	Итог
Спектр 1	Да						100.00	100.00
Спектр 2	Да						100.00	100.00
Спектр 3	Да						100.00	100.00
Спектр 4	Да		2.86		10.90	62.55	23.69	100.00
Спектр 5	Да	0.88			16.82	76.41	5.88	100.00
Спектр 6	Да				15.26	78.85	5.89	100.00
Спектр 7	Да				39.14	54.96	5.90	100.00
Спектр 8	Да				31.43	61.23	7.35	100.00
Спектр 9	Да				52.49	47.51		100.00
Спектр 10	Да			1.41	98.59			100.00
Спектр 11	Да			1.78	98.22			100.00
Спектр 12	Да			1.53	98.47			100.00
Макс.		0.88	2.86	1.78	98.59	78.85	100.00	
Мин.		0.88	2.86	1.41	10.90	47.51	5.88	

c)

Fig7. - SEM-images of characteristic areas of molten-coated layers and local EDS-analysis points are shown: a) EnDOtec DO351, b) DO332 and c) DO*11.

Figure 7 presents the results of Energodispersion (EDS) spectral analysis aimed at determining the chemical composition of the molten coating layer. For samples obtained using EnDOtec DO351 wire, the iron-based composition was found to prevail. At individual analysis points, the silicium content is 0-1.88 wt.%, Chromium-0-6.14 wt.%, manganese-0.42-1.01 wt.% of iron as the main component is 91.04–99.58 wt.% observed in the % range. Average estimated values Si – 1.11 wt.%, Cr - 3.42 wt.%, Mn - 0.79 wt.% and Fe - 94.69 wt.%. These indicators mean that the coating has a relatively homogeneous structure and a low level of alloying [13].

In coatings obtained on the basis of EnDOtec DO332 wire, a pronounced unevenness of the elemental composition was recorded. In particular, the chromium content varied between 7.30 to 38.63 wt.%, molybdenum fluctuates from 0.71 to 3.72 wt.%, and iron varied from 56.95 to 99.17 wt.%. At the same time, the manganese content reached up to 2.05 wt.%. Such differences indicate that areas with varying degrees of alloy are formed in the coating layer. This phenomenon is explained by the specificity of the DO332 wire, that is, the formation of an austenitic Matrix and the presence of chromium and Cr–Mo carbides in it. However, it should be noted that the EDS method used does not allow to fully determine the exact nature of the phases.

The highest heterogeneity of the chemical composition was observed in the samples obtained on the basis of the endotec do11 wire. In some regions, the tungsten content is significantly higher, varying within the range of 5.88–23.69 wt.%. At the same time, the proportion of iron ranged from 47.51 to 78.85 wt.% and manganese varied between 10.90 and 52.49 wt.%. In layers close to the base metal, the iron content increased to 98.22–98.59 wt.%, manganese emained at the level of 1.41–1.78 wt.%. These results show that there are tungsten-rich solid phases in the coating structure and that the composition gradually changes in thickness (gradient character). Such a feature corresponds to the chemical and structural properties of the wire DO11 used.

The studies carried out have shown that melt coating technology allows you to form a stable and high-quality coating that has the necessary structural and mechanical characteristics. The results obtained prove that the presented materials can be effectively used in increasing the wear resistance of the working bodies of mining machines.

According to the data presented in Table 3, the highest micro-strength indicator was recorded in sample №3 (EnDOtec DO351) with a value of 1705 HV0.1, which is explained by the high strength of the initial solid carbide phases. At the same time, the microhardness of the matrix area is approximately at the level of 445 HV0.1, providing sufficient viscosity of the material and resistance to impact loads. In samples №1 (671.4 HV0.1) and №2 (625.7 HV0.1), it was found that the average hardness of the coating layer is several times higher compared to the base material (C45 steel, about 200 HV0.1).

Table 3. Results of micro-strength measurements of Melt-coated samples ($HV_{0.1}$)

Example	Melting plating material	Microhardness of the Matrix near the sewing area $HV_{0.1}$	Micro-strength of the melt-coated layer $HV_{0.1}$	Explanation
№1	EnDOtec DO*11	320.7	671.4	Average hardness of molten coated metal
№2	EnDOtec DO*332	310.2	625.7	Average hardness of molten coated metal
№3	EnDOtec DO*351	248.0	1705.0	Solid carbide phase measurement (Cr_7C_3)

Conclusion

The results of the conducted study showed that melt-coated coatings formed using GMAW technology, implemented in a protective gas environment, significantly increase the wear resistance of Rotary mining tools.

As a result of metallographic analysis, it was found that a heterogeneous structure was formed in the coating layer, characterized by a uniform distribution of the matrix and solid carbide phases. The gradual change of structure in the transition zone ensures a strong metallurgical bond between the base metal and the coating.

The results of the energo-dispersion spectral analysis showed that the coating contains iron, chromium, tungsten and other alloying elements, ensuring high hardness and resistance to abrasive wear of the coating.

It was found as a result of micro-hardness measurements, that the hardness of the melt-coated layer is several times higher than that of the base metal. The highest value reaches the level of 1705 HV0.1, and it has been proven that this is associated with the formation of carbide phases.

Thus, the use of GMAW technology makes it possible to extend the service life of Rotary mining knives, increase the reliability of their operation and reduce production costs. The presented technology is suitable for use in industrial conditions and appears to provide a cost-effective solution.

This study will be continued, and in-depth analysis of its results plus scientifically substantiated conclusions will be presented in full in the doctoral dissertation work of Kapkenova M. T.

Funding: This research was funded by the Science Committee of the Ministry of Science and Higher Education of the Republic of Kazakhstan (grant no. AP22683698).

References

[1] Sagyndykov Zh.M., Burkitbaev M.M., Kaliev B.S. Tau-ken zhabdyqtarynyñ tozu mehanizmderi zhäne olardyñ aldyn alu ädisteri [Wear mechanisms of mining equipment and methods of their prevention] //Qarağandy Tehnikalyq Universitetiniñ Habarshysy, 2023, no. 2(110), P. 54–62.

[2] Kapkenova M.T., Kapayeva S.D., Gabdyssalyk R., Cieślik J., Bekmyrza Zh.A. Tozuğa tözimdi zhabyndardy balqytyp qaptau әdisімен ainalmaly tau-ken-shahta pyshaqtarynyñ resursyn artyru [Increasing the service life of rotary mining picks by hardfacing wear-resistant coatings] //Journal of Engineering Science, 2026, no. 1. DOI: 10.51885/3134-8009_JES,_2026,_1,_11.

[3] Aubakiro, Zh.K., Sembaev, N.S., Nurlanov, E.K. Qazaqstannyñ tau-ken önerkäsibinde tozuğa tözimdi zhabyndardy qoldanu perspektivalary [Prospects for the use of wear-resistant coatings in the mining industry of Kazakhstan] //QazUTZU Habarshysy, 2023, no. 5(145), P. 67–74.

[4] Pawlik, J., Cieślik, J., Bembenek, M., Góral, T., Kapayeva, S., Kapkenova, M. On the influence of linear energy/heat input coefficient on hardness and weld bead geometry in chromium-rich stringer GMAW coatings //Materials, 2022, vol. 15, no. 17, article 6019. DOI: 10.3390/ma15176019.

[5] Bisenov E.I., Abdrakhmanov, S.T., Zhunisov, K.K. Tau-ken zhabdyqtaryn dänekerleu tehnologiyalary [Welding technologies for mining equipment] //Qazaqstan Tau-Ken Zhurnaly, 2024, no. 3(182), P. 45–52.

[6] Nazarbaev, T.A., Kozhakhmetov, E.A., Ospanov, D.S. Mashina bölshekteriniñ tozuğa tözimdiligin dänekerleu әdisімен artyru [Improving the wear resistance of machine parts by welding method] //KarTU Habarshysy, 2023, no. 4(112), P. 89–97.

[7] Smagulov D.U., Abilov, B.T. GMAW tehnologiyasymen alyngan hromdy zhabyndardyñ mikroqurylymy [Microstructure of chromium coatings produced by GMAW technology] //Metallurgiya zhäne Materialtanu, 2024, no. 1(38), P. 23–31.

[8] Seitkaziev A.Kh., Nurbosynov D.N. Qarağandy oblysy кәсіпорындарynda zhabyn tehnologiyalaryn engizu täzhiribesi [Experience in implementing coating technologies at enterprises of Karaganda region] //Qazaqstan Ken Öndirisi, 2024, no. 1(89), P. 78–85.
[9] Mrowiec L.B. et al. Influence of dilution on wear resistance of hardfaced coatings in mining applications //Materials, 2023, vol. 16, no. 3, article 1123. DOI: 10.3390/ma16031123.
[10] Fernández J., García A. Laser cladding of Ni-based alloys for mining tools //Materials & Design, 2018, vol. 142, P. 312–320. DOI: 10.1016/j.matdes.2018.02.047.
[11] Zharkevich O., Nurzhanova O., Bessonov A., Naboko Ye, Abdugaliyeva G., Taimanova G., Nikonova T. Simulation of the distribution of temperature, stresses and deformations during splined shafts hardfacing //Journal of Applied Engineering Science, 2023, 21(3), P.837–845
[12] Badisch, E., Kirchgaßner, M. Microstructure and wear resistance of chromium-rich hardfacing alloys //Surface and Coatings Technology, 2023, vol. 454, article 129167. DOI: 10.1016/j.surfcoat.2023.129167.
[13] Isagulov A., Akberdin A., Sultangaziyev R., Kim A., Kulikov V., Isagulova D. Diagram of equilibrium phase composition of Fe–C–Si–B system // Metalurgija, 2016, 55, 3, 305-308

Information of the authors

Kapkenova Madina Turlybekovna, doctoral student, D. Serikbayev East Kazakhstan Technical University
e-mail: mkapkenova@ektu.kz

Gabdyssalyk Riza, PhD, associate professor, D. Serikbayev East Kazakhstan Technical University
e-mail: riza.gabdyssalyk@mail.ru

Kapayeva Sarken Dzhulgazyvna, c.t.s., professor D. Serikbayev East Kazakhstan Technical University
e-mail: sarkenkapayeva@yahoo.com

Cieślik Jacek , PhD, professor, AGH University of Science and Technology, Krakow, Poland
e-mail: cieslik@agh.edu.pl

DOI 10.52209/2706-977X_2026_2_25 **IRSTI 55.01.77** **UDC 658.984**

A Methodology for Optimizing Material Flows in Mechanical Engineering Enterprises Based on Big Data Technologies

Zhetessova G.S.[1], Zharkevich O.M.[1], Kozhanov M.G.[1], Khrustaleva I.N.[2], Buzauova T.M.[1*]
[1]Abylkas Saginov Karaganda Technical University, Karaganda, Kazakhstan
[2]Peter the Great St. Petersburg Polytechnic University, St. Petersburg, Russia
*corresponding author

Abstract. This paper presents the development of a digital model of the production process at a mechanical engineering enterprise, aimed at improving management efficiency using Big Data technologies and multi-criteria optimization methods. The structure of a machine shop was formalized, identifying the main functional elements of the production system, including production areas, buffers, product flow routes, and intra-shop logistics. Parametric models of production units were developed, enabling the assessment of throughput, equipment utilization, work-in-progress volumes, and operating costs.The study analyzed the influence of machining process parameters on surface quality indicators. Predictive dependences of machining quality on cutting speed, feed rate, vibration level, spindle power, and tool wear were constructed. Three-dimensional models of surface roughness variations and heat maps of equipment utilization were developed, enabling the identification of bottlenecks in the production process. An intelligent methodology for optimizing a production system is proposed, based on machine learning, multi-criteria analysis, and digital modeling. The obtained results confirm the possibility of applying the developed approach to creating digital twins of production processes and improving the management efficiency of mechanical engineering enterprises.

Keywords: Big Data, digital model, digital twin, mechanical engineering enterprise, multi-criteria optimization, production process, parameterization, machine learning, work in progress, workload heat map.

Introduction

In today's evolving mechanical engineering industry, improving the efficiency of production processes is becoming a priority for industrial enterprises. Increased competition, rising demands on product quality, reduced manufacturing lead times, and the need to quickly respond to changes in the production program require the implementation of intelligent production system management methods [1]. This problem is particularly pressing for multi-product and single-item production [2], where process routes are characterized by high variability, uneven equipment loading [3], and significant volumes of work in progress. Under these conditions, optimization of material flows is particularly important, ensuring the consistency of process operations, rational resource allocation, and the stable functioning of the production system.

Material flows in mechanical engineering represent the combined movements of blanks [4], semi-finished products, tools [5], fixtures, and auxiliary resources between different production areas [6]. The efficient organization of these flows directly impacts the duration of the production cycle, equipment loading, operating costs, and the quality of the manufactured products [7]. Insufficient synchronization of process operations leads to downtime, the accumulation of work in progress, the formation of bottlenecks, and a decrease in overall enterprise productivity. Therefore, optimizing the structure and parameters of material flows is a key area for improving production processes at mechanical engineering enterprises.

The current development of digital technologies, industrial automation systems, and the Industry 4.0 concept are creating the preconditions for the transition to intelligent production process management based on big data analysis [8]. The use of Big Data technologies enables the collection, processing, and analysis of information on equipment status, process mode parameters, production area loads, product quality, and material flow in real time. The use of data mining and machine learning methods enables the identification of hidden patterns, forecasting the state of a production system, and the development of adaptive solutions for production flow management [9].

Scientific research devoted to the optimization of production processes [10] examines various approaches to improving the performance of mechanical engineering enterprises, including mathematical modeling, [11] digital design, multi-criteria optimization, and the construction of digital twins of production systems [12]. Particular attention is paid to synchronizing process operations [13], reducing the volume of work in progress, balancing equipment loads, and ensuring the stability of the production process [14] in the face of changing production factors. However, existing approaches are often focused on solving individual local problems and do not provide for the comprehensive integration of process parameters, production logistics, and analytical data processing tools into a single intelligent material flow management system.

In this regard, a pressing scientific challenge is the development of a methodology for optimizing material flows at mechanical engineering enterprises based on Big Data technologies. This methodology provides a comprehensive analysis of the production system, formalization of its structural elements, and the application of intelligent data processing methods to improve the efficiency of production process management. The development of such a methodology requires

the creation of parametric models of production areas, the development of mechanisms for analyzing equipment loading, assessing the throughput of process routes, and identifying factors that influence the quality of processing and the productivity of the production system [15].

1. Research methology

The research methodology is based on systems analysis, mathematical modeling, data mining, and multi-criteria optimization of production processes. Parametric models were developed to calculate throughput, cycle time, and work-in-progress volume. The study focused on the production route for a flange-type part. Machine learning methods were used to analyze the processing quality and operational efficiency of the production system, and the results were visualized using 3D models and equipment utilization heat maps.

1.1 Mechanical processing section

Here, a single production cell is a group of identical workstations (for example, a turning or drilling section), and the optimization parameters are the number of workstations, average workload, order distribution, and reserves.

The parameterized model will look like this:

$$THU = (M_U \cdot 60/CT_U^{avg}) \cdot \eta \quad (1)$$

where THU - throughput capacity of the node, pcs/h,

M_U - number of workstations/machines in the unit,

CT_U^{avg} - average cycle time per element (min),

η - technical readiness coefficient (uptime).

1.2 General warehouse

WIP Pool, where the single production cell is a centralized warehouse/buffer for shift batches, and the optimization parameters are turnover, average time, and availability index.

The parameterized model will look like this:

$$DB = f(KB,THin,THout) \quad (2)$$

1.3 Workshop

Shop-Floor Level, where a single production cell is the collection of all routes, nodes, and buffers, and the optimization parameters are global WIP, turnover, balancing, and energy profile.

The parameterized model will look like this:

$$CTtotal = \sum(u=1,N)CTu+\sum(b=1,M)D_B+ \sum(tr)Ttrans \quad (3)$$

$$Ctotal=\sum(u)(Cenergy+Cwage+Ctool+Cmaint) \quad (4)$$

Cost model:

$$OPEXu=Cenergy \cdot t+Ctool^{use}+Clabor+Crepair. \quad (5)$$

Table 1 presents the main variables and parameters of the workshop.

Table 1. Main variables and parameters of the workshop

Designation	Description
(CT_i)	Average cycle time in section (i), min
(TH_i)	Section capacity (i), part/hour
(\rho_i)	Equipment loading at site (i), share
(WIP_i)	Work in progress at site (i), parts
(Q_i)	Yield in section (i), %
(OPEX_i)	Operating costs at site (i), USD/day
(E_i)	Energy consumption, kW·h
(K_{ij})	Buffer size between sections, parts

Therefore, the structural elements of the workshop can be represented in the form of the following dependencies:

- production areas (units): $Ui \in \{ U\text{turning}, U\text{milling}, U\text{grinding}, U\text{control}\}$;
- buffers/warehouses between sections: Bi,j;
- product movement routes: $R=\{U1 \rightarrow U2 \rightarrow ... \rightarrow Un\}$;
- logistics/transport: intra-shop movements Tij.

The workshop can be represented as a directed graph:

$$G=(V,E),\ V=\{U1,U2,...,Un\},\ E=\{(Ui,Uj)\} \quad (6)$$

Each edge $(Ui,)$ contains:
- buffer Kij;
- travel time $Ttransij$.

The visual model of the workshop structure is presented by the code:

```
[Warehouse]
  ↓
[Lathe unit] --→ [Milling unit] --→ [Grinding unit] --→ [Control]
  ↓          ↓          ↓
 K12        K23        K34          ...
```

Each node contains:
- machines Mi,
- processing parameters v, s, ap,
- technical constraints,
- queue and buffer.

Using a flange-type part as an example, a calculation for the structural elements of the workshop was obtained (Table 2).

Table 2. Calculation of structural elements of the workshop

Plot	CT_i (min)	M_i (machine tools)	η (accessibility)
Lathe	6.5	3	0.95
Milling	5.0	2	0.90
Drilling	4.5	2	0.92
Control	2.0	1	0.88

The throughput of the TH is the bottleneck of the milling machine, which limits productivity (Table 3).

Table 3. Section capacity

Plot	TH_i (part/hour)
Lathe	≈ 26.31
Milling	≈ 21.6
Drilling	≈ 24.53
Control	≈ 26.4

Work in progress is distributed efficiently, without overload (Table 4).

Table 4. Average number of unfinished parts

Plot	WIP_i (unit)
Lathe	≈ 2.85
Milling	≈ 1.80
Drilling	≈ 1.84
Control	≈ 0.88

The developed shop-floor parametric model enables multi-criteria optimization of the production process, as well as a comprehensive assessment of equipment utilization, manufacturing costs, overall operational efficiency, and product quality indicators. This model creates the prerequisites for the creation of digital twins of production routes and supports the implementation of adaptive methods for planning and optimizing material flows in real time.

The resulting parametric model of the production site defines the computational and structural basis for implementing multi-criteria optimization. However, the effectiveness of its practical application directly depends on the correct selection and formalization of evaluation criteria. In the context of multi-parameter technological processes, a key aspect is the transition from describing the structure and parameters of the production system to quantitatively assessing its performance. The use of formalized criteria allows for linking the parameters of process modes and organizational characteristics of the production process with optimization targets, ensuring the comparability of alternative management decisions.

Based on the developed system of criteria, analytical and predictive analysis becomes possible, including the construction of dependencies between output quality indicators and key production process parameters. This approach creates the preconditions for the application of forecasting and optimization algorithms, which is implemented in the further presentation.

Prediction code:

```
import matplotlib.pyplot as plt
import seaborn as sns

# Add model predictions to a DataFrame
X_test_copy = X_test.copy()
X_test_copy['quality_predicted'] = model.predict(X_test)

# Plot graphs of quality dependence on each parameter
fig, axes = plt.subplots(2, 3, figsize=(18, 10))
axes = axes.flatten()

for idx, column in enumerate(X.columns):
    sns.scatterplot(
        ax=axes[idx],
        x=X_test_copy[column],
        y=X_test_copy['quality_predicted'],
        alpha=0.6,
        color="teal"    )
    axes[idx].set_title('quality vs {column}')
    axes[idx].set_ylabel('quality forecast)
    axes[idx].set_xlabel(column)

# Delete the empty last cell
fig.delaxes(axes[-1])
plt.tight_layout()
plt.show()
```

2.Results and discussion

The results of the study of the influence of the main technological parameters on the quality indicators of surface treatment are presented in Figure 1.

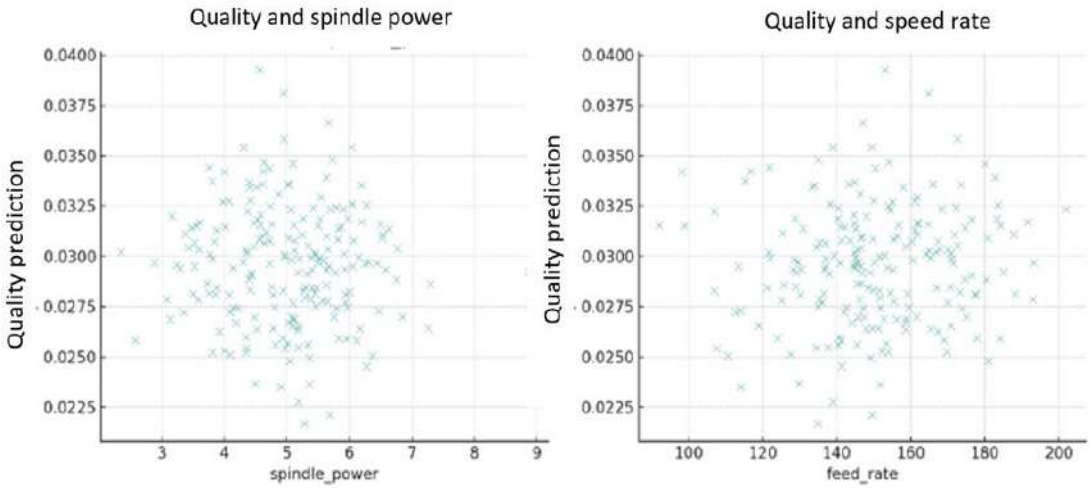

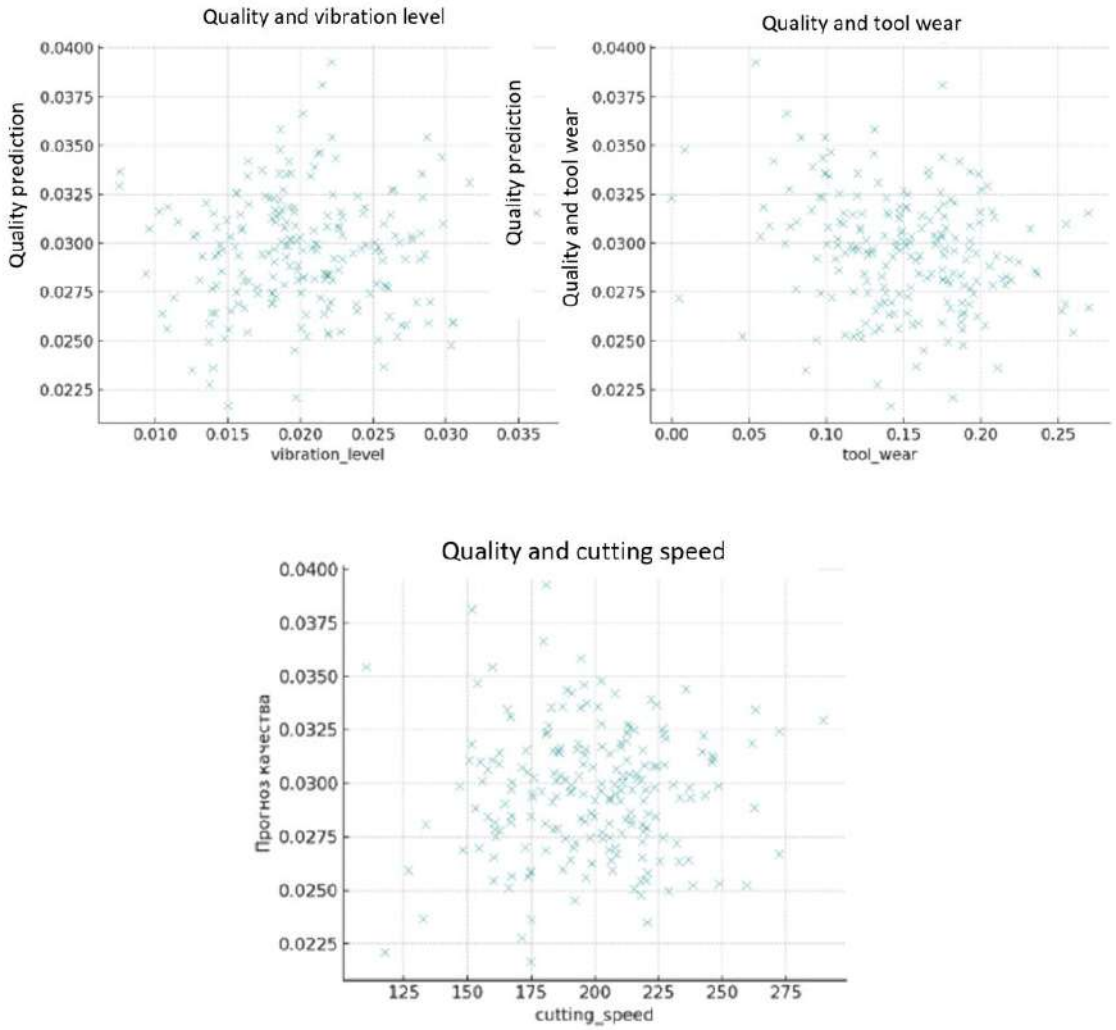

Fig. 1. - Quality dependencies on the mechanical processing modes of the technological process

Based on the analysis of the presented graphical dependencies (Figure 1), the following conclusions can be drawn regarding the influence of the main process parameters on surface finish quality:

- spindle power has a noticeable, but not dominant, effect on the quality of the formed surface. In the range up to approximately 6.5 kW, changing this parameter does not lead to a significant deterioration in roughness. However, when this threshold is exceeded, a tendency toward an increase in surface defects is observed, which is likely due to increased dynamic loads and heat generation in the cutting zone;

- feed rate is a significant factor determining machining quality. An increase in feed rate is accompanied by an increase in the roughness parameter Ra, indicating a deterioration in surface quality. For high quality machining requirements, it is advisable to limit the feed rate to no more than 160 mm/min, since further increases in this parameter lead to a sharp decrease in quality.

- cutting speed exhibits a pronounced nonlinear relationship with quality indicators. An analysis of the graphs reveals an optimal cutting speed range of 180–220 m/min, which achieves the most favorable combination of cutting conditions and surface quality. Deviations from this range are accompanied by deterioration in machining results.

- vibration level is the most sensitive and critical parameter in terms of machining quality. Even a slight increase in vibration amplitude, for example, from 0.02 to 0.03, leads to a sharp increase in surface roughness and the appearance of defects. This indicates the dominant role of the dynamic stability of the process system in determining surface quality.

- cutting tool wear has a consistent and virtually linear effect on machining quality. As wear increases, surface roughness consistently increases. At wear values exceeding 0.2 mm, the likelihood of producing a surface with unsatisfactory quality becomes extremely high, indicating the need for timely tool replacement or repair. A three-dimensional dependence (Figure 2) of the machining quality indicator, expressed through the surface roughness parameter *Ra*, on the main machining parameters - cutting speed and feed rate is constructed. The visualization is presented as a spatial surface, allowing for a clear depiction of the combined influence of these factors on surface quality.

In this model, the X-axis corresponds to the cutting speed expressed in m/min, the Y-axis to the feed rate in mm/min, and the Z-axis to the surface roughness value *Ra*. This 3D dependence allows for the identification of areas of optimal cutting mode combinations that achieve minimal roughness values, as well as areas of parameters that lead to deterioration in machining quality.

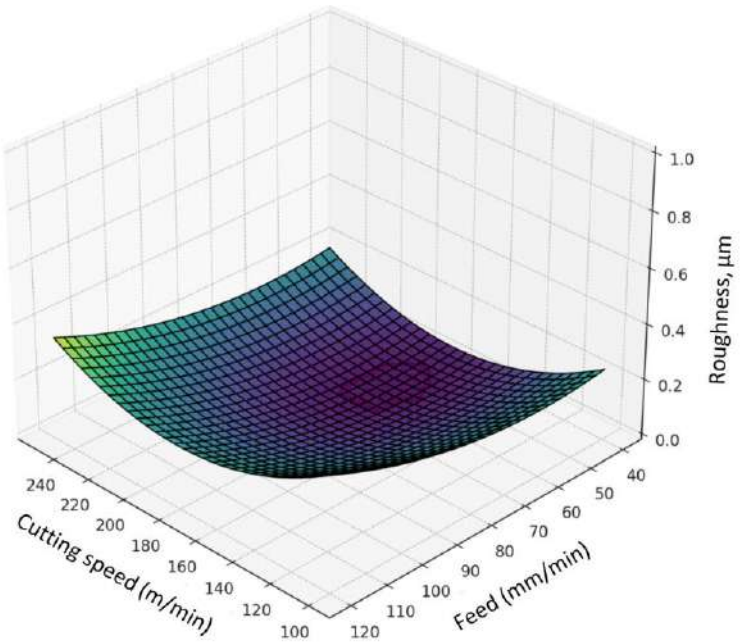

Fig. 2. - Three-dimensional dependence of the processing quality indicator expressed through the surface roughness parameter *Ra*

An analysis of the graphical dependence shows that the greatest risk in terms of machining quality is posed by conditions in which the surface roughness parameter Ra exceeds 0.03, which is outside the permissible limits. Operating the process in these conditions results in a surface with unsatisfactory quality characteristics and requires prompt adjustment of the machining parameters.

To prevent deterioration in surface quality and stabilize the machining process, it is advisable to implement daptive adjustment of the process parameters. Specifically, a 10–20% reduction in feed rate is recommended, which reduces the height of surface irregularities. Additionally, the cutting speed should be adjusted toward the nominal value of approximately 180 m/min, which ensures the most stable cutting process. Monitoring the condition of the cutting tool is also essential, as increased wear is a key factor in increasing roughness and the appearance of surface defects.

As part of the study, the structural elements of the production shop were parameterized for the manufacture of a flange-type part. Parameterization encompasses the key elements of the production system, including process equipment, workstations, workpiece and semi-finished product flows, and the relationships between individual operations along the process flow. Implementing this stage allows us to formalize the shop floor structure and represent it as a set of parameters suitable for subsequent analysis, modeling, and optimization of the production process.

Code for loading machines has been created:

```
import pandas as pd
import numpy as np
import seaborn as sns
import matplotlib.pyplot as plt
# Example of machine loading data
data = {
  'Machine': [' Machine _1', ' Machine _2', ' Machine _3', ' Machine _4', ' Machine _5'],
  '08:00–10:00': [75, 30, 55, 20, 90],
  '10:00–12:00': [85, 60, 40, 70, 95],
  '12:00–14:00': [65, 80, 90, 30, 60],
  '14:00–16:00': [50, 45, 80, 100, 55],
  '16:00–18:00': [40, 35, 70, 90, 60]}

df = pd.DataFrame(data)
df.set_index('Machine', inplace=True)
```

```
# Building a heat map of machine loading
plt.figure(figsize=(10, 6))
sns.heatmap(df, cmap='coolwarm', annot=True, fmt=".0f", linewidths=0.5, cbar_kws={'label': 'Загрузка (%)'})
plt.title('Machine tool loading heat map (flange batch))')
plt.ylabel('Machine')
plt.xlabel('Time interval)
plt.tight_layout()
plt.show()
```

During the study, a heat map of the workload of metal-cutting machines in the production area was constructed (Figure 3), which makes it possible to evaluate the distribution of the production load over time and identify potential bottlenecks in the technological process.

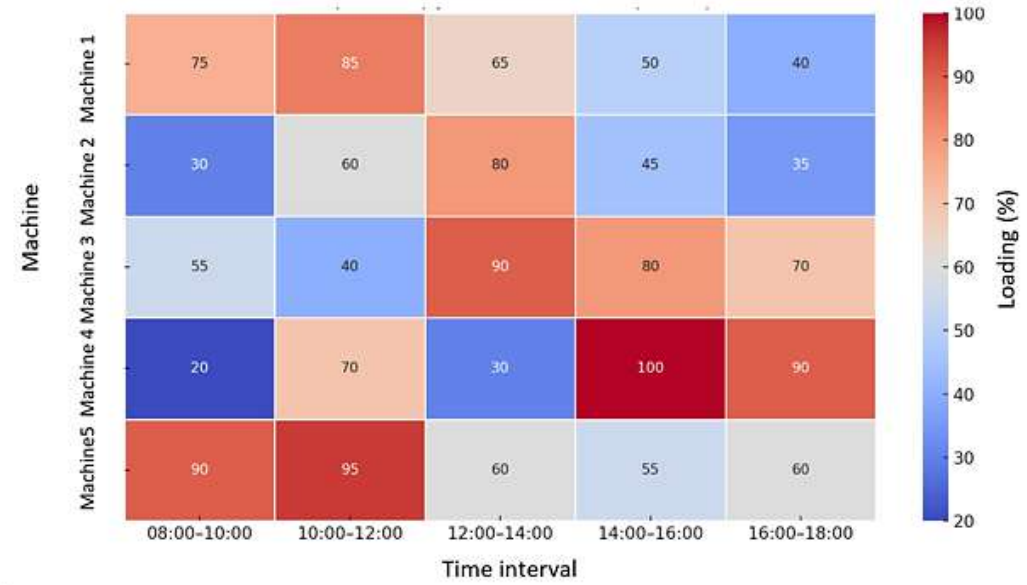

Fig. 3. - Machine tool loading heat map

Heat map analysis revealed that machine 5 is characterized by its highest utilization rate between 8:00 AM and 12:00 PM, indicating a high concentration of operations and a potential bottleneck in the production flow structure. Machine 4 exhibits full utilization (100%) between 2:00 PM and 4:00 PM, potentially leading to equipment overload, increased waiting times for operations, and increased work-in-progress (WIP). Meanwhile, machines 2 and 3 are characterized by a more uniform utilization distribution throughout the shift, allowing them to be considered as reserve resources for the redistribution of individual process steps to stabilize the production flow.

Additionally, the study constructed a Pareto frontier for five alternative machining modes based on a combination of three criteria: machining time, surface quality, and manufacturing operating costs. The analysis was conducted taking into account the requirements of minimizing machining time, reducing surface roughness values, and reducing operating costs. The results of the multicriteria analysis show that mode X4 is the most balanced option, providing minimal surface roughness and operating costs with an acceptable processing time. Therefore, it can be recommended as the preferred mode. Mode X2 demonstrates advantages in terms of cost and surface quality, but is characterized by a slightly increased processing time, making it suitable for use in situations where flexible equipment load redistribution is required. Mode X3 is inferior to the alternatives in all analyzed parameters, characterized by higher roughness and operating costs, and therefore should be excluded from further consideration. Modes X1 and X5 occupy an intermediate position and can be considered as compromise solutions, acceptable for auxiliary or secondary operations.

The study generated a dynamic heat map of the production area's operational efficiency based on a set of key indicators characterizing the time, production, and economic aspects of the process (Figure 4). The following integral indicators were used: average production cycle time for processing one part (Cycle Time, CT), throughput of the section (Throughput, TH), average volume of work-in-progress (Work-In-Progress, WIP) and operating costs for manufacturing a unit of output (Cost, C) (Table 5).

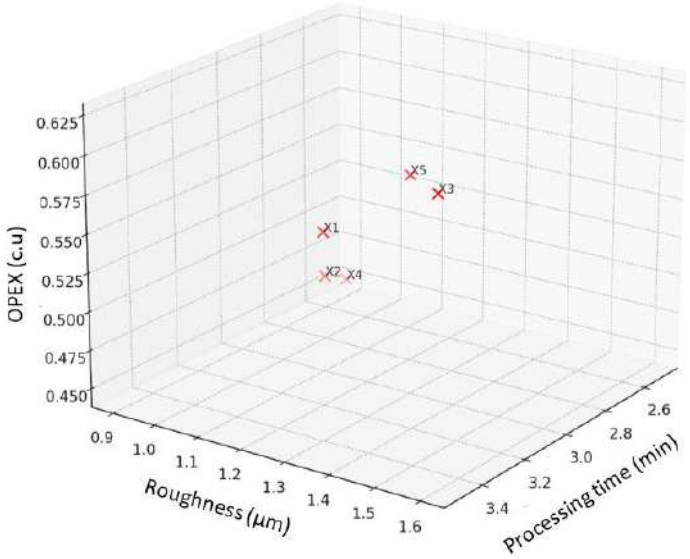

Fig. 4. - Efficiency of the production plot

Table 5. Integral process indicators

Indicator	Designation	Description
CT	Cycle Time (min/unit)	Average processing time per part
TH	Throughput (unit/min)	Production throughput
WIP	Work-In-Progress	Average number of unfinished parts
C	Стоимость (c.u./unit)	Operating costs per unit

Heat map analysis (Figure 5) revealed that Batch A, with the shortest average processing time per part, demonstrated the best results in terms of CT (average processing time per part). Batch B, however, had the longest production cycle, indicating possible equipment overload or a bottleneck in the process flow.

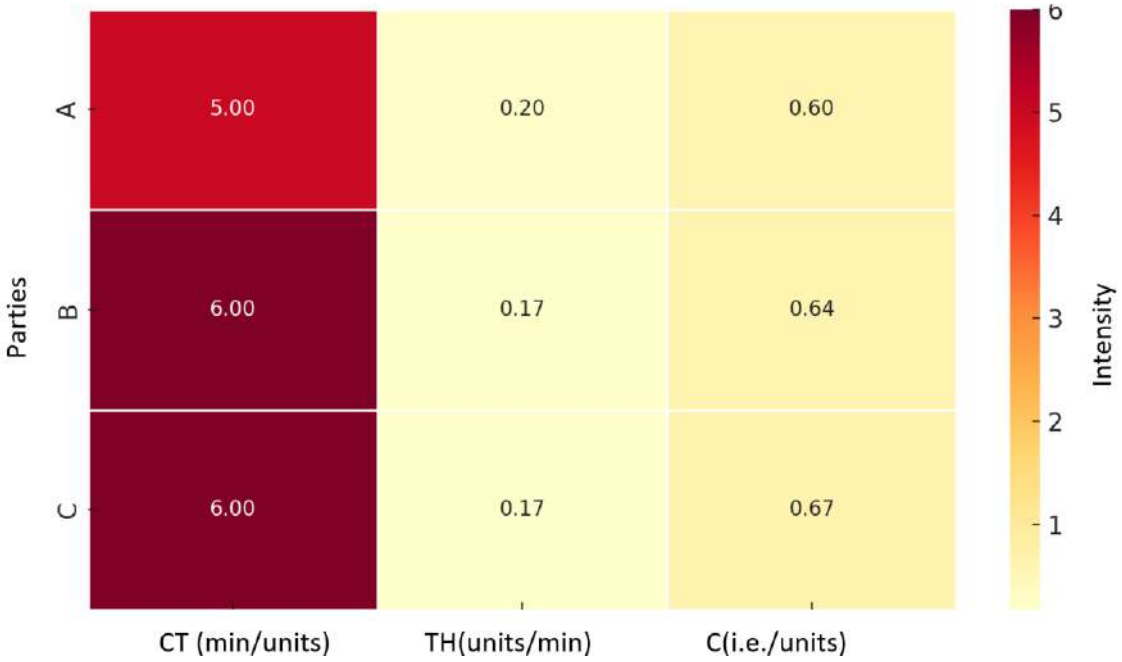

Fig. 5. - Heat map

In terms of TH (throughput), Batch A also leads the way, demonstrating the highest throughput value, indicating a high degree of synchronization of operations and a streamlined production flow. Batch B exhibits minimal values for this indicator, confirming its low efficiency in terms of production speed.

An analysis of unit operating costs (C) shows that Batch A also exhibits minimal costs, suggesting it is the most cost-effective option. Batch C has slightly higher costs, but demonstrates a more balanced balance between processing time and quality indicators, making it an acceptable alternative in the face of changing production priorities.

Based on the results obtained, it can be concluded that this study has developed and validated an intelligent methodology for optimizing the production process based on the principles of multi-criteria analysis. The proposed approach simultaneously accounts for time, production, and economic indicators, utilizes real production data and machine learning methods, and is capable of adapting to changing production system operating conditions and updating as new data accumulates. The developed methodology can be integrated into a digital smart manufacturing platform and used to improve the efficiency of production process management.

Conclusions

A digital model of the production process at a mechanical engineering enterprise was developed, based on the parameterization of production areas and the use of Big Data technologies. The structure of the machine shop was formalized as a directed graph, taking into account production units, buffers, parts flow routes, and transport links. Mathematical models were developed to estimate throughput, production cycle time, volume of work in progress, and operating costs.

It was established that the key factors influencing surface finish quality are vibration level, feed rate, and wear of the cutting tool. Rational ranges of cutting conditions were determined to reduce surface roughness and improve process stability. Heat maps of equipment utilization were developed to identify bottlenecks in the production system and optimize production load distribution.

The use of multicriteria analysis and the Pareto frontier allowed us to determine the most efficient machining modes based on a combination of technological and economic criteria. The proposed methodology can be used to create digital twins of production processes and implement intelligent control systems in mechanical engineering enterprises.

References

[1] Zharkevich O.M., Nikonova T., Gierz Ł., Reshetnikova O., Berg A., Warguła Ł., Berg A., Wieczorek B., Łykowski W., Nurzhanova O. Improving the Design of a Multi-Gear Pump Switchgear Using CFD Analysis //Applied Sciences (Switzerland), 2024, 14(13), 5394

[2] Nikonova T., Zhetessova G., Yurchenko V., Zharkevich O. The development of the computer-aided design system for production processes of component part machining for single-piece production and repair conditions //Journal of Applied Engineering Science, 2019, 17(4). - P. 599–609. doi:10.5937/jaes17-21470.

[3] Khrustaleva I., Khrustalev M., Brovkina Ya., Khokhlovskiy V., ShkodyrevV. The Model for optimizing cutting parameters for processing products on metal-cutting machines //Cybernetics and Physics, 2024, Vol.13, 2, 111-122.

[4] Vasendina E., Plotnikova I., Levitskaya A., Kvesko S. Detection and defect correction of operating process// IOP Conference Series Materials Science and Engineering, 2016, 110(1), 012070 DOI: 10.1088/1757-899X/110/1/012070

[5] Zhetessova G.S., Zharkevich O.M., Kozhanov M.G., Khrustaleva I.N. Method for Optimizing the Parameters of Mechanical Processing of Holes to Ensure Cutting Tool Stability and Cost-Effective Machining // Material and Mechanical Engineering Technology, №3, 2025. doi.org/10.52209/2706-977X_2025_3_84 mmet.kstu.kz/download/articles/09012026103035_digest.pdf

[6] Zhetessova G., Khrustaleva I., Shkodyrev V., Zharkevich O., Kanatova A., Kozhanov M., Tattimbetova G., Abdugaliyeva G. Model of Optimization of Process Parameters for Machining of Separate Design Elements of the Product // Applied Sciences, 2025, 15(10), 5395 doi.org/10.3390/app15105395 mdpi.com/2076-3417/15/10/5395

[7] Kozinski O., Kotyrba M., Volna, E. Improving the Production Efficiency Based on Algorithmization of the Planning Process //Appl. Syst. Innov., 2023, 6, 77. https://doi.org/ 10.3390/asi6050077

[8] Berg A., Nurzhanova O., Vytautas T., Vitushenko D. Improvement of Base Sets for Complex Configuration Parts when Assessing their Manufacturability within Industry 4.0 //Material and Mechanical Engineering Technology 2024, 2, 25 – 35

[9] Song Z., Luo S. Application of Machine Learning and Data Mining in Manufacturing Industry //International Journal of Computer Science and Information Technology, Volume 2, Number 1, 2024. - P. 426- 435.

[10] Investigation of materials flow during the cold-rolling process by experimental evidence and numerical approaches //Engineering and it solutions, II, 2022. – P. 39 - 51

[11] Optimizing production processes in machine-building enterprises: a case study on microelement rationing and operational excellence // International Journal on Technical and Physical Problems of Engineering, Issue 6, 2 Volume, 17 Number 1, 2025. – P. 261-269

[12] Zhetessova G., Khrustaleva I., Shkodyrev V., Chernykh L., Zharkevich O., Kozhanov M., Buzauova T. Model for Structural and Parametric Optimization of the Mechanical Processing Technology for a Product //Applied Sciences (Switzerland), 2026, 16(8), 3639. doi:10.3390/app16083639

[13] Aizhambaeva S., Zhetessova G., Nikonova T., Vavilova G., Belik M. Modeling arc spraying process for eccentric sleeve of cone crusher gp 500 using computer-aided design // Materials Science Forum, 2019, 970. - P. 343–355. doi: 10.4028/www.scientific.net/MSF.970.343.

[14] Buzauova T., Smagulov A. Selection of Optimal Parameters for a Cutting Tool When it Comes to Machining Shaped Parts Made of Alloy Steel // Material and mechanical engineering technology, Volume 1, 2021. - P.19-44.

[15] Zhetessova G., Nikonova T., Gierz Ł., Berg A., Yurchenko V., Zharkevich O., Alexey K. A Comparative Analysis of the Dynamic Strength Properties of the Long Guides of Intelligent Machines for a New Method of the Thermal Spraying of Polymer Concrete //Appl. Sci. 2022, 12, 10376. https://doi.org/10.3390/app122010376

Information of the authors

Zhetessova Gulnara Santayevna, d.t.s., professor, Abylkas Saginov Karaganda Technical University
e-mail: zhetesova@mail.ru

Zharkevich Olga Mikhailovna, c.t.s., professor, Abylkas Saginov Karaganda Technical University
e-mail: zharkevich82@mail.ru

Khrustaleva Irina Nikolaevna, c.t.s., docent, Peter the Great St. Petersburg Polytechnic University
e-mail: irina.khrustaleva@mail.ru

Kozhanov Murat Galiaskarovich, m.t.s, Abylkas Saginov Karaganda Technical University
e-mail: spark@mail.ru

Buzauova Toty Meierbekovna, c.t.s., professor, Abylkas Saginov Karaganda Technical University
e-mail: toty_77@mail.ru

DOI 10.52209/2706-977X_2026_2_35 **IRSTI 55.43.03** **UDC 658.984**

Testing the Grip Strength of Individual Fingers of the Hand in Relation to the Grip Strength of the Whole Hand

Bąk E., Czajka K., Dudziak A., Fabiańska A., Wieczorek B.*
Poznan University of Technology, Poznan, Poland
*corresponding author

Abstract. This paper investigates the grip strength of individual fingers, utilising a medical dynamometer to measure the force exerted by each finger and both hands across multiple series of tests. The objective of this study is to provide a comprehensive analysis of finger grip strength among different groups, segmented by centile, gender, activity levels, and BMI. The scope includes detailed measurements of each finger's strength, aggregate hand strength, and statistical processing of the data to compute mean values, standard deviations, confidence intervals, and Student's t-distributions for the various centile groups. Results highlight significant variations in grip strength, correlated with physical activity and BMI. This detailed data set is critical for indexing, abstracting, and retrieval purposes, offering valuable insights for fields such as ergonomics, physical therapy, and sports science.

Key words: grip strength, finger strength measurement, centile, physical activity, BMI, statistical analysis

Introduction

Modern design of technical equipment requires not only innovative technological solutions, but also a deep understanding of human physiological capabilities. One of the key parameters that has a significant impact on the ergonomics and safety of machine operation is finger grip strength. Measuring this force provides valuable data necessary for creating equipment tailored to the actual abilities of operators, both in industry and in everyday use. At the same time, there is a noticeable lack and need for such knowledge in manually operated machines [1, 2]. A particular group of devices that work with the hand are wheelchair drive systems. In the case of these devices, the strength of the handshake translates into the efficiency [3, 4] of the drive operation and its accessibility [5, 6] for people with disabilities. Knowledge of hand grip strength allows engineers and designers to optimize tools and machines to minimize the risk of injury and fatigue to users, while maximizing work efficiency . Understanding grip strength is also crucial in designing assistive devices that support people with limited manual dexterity, enabling them to use everyday equipment safely and comfortably [7, 8]. Parameterizing handshake strength is a difficult research problem for the entire population of potential users of technical devices because the value of handshake strength depends on the individual physical capabilities of the user. For example, on age [9], health status [10] and gender [11]. Grip strength is a measure of the hand muscles' ability, and actually the entire arm, as muscles of the arms are engaged to increase the force generated, to exert pressure. Physical activity has a direct and significant impact on hand grip strength, being one of the key factors that can improve it [12]. Regular exercise that engages the muscles of the hands, forearms and arms, such as weightlifting, climbing, weight training or sports that require a precise grip (e.g., tennis, gymnastics), leads to the strengthening of the muscles responsible for grip strength. These exercises increase the strength and endurance of the hand muscles and improve neuromuscular coordination, resulting in a better and stronger grip [13].

Most articles focus on the study of grip strength in relation to various factors. The most common of those are gender and age [14]. With the researchers focusing mainly on analysing the strength of the whole handshake. There are publications describing the grip strength of individual fingers [15]. However, they take into account hand clenching shapes corresponding to common hand tools and only present results in terms of grip strength. Given the complexity of the anatomical structure of the hand and the muscular system that supports it, as well as the individual physical capabilities of people, it is a complex research problem to describe the grip strength of individual fingers into a catalogue as input for the design process.

With this in mind, the research problem was formulated to determine the percentage of individual fingers in the total grip strength and the correlation of finger grip strength with BMI and physical activity. Solving such a research problem will allow the research objective of being able to calculate the grip strength of individual fingers on the basis of a single measurement of the whole hand grip with a dynamometer. This idea can be applied to the design process of personalised technical devices and the development of design methodologies.

1. Material and method

The research and experimental protocols has been positively evaluated by Bioethical Commission at the Karol Marcinkowski Medical University in Poznań Poland, Resolution No. 1100/16 of 10 November 2016, under the guidance of Prof. MD P. Chęciński for the research team led by Wieczorek B. The authors obtained the written informed consent of the examined person for the publication of research results with their participation. The data was presented in such a way as to ensure their complete anonymity. The measurement method and data acquisition were carried out in accordance

with the directives of the Bioethics Commission at the Karol Marcinkowski Medical University in Poznań Poland, which are in line with the guidelines Declarations of Helsinki.

The subjects of this study were 9 people, 3 male and 6 female. All were of Central European nationality, aged 21-22 and right-handed. Their dominant hands and fingers were measured using anthropometric measure tape as shown in Fig. 1.

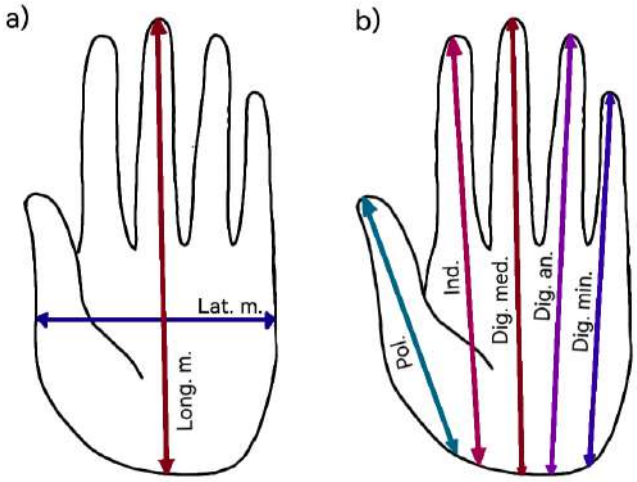

Fig. 1. - Measurement of a) length and width of the hand b) length of the fingers: Pollex – Pol., Index – Ind., Digitus medius – Dig. med., Digitus annularis – Dig. an., Digitus minimus – Dig. min., Latitudo manus - Lat. m., Longitudo manus - Long. m.

Using measurements, subjects were divided into hand size centile groups [16]. On the basis of the measurements taken, three subjects were allocated to the 50th centile group of women, three to the 5th centile of women and three to the 50th centile of men. The results of the hand measurements by centile group are shown in Table 1.

Table 1. Right hand sizes of subjects in each centile group

Subject	*Lat. m.* [mm]	*Long. m.* [mm]	*Long. Ind* [mm]	*Long. Dig. med.* [mm]	*Long. Dig. an.* [mm]	*Long. Dig. min.* [mm]	*Long. Pol.* [mm]
5 centile (female)							
Woman 1	80	160	145	160	150	127	105
Woman 2	87	170	165	170	161	135	120
Woman 3	78	170	164	170	154	135	114
50 centile (female)							
Woman 4	97	176	173	176	164	139	128
Woman 5	97	178	176	178	168	139	129
Woman 6	97	179	166	179	171	143	121
50 centile (male)							
Man 1	109	188	175	188	176	151	140
Man 2	105	189	188	189	183	154	149
Man 3	109	199	187	199	188	156	139

Subjects were also split into groups by their physical activity levels (4 were active, 5 not active) and by BMI categories (4 in healthy range, 5 overweight). Person was considered active if they reported exercising at least 3 times a week. Participants' activity levels and BMIs are presented in Table 2.

Table 2. Activity levels and BMI of subjects in each centile group

Subject	Activity level	BMI
5 centile (female)		
Woman 1	not active	27.7 (overweight)
Woman 2	active	21.7 (healthy)
Woman 3	not active	24.9 (healthy)
50 centile (female)		
Woman 4	active	23.3 (healthy)
Woman 5	not active	29.1 (overweight)
Woman 6	not active	29.4 (overweight)
50 centile (male)		
Man 1	active	25.9 (overweight)
Man 2	not active	24.2 (healthy)
Man 3	active	26.8 (overweight)

Force measurement was performed using a medical dynamometer (Fig. 2) with a measuring range of up to 130 kg and a measurement accuracy of 100 g. The dynamometer had a grip span of 64 mm and an empty weight of 0.3 kg. Standard measuring tools such as an anthropometric tape, an anthropometer and an anthropometric compass were used to measure the anthropometric dimensions of the hands.

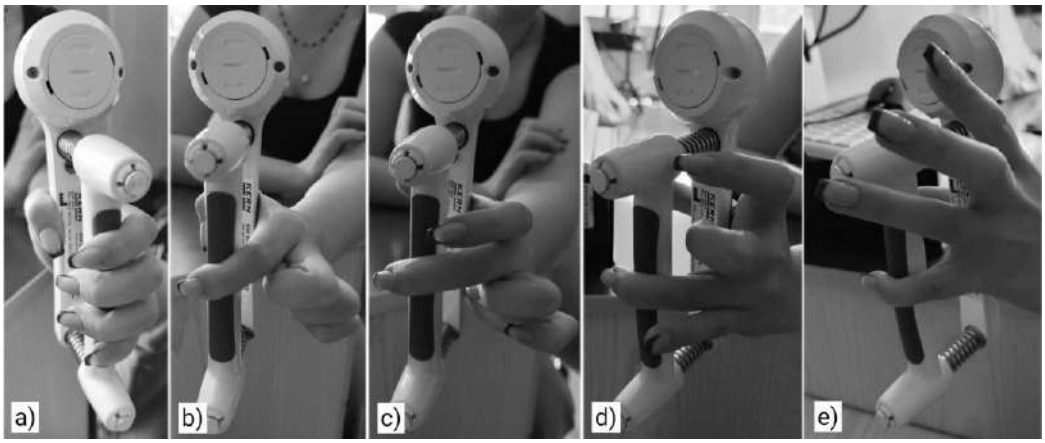

Fig. 2. - Method of measuring the grip strength of a: a) Mns, b) Ind., c) Dig. med., d) Dig. an., e) Dig. min.

The measurement procedure involved measuring the grip strength of each finger in 10 repetitions, with the measurement series separated by a recovery break. During the measurements, the patient was in a seated position. Their forearm was supported on a table so that a 90-degree angle was maintained between the arm and forearm. The wrist and hand extended beyond the edge of the table, and the wrist was not subjected to any rotations, flexions, or deviations.. The results measured according to the above procedure were averaged, and for each mean value, a confidence interval was calculated using a confidence level of $p = 0.05$, applying the Student's t-distribution.

2. Results and discussion

Averaged values of grip strength for individual fingers, categorized by percentile dimension groups, are presented in Tables 3 - 6. For the entire study population of women (5 and 50 centiles) (Table 6) it was found that the hand grip generates an average force of 199.3±11.8 N for the right hand and 176.7±13.7 N for the left. This represented a difference of 12.8% between the dominant and non-dominant limb. This trend was also observed among men (Table 5) in this case, for the right hand, the grip strength was measured at 418.2±24.0, which was 82.7% the difference from women of the same centile group (50 centile) (Table 4). The conducted research showed that regardless of the centile dimension of the hand and the sex of the patient, the largest grip force is generated by the index and the smallest digitus minimus. An interesting relationship was observed for the second in the order of the strongest finger. In the case of the centile group 50, it was the index, while for women from the centile group 5 digitus medius. For women with palm dimensions of 50 centile (Table 3) digitus medius achieved a huge value of 86.4±9.7 N and an index of 74.4±7.0 N, which was a difference of 16.1%, greater than between the left and right hands. Analysing the average percentage difference between the fingers of the right hand and the left hand, it was found that not all fingers of the dominant hand generate greater grip strength than the fingers of the non-dominant hand (for the examined patients, the left hand). For example, for men with 50 centile dimensions of length the highest grip strength for a single finger was measured for the digitus medius left hand (non-dominant hand) 155.7±13 N, which was 16.5% higher than on the right hand. Similar differences in the greater grip strength were observed for digitus minimus and digitus annularis, where the difference between dominant and non-dominant hands was 13.9% and 29.7%. In turn, for the manus and index slightly larger values were examined for the right hand. The value of the grip force for the entire right hand was 418.2±24 N, and for the left hand 397.4±27.7 N, which gave a difference of 5.2% in the results. Similarly, for the index fingers, the pressure in the right hand was 5.7% greater than in the other hand.

Table 3. Measurement results for women in the 5 centile

Parameters	Grip strength (right hand), [N]					Grip strength (left hand), [N]				
	Dig. min.	*Dig. an.*	*Dig. med.*	*Ind*	*Mns*	*Dig. min.*	*Dig. an.*	*Dig. med.*	*Ind*	*Mns*
Mean	39.44	62.36	86.36	74.39	169.71	34.89	61.97	73.9	63.11	146.46
Standard deviation	9.75	25.46	27.02	19.46	40.46	10.11	15.79	19.12	16.99	58.52
Confidence interval	3.49	9.11	9.67	6.96	14.48	3.62	5.65	6.84	6.08	20.94

Table 4. Measurement results for women in the 50 centile

Parameters	Grip strength (right hand), [N]					Grip strength (left hand), [N]				
	Dig. min.	*Dig. an.*	*Dig. med.*	*Ind*	*Mns*	*Dig. min.*	*Dig. an.*	*Dig. med.*	*Ind*	*Mns*
Mean	31	32.47	50.39	85.54	228.87	27.6	37.15	51.04	73.38	206.99
Standard deviation	8.74	6.77	13.42	16.46	31.45	3.63	9.11	6.67	17.29	25.28
Confidence interval	3.13	2.42	4.8	5.89	11.25	1.3	3.26	2.39	6.19	9.05

Table 5. Measurement results for men in the 50 centile

Parameters	Grip strength (right hand), [N]					Grip strength (left hand), [N]				
	Dig. min.	*Dig. an.*	*Dig. med.*	*Ind*	*Mns*	*Dig. min.*	*Dig. an.*	*Dig. med.*	*Ind*	*Mns*
Mean	58.17	81.59	133.61	127.53	418.17	66.28	105.78	155.68	117.43	397.4
Standard deviation	15.82	25.55	50.46	33.4	67.05	19.47	38.79	45.56	36.22	69.13
Confidence interval	5.66	9.14	18.06	11.95	23.99	6.97	13.88	16.3	12.96	24.74

Table 6. Measurement results for men in the 50 centile

Parameters	Grip strength (right hand), [N]					Grip strength (left hand), [N]				
	Dig. min.	*Dig. an.*	*Dig. med.*	*Ind*	*Mns*	*Dig. min.*	*Dig. an.*	*Dig. med.*	*Ind*	*Mns*
Mean	35.22	56.37	59.42	79.97	199.29	31.24	56.51	55.52	68.24	176.73
Standard deviation	10.17	21.22	33.38	18.86	46.78	8.42	13.29	23.71	17.89	54.3
Confidence interval	2.57	5.37	8.44	4.77	11.84	2.13	3.36	6	4.53	13.74

The analysis of the percentage share showed that the largest percentage of the total strength of the handshake is index and digitus medius. For men with 50 centile (C50), the largest percentage of the total strength of the handshake was digitus medius and it was 31.9% (Fig. 5). A similar relationship was observed for women with 5 percentile (C5) because in this group also the largest percentage share of 50.9 % had digitus medius (Fig. 3). The exception was a research group of women with 50 percentile of hand dimensions. In this group, the largest percentage share was index and it was 37.3% (Fig. 4).

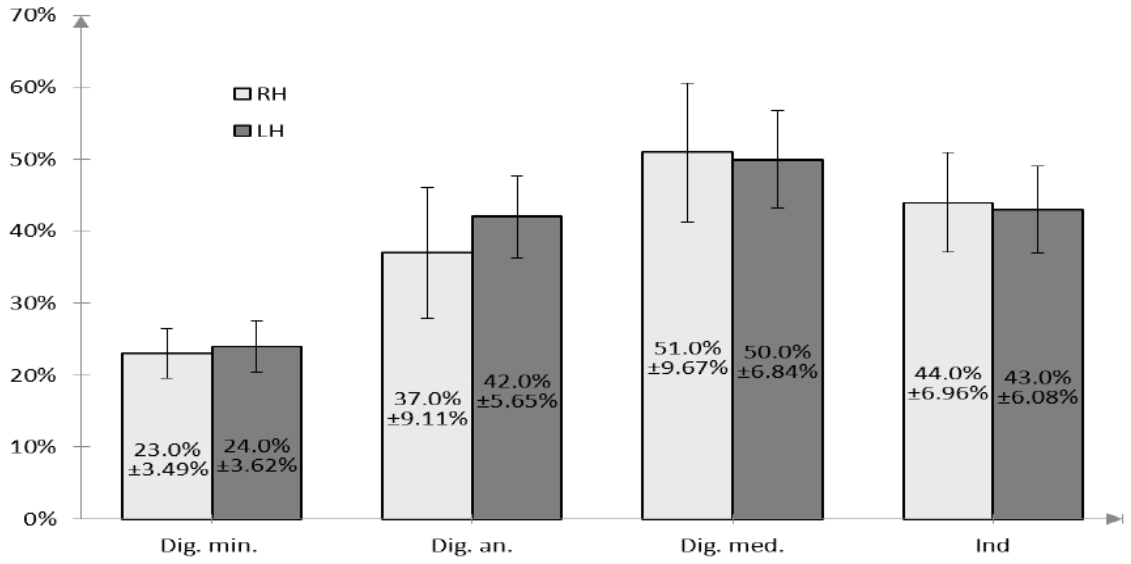

Fig. 3. - Graph of the percentage of grip strength for women in the 5 centile

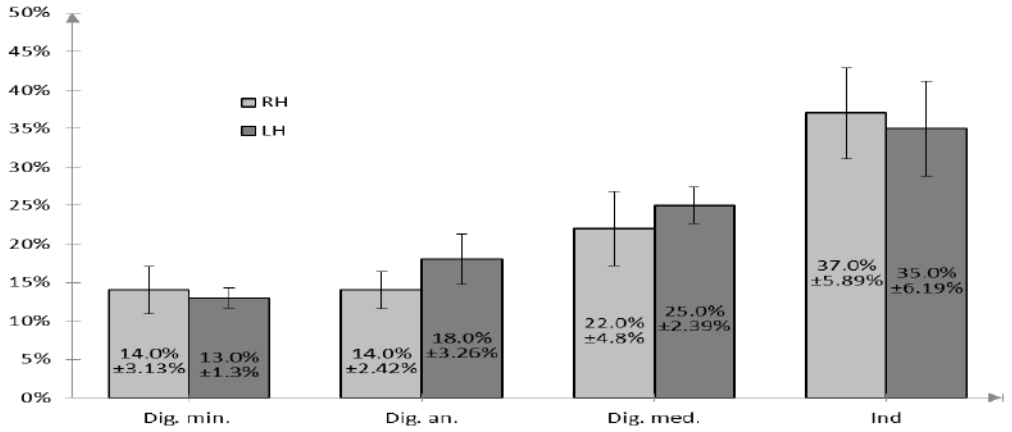

Fig. 4. - Graph of the percentage of grip strength for women in the 50 centile

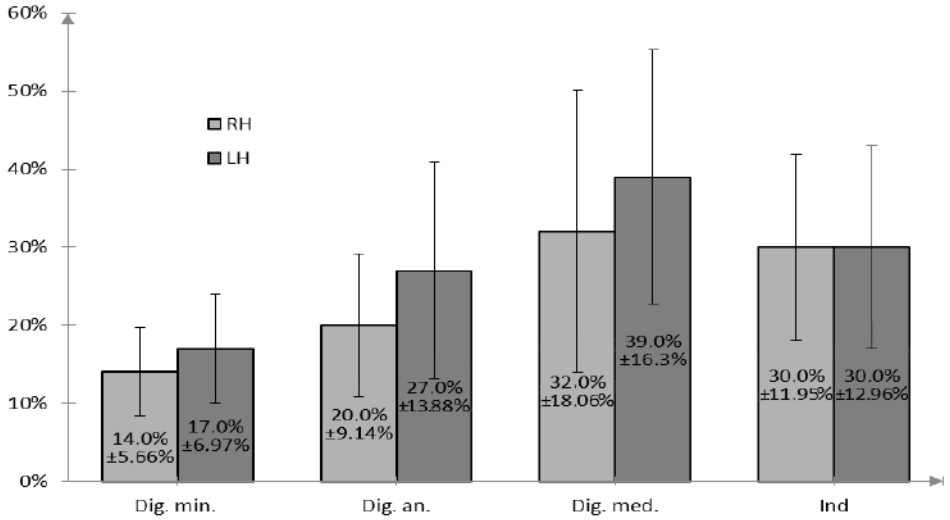

Fig. 5. - Graph of the percentage of grip strength hand for men in the 50 centile

Meanwhile, for all groups, the digitus minimus achieved the lowest result. Thepercentage grip strength for this finger was similar for women and men in 50 percentile (C50) and are respectively 13.9% (Fig. 4) and 13.5% (Fig. 5). For 5 centile of women (C5) digitus minimus has the lowest percentage of grip strength, it is, 23.2% (Fig. 3). However, compared to the group of 50 centile women and men, we notice more than 10% difference for 5 centile and other groups.

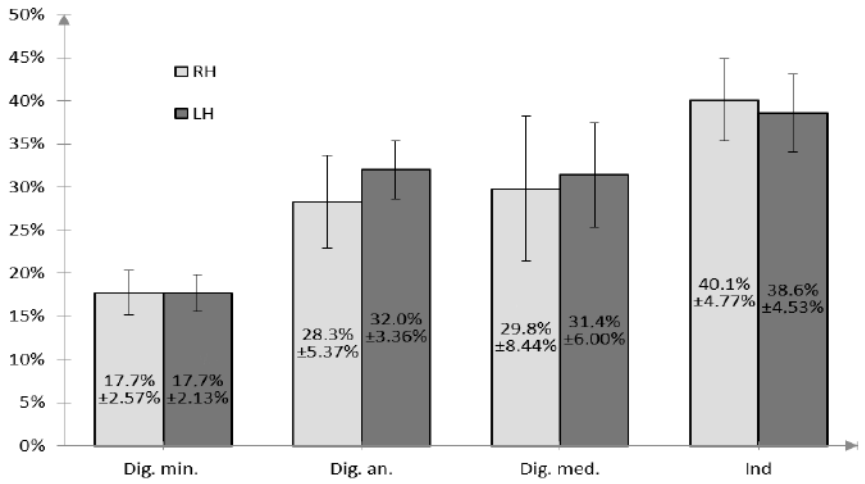

Fig. 6. - Graph of the percentage of grip strength hand for women in the 50 centile

Below (Fig. 3 to 6), a graphical interpretation of the results is presented in the form of charts for each centile group.

Other studies have shown similar results despite experimental groups varying in size and type and different testing methods being used. Mühldorfer-Fodor et al [17] in the study used cylinders of 3 different sizes, obtaining an average result of the percentage of the force of individual fingers: Ind. - 35%, Dig. med. - 33%, Dig. an. - 22%, Dig. min. - 12%. Obtained percentages are the result of combining the measurements of the group of men with the measurements of the group of women. Amis [18] used 6 cylinders of different sizes in their research obtaining the following results: Ind. - 30%, Dig. med. - 30%, Dig. an. - 22%, Dig. min. - 18%. The group in these studies consisted mostly of women, however their results were combined with the results obtained by the men studied. Radhakrishnan [19] and Lee [20] also used 4 cylinders of different diameters in their research and obtained the following results: Ind. - 31%, Dig. med. - 33%, Dig. an. - 22%, Dig. min. - 14%. [19] and Ind. - 33%, Dig. med. - 30%, Dig. an. - 23%, Dig. min. - 15% [20]. Additionally, both studies did not specify the gender of the study participants. Other studies of the percentage of individual finger strength were conducted using dynamometers, similar to this study. Both Hazelton [21] and Talsania [22] used dynamometers to conduct the measurements. For the first of these studies [21], the study group consisted of 30 men who obtained the following results: Ind. - 26%, Dig. med. - 33%, Dig. an. - 22%, Dig. min. - 17%. In the case of subsequent studies [22], the research group consisted of both men and women, again the results obtained are the result of combining the measurements of both groups: Ind. - 25%, Dig. med. - 35%, Dig. an. - 26%, Dig. min. - 15%. The results we obtained for the male group are consistent with the results obtained in previous studies: Ind. - P 30%, Dig. med. - 32-39%, Dig. an. - 20-27%, Dig. min. - 14-17%. In the case of the entire group of women studied (combination of the C5 and C50 groups), the results obtained are slightly higher for some fingers compared to previous studies: Ind. - 38,6-40,1%, Dig. med. - 29,8-31,4%, Dig. an. - 28,3-32%, Dig. min. - 17,7%. This may be due to the higher results obtained by the woman's C5 group: Ind. - 43-44%, Dig. med. - 50-51%, Dig. an. - 37-42%, Dig. min. - 23-24% compared to the woman's C50 group: Ind. - 35-37%, Dig. med. - 22-25%, Dig. an. - 14-18%, Dig. min. - 13-14%.

Analyzing the changes in the strength of the grip of the fingers for all sex and centile groups (Fig. 7) it was found that the percentage of the grip force of individual fingers decreases as the pollex moves away towards the digitus minimus. On the basis of this comparison, a universal mathematical model (1) was derived, on the basis of which it is possible to determine the approximate percentage of the finger grip force kF(i) in the grip strength of the whole hand.

$$k_F(i) = 0.172652 + 0.150211 \cdot i \qquad (1)$$

where i is the finger number matching the key: 1 – digitus minimus, 2 – digitus anularis, 3 – digitus medius, 4 – index.

The model is a universal tool that allows you to determine the kF coefficient, which is enough to multiply with an easy to measure grip force of the entire Fh hand and obtain an approximate value of the grip force of a single finger Fi (2).

$$F_i = F_h k_F(i) = F_h(0.172652 + 0.150211 \cdot i\,) \qquad (2)$$

where Fi - single finger grip strength with key number i,

Fh – whole hand grip force measured by dynamometer,

kF(i) – single finger grip strength percentage ratio, whole hand grip strength,

i – finger number matching key: 1 – digitus minimus, 2 – digitus annularis, 3 – digitus medius, 4 – index.

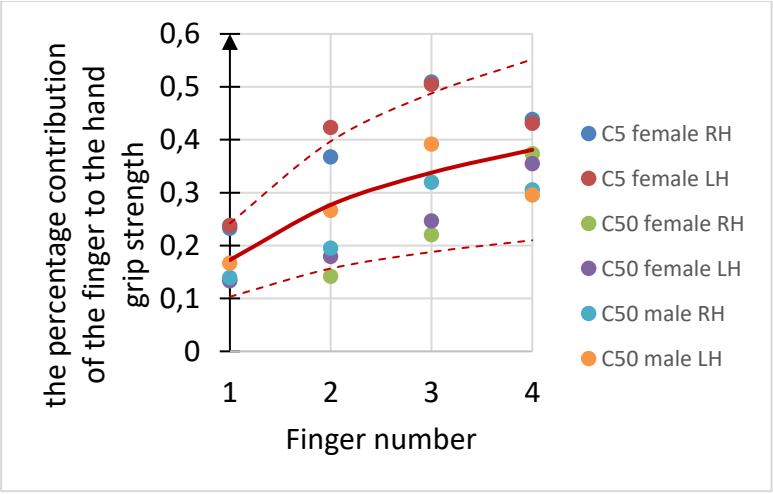

Fig. 7. - Graph of the percentage of grip strength hand for all the women

In addition to distinguishing centile groups, the subjects were divided into BMI and physical activity groups. Due to the insufficient size of the men's groups, they were not considered in the following summary. Two groups of physical activity were distinguished: low and high physical activity. The criterion for the latter was working out or practising sports at least 3 times a week. Statistic analysis was also performed for both measurements. Analysis of physical activity showed that in the group of women studied, the effect of physical activity on the equalization of grip strength between the right (dominant) limb and the left limb could be observed (Table 7, Fig. 8). In the group of physically active women, the difference in grip strength was 1.1%. In comparison, in the group of women with low physical activity the difference was already 16.1%. The reason for such differences is the symmetrical development of musculoskeletal organs in physically active people, as opposed to people with low physical activity who perform most activities with the dominant limb, thus replacing the other non-dominant limb. The numerical values (Table 7) of the analysis of the impact of physical activity are only the basis for determining the percentage differences in the grip force generated by the two limbs. The calculated average values take into account in each group different dimensional centiles therefore also different physical predisposition and muscle mass.

Table 7. Measurement results for men in the 50 centile

Parameters	**People with high physical activity**		**People with low physical activity**	
	Right hand grip strength [N]	Light hand grip strength [N]	Right hand grip strength [N]	Light hand grip strength [N]
Mean	191.1	188.99	203.39	170.6
Standard deviation	26.04	12.86	53.78	65.01
Confidence interval	11.41	5.63	16.67	20.15

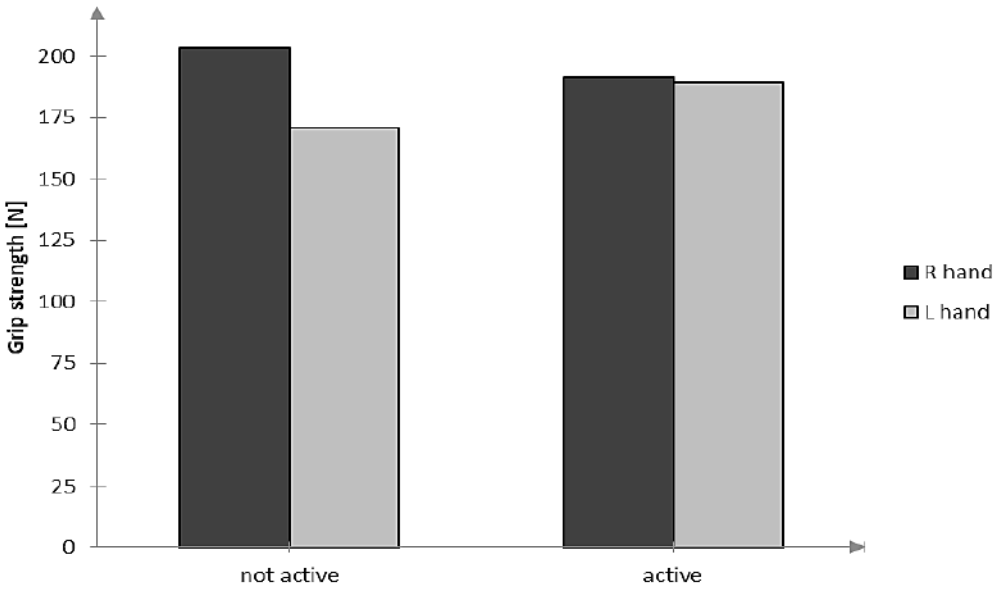

Fig. 8. - Graph of women grip strength in relation to physical activity

The analysis of the effect of BMI on the value of grip strength showed an increasing trend according to which, the strength of the hand grip increases as BMI number grows. This is a significant increase, with the slope value of the calculated trend of 82.1 degrees for right hand and 71.3 degrees for left hand (Fig. 9). For woman 2 with a BMI of 21.7, the right hand grip strength was 190.8N, and for woman 6 with a BMI of 29.4, the strength was 272.7N. This represented a 30% increase in right hand grip strength with a 16% increase in BMI. Woman 3 was deemed an outlier and was not included in the calculated trend.

Most of the articles studying the correlation between grip strength and BMI use different categories to systemise the results of the studies. For BMI range between 16,5 to 18,49 kg/m^2 the person is underweight, between 18,5 to 24,99 kg/m^2 has normal weight, and between 25 and 29,99 kg/m^2 overweight. More than that means the person is obese. In our research we had 3 women with normal BMI. Their grip strength was: Women 2 RH-169,81N and LH-182,66 N, women

4 RH-212,39 N and LH-195,32 N, women 3 RH-122,82 N and LH-66,41 N. The 3 overweight women had grip strength: women 1 RH-116,51 N and LH-190,31 N, women 5 RH- 205,03 N and LH-187,86 N, women 6 RH-269,19 N and LH-237,79 N.

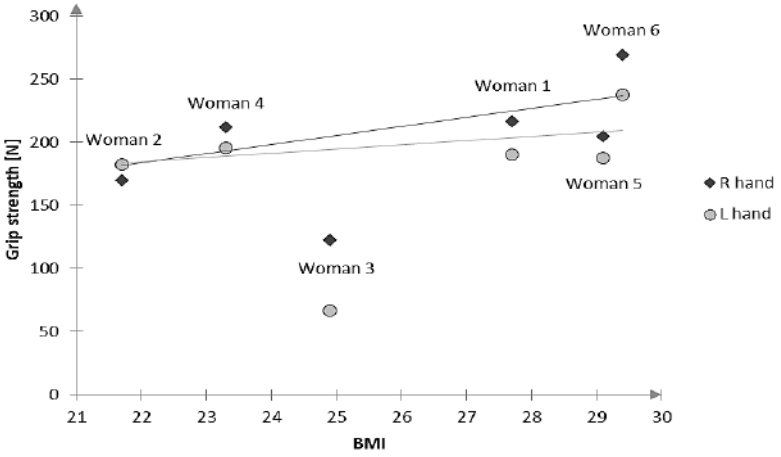

Fig. 9. - Graph of women grip strength in relation to BMI

In Lad U.P. research [23] that focused on the grip strength of the dominant hand of young adults between 18-21 years old there were three categories of BMI. The force for underweight was 265,56±44,14 N, normal weight 263,99±31,88 N and overweight 240,35±62,49 N. The results of overweight people in our study are in the range of this study, but the grip strength of normal BMI in our research is significantly lower.

The results are a little higher than the ones we achieved because the study didn't differ between women and men. Men have on average higher grip strength than women which means that the average grip strength for women is lower. There is some research which difference between dominant and non-dominant hand like the study by Kun-Hsi Liao [24], who worked with 18-27 year old people. For the women, results showed that underweight women have grip strength of RH-283,71±57,78 N and LH- 242,21±60,82 N, normal weight RH-354,44±80,15 N and LH- 323,34±76,91 N, overweight RH- 433,7±55,62 N, LH- 396,32±54,15 N. Looking at even those results we can see that in the first study the strength was decreasing by 8,95 % between normal and overweight BMI. This result is different in our and Kun-Hsi Liao study where in the latter one the trend increased by 22,36%. R. Pavlović [25] notices the same increasing tren, but far less significant. Most of the studies showed that the higher a person's BMI is, the stronger their grip strength is.

Conclusions

For women in the 5th centile, the middle finger achieved the highest pressure value. This group also exhibited significantly greater pressure strength in the little fingers of both hands compared to the other study groups. This is likely due to the necessity of holding objects using the little finger's strength, as most objects are not adapted for people with small hand sizes (5th centile women). This observation is crucial in designing ergonomic handles [26, 27] as people on the smaller centile need a specific approach when using input data on their pressure distribution. By adding value to the biomechanical data currently used [28,29], this observation complements the current knowledge about the distribution of pressure force of individual fingers. In the case of women with larger hand sizes (50th centile), they do not have this necessity, which can be seen by the highest contribution to total pressure strength from digitus anularis and index. These fingers, along with the thumb and middle finger, form the basis of many types of grips used during daily activities.

For men, the middle finger exhibited the highest strength, with strength gradually decreasing in the subsequent fingers. The middle finger is the longest finger, allowing for better distribution of force during a grip. Its central position also helps stabilise the grip [30, 31]. Based on this relationship, it can be concluded that the anatomical structure, particularly the differences in anthropometric dimensions between men and women of the same centile, should be utilised in the design of individualised and ergonomic technical devices [32, 33].

For physically active individuals, we observe similar grip strength values in both hands, whereas for the non-active group, there is a significant dominance of the dominant hand. The differences in hand strength between highly active and inactive individuals can be explained by several training-related factors. Many training programs recommend performing exercises using both hands (e.g., deadlifts, barbell presses) [34, 35]. Even unilateral exercises are often performed on both sides of the body to ensure symmetry and avoid muscle disproportions. Physically inactive individuals typically use their dominant hand for most daily activities, such as writing, eating, and opening doors. Such habits lead to greater stimulation and development of muscles in the dominant hand, resulting in a larger difference in strength between the hands.

The use of BMI to evaluate the strength of a handshake may be the biggest mistake. Weight doesn't always correlate with muscle mass, even though body mass is associated with growth [36, 37]. However, the presented research showed an upward trend according to which the increase in BMI translates into an increase in the strength of the handshake. This may be because a larger body mass often correlates with greater muscle mass. Even if part of the mass comes from adipose tissue, individuals with a higher BMI may have more muscles contributing to their heavier weight. In the future, it would be necessary to examine the relationship between grip strength and muscle mass for different BMI groups. This would provide a proper understanding of the dependency of strength on BMI.

Analysing the grip strength measurement results for men and women, we notice that it is significantly higher for men than for women. For the entire hand, the average grip strength for men is 418.17 N for the right hand and 397.4 N for the left hand, while for women, it is 199.29 N and 176.73 N, respectively ө the differences are more than twofold. Such a glaring disparity may be due to the fact that men typically have greater muscle mass than women. Men's arm and hand muscles are better developed, leading to greater grip strength [39–40]. Additionally, the male skeletal system is stronger and more resilient than the female skeletal system. Men have denser, stronger bones, tendons, and ligaments than women. All these factors predispose men to work involving the operation of hand-held machinery [41, 42].

The research goal of determining the percentage of individual fingers in the total adhesion strength and correlation of the finger grip strength with BMI and physical activity was successfully achieved. The findings can be applied to the design of personalised technical devices and assistive technologies. However, potential errors may have occurred during measurements such as individual changes in grip strength due to fatigue, hand positioning or environmental factors. Future research should focus on improving measurement methods, including a wider sample of the population, and on exploring other factors that may affect adhesion strength, such as regional or environmental influences. Additionally, future research should include larger testing groups in order to increase the accuracy of obtained results and decrease probability of abnormal data.

References

[1] Warguła Ł. Kukla M., Krawiec P., Wieczorek B.Impact of Number of Operators and Distance to Branch Piles on Woodchipper Operation //Forests, 2020, 11. DOI: 10.3390/f11050598

[2] Warguła Ł., Wieczorek B., Giedrowicz M., Kukla M., Nati C. Wood Chippers: Influence of Feed Channel Geometry on Possibility of Musculoskeletal System Overload //Croatian Journal of Forest Engineering: Journal for Theory and Application of Forestry Engineering, 2025, 46(1), pp. 59-76. DOI: 10.5552/crojfe.2025.2501

[3] Shechtman O., MacKinnon L., Locklear C. Using the BTE Primus® to Measure Grip and Wrist Flexion Strength in Physically Active Wheelchair Users: An Exploratory Study //Am. J. Occup. Ther., 2001, 55, pp. 393-400. DOI: 10.5014/ajot.55.4.393

[4] Kanjanasilanont A., Mongkolsomlit S., Earde P., Kooncumchoo P. Differences in Grip Strength among Wheelchair Basketball Athletes: Variations by Hand Size and Handrim-Tire Diameter //Sci. Technol. Asia, 2020, 25, pp. 141-151. DOI: 10.14456/SCITECHASIA.2020.42

[5] Neto F.R., Costa G., Dorneles J.R., Gonçalves C.W., Veloso J.H.C.L., Carregaro R.L. Handgrip Strength Cutoff Points for Functional Independence and Wheelchair Ability in Men With Spinal Cord Injury //Top. Spinal Cord Inj. Rehabil., 2021, 27, pp. 60-69. DOI: 10.46292/sci20-00040

[6] Rashedi E., Kim S., Nussbaum M.A., Agnew M.J., "Ergonomic Evaluation of a Wearable Assistive Device for Overhead Work //Ergonomics, 2014, 57, pp. 1864-1874. DOI: 10.1080/00140139.2014.952682

[7] Stefana E., Marciano F., Rossi D., Cocca P., Tomasoni G. Wearable Devices for Ergonomics: A Systematic Literature Review // Sensors, 2021, 21, p. 777. DOI: 10.3390/s21030777

[8] Zare M., Black N., Sagot J.-C., Hunault G., Roquelaure Y. Ergonomics Interventions to Reduce Musculoskeletal Risk Factors in a Truck Manufacturing Plant //Int. J. Ind. Ergon., 2020,75, 102896. DOI: 10.1016/j.ergon.2019.102896

[9] Aoki H., Demura S. Age Differences in Hand Grip Power in the Elderly //Arch. Gerontol. Geriatr., 2011, 52, pp. 176-179. DOI: 10.1016/j.archger.2010.10.025

[10] Vaishya R., Misra A., Vaish A., Ursino N., D'Ambrosi, R. Hand Grip Strength as a Proposed New Vital Sign of Health: A Narrative Review of Evidences //J. Health Popul. Nutr., 2024, 43, 7, DOI: 10.1186/s41043-024-00500-y

[11] Nicolay C.W., Walker A.L. Grip Strength and Endurance: Influences of Anthropometric Variation, Hand Dominance, and Gender //Int. J. Ind. Ergon., 2005, 35, pp. 605-618. DOI: 10.1016/j.ergon.2005.01.007

[12] Labott B.K., Bucht H., Morat M., Morat T., Donath L. Effects of Exercise Training on Handgrip Strength in Older Adults: A Meta-Analytical Review //Gerontology, 2019, 65, pp. 686-698. DOI: 10.1159/000501203

[13] Shields R.K., Leo K.C., Messaros A.J., Somers V.K. Effects of Repetitive Handgrip Training on Endurance, Specificity, and Cross–Education // Phys. Ther., 1999, 79, pp. 467-475. DOI: 10.1093/ptj/79.5.467

[14] Aadahl M., Beyer N., Linneberg A., Thuesen B.H., Jørgensen T. Grip Strength and Lower Limb Extension Power in 19–72-Year-Old Danish Men and Women: The Health2006 Study //BMJ Open, 2011, 1, e000192. DOI: 10.1136/bmjopen-2011-000192

[15] Kong Y.-K., Kim D.-M. The Relationship between Hand Anthropometrics, Total Grip Strength and Individual Finger Force for Various Handle Shapes // Int. J. Occup. Saf. Ergon., 2015, 21, pp. 187-192. DOI: 10.1080/10803548.2015.1029726

[16] Fryar C.D., Gu Q., Ogden C.L., Anthropometric Reference Data for Children and Adults, 2007-2010 United States.

[17] Mühldorfer-Fodor, M., Ziegler, S., Harms, C., Neumann, J., Kundt, G., Mittlmeier, T., Prommersberger, K. J. Load distribution of the hand during cylinder grip analyzed by Manugraphy // J. Hand. Ther., 2017, 30(4), pp. 529-537. DOI: 10.1016/j.jht.2016.10.009

[18] Amis A.A. Variation of finger forces in maximal isometric grasp tests on a range of cylinder diameters //J. Biomed. Eng., 1987, 9(4), pp. 313-320. DOI: 10.1016/0141-5425(87)90079-3

[19] Radhakrishnan S., Nagaravindra M. Analysis of hand forces in health and disease during maximum isometric grasping of cylinders //Med. Biol. Eng. Comput., 1993, 31, pp. 372-376. DOI: 10.1007/BF02446690

[20] Lee J.W., Rim K., Measurement of finger joint angles and maximum finger forces during cylinder grip activity //J. Biomed. Eng., 1991, 13(2), pp. 152-162. DOI: 10.1016/0141-5425(91)90062-C

[21] Nikonova T., Zharkevich O., Dandybaev E., Baimuldin M., Daich L., Sichkarenko A., Kotov E. Developing a Measuring System for Monitoring the Thickness of the 6 m Wide HDPE/LDPE Polymer Geomembrane with Its Continuous Flow Using Automation Equipment //Appl. Sci. 2021, 11, 10045. https://doi.org/10.3390/app112110045
[22] Talsania J.S., Kozin S.H. Normal digital contribution to grip strength assessed by a computerized digital dynamometer // J. Hand. Surg. Br., 1998, 23(2), pp. 162-166. DOI: 10.1016/S0266-7681(98)80165-4
[23] Lad U.P., Satyanarayana P., Shisode-Lad S., Chaitanya Siri Ch., Kumari N.R. A Study on the Correlation Between the Body Mass Index (BMI), the Body Fat Percentage, the Handgrip Strength and the Hand Grip Endurance in Underweight, Normal Weight and Overweight Adolescents //J Clin Diagn Res., 2013, 7(1), pp. 51–54. DOI: 10.7860/JCDR/2012/5026.2668
[24] Liao K. Hand Grip Strength in Low, Medium, and High Body Mass Index Males and Females //M. E. Journal of Reh. and Health, 3(1), 2016, DOI: 10.17795/mejrh-33860
[25] Pavlović R., Petrović B., Kozić G., Ćeho J. The influence of body height, body weight and body mass index on hand grip strength:A pilot study //Slovak Journal of Sport Science, 2021, 7(2). DOI: 10.24040/sjss.2021.7.2.19-30
[26] Fransson C., Winkel J. Hand Strength: The Influence of Grip Span and Grip Type // Ergonomics, 1991, 34, pp. 881-892. DOI: 10.1080/00140139108964832
[27] Lewis W.G., Narayan C.V. Design and Sizing of Ergonomic Handles for Hand Tools // Appl. Ergon., 1993, 24, pp. 351-356. DOI: 10.1016/0003-6870(93)90074-J
[28] Mitsionis G., Pakos E.E., Stafilas K.S., Paschos N., Papakostas T., Beris A.E. Normative Data on Hand Grip Strength in a Greek Adult Population // Int. Orthop., 2009, 33, pp. 713-717. DOI: 10.1007/s00264-008-0551-x
[29] Massy-Westropp N.M., Gill T.K., Taylor A.W., Bohannon R.W., Hill C.L. Hand Grip Strength: Age and Gender Stratified Normative Data in a Population-Based Study // BMC Res. Notes, 2011, 4, 127. DOI: 10.1186/1756-0500-4-127
[30] Sirajudeen M., Shah U., Pillai P., Mohasin N., Shantaram M. Correlation between Grip Strength and Physical Factors in Men // Int. J. Health Rehabil. Sci. IJHRS, 2012, 1, pp. 58-63. DOI: 10.5455/ijhrs.000000010
[31] Abaraogu U.O., Ezema C.I., Ofodile U.N., Igwe S.E. Association of Grip Strength with Anthropometric Measures: Height, Forearm Diameter, and Middle Finger Length in Young Adults //Pol. Ann. Med., 2017, 24, pp. 153-157. DOI: 10.1016/j.poamed.2016.11.008
[32] Strasser H. Assessment of the Ergonomic Quality of Hand-Held Tools and Computer Input Devices, IOS Press. 2007, ISBN: 978-1-60750-277-7
[33] Halim I., Umar R.Z.R., Mohamed M.S.S., Ahmad N., Padmanathan V., Saptari A. The Influence of Hand Tool Design on Hand Grip Strength: A Review //Int. J. Integr. Eng., 2019, 11, pp. 53-69.
[34] Kanehisa H., Nagareda H., Kawakami Y., Akima H., Masani K., Kouzaki M., Fukunaga T. Effects of Equivolume Isometric Training Programs Comprising Medium or High Resistance on Muscle Size and Strength //Eur. J. Appl. Physiol., 2002, 87, pp. 112-119. DOI: 10.1007/s00421-002-0604-6
[35] Davies J., Parker D.F., Rutherford O.M., Jones D.A. Changes in Strength and Cross Sectional Area of the Elbow Flexors as a Result of Isometric Strength Training //Eur. J. Appl. Physiol., 1988, 57, pp. 667-670. DOI: 10.1007/BF01075986
[36] Nordander C., Willner J., Hansson G.-Å., Larsson B., Unge J., Granquist L., Skerfving S. Influence of the Subcutaneous Fat Layer, as Measured by Ultrasound, Skinfold Calipers and BMI, on the EMG Amplitude //Eur. J. Appl. Physiol., 2003, 89,pp. 514-519. DOI: 10.1007/s00421-003-0819-1
[37] Sartorio A., Proietti M., Marinone P.G., Agosti F., Adorni F., Lafortuna C.L. Influence of Gender, Age and BMI on Lower Limb Muscular Power Output in a Large Population of Obese Men and Women //Int. J. Obes., 2004, 28, pp. 91-98. DOI: 10.1038/sj.ijo.0802433
[38] Abe T., Kearns C.F., Fukunaga T. Sex Differences in Whole Body Skeletal Muscle Mass Measured by Magnetic Resonance Imaging and Its Distribution in Young Japanese Adults //Br. J. Sports Med., 2003, 37, pp. 436-440. DOI: 10.1136/bjsm.37.5.436
[39] Gallagher D., Visser M., De Meersman R.E., Sepúlveda D., Baumgartner R.N., Pierson R.N., Harris T., Heymsfield S.B., "Appendicular Skeletal Muscle Mass: Effects of Age, Gender, and Ethnicity //J. Appl. Physiol., 1997, 83, pp. 229-239. DOI: 10.1152/jappl.1997.83.1.229
[40] Shephard, R.J., Bouhlel, E., Vandewalle, H., Monod, H. Muscle Mass as a Factor Limiting Physical Work //J. Appl. Physiol., 1988, 64, pp. 1472-1479. DOI: 10.1152/jappl.1988.64.4.1472
[41] Warguła Ł., Nati C., Wieczorek B., Bembenek M. The carbon dioxide emission balance and ability to chip wood by 10 kW machines used in urban areas in terms of increasing interest in using wood biomass resources for personal use //Advances in Science and Technology Research Journal, 2025, 19(4), pp.401–415. DOI: 10.12913/22998624/196263
[42] Gierz Ł., Warguła Ł., Kukla M., Koszela K., Zwiachel T.S. Computer Aided Modeling of Wood Chips Transport by Means of a Belt Conveyor with Use of Discrete Element Method //Applied Sciences, 2020, 10(24), 9091. DOI: 10.3390/app10249091

Information of the authors

Bąk Emilia, student, Poznan University of Technology
e-mail: emilia.bak@student.put.poznan.pl

Czajka Karolina, student, Poznan University of Technology
e-mail: karolina.czajka@student.put.poznan.pl

Dudziak Adrianna, student, Poznan University of Technology
e-mail: adrianna.dudziak@student.put.poznan.pl

Fabiańska Amelia, student, Poznan University of Technology
e-mail: amelia fabiańska@student.put.poznan.pl

Wieczorek Bartosz, DSc Eng., associate professor, Poznan University of Technology
e-mail: bartosz.wieczorek@put.poznan.pl

DOI 10.52209/2706-977X_2026_2_46 **IRSTI 55.01.37** **UDC 004.50**

Fault Diagnosis Using Limited Vibration Dataset with Hyperparameter Optimization

Zarog M.*, Al-Adawi S., Al-Nabhani M., Al-Aufi I.
Department of Mechanical and Industrial Engineering, College of Engineering, Sultan Qaboos University
*corresponding author

Abstract. Fault diagnosis in mechanical systems plays a critical role in predictive maintenance and operational safety. This study presents a machine learning-based approach for identifying common mechanical faults using a limited vibration dataset. An experimental setup was developed to simulate and record vibrations from various conditions, including healthy operation, bearing faults, gear defects, and screw looseness. Vibration data were collected in three dimensions and transformed into the frequency domain. Several classification algorithms, including Naïve Bayes, Logistic Regression, Decision Table, Random Tree, and Random Forest, were trained to detect these faults. Additionally, Auto-WEKA was employed to optimize both algorithm selection and hyperparameters. Among all tested methods, the Random Forest classifier with hyperparameter optimization achieved superior performance with a classification accuracy of 97.1% and an estimated error rate of 0.85%. The study highlights that even with a relatively small dataset, high diagnostic performance is achievable through proper algorithm selection and hyperparameter tuning. The findings are particularly relevant for applications in industrial environments where collecting large labelled datasets is costly or impractical.

Keywords: condition monitoring, machine learning, fault diagnosis, vibration monitoring, preventive maintenance, and fault detection

Introduction

To keep rotating machinery, such as pumps and motors, reliable and functionally efficient, fault detection and classification are crucial. Vibration analysis has long been used as an important method for monitoring the status of such equipment. Machine learning techniques can be utilized to analyse measured vibration data. However, these approaches highly depend on past historical data for training, which might not be available, or costly. Traditional machine learning methods, though effective in many cases, often require large amounts of labeled data to achieve high accuracy in fault classification. This limitation has driven researchers to explore advanced machine learning techniques, such as Hyperparameter Optimization This adaptability is critical in industrial settings where the amount of data available for model training may be limited. Several studies have shown that ANNs can outperform traditional models in terms of classification accuracy when dealing with small datasets. For instance, Kankar et al. [1] demonstrated the effectiveness of ANNs in classifying bearing faults using a relatively small vibration dataset, highlighting the model's ability to generalize from limited information. Similarly, Khan and Yairi [2] investigated fault diagnosis using deep learning approaches and found that neural networks could achieve superior results with constrained data availability. Research by Jia et al. [3] demonstrated that ANN-based models could automatically identify relevant features from raw vibration signals, and had shown promise in limited data scenarios, their success largely depends on network architecture, training techniques, and data preprocessing. Also, Lei et al. [4] proposed an improved ANN framework for fault classification in mechanical systems, emphasizing the importance of these techniques in optimizing model performance on small datasets.

The use of convolutional neural networks (CNNs) has also been explored for fault classification. Bouvrie [5] and Chen et al. [6] showed that CNNs are capable of learning spatial hierarchies from vibration signals, enabling accurate classification of gearbox and motor faults. Gude et al. [7] provided evidence that time-frequency analysis combined with machine learning can detect engine-related anomalies effectively using vibration data. Many more attempts were carried out for fault discriminative features using unlabelled and a limited number of labelled samples for classification [8-12]. Deep learning was not pursued because the available dataset was relatively small, increasing the risk of severe overfitting and poor generalization. Traditional machine learning methods were considered more appropriate because they typically perform better than deep learning on limited datasets with structured features. Considering the risk of overfitting and the absence of large-scale training data, traditional machine learning models optimized through Auto-WEKA offered a more reliable and practical solution.

Despite these advances, many models require large datasets and computational resources. In this context, the current study emphasizes the practicality of using limited datasets and traditional classifiers, enhanced through Auto-WEKA optimization, to achieve comparable performance in fault diagnosis tasks. Given the increasing use of fault classification in industrial applications, it is essential to assess their efficiency, particularly when dealing with limited vibration datasets. This paper aims to explore the performance of hyperparameter optimization in classifying faults from vibration data, focusing on how the training methods can be optimized to ensure reliable fault detection with minimal data.

1. Experimental set up and data collection

A mechanical system, as shown in Figure.1, was designed to simulate different faults in the system components (e.g. bearings, gears and screws looseness). The electric motor provides the system with kinetic energy, through which the system is operated. The motor was installed in the base using screw and nuts. the power produced by the motor is transmitted through gear box, that alter the speed and torque, along the pulleys and belts to shaft, through bearing. The system was mounted on base frame via screws, as shown in Figure.1. Vibration was measured at different faulty scenarios as well as during normal condition (vibration when no fault is there). Measurements were taken for the vibration amplitude and frequency in the x, y, and z directions. Measurement was repeated 10 times for each condition (healthy condition, faulty bearings, faulty gears, and screws looseness). Figure.2 shows faults in gears, bearing, and looseness of the screw. Figure.3, 4, 5, and 6 shows vibration measurement in frequency domain for healthy and faulty components. The experimental readings from the sensor were taken over wide range of frequencies (0 to 512 Hz, with interval of 0.5 Hz). The readings were taken for the normal condition and then for different faults of each component.

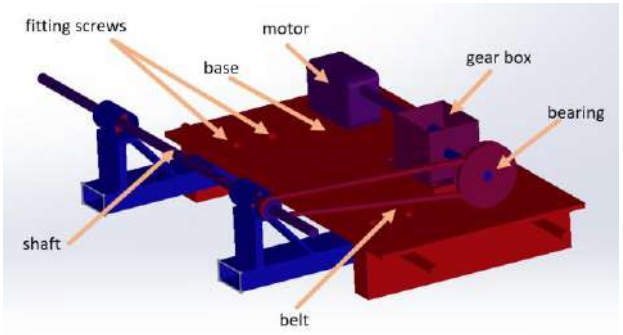

Fig.1. - 3D view of the system components.

(a) (b) (c)

Fig.2. - Faults in gears (a), bearing (b), and looseness (c)

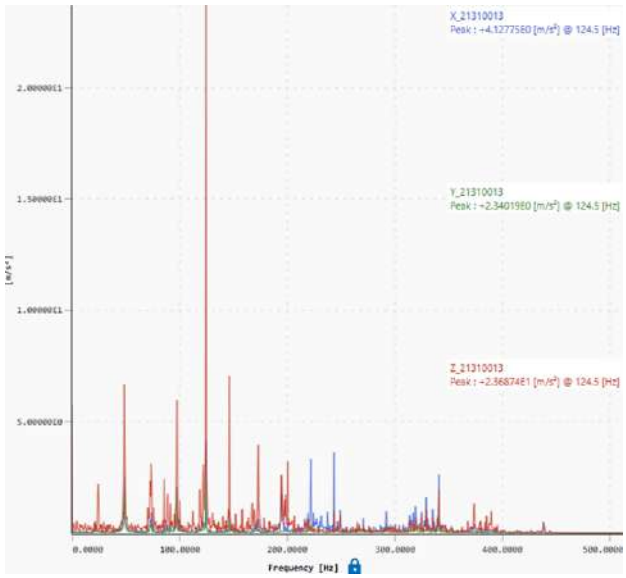

Fig.3. - Measured data of healthy system in frequency domain

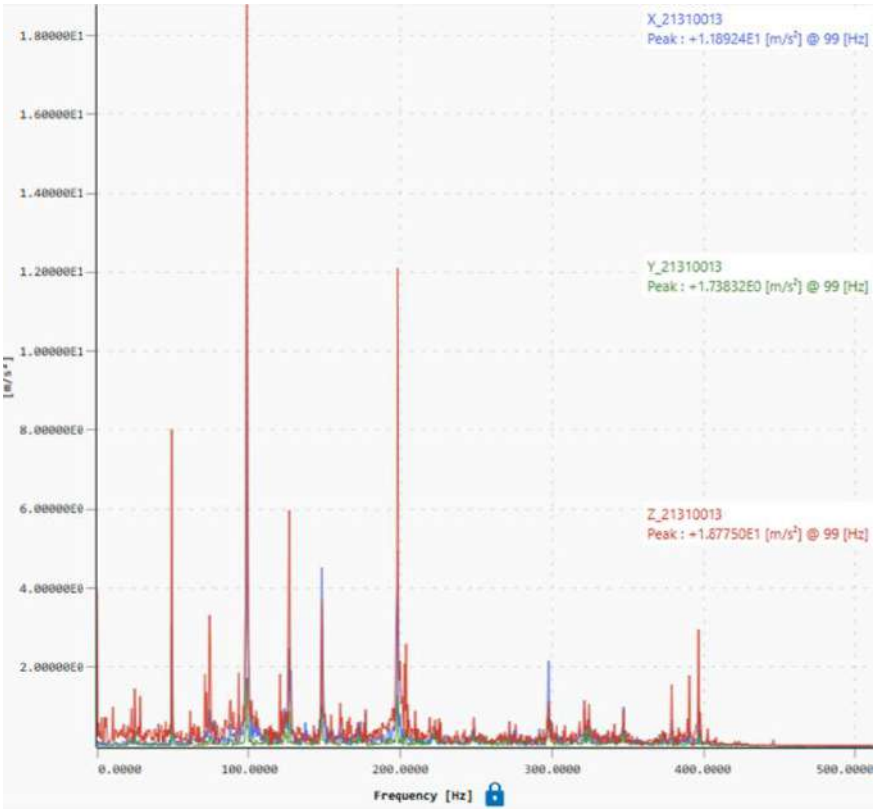

Fig.4. - Measured data with faulty system in frequency domain (Screw looseness fault)

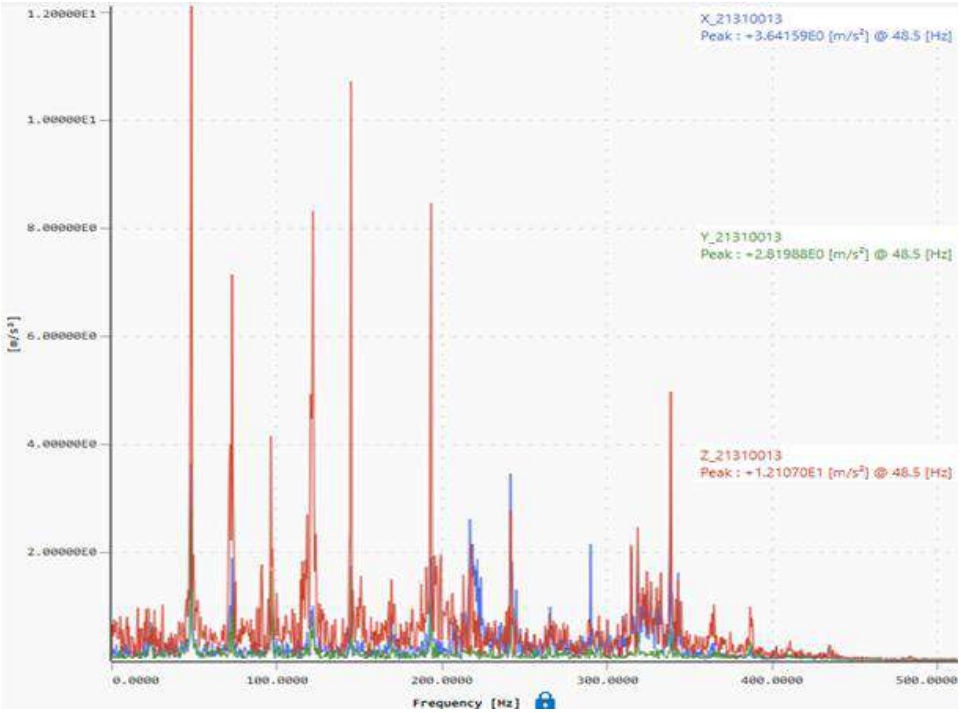

Fig.5. - Measured data with faulty system in frequency domain (Bearing fault)

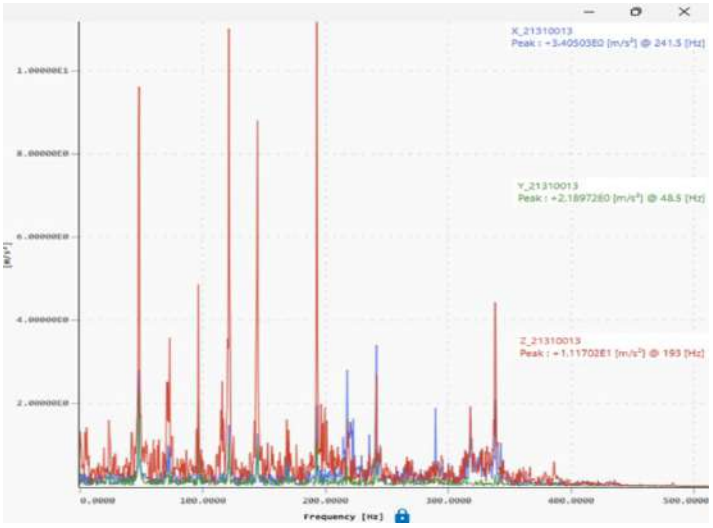

Fig.6. - Measured data with faulty system in frequency domain (Gear fault)

2. Results

The obtained dataset from the captured vibration signals were utilized for training using ML algorithms. The evaluation was conducted using five widely used classifiers - Naïve Bayes, Logistic Regression, Decision Table, Random Tree, and Random Forest - under two classification scenarios: multiclass classification involving four distinct fault conditions as shown in Table.1, and binary classification comparing normal operation against each individual fault type as shown in Table.2. The vibration signal for each of the four fault conditions was measured over the frequency range of 0–512 Hz with a frequency resolution of 0.5 Hz, resulting in 1024 readings for each fault condition. Since four fault conditions were considered, the total number of instances in the dataset was 4096.

Table 1. Classification results for all four conditions

Algorithm/Measures (using 10 folds)	Naïve Bayes	Logistic	Decision Table	Random Tree	Radom Forest (4 conditions)
Correctly Classified Instances	1150	1481	1701	1857	2163
Incorrectly Classified Instances	2950	2619	2399	2243	1937
correctly classified instances	28%	36.0%	42.0%	45.0%	53.0%
Mean absolute error	0.37	0.36	0.336	0.27	0.28
Root mean squared error	0.45	0.43	0.4101	0.52	0.38
Relative absolute error	98.0 %	97.0 %	89.6 %	72.9 %	74.6 %
Root relative squared error	104.0 %	98.4 %	94.7 %	120.8 %	88.6 %
Total Number of Instances	4096	4096	4096	4096	4096

Table 2. Classification results for normal conditions Vs other conditions

Class	Normal Vs looseness fault	Normal Vs bearing fault	Normal Vs Gear fault
Naïve Bayes			
Correctly Classified Instances	1068	1078	1178
Incorrectly Classified Instances	982	972	872
correctly classified instances %	52 %	52.6 %	57.5 %
Mean absolute error	0.49	0.48	0.44
Root mean squared error	0.54	0.55	0.51
Relative absolute error	97.1 %	96.1 %	88.9 %
Root relative squared error	108.0%	111.0 %	102.4 %
Total Number of Instances	2048	2048	2048

Continuation of Table 2

Logistic			
Correctly Classified Instances	1318	1224	1424
Incorrectly Classified Instances	732	826	626
correctly classified instances %	64.3 %	59.7 %	69.4 %
Mean absolute error	0.45	0.48	0.41
Root mean squared error	0.47	0.49	0.45
Relative absolute error	90.3 %	96.6 %	82.9 %
Root relative squared error	94.9 %	98.3 %	90.4 %
Total Number of Instances	2048	2048	2048
Decision Table			
Correctly Classified Instances	1365	1304	1492
Incorrectly Classified Instances	685	746	558
correctly classified instances %	66.6%	63.6 %	72.8 %
Mean absolute error	0.43	0.43	0.37
Root mean squared error	0.45	0.47	0.43
Relative absolute error	86.0 %	86.3 %	74.4 %
Root relative squared error	93.0 %	93.1 %	86.9 %
Total Number of Instances	2048	2048	2048
Random Tree			
Correctly Classified Instances	1478	1333	1552
Incorrectly Classified Instances	572	717	498
correctly classified instances %	72.1%	65.0 %	75.7 %
Mean absolute error	0.28	0.35	0.24
Root mean squared error	0.52	0.59	0.49
Relative absolute error	55.8 %	70.0 %	48.6 %
Root relative squared error	105.6%	118.3 %	98.6 %
Total Number of Instances	2048	2048	2048
Radom Forest algorithm			
Correctly Classified Instances	1596	1452	1674
Incorrectly Classified Instances	454	598	376
correctly classified instances %	77.9 %	70.8 %	81.7 %
Mean absolute error	0.30	0.35	0.26
Root mean squared error	0.39	0.44	0.37
Relative absolute error	60.3 %	70.9 %	51.2 %
Root relative squared error	78.2 %	87.1 %	73.4 %
Total Number of Instances	2048	2048	2048

3. Hyperparameter Optimization

Given a set of learning algorithms $\mathcal{A}$ and a limited amount of training data $D = \{(X_1, Y_1), \ldots\ldots, (X_n, Y_n)\}$, the goal of model selection is to determine the algorithm $A^* \in \mathcal{A}$ with optimal generalization performance. Generalization performance is estimated by splitting D into disjoint training and validation sets $D_{train}^{(i)}$ and $D_{valid}^{(i)}$, learning functions f_i by applying A^* to $D_{train}^{(i)}$, and evaluating the predictive performance of these functions on $D_{valid}^{(i)}$. This allows for the model selection problem to be written as [13]:

$$A^* \in argmine_{A^* \in \mathcal{A}} \ \frac{1}{k} \sum_{i=1}^{k} \mathcal{L}(A, D_{train}^{(i)}, D_{valid}^{(i)}).$$

where $\mathcal{L}(A, D_{train}^{(i)}, D_{valid}^{(i)})$ is the loss (here: misclassification rate) achieved by A When trained on $D_{train}^{(i)}$ and evaluated on $D_{valid}^{(i)}$.

We use k-fold cross-validation [18], which splits the training data into k equal-sized partitions $D_{valid}^{(1)}$,…, $D_{valid}^{(K)}$, and sets $D_{train}^{(i)} = D / D_{valid}^{(i)}$ for $i = 1, \ldots, K$.

More formally, following [15], we say that a hyperparameter λ_i is conditional on another hyperparameter λ_j, if λ_i is only active if the hyperparameter λ_j takes values from a given set $V_i(j) \subsetneq \Lambda_j$; In this case, we call λ_j a parent of λ_i. Conditional hyperparameters can in turn be parents of other conditional hyperparameters, giving rise to a tree-structured space [3] or, in some cases, a directed acyclic graph (DAG) [15]. Given such a structured space Λ, the (hierarchical) hyperparameter optimization problem can be written as [13]:

$$\lambda^* \in argmine_{\lambda \in \mathcal{A}} \ \frac{1}{k}\sum_{i=1}^{k} \mathcal{L}\left(A_\lambda, D_{train}^{(i)}, D_{valid}^{(i)}\right).$$

Given a set of algorithms $\mathcal{A} = \{A^{(1)}, \ldots, A^{(k)}\}$ with associated hyperparameter spaces $\Lambda^{(1)}, \ldots, \Lambda^{(k)}$, we define the combined algorithm selection and hyperparameter optimization problem (CASH) as computing [13]:

$$A^*_{\lambda^*} \in argmine_{A^{(j)} \in \mathcal{A},\ \lambda \in \Lambda^{(j)}} \ \frac{1}{k}\sum_{i=1}^{k} \mathcal{L}\left(A_\lambda{}^{(j)}, D_{train}^{(i)}, D_{valid}^{(i)}\right). \qquad (1)$$

Auto-WEKA can automatically and simultaneously choose a learning algorithm and set its hyperparameters to optimize empirical performance [13]. Auto-WEKA tested various algorithms (e.g., SVMs, decision trees, etc.) and found that the Random Forest classifier produced the lowest estimated error rate on the dataset. Auto-WEKA optimized for the lowest error rate, which is defined as the percentage of incorrect predictions, which was found to be 0.0085. This means only about 0.85% of the test instances are expected to be misclassified using this configuration.The forest is composed of 130 decision trees. More trees can lead to better performance (to a point), but with increased computation. Maximum depth of trees: Limits the depth of each individual tree to prevent overfitting. A value of 15 allows moderately deep trees that capture complex patterns without going too deep. No feature selection (attribute search) was applied like BestFirst or GreedyStepwise.

Table 3. Classification results for all four conditions using hyperparameter optimization

Correctly Classified Instances	3982
Incorrectly Classified Instances	118
correctly classified instances %	97.1%
Mean absolute error	0.17
Root mean squared error	0.23
Total Number of Instances	4096

		Actual Class			
		Normal pump	Bearing	Screw	Gear
Predicted Class	Normal pump	1023	39	43	23
	Bearing	2	985	2	6
	Screw	0	0	978	0
	Gear	0	1	2	996

Fig.7. - Confusion matrix using hyperparameter optimization

True Positive Rate (TP Rate) / Sensitivity / Recall is the proportion of actual positive cases that were correctly identified by the model. A higher TP rate means the model is good at detecting positive instances (e.g., correctly identifying a fault when it is actually present).

$$Recall = \frac{True\ Positives}{True\ Positives + False\ Negatives}$$

False Positive Rate (FP Rate) represents proportion of negative cases that were incorrectly classified as positive. A lower FP rate is desirable as it indicates fewer false alarms.

$$FP\ Rate = \frac{False\ Positives}{True\ Negatives + False\ Positives}$$

Precision represents the proportion of predicted positive cases that were actually correct. Precision focuses on the quality of positive predictions. High precision means fewer false positives.

$$Precision = \frac{True\ Positives}{True\ Positives + False\ Positives}$$

F-Measure (F1-Score) is the harmonic mean of Precision and Recall, providing a single metric that balances both. It is useful when you want a balance between precision and recall. A high F1-score means both false positives and false negatives are low.

$$\mathrm{F-Measure\ (F1-Score)} = 2 \times \frac{Precision \times Recall}{Precision + Recall}$$

Matthews Correlation Coefficient (MCC) is a measure of the quality of binary classifications, considering all four confusion matrix categories: TP, TN, FP, and FN. It ranges from -1 to +1. A value of +1 indicates perfect prediction, 0 indicates random prediction, and -1 indicates total disagreement

$$\mathrm{MCC} = \frac{(TF \times TN) - (FP \times FN)}{\sqrt{(TP + FP)(TP + FN)(TN + FP)(TN + FN)}}$$

ROC Area (Area Under the ROC Curve – AUC-ROC) is the area under the Receiver Operating Characteristic (ROC) curve, which plots TP Rate against FP Rate at various thresholds. It ranges from 0 to 1.Higher values (closer to 1) indicate better model discrimination ability between classes.

RC Area (Area Under the Precision-Recall Curve – AUC-PR)is the area under the curve that plots Precision against Recall for different threshold values. It ranges from 0 to 1. It is especially useful when dealing with imbalanced datasets. A high PRC area indicates the model maintains high precision and recall across thresholds.

Table 4. Detailed accuracy by class using hyperparameter optimization

TP Rate	FP Rate	Precision	Recall	F-Measure	MCC	ROC Area	PRC Area	Class
0.954	0.000	1.000	0.954	0.977	0.969	1.000	0.999	screw
0.998	0.034	0.907	0.998	0.950	0.935	0.998	0.995	normal
0.972	0.001	0.997	0.972	0.984	0.979	0.998	0.995	gear
0.961	0.003	0.990	0.961	0.975	0.967	0.999	0.998	bearing
0.971	0.010	0.973	0.971	0.972	0.963	0.999	0.997	Weighted Avg

4. Results discussion

The experimental results from this study clearly demonstrate the efficacy of various machine learning classifiers in identifying mechanical faults using vibration signals. The performance was evaluated across five common classifiers—Naïve Bayes, Logistic Regression, Decision Table, Random Tree, and Random Forest—using both multiclass

classification (four fault conditions) and binary classification (normal vs. each fault type). Furthermore, Auto-WEKA was employed to optimize model hyperparameters, resulting in a significant boost in predictive accuracy.

Table 1 presents the classification accuracy for the multiclass fault diagnosis task using unoptimized models. Among the five classifiers; Naïve Bayes achieved the lowest accuracy (28%), primarily due to its strong assumption of feature independence, which is often violated in vibration data. Logistic Regression and Decision Table showed moderate improvement, with accuracies of 36% and 42%, respectively. Random Tree outperformed the earlier models with a 45% accuracy. Random Forest achieved the highest accuracy of 53%, confirming its strength in handling complex patterns through ensemble learning. However, even the best performance from unoptimized models remained suboptimal, likely due to default parameter settings and the complexity of distinguishing between similar vibration patterns in mechanical components.

In binary classification tasks (Table 2), where normal conditions were compared individually against looseness, bearing faults, and gear faults. All classifiers showed improved accuracy compared to the multiclass task. Random Forest again outperformed other models, achieving up to 81.7% accuracy when distinguishing normal from gear faults. The accuracy declined slightly for bearing faults (70.8%) and looseness faults (77.9%), indicating overlapping features between these fault types and healthy conditions. These results suggest that binary classification simplifies the decision boundaries, allowing models to focus on more distinct patterns between two classes. However, this approach is less practical in real-world settings, where simultaneous detection of multiple faults is required.

To address the limitations of default settings, Auto-WEKA was employed to perform algorithm selection and hyperparameter tuning. The optimized Random Forest model was configured with 130 trees and a maximum depth of 15, enabling it to capture deeper interactions without overfitting. As shown in Table 3, the optimized model achieved a classification accuracy of 97.1% on the full dataset (four-class classification), a dramatic improvement from the initial 53%. The estimated error rate was reduced to 0.85%, signifying highly reliable classification and

further confirming the robustness of the optimized model.

Figure 7 illustrates the confusion matrix, showing that most samples were correctly classified across all categories. The model showed near-perfect classification of screw looseness and gear faults, with almost no misclassifications. Some misclassification occurred between normal and bearing faults, which may be attributed to subtle vibration differences in early bearing degradation. The class-wise evaluation metrics in Table.3 shows that the Precision and Recall values exceeded 0.95 across all fault types. The F1-score, which balances precision and recall, was above 0.97 for most classes. The Matthews Correlation Coefficient (MCC) values, a balanced measure even for imbalanced data, were all above 0.96, indicating strong predictive reliability. Both the ROC Area and PRC Area were close to 1.0, reflecting excellent separability between classes. These results validate the effectiveness of using optimized Random Forest models for real-time fault detection with limited data. The model not only generalizes well but also maintains high sensitivity and specificity across all fault categories.

However, limitations remain such as the system was tested under controlled laboratory conditions; field environments may introduce noise and variability not captured here.

Future work should explore transfer learning or domain adaptation to apply the model across different machines or operational scenarios. Incorporating time-domain features or additional sensor modalities (e.g., acoustic or thermal signals) could further enhance diagnostic robustness.

Conclusion

This study demonstrated that machine learning algorithms, particularly the Random Forest model, are highly effective in diagnosing mechanical faults using vibration signals. The experimental setup enabled the generation of a compact yet diverse dataset encompassing four operational conditions. Initial tests across multiple classifiers showed moderate performance, with Random Forest achieving the highest accuracy at 53% before optimization. By applying Auto-WEKA for hyperparameter tuning and algorithm selection, the optimized Random Forest model achieved a significantly improved classification accuracy of 97.1% and a low error rate of 0.85%. This confirms that hyperparameter optimization can greatly enhance model performance, even when using limited datasets. The outcome supports the integration of intelligent diagnostic systems in predictive maintenance applications, improving system reliability while minimizing downtime and inspection costs. These findings highlight the effectiveness of optimized ensemble learning techniques for early fault detection in mechanical systems with limited data.

Conflict of Interest

The authors declare no conflict of interest.

Acknowledgment

This work was funded by Sultan Qaboos University-Qatar University joint fund Grant No. CL/SQU\QU/ENG/24/01.

References

[1] Kankar P., Sharma S. C., Harsha S. P. Fault diagnosis of ball bearings using machine learning methods //Expert Systems with Applications, 2011, vol. 38, no. 3, pp. 1876–1886
[2] Khan S., Yairi T. A review on the application of deep learning in system health management //Mechanical Systems and Signal Processing, 2018, vol. 107, pp. 241–265
[3] Jia F., Lei Y., Lin J., Zhou X., Lu N. Deep neural networks: A promising tool for fault characteristic mining and intelligent diagnosis of rotating machinery with massive data //Mechanical Systems and Signal Processing, 2016, vol. 72-73, pp. 303–315
[4] Lei Y., He Z., Zi Y. A new approach to intelligent fault diagnosis of rotating machinery //Expert Systems with Applications, vol. 2008, 35, no. 4, pp. 1593–1600
[5] Bouvrie J. Notes on convolutional neural networks //Tech. Rep., MIT, 2006.
[6] Chen Z., Li C., Sanchez R. V. Gearbox fault identification and classification with convolutional neural networks //Shock and Vibration, 2015.
[7] Gude A., Pawar S., Alhat S., Mishra S. Vibration analysis for engine fault detection //Journal of Robotics and Control (JRC), 20212(3), 205-208.
[8] Berenji A., Taghiyarrenani Z., Bastami A. R. Fault identification with limited labeled data //*Journal of Vibration and Control*. 2023, 30(7-8),1502-1510
[9] Li C., Gilad A., Glavic B., Miao Z., Roy, S. Refining labeling functions with limited labeled data // arXiv:2505.23470
[10] Gilanifar, M., Wang, H., Cordova, J., Ozguven, E. E., Strasser, T. I., Arghandeh R. Fault classification in power distribution systems based on limited labeled data using multi-task latent structure learning //Sustainable Cities and Society, 2021, 73, 1–10.
[11] Jin Y., Hou L., Du M., Chen Y. A limited labeled data bearing fault diagnosis method based on self-supervised learning. arXiv. https://arxiv.org/abs/2207.10432, 2022
[12] Zhao R., Yan R., Chen Z., Mao K., Wang P., Gao R. X. Iterative deep graph learning and embedding for industrial fault diagnosis with limited labeled data //IEEE Transactions on Industrial Informatics, 2021, 17(6), 4090–4099.
[13] Thornton C., Hutter F., Hoos H. H., Leyton-Brown K. Auto-WEKA: Combined selection and hyperparameter optimization of classification algorithms // Proceedings of the 19th ACM SIGKDD International Conference on Knowledge Discovery and Data Mining, 2013, pp. 847–855.

Information of the authors

Zarog Musaab, PhD, assistant professor, Department of Mechanical and Industrial Engineering, College of Engineering, Sultan Qaboos University
e-mail: musaabh@squ.edu.om

Al-Adawi Sulaiman, BEng, graduate student, Department of Mechanical and Industrial Engineering, College of Engineering, Sultan Qaboos University
e-mail: s131265@student.squ.edu.om

Al-Nabhani Mohammed, BEng, graduate student, Department of Mechanical and Industrial Engineering, College of Engineering, Sultan Qaboos University
e-mail: s131265@student.squ.edu.om

Al-Aufi Isehaq, BEng, graduate student, Department of Mechanical and Industrial Engineering, College of Engineering, Sultan Qaboos University
e- mail: s131265@student.squ.edu.om

DOI 10.52209/2706-977X_2026_2_55 **IRSTI 81.09.03** **UDC 666.952.2**

Natural Radioactivity of Solid Fuels and Ash-And-Slag Materials in the Context of their Environmental Impact

Pak D.*, Pak Yu., Ibragimova D., Tebayeva A.
Abylkas Saginov Karaganda Technical University, Karaganda, Kazakhstan
*corresponding author

Abstract. The indicators of natural radioactivity of solid fuels and ash-and-slag materials are examined in the context of assessing their environmental impact. The distribution of naturally occurring radionuclides in fuels and combustion products is analyzed based on gamma-spectrometric and neutron activation studies. It is shown that fuel combustion leads to a significant concentration of natural radionuclides in ash-and-slag materials, resulting in an increase in their specific activity compared to the parent fuel. Radionuclide concentration factors and effective specific activity values are calculated. An assessment of the potential radioecological burden is performed. Statistically significant correlations between rare-earth elements and radioactive nuclides are identified. The obtained results demonstrate the feasibility of using natural radioactivity indicators as an informative tool for environmental monitoring of coal-based power generation and for assessing anthropogenic impacts on the environment.

Keywords: ash-and-slag materials, solid fuels, naturally occurring radioactive elements, rare-earth elements, radioecological monitoring

Introduction

Coal-based power generation plays a key role in the energy balance of the Republic of Kazakhstan. A substantial share of electricity production is provided by the combustion of coal from the Ekibastuz and Karaganda basins, which results in a persistent anthropogenic impact on the environment. One of the most significant environmental factors associated with the operation of coal-fired thermal power plants is the generation and accumulation of ash-and-slag wastes containing a wide spectrum of chemical and radioactive components.

According to data from the United Nations Scientific Committee on the Effects of Atomic Radiation (UNSCEAR) [1], the average concentrations of naturally occurring radionuclides in coal are as follows: U-238–16–110Bq/kg; Ra-226–17–60Bq/kg; Th-232 – 11–64 Bq/kg; K-40 – 40–850 Bq/kg. The concentrations of radioactive elements vary over a wide range depending on coal genesis, quality, and the compositional characteristics of both organic and mineral constituents. The issue of natural radioactivity of Kazakhstan's coals and the distribution of individual radionuclides remains insufficiently studied. In general, Kazakhstan's coals are characterized by low levels of radioactivity, with concentrations of naturally occurring radionuclides (U-238, Th-232, Ra-226, K-40) close to Clarke values [2,3].

According to the International Atomic Energy Agency (IAEA), the global total release of uranium and thorium during coal combustion amounts to approximately 37.3 t per year [4]. As reported in [5], more than 750 million tonnes of ash-and-slag waste have accumulated in ash disposal sites of Kazakhstan over several decades of coal-fired power plant operation. It can therefore be readily inferred that existing ash-and-slag materials are effectively transforming into quasi-technogenic deposits of radioactive elements and numerous rare metals, including toxic ones.

Ash-and-slag disposal sites of coal-fired power generation represent long-term sources of anthropogenic impact, capable of forming elevated radiation backgrounds in adjacent areas and affecting the atmosphere, soils, and surface waters. The radioecological hazard of such facilities is determined not only by the absolute values of radionuclide specific activity, but also by the scale of waste accumulation, storage conditions, and the potential for secondary dust formation and migration of radioactive components into the environment [6].

The degree of trace element enrichment in combustion products depends on their modes of occurrence in coal, the volatility of their oxides, and other compounds formed during the combustion process. Low-volatility compounds tend to accumulate in ash-and-slag wastes, whereas more volatile species are preferentially concentrated in emissions, particularly in fly ash [7].

Particular attention should be given to establishing the relationship between the contents of rare-earth elements (REEs) and naturally occurring radionuclides (NORs). Many REE-bearing minerals, such as monazite, xenotime, and bastnäsite, simultaneously incorporate uranium and thorium into their crystal structures [8]. Consequently, enrichment of coal and ash-and-slag materials with REEs is often accompanied by increased radioactivity. In addition to natural radionuclides, coals and ash-and-slag wastes contain a wide spectrum of metals, including rare-earth elements of both environmental and geochemical significance. During coal combustion, redistribution of chemical elements occurs, whereby rare-earth elements, as well as uranium and thorium, are preferentially concentrated in the mineral phase and subsequently accumulated in ash-and-slag wastes. The co-occurrence of rare-earth elements and naturally occurring radionuclides is controlled by their common geochemical hosts, primarily aluminosilicate, phosphate, and oxide minerals.

In this context, analysis of the relationship between the distribution of rare-earth elements and indicators of natural radioactivity provides deeper insight into element migration within the “coal–ash–environment” system and enhances the informativeness of radioecological assessments of coal-based power generation.

Despite the existence of individual studies addressing the natural radioactivity of coal and ash-and-slag wastes, there remains a need - under the conditions of Kazakhstan - for a comprehensive analysis of radiometric indicators specifically from the perspective of assessing the environmental impact of fuel-based power generation. This need is driven by both the scale of coal-fired electricity production and the specific characteristics of the high-ash coals utilized, which result in substantial accumulation of combustion wastes.

Accordingly, the use of natural radioactivity indicators of coal and ash-and-slag wastes as a tool for radioecological assessment is of practical importance for monitoring coal power facilities, analyzing environmental risks, and substantiating measures aimed at reducing anthropogenic impacts on the environment.

1. Materials and methods

Coal and ash-and-slag waste samples were collected at the Temirtau power plant and at the power plant located in the settlement of Topar, taking into account zones of technological impact. The Temirtau power plant utilizes coal from the Ekibastuz basin, while the Topar power plant operates on coal from the Borly deposit; accordingly, the samples in Tables 1 and 2 are labeled by the source coal deposit (Borly and Ekibastuz) rather than by the sampling site.

Gamma-spectrometric analysis of coal samples and ash-and-slag wastes with a mass of approximately 1 kg was performed at Ecoexpert LLP (Karaganda) using a CANBERRA spectrometer and Genie-2000 software. The specific activities of the radionuclides U-238, Ra-226, Th-232, and K-40 were determined. The measurement duration was approximately 5 h, ensuring minimal statistical uncertainty. Uranium and thorium activities were calculated based on the characteristic gamma lines of their daughter decay products. For the given measurement geometry (Marinelli beaker, sample mass of about 1 kg) and counting time, the minimum detectable activity (MDA) for K-40 was 23 Bq/kg; specific activities below this threshold are reported as '<23' in Table 1.

For a subset of samples, additional measurements were carried out using an MKS-01A “MULTIRAD” scintillation gamma spectrometer with PROGRESS software. The analysis was conducted for samples with a mass of about 1 kg over an energy range of 60–2000 keV. Instrument calibration was performed using standard Cs-137 and K-40 sources. The calculation of radionuclide specific activity was carried out in an automated mode in accordance with methodologies applied in radiation monitoring.

The recorded natural gamma-radiation spectra of coal and ash clearly exhibit the main photopeaks of radionuclides from the uranium and thorium decay series, as well as the single gamma line of K-40, confirming the reliability of identification and quantitative assessment of the natural radioactivity of the studied samples.

For a subset of samples, high-sensitivity neutron activation analysis was additionally applied (Laboratory of Tomsk Polytechnic University, Tomsk, Russia), enabling quantitative determination of naturally occurring radionuclides and associated trace elements. The samples were irradiated in a thermal neutron flux at a research nuclear reactor, followed by spectrometric measurement of the induced gamma activity and calculation of elemental concentrations through comparison with reference standards. The experimental workflow is illustrated in Figure 1.

Coal ash yield was determined using standard laboratory methods in accordance with applicable regulatory documents and ranged from 32.8 to 38.8%. To assess the redistribution of radionuclides during combustion, concentration factors were calculated as the ratio of the specific activity of a radionuclide in ash-and-slag wastes to its activity in the parent fuel.

Radioecological assessment was performed based on the calculation of the effective specific activity of ash-and-slag wastes, taking into account the contribution of the main naturally occurring radionuclides. In addition, a potential dose burden was evaluated using the calculated specific activity values, which made it possible to characterize the potential environmental impact of coal-based power generation [9]:

$$D=0.462A_{Ra}+0.604A_{Th}+0.042A_{K40}, \quad (1)$$

where D is the absorbed dose rate (nGy/h^{-1}), and A_{Ra}, A_{Th}, and A_{K40} are the specific activities of the corresponding radionuclides (Bq kg^{-1}).

The total content of light rare-earth elements (∑LREE) was calculated as the sum of the concentrations of La, Ce, Nd, and Sm. In addition, concentration factors and correlation coefficients between ∑LREE, Th, and U were calculated, with the level of statistical significance (p) being evaluated. These calculations enabled an analysis of the potential co-migration and mineralogical association of the elements, as well as the identification of radiogenic sources of REEs in the coal matter.

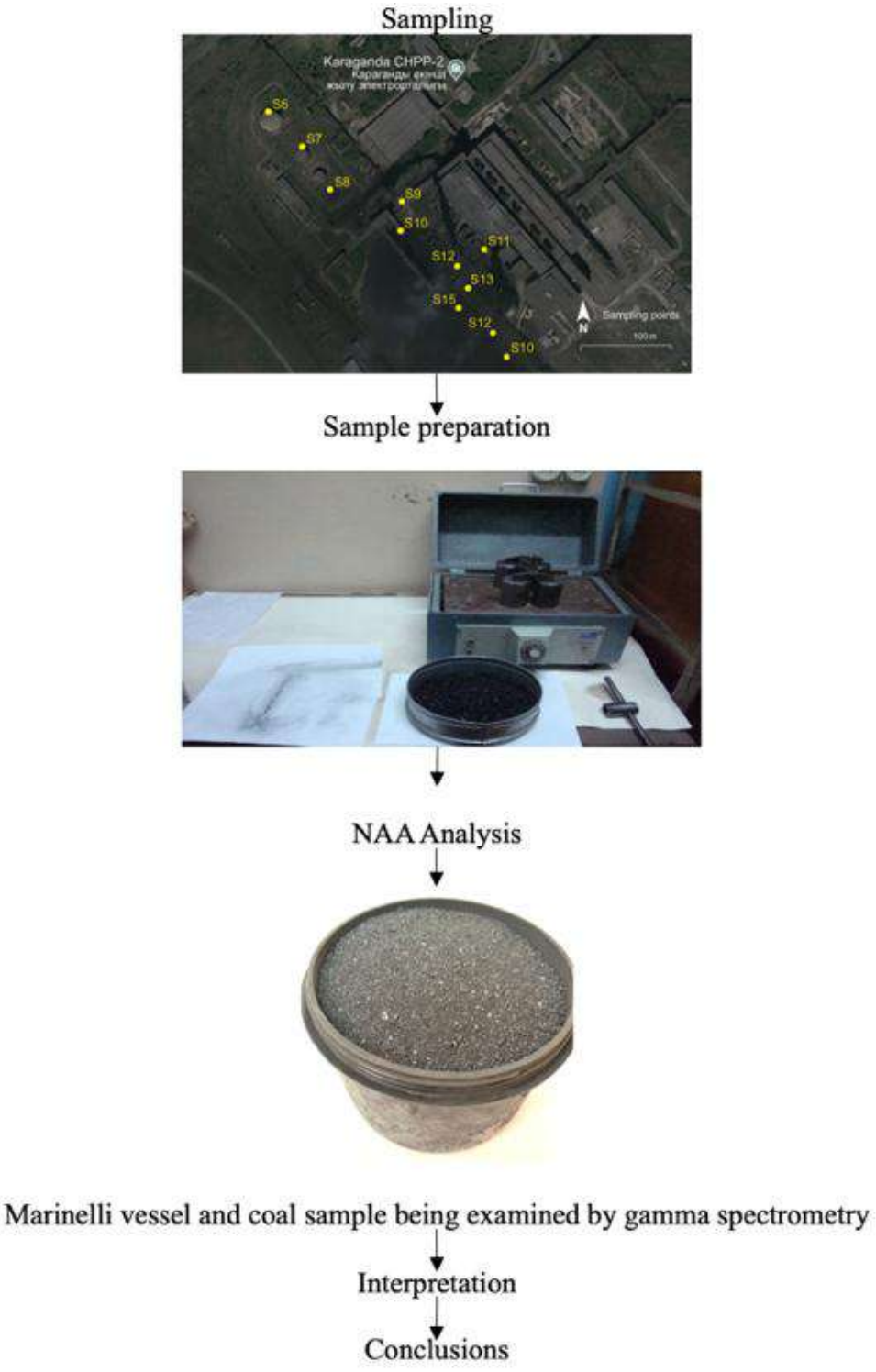

Fig. 1. – Schematic of the research workflow

2. Results

Gamma-spectrometric investigations showed that coals from the Ekibastuz and Borly coal basins are characterized by relatively low specific activities of naturally occurring radionuclides of the uranium and thorium decay series, as well as of the K-40 isotope. In most cases, the obtained values are comparable to background and global average levels typical of fossil coals, which allows the studied coals to be classified as low-radioactivity materials.

Data on the radioactivity of coals and ash-and-slag wastes obtained in this study are presented in Tables 1 and 2.

Table 1. Results of gamma-spectrometric analysis of natural radioactivity

Series	Radionuclide	Borly	Borly	Ekibastuz	Ekibastuz
		Bq/kg			
		Coal	Ash-and-slag materials	Coal	Ash-and-slag materials
U^{238}	U^{238}	26,2	68,2	17,5	33,5
	Th^{234}	26,2	68,2	17,5	33,5
	Pb^{214}	26,3	65,2	24,1	34,5
	Pb^{210}	43,3	75,1	18,3	24,3
	$Ra-^{226}$	22,0	64,2	18,4	32,9
	Bi^{214}	23,4	59,7	24,6	33,0
Th^{232}	Th^{232}	21,8	45,4	15,2	30,4
	Ac^{228}	21,8	45,4	15,2	30,4
	Pb^{212}	20,9	44,3	16,3	32,2
	Ra^{224}	20,1	42,8	17,0	30,2
	Bi^{212}	16,2	46,1	18,5	34,3
	Tl^{208}	7,2	15,2	5,3	11,1
	K^{40}	<23	113,0	97,0	144,0

Note: Note: '<23' denotes a K-40 specific activity below the minimum detectable activity (MDA = 23 Bq/kg) for the applied measurement conditions.

Table 2. Results of instrumental neutron activation analysis

Deposit	Number of samples	Sample	INAA			
			U, g/t	Th, g/t	K^{40}, Bq/kg	Th/U, g/t
Ekibastuz	11	Coal	0,8-1,5	2,6-3,6	61,4-87,6	3,3-2,4
	9	Ash-and-slag materials	4,2-8,2	11,8-17,9	112,1-243	2,8-2,9

The results of gamma-spectrometric and neutron activation analyses of coal indicate low levels of natural radioactivity. Radionuclide concentrations in coals from the studied deposits are close to global average values. At the same time, coal combustion products–ash-and-slag materials–exhibit significantly higher specific activities of naturally occurring radionuclides compared to the parent fuel. For all investigated sites, a consistent increase in the concentrations of U-238, Th-232, and K-40 in ash-and-slag materials was observed, which is attributed to the burnout of the organic matter of coal and the redistribution of radionuclides into the mineral phase. This effect confirms the well-established pattern of natural radionuclide concentration in solid combustion residues previously reported for coal-based power generation in other regions.

Radionuclide concentration factors, defined as the ratio of a radionuclide's specific activity in ash-and-slag materials to that in the parent coal, were calculated from the gamma-spectrometric data (Table 1). They amount to 2.6 (Borly) and 1.9 (Ekibastuz) for U-238, 2.9 and 1.8 for Ra-226, and 2.1 and 2.0 for Th-232; for K-40, the factor is 1.5 for the Ekibastuz samples, while for Borly only a lower-bound estimate (>4.9) is possible due to below the MDA in the parent coal (<23 Bq/kg). These values are consistent with the ash yield of the studied coals (32.8–38.8%), corresponding to a theoretical maximum enrichment factor of 2.6–3.0. Higher apparent factors derived from the non-paired INAA data (Table 2; ~4.5–5.5 for U and Th) should be regarded as indicative only.

A comparison with the worldwide average specific activities of naturally occurring radionuclides in soils (U-238 – 33 Bq/kg, Ra-226 – 32 Bq/kg, Th-232 – 45 Bq/kg, K-40 – 420 Bq/kg [1]) shows that the U-238 and Ra-226 activities in the Borly ash-and-slag materials exceed the average soil levels by approximately a factor of two, while the Th-232 activity is comparable to that of soils and the K-40 activity remains below the soil average. Although the absolute specific activities of ash-and-slag materials are only moderately elevated relative to soils, their radioecological significance is determined primarily by the large scale of waste accumulation, long-term open storage, and the potential for secondary dust formation and migration of radionuclides into adjacent environments.

The total content of light rare-earth elements (∑LREE) was determined as the sum of the concentrations of La, Ce, Nd, and Sm. In addition, concentration factors and correlation coefficients between ∑LREE, thorium, and uranium were calculated, with evaluation of their statistical significance (p). These calculations made it possible to analyze potential patterns of co-redistribution of the investigated elements and their mineralogical associations, as well as to assess the role of radiogenic components in shaping the rare-earth element composition of coals.

A significant correlation was observed between ∑LREE and uranium content ($r = 0.68$, $p = 0.022$), as well as between ∑LREE and thorium content ($r = 0.63$, $p = 0.038$). An even stronger correlation was identified between ∑LREE and the combined content of U + Th ($r = 0.75$, $p = 0.008$) (Figure 2).

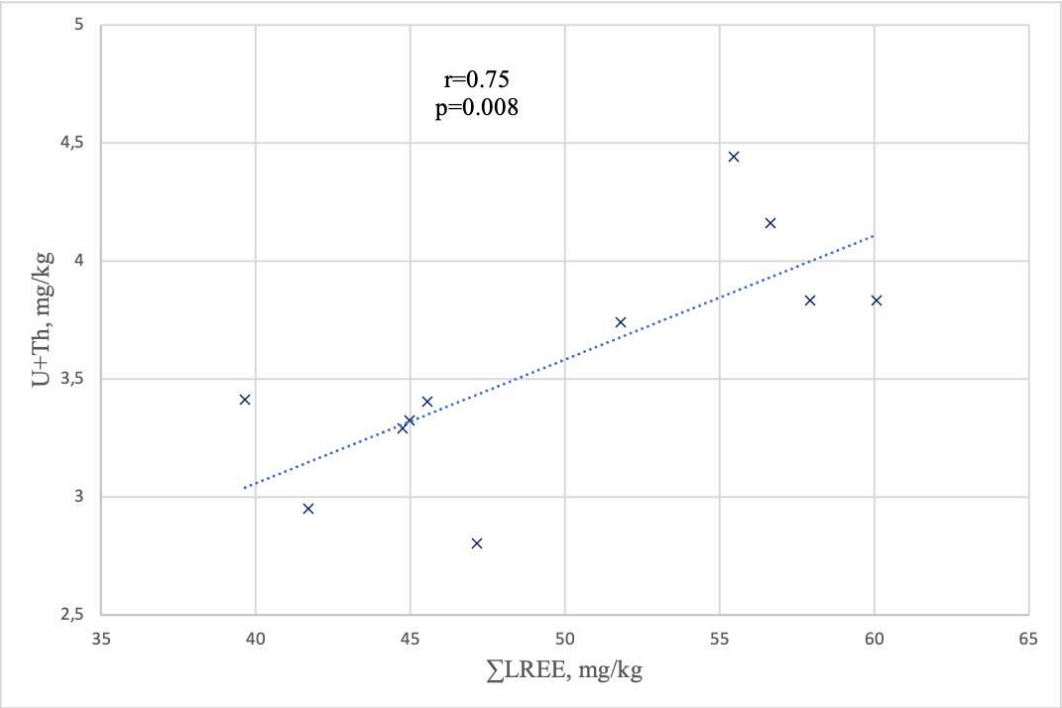

Fig. 2. – Relationship between the total uranium and thorium concentration and the total concentration of light REEs in coal

The assessment of potential dose burden based on the calculated specific activity values indicates that ash-and-slag disposal sites may serve as sources of additional external exposure in adjacent areas. The magnitude of this impact is governed not only by the radioactivity of the wastes but also by their operational conditions, the area of ash disposal sites, and the effectiveness of dust suppression and reclamation measures. Under conditions of long-term accumulation and open storage of ash-and-slag wastes, this factor becomes particularly important for environmental safety. The calculated absorbed dose rate D was 176 nGy h^{-1}, corresponding to an equivalent dose rate of 0.18 μSv h^{-1}, which results in an annual effective dose of 1.6 mSv. The obtained values slightly exceed global average levels and are comparable with the results of radioecological studies of coal in Poland [10], India [11], and Serbia [12].

Thus, regardless of the deposit or the type of coal used, ash-and-slag materials are characterized by significantly higher levels of natural radioactivity compared to the parent fuel. This fact is of fundamental importance for the radioecological assessment of fuel-based power generation, as ash-and-slag materials represent long-term sources of anthropogenic impact on the environment.

Conclusions

The studies have shown that the natural radioactivity of solid fuels and ash-and-slag materials serves as an informative tool for assessing the environmental impact of coal-based power generation. The investigated coals are characterized by relatively low levels of natural radioactivity corresponding to background values, whereas a significant concentration of naturally occurring radionuclides occurs in ash-and-slag materials.

It has been established that rare-earth elements exhibit geochemical affinity with elements of the uranium–thorium series, as evidenced by the identified correlations between the total content of light rare-earth elements and the concentrations of uranium and thorium. This indicates a preferential association of rare-earth elements with the mineral matter of coal and its combustion products.

Dose assessment has shown that ash-and-slag disposal sites can generate additional external gamma radiation in adjacent areas. The obtained dose values are comparable to those reported for coal-mining regions in other countries and indicate the necessity of considering the radiation factor in environmental monitoring of coal-based power facilities.

Funding. This research was funded by the Science Committee of the Ministry of Science and Higher Education of the Republic of Kazakhstan (grant no. AP26199353).

References

[1] United Nations Scientific Committee on the Effects of Atomic Radiation. Sources and Effects of Ionizing Radiation. UNSCEAR 2000 Report to the General Assembly, with Scientific Annexes. Volume I: Sources, Annex B: Exposures from natural radiation sources; United Nations: New York, NY, USA, 2000.
[2] Pak Yu. N., Pak D. Yu., Ibragimova D. A., Matonin V., Tebayeva A. Yu. Assessment of Natural Radioactivity and Trace Element Composition of Coals and Ash and Slag Waste in Kazakhstan// Atmosphere, 2025 16(2), 125 https://doi.org/10.3390/atmos16020125
[3] Pak Yu.N., Pak D.Yu., Nuguzhinov Zh.S., Tebaeva A.Iu. Natural radioactivity of coal in the context of radioecological safety and rational use// Izvestiya Vysshikh Uchebnykh Zavedenii. Gornyi Zhurnal, 2021, №1. – C. 97-106.
[4] Ionizing Radiation: Sources and Effects. UNSCEAR 1982 Report to the General Assembly, with annexes. New York, 1982. 773 p.
[5] Sidorova G.P., Krylov D.A., Ovcharenko N.V. Radiation conditions in areas of coal-fired thermal power plants in Russia. *Vestnik ZabGU*, 2017, vol. 23, no. 5, pp. 36–44.
[6] Schneider L., Neil R. L., Lintern A., Sinclair D., Zawadzki A., Holley C., Aquino-López M. A., Haberle S. Assessing environmental contamination from metal emission and relevant regulations in major areas of coal mining and electricity generation in Australia. //Science of the Total Environment, 2020, vol. 728, pp. 137–398
[7] Maria de Lurdes Dinis, António Fiúza, Joaquim Góis, José Soeiro de Carvalho, Ana C. Meira Castro Assessment of Natural Radioactivity, Heavy Metals and Particulate Matter in Air and Soil around a Coal-Fired Power Plant—An Integrated Approach//Atmosphere, 2021, 12, 1433. https://doi.org/10.3390/atmos12111433
[8] Ren W., Cao Q., Yang L., Huang S. Uranium in Chinese coals: Concentration, spatial distribution, and modes of occurrence//Journal of Environmental Radioactivity, 2022, V.246, 106848 https://doi.org/10.1016/j.jenvrad.2022.106848
[9] Adrovic F.; Prokic M.; Nincovic M.M.; Glissic N. Measurements of environmental background radiation at location of coal-fired power plants //Radiat. Prot. Dosimetry, 2004, 112, 439–442.
[10] Walenchik-Lata A., Smolka-Danielowska D. ^{234}U, ^{238}U, ^{226}Ra, ^{228}Ra and ^{40}K concentrations in feed coal and its combustion products during technological processes in the Upper Silesian Industrial Region, Poland. Environmental Pollution, 2020, 267, 115-462. https://doi.org/10.1016/j.envpol.2020.115462
[11] Bhangare R.C., Ajmal P.Y., Sahu S.K., Puranik V.D. Distribution of trace elements in coal and combustion residues from five thermal power plants in India // International Journal of Coal Geology, 2011,V.86, 349-356. doi:10.1016/j.coal.2011.03.008
[12] Dragovic S., Jankovic Lj., Onjia A. Assessment of gamma dose rates from terrestrial exposure in Serbia and Montenegro //Radiation Protection Dosimetry, 2006. doi:10.1093/rpd/ncl099

Information of thew authors

Pak Dmitri Yuryevich, c.t.s., ass. professor, Abylkas Saginov Karaganda Technocal University
e-mail: d.pak@ktu.edu.kz

Pak Yuri Nikolayevivh, Dr. Eng, professor, Abylkas Saginov Karaganda Technocal University
e-mail: yu.pak@ktu.edu.kz

Ibragimova Diana Andreevna, PhD, research fellow, Abylkas Saginov Karaganda Technocal University
e-mail: podgornaya1992@mail.ru

Tebayeva Anar Yulayevna, master, lecturer, Abylkas Saginov Karaganda Technocal University
e-mail: tebaeva@ktu.edu.kz

DOI 10.52209/2706-977X_2026_2_61 **IRSTI 55.13.17** **UDC 621.9**

The Influence of Cutting Depth on Surface Finish and Dimensional Accuracy

Juraev M.A.[1], Sherov K.T.[2], Tuyboyov O.V.[3], Kardassinov S.M.[4*], Khan V.A.[5]
[1]Almalyk branch of Tashkent state technical university, Almalyk, Uzbekistan
[2,5]S.Seifullin Kazakh Agro-Technical Research University, Astana, Republic of Kazakhstan
[3]Ministry of Higher Education, Science and Innovation of the Republic of Uzbekistan, Tashkent, Uzbekistan
[4]Kazakh Automobile and Road Institute, Almaty, Kazakhstan
*corresponding author

Abstract. This study investigates the effect of cutting depth on surface finish and dimensional accuracy in CNC turning of AISI 4340 steel using TiAlN - coated carbide inserts under dry conditions. A comprehensive experimental methodology was employed, incorporating precise control of machining parameters, surface topography measurements via profilometry and atomic force microscopy (AFM), dimensional inspection using coordinate measuring machines (CMM), and dynamic analysis through force and vibration monitoring. The results reveal a strong nonlinear relationship between depth of cut and both surface roughness and dimensional deviation. Surface quality remained stable at shallow depths (0.1 - 0.3 mm) but deteriorated sharply beyond 0.7 mm due to the onset of regenerative chatter. Similarly, dimensional accuracy declined significantly at greater depths due to increased tool deflection and thermal expansion. Cutting forces and tool wear exhibited exponential growth beyond 0.5 mm depth, with flank wear and edge degradation confirmed through SEM analysis. ANOVA results identified depth of cut as the most statistically significant factor influencing machining quality, with contribution ratios of 48.2% for surface roughness and 42.7% for dimensional deviation. The optimal depth of cut was identified within the 0.3 - 0.5 mm range, offering the best balance between material removal rate, surface integrity, and dimensional precision.

Keywords: cutting depth, surface roughness, dimensional accuracy, cnc machining, tool wear, regenerative chatter, cutting forces, AISI 4340 steel, vibration analysis, TiAlN-coated inserts

Introduction

Achieving high-quality surface finish [1] and dimensional accuracy is a fundamental objective in precision machining, directly impacting the functionality, performance, and service life of manufactured components. In this context, the depth of cut emerges as a critical process parameter, with profound effects on material removal behavior, tool-workpiece interaction [2], thermal and mechanical loads, and the overall quality of the machined surface. While traditionally considered a basic input variable, depth of cut has gained renewed attention due to its complex interdependence with cutting forces, vibration dynamics [3], tool deflection [4], and heat generation-factors that collectively influence both surface integrity and geometric precision. In advanced manufacturing sectors such as aerospace, biomedical, and automotive engineering, stringent specifications on surface roughness and dimensional tolerances necessitate meticulous control over machining parameters. Surface roughness, typically expressed through Ra and Rz values, governs functional attributes such as friction, wear resistance, and fatigue strength. Meanwhile, dimensional accuracy ensures proper part assembly and operational performance. Extensive research has identified depth of cut as a key variable influencing these outputs, with its effects modulated by material properties, tool geometry, machining environment, and dynamic system behavior.

Studies have shown that increasing the depth of cut generally raises cutting forces, leading to elevated temperatures, tool wear [5], and vibrational instabilities-all of which deteriorate surface finish. Conversely, excessively shallow cuts, while potentially improving surface quality, may compromise material removal rates and economic efficiency. For example, in hard turning of alloy steels and superalloys [6], optimal surface finish is often achieved at moderate depths of cut, where the trade-off between tool engagement stability and cutting efficiency is balanced. Similarly, in the milling of aluminum alloys, smaller depths reduce chatter susceptibility and improve surface morphology, particularly under dry or near-dry lubrication conditions. The impact on dimensional accuracy is equally significant. As the depth of cut increases, tool deflection becomes more pronounced due to higher bending moments, especially in slender or overhanging tool configurations. This deflection results in profile deviation, geometric inaccuracy, and poor repeatability. Furthermore, heat accumulation during deeper cuts causes localized thermal expansion, which can lead to out-of-tolerance features. These effects are especially critical in the machining of thin-walled structures [7], micro-components [8], and heat-sensitive materials, where dimensional deviations can render components non-functional. Beyond static effects, the depth of cut dynamically influences machining stability. It governs the regenerative mechanism responsible for self-excited vibrations or chatter, which in turn affects surface texture, tool life, and process reliability. Stability lobe theory illustrates that at specific spindle speeds, certain depths of cut yield chatter-free machining zones [9], while others induce instability. Hence, understanding the depth-dependent dynamic behavior of the cutting system is vital for selecting parameters that optimize both surface finish and dimensional accuracy. The influence of depth of cut is

further nuanced by machining strategies and technological advancements. In ultra-precision machining and micro-milling, where submicron accuracy is required, the transition from cutting to plowing at low depths introduces nonlinearities in surface generation and tool wear mechanisms. In vibration-assisted machining and hybrid techniques, depth of cut must be finely tuned to exploit the synergistic effects of superimposed motions or external energy fields, which enhance chip evacuation and reduce process-induced damage.

The interaction between depth of cut and other variables, such as feed rate, spindle speed, tool geometry, and cooling conditions, must also be carefully managed. Multi-objective optimization techniques, including Taguchi methods, response surface methodology (RSM) [10], and machine learning models, have been employed to map these interdependencies and identify optimal machining windows. However, many of these approaches are material-specific and lack general applicability across different machining contexts. Despite substantial progress, challenges remain in developing predictive models that holistically capture the influence of cutting depth across a wide spectrum of materials, machining regimes, and operational conditions. Additionally, integrating real-time monitoring of forces, vibrations, and temperatures with adaptive control systems remains an open area of research for improving process consistency and automation.

This study addresses these gaps by systematically investigating the influence of cutting depth on surface roughness and dimensional accuracy across varying machining conditions. Through a combination of experimental analysis, vibration and force monitoring, and process modeling, the research aims to provide mechanistic insights and practical guidelines for depth-of-cut optimization [11]. The findings will contribute to the advancement of precision machining methodologies and the development of intelligent, stable, and high-performance manufacturing systems.

1. Methodology

This study employed a systematic experimental approach to investigate the influence of cutting depth on surface finish and dimensional accuracy during CNC machining operations [12]. The methodology integrates material and tool selection, controlled variation of machining parameters, high-resolution metrological assessments, dynamic signal acquisition, and statistical optimization to ensure comprehensive and repeatable results. The workpiece material selected for this investigation was AISI 4340 alloy steel [13], chosen due to its industrial relevance and sensitivity to cutting conditions. Known for its toughness and moderate machinability, AISI 4340 provides an ideal testbed for analyzing surface integrity and geometric deviations under varying depths of cut.

Machining was performed using cemented tungsten carbide inserts, coated with TiAlN [14], selected for their superior thermal resistance, wear resistance, and performance under dry cutting conditions. The inserts featured a standardized nose radius of 0.8 mm and a positive rake angle of 6°, based on prior research suggesting their efficacy in minimizing cutting forces and improving surface texture.

Figure 1 shows an integrated CNC test rig for evaluating the influence of cutting depth on surface quality, dimensional accuracy and dynamic stability.

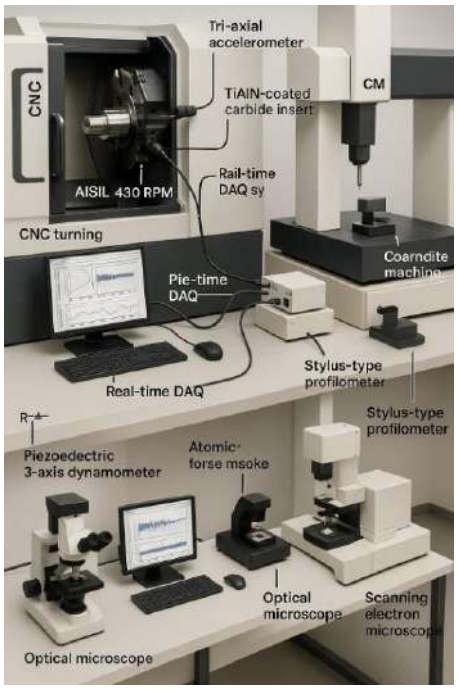

Fig.1. - Integrated CNC Machining Test Rig for Evaluating the Influence of Cutting Depth on Surface Finish, Dimensional Accuracy, and Dynamic Stability

All machining operations were carried out on a high-precision CNC turning center under ambient dry conditions to isolate the mechanical influence of cutting parameters. The cutting parameters investigated were:

- depth of cut (DoC): 0.1 mm to 1.0 mm (in increments of 0.1 mm);
- spindle speed: 800 to 2000 RPM;
- feed rate: 0.05 to 0.25 mm/rev.

These parameters were selected based on prior empirical ranges known to influence surface quality and dimensional accuracy. A Taguchi L9 orthogonal array was used to systematically vary the process variables, ensuring robust data collection with minimized experimental repetition. This design allowed for the subsequent application of Analysis of Variance (ANOVA) [15] to quantify the statistical significance of each parameter on the quality responses. Surface roughness (Ra) was measured using a two-tiered approach: Stylus-based contact profilometer for macro-scale roughness evaluation. Atomic Force Microscopy (AFM) for high-resolution surface analysis below 0.2 μm. AFM scans were conducted in tapping mode to prevent surface damage and to capture nanoscale surface morphology. Multiple readings were recorded along the tool path to account for variation and to derive average roughness values. This dual-mode measurement ensured both breadth and depth in surface characterization, allowing for robust correlation with depth-of-cut variations. Dimensional deviations were measured using a Coordinate Measuring Machine (CMM) with an accuracy of ±2 μm. Critical geometric features were compared against the nominal CAD model using 3D inspection routines. Supplementary measurements were carried out using digital micrometers (±1 μm resolution) for features where CMM accessibility was limited. Each part was measured at multiple points, and deviations were quantified using both mean absolute error and standard deviation to assess repeatability and dimensional consistency. To capture real-time dynamic responses during cutting, a piezoelectric 3-axis dynamometer was integrated beneath the workpiece to measure cutting force components (Fx, Fy, Fz).

The signals were logged at high sampling rates and processed to compute Root Mean Square (RMS) force values at each depth level.

In parallel, tri-axial accelerometers were affixed to the tool holder to monitor vibration amplitudes and frequencies. Data were analyzed using Fast Fourier Transform (FFT) [16] and wavelet decomposition to detect chatter onset and assess the dynamic stability of the machining system as a function of depth. Post-machining tool inspection was conducted using optical microscopy and scanning electron microscopy (SEM). Wear patterns such as flank wear, crater formation, and edge chipping were documented and correlated with surface roughness and dimensional error trends. This analysis helped identify the depth-of-cut thresholds beyond which tool wear accelerated, adversely affecting machining quality.

3. Results and Discussions

The experimental investigation revealed a strong dependence of both surface finish and dimensional accuracy on the applied depth of cut. As the depth of cut increased, significant changes were observed in cutting force magnitudes, surface topography, geometric deviation, and tool wear behavior. The outcomes of the study are presented in a structured manner, highlighting key findings related to surface roughness trends, dimensional deviations, dynamic responses, and tool condition. Surface roughness (Ra) demonstrated a consistent increase with rising depth of cut across all trials. At lower depths (0.1 - 0.3 mm), the machined surfaces exhibited uniform texture with average Ra values between 0.35 - 0.45 μm, indicative of stable cutting conditions and minimal tool-workpiece interface disruption. At moderate depths (0.4 - 0.6 mm), Ra values increased to 0.5 - 0.7 μm, accompanied by the onset of micro-patterns aligned with tool feed direction.

Notably, at depths exceeding 0.7 mm, surface roughness values escalated sharply, with Ra reaching 1.0 - 1.4 μm. At 1.0 mm depth, surface morphology became highly irregular, as confirmed by AFM scans, with observable plowing marks and feed-direction tearing. These patterns coincided with increased vibration amplitudes and suggest that beyond a critical depth threshold (~0.7 - 0.8 mm), regenerative chatter begins to degrade surface integrity.

Fig. 2 illustrates the quantitative relationship between depth of cut (DoC) and surface roughness (Ra) during precision turning operations of AISI 4340 steel using TiAlN-coated carbide tools under dry conditions. At low cutting depths (0.1 - 0.3 mm), the surface roughness remains relatively low and consistent (Ra ≈ 0.35 - 0.45 μm), reflecting stable tool-workpiece interaction and minimal cutting-induced deformation. In this region, the machining process operates within a dynamically stable regime, characterized by minimal vibration, low cutting forces, and reduced tool-material friction. As the depth of cut increases to 0.4 - 0.6 mm, the Ra values begin to rise (up to \~0.70 μm), indicating the emergence of surface irregularities due to increased mechanical load, moderate tool deflection, and the onset of minor dynamic disturbances. This transitional phase marks the sensitivity zone where machining stability begins to degrade. Beyond a critical depth threshold (\~0.7 mm), the plot shows a sharp escalation in surface roughness (Ra > 1.0 μm). This is attributed to the initiation of regenerative chatter, a self-excited vibration phenomenon that arises from feedback between the tool and previously cut surface. The resulting chatter increases cutting force fluctuations, destabilizes chip formation, and generates non-uniform surface textures such as plowing marks, tearing, and waviness.

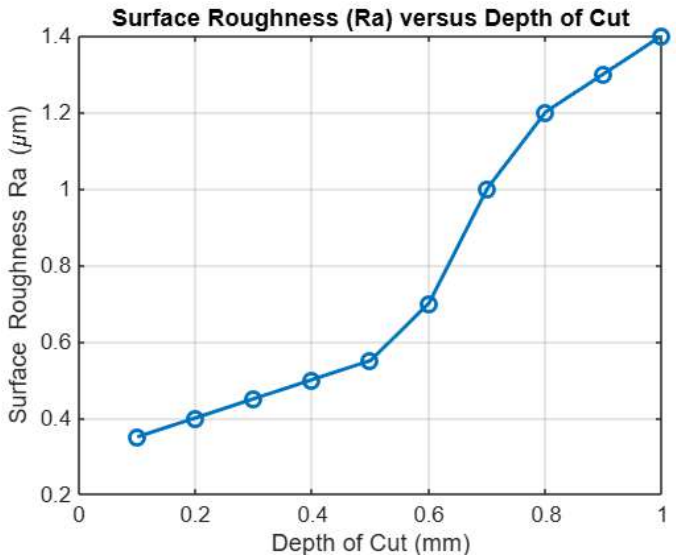

Fig. 2. - Surface Roughness Evolution as a Function of Cutting Depth in CNC Machining of AISI 4340 Steel

The rising trend observed in the high-depth region (0.8 - 1.0 mm) signifies the system's entry into a dynamically unstable regime, where surface integrity is severely compromised, and machining performance deteriorates. This transition highlights the importance of identifying and avoiding excessive depths of cut in high-precision applications, particularly when surface finish is a critical functional requirement.

Dimensional accuracy declined progressively with increasing depth of cut. Measurements from the CMM showed that geometric deviation from nominal dimensions remained within ±5 µm at depths of 0.1 - 0.3 mm, indicating excellent conformity and minimal tool deflection. However, as the depth of cut increased beyond 0.5 mm, deviations rose significantly, reaching ±12 - 18 µm at 0.8 mm and exceeding ±25 µm at 1.0 mm. This dimensional loss was attributed to increased tool deflection and elastic deformation of the workpiece under higher cutting loads. Additionally, measurements from digital micrometers validated the CMM findings, particularly for cylindrical diameters, which showed clear signs of tapering and overcutting at higher depths.

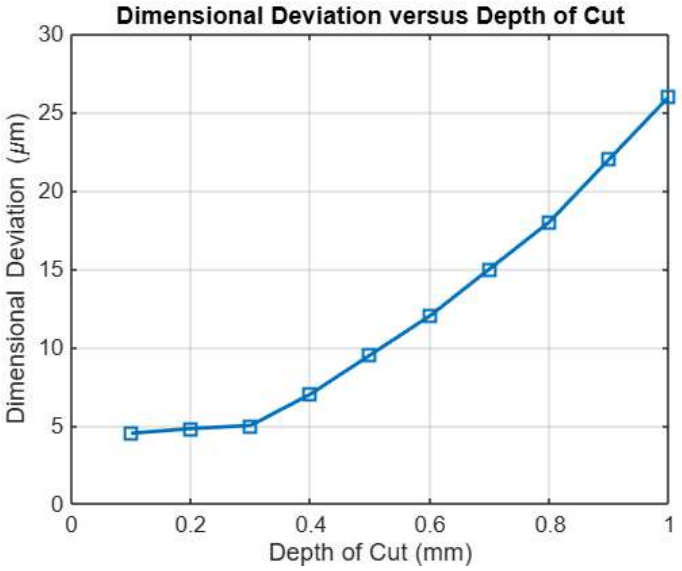

Fig. 3. - Effect of Depth of Cut on Dimensional Deviation in Precision CNC Machining of AISI 4340 Steel

Fig. 3 illustrates the relationship between depth of cut (DoC) and dimensional deviation during CNC turning of AISI 4340 steel, using TiAlN-coated carbide tools under dry machining conditions. At shallow depths (0.1 - 0.3 mm), the dimensional deviation remains minimal (≈ ±5 µm), indicating excellent machining precision. In this region, the cutting forces and tool deflection are relatively low, maintaining close conformity to nominal geometry. The system operates in a quasi-static regime, where elastic deformation of the tool and workpiece remains negligible. As the depth of cut increases beyond 0.5 mm, the dimensional deviation begins to rise markedly, reflecting the effects of increased mechanical load

and tool deflection. At 0.8 mm, deviation reaches ±18 µm, and at 1.0 mm, it exceeds ±25 µm. These changes are caused by: Bending moments acting on the tool due to higher cutting forces, leading to radial displacement. Elastic deformation of the workpiece under increased contact pressure. Localized thermal expansion from elevated cutting temperatures, further distorting part geometry. Micrometric tapering and overcutting observed at high depths confirm the compounding effect of both static deflection and dynamic instability. Such dimensional inaccuracies are particularly detrimental in aerospace, mold, and biomedical manufacturing, where tight tolerances are mandatory. The nonlinear trend emphasizes the need to identify safe depth-of-cut thresholds that balance productivity with dimensional integrity. This plot, therefore, serves as a quantitative diagnostic tool for parameter optimization in high-precision machining.

Force measurements revealed a nonlinear relationship between depth of cut and RMS cutting force values. At the lowest tested depth (0.1 mm), RMS forces were stable and low, averaging around 35 N. However, with each incremental increase in depth, the force magnitudes rose, reaching 92 N at 0.6 mm and peaking at 156 N at 1.0 mm. The force profiles showed transient spikes at higher depths, suggesting loss of steady-state conditions. Concurrently, vibration data obtained from the accelerometers revealed a marked increase in tool-tip displacement amplitude beyond 0.7 mm depth, with spectral energy concentrated around 420-680 Hz. FFT and wavelet analyses identified dominant chatter signatures beginning near the 0.8 mm depth mark. These frequencies aligned closely with the tool's natural frequency range, reinforcing the conclusion that excessive cutting depths excite system resonance and induce dynamic instability.

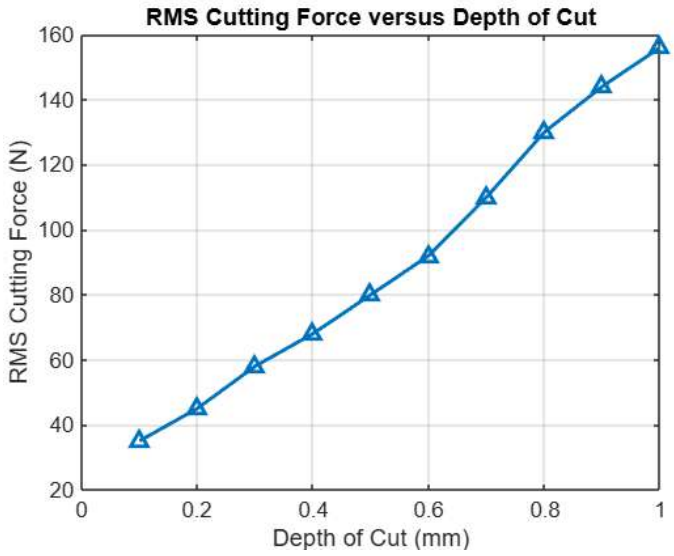

Fig. 4. - Nonlinear Growth of RMS Cutting Forces with Increasing Depth of Cut in CNC Turning of AISI 4340

Fig. 4 visualizes the relationship between depth of cut and the root mean square (RMS) cutting force during CNC turning of AISI 4340 steel under dry machining conditions. The RMS force values represent the effective cutting load experienced by the tool in response to the material removal process and are a critical indicator of machining stability and energy input. At lower depths (0.1 - 0.3 mm), the RMS cutting forces remain relatively low and stable (35 - 58 N), indicating favorable engagement conditions with minimal mechanical resistance. The system operates in a linearly elastic and stable regime, with uniform chip formation and steady cutting dynamics. As the depth of cut increases beyond 0.5 mm, the cutting forces exhibit a nonlinear upward trend, reaching 92 N at 0.6 mm and escalating sharply beyond 0.7 mm, where the RMS force climbs to 156 N at 1.0 mm. This nonlinear behavior is attributed to: Increased material removal volume, leading to greater shear zone resistance. Elevated thermal loads at the tool-chip interface, softening the workpiece and intensifying adhesion. Tool deflection and contact area expansion, increasing radial forces and friction. Onset of regenerative chatter, particularly beyond 0.7 mm, which adds dynamic fluctuations to the cutting force signal.

The plot confirms that excessive depths of cut introduce mechanical and dynamic instability, compromising tool life, dimensional precision, and surface integrity. The sharp force amplification corresponds to critical depths where system stiffness and damping are insufficient to suppress vibratory modes excited near the tool's natural frequency (420 - 680 Hz, as identified in vibration analyses). This representation supports predictive modeling and adaptive control efforts by clearly demarcating safe operating regions (<0.6 mm) and unstable zones (>0.7 mm), providing essential input for chatter avoidance and process optimization in high-performance machining applications. Microscopic examination of the cutting tools showed minimal wear at lower depths. Flank wear remained below VB = 0.05 mm for depths up to 0.4 mm. However, at higher depths, SEM analysis revealed severe flank wear, crater formation, and micro-chipping at the cutting edge. At the maximum tested depth of 1.0 mm, edge rounding and material adhesion were observed, indicating accelerated wear due to elevated temperature and abrasive action. These wear patterns directly correlated with surface degradation and profile inaccuracies, confirming that tool wear acts as a compounding factor in reducing both surface finish and

dimensional fidelity at high depths of cut. Fig. 5 illustrates the evolution of tool flank wear (VB) with respect to increasing depth of cut (DoC) during CNC turning of AISI 4340 steel using TiAlN-coated carbide inserts under dry machining conditions. At lower depths (0.1 - 0.4 mm), flank wear progression is minimal (VB ≤ 0.045 mm), indicating favorable tool-workpiece interaction, low cutting temperatures, and limited abrasive or adhesive wear. In this regime, the cutting edge maintains its integrity, and the machining process operates under stable thermal-mechanical conditions. Surface finish and dimensional accuracy are preserved due to minimal edge deformation and contact stress. As the depth of cut increases beyond 0.5 mm, a noticeable escalation in flank wear is observed, reaching VB = 0.22 mm at 1.0 mm DoC. This rapid wear accumulation is caused by: Elevated cutting forces, generating higher contact pressure and mechanical abrasion. Increased frictional heat, softening the tool material and accelerating wear mechanisms. Micro-chipping and crater formation, as confirmed by SEM observations, which compromise cutting edge sharpness. Material adhesion, leading to edge rounding and built-up edge (BUE) formation, particularly at maximum depths. These wear patterns degrade both surface finish (via roughness amplification and texture inconsistency) and dimensional accuracy (via altered tool geometry and increased deflection).

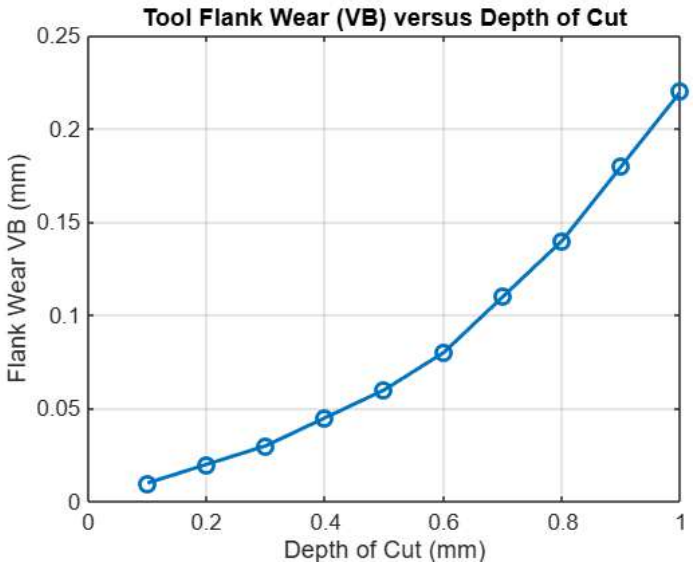

Fig. 5. - Progressive Tool Flank Wear as a Function of Depth of Cut in Dry Turning of AISI 4340 Steel

Beyond a critical depth threshold (\~0.7 mm), flank wear enters an exponential growth phase, reinforcing its role as a limiting factor in high-depth, high-speed machining. The plot quantitatively supports the conclusion that depth of cut is directly proportional to wear severity, and emphasizes the importance of wear-aware parameter selection in precision machining. It serves as a valuable tool for predicting tool life, scheduling tool changes, and optimizing depth constraints for sustainable process performance.

ANOVA results revealed that depth of cut was the most statistically significant factor influencing both surface roughness and dimensional deviation, with contribution ratios of 48.2% and 42.7%, respectively. Feed rate was the second most influential factor, particularly affecting roughness in moderate depth regions. Spindle speed had a lesser but stabilizing effect, particularly in suppressing vibration at intermediate depths. Based on the combined evaluation of Ra, dimensional accuracy, RMS force, and tool wear, the optimal depth of cut was identified in the range of 0.3 - 0.5 mm for AISI 4340 under dry conditions with TiAlN-coated inserts. This range provided the best trade-off between material removal rate, surface integrity, and geometric precision.

Fig. 6 presents a comparative bar chart showing the percentage contribution of three key machining parameters-depth of cut, feed rate, and spindle speed-to two critical quality responses: surface roughness (Ra) and dimensional deviation, based on Analysis of Variance (ANOVA).

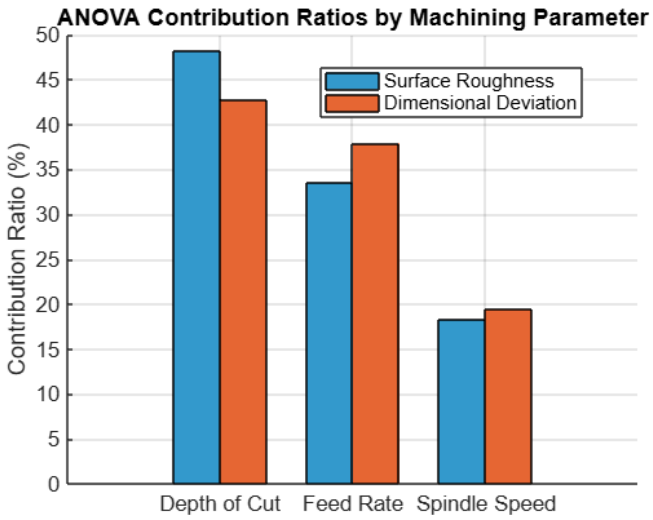

Fig. 6. - ANOVA-Based Contribution Analysis of Machining Parameters on Surface Roughness and Dimensional Accuracy in Turning of AISI 4340

1. Depth of Cut emerges as the most influential factor, contributing 48.2% to surface roughness and 42.7% to dimensional deviation. This highlights its dual role: as depth increases, so do cutting forces, thermal load, and tool-workpiece contact, which collectively impact both surface integrity and geometric precision. Beyond a critical depth threshold (\~0.7 mm), instability such as tool deflection and chatter further amplify surface and dimensional errors.

2. Feed Rate shows a secondary influence, contributing 33.5% to roughness and 37.9% to dimensional deviation. At moderate depths, feed rate directly impacts feed marks and texture uniformity, which in turn affects surface finish. Higher feed rates also induce greater force and tool vibration, indirectly affecting profile accuracy.

3. Spindle Speed has the least contribution-18.3% for surface roughness and 19.4% for dimensional deviation. Although not a dominant factor, spindle speed plays a stabilizing role, especially at mid-frequency stability lobes, where it suppresses regenerative chatter and helps maintain cutting consistency. From the combined evaluation, the optimal range of depth of cut (0.3 - 0.5 mm) offers the best trade-off between material removal rate, surface quality, dimensional control, and tool life-especially under dry turning conditions with TiAlN-coated carbide inserts.

3. Discussions

The experimental and analytical findings of this study provide comprehensive insights into the influence of cutting depth on surface finish and dimensional accuracy during CNC machining of AISI 4340 steel under dry conditions. The results validate the hypothesis that cutting depth is not merely a linear input parameter but a dynamic and multifactorial determinant of machining quality, with interdependent effects on cutting forces, vibration behavior, tool wear, and material deformation. The surface roughness results revealed a clear trend of degradation with increasing depth of cut. While shallow cuts (0.1 - 0.3 mm) maintained low Ra values (<0.45 μm) indicative of stable tool-workpiece interactions and consistent chip removal, deeper cuts introduced significant surface irregularities. This transition corresponds to a threshold zone around 0.7 - 0.8 mm, beyond which surface morphology exhibited plowing, tearing, and chatter marks. These findings are aligned with stability lobe theory, which suggests that certain combinations of cutting depth and spindle speed induce regenerative chatter due to phase mismatch between the tool and workpiece vibrations. The emergence of these chatter signatures beyond 0.7 mm was substantiated by spectral energy concentrations in the 420-680 Hz range, coinciding with the system's natural frequencies. This observation underscores the critical need for dynamic stability assessment in depth-of-cut optimization, particularly for high-performance or high-precision applications. Dimensional accuracy also exhibited a depth-dependent deterioration. At low depths, geometric deviations remained within ±5 μm, suitable for precision applications. However, increased depths resulted in progressive loss of accuracy, with deviations surpassing ±25 μm at 1.0 mm. The primary contributors to this dimensional inaccuracy were tool deflection, elastic deformation of the workpiece, and localized thermal expansion-effects exacerbated by increased cutting forces and vibrational instability. This nonlinear behavior reinforces the necessity of integrating depth-of-cut constraints into tool path planning, particularly when machining slender geometries or heat-sensitive materials.

Conclusions

The RMS cutting force trends further illustrated the compounding effects of mechanical and dynamic loading at higher depths. Forces increased from 35 N at 0.1 mm to 156 N at 1.0 mm, mirroring the nonlinear increase in both surface roughness and dimensional deviation. These elevated forces not only stress the tool-workpiece interface but also induce tool deflection, affecting both surface generation and geometrical fidelity. Additionally, transient spikes in force signals at higher depths confirmed the onset of chatter, highlighting the loss of steady-state cutting conditions. Tool wear analysis

offered additional evidence of the detrimental effects of excessive cutting depths. Minimal wear was observed up to 0.4 mm depth, but flank wear increased exponentially beyond this point, reaching VB = 0.22 mm at 1.0 mm. SEM analysis revealed micro-chipping, crater formation, and built-up edge (BUE) at the cutting edge, especially under high thermal and mechanical loads. These wear patterns correlated directly with the degradation of both surface finish and dimensional accuracy, affirming that tool wear acts as a compounding variable in machining quality loss.

Statistical validation via ANOVA provided quantitative confirmation of the dominant role of cutting depth in machining performance. Depth of cut contributed 48.2% and 42.7% to surface roughness and dimensional deviation, respectively-significantly more than feed rate or spindle speed. Although feed rate showed notable influence, especially on surface finish, and spindle speed provided a stabilizing effect at mid-frequency ranges, neither was as impactful as cutting depth. This reinforces the importance of depth-of-cut control in precision machining parameter optimization. The findings converge on the conclusion that an optimal depth of cut range of 0.3 - 0.5 mm offers the best compromise between productivity (material removal rate), surface integrity, dimensional fidelity, and tool longevity. This range maintains mechanical stability, minimizes tool deflection, limits thermal buildup, and avoids vibrational resonance, thereby supporting consistent, high-quality machining outcomes.

References

[1] Kim U. S., Park J. W. High-quality surface finishing of industrial three-dimensional metal additive manufacturing using electrochemical polishing. *International Journal of Precision Engineering and Manufacturing-Green Technology*, 2019, 6, 11-21.

[2] Chen J., Wang X., Shi L., Wu C., Liu H., Chen G. Numerical simulation of weld formation in friction stir welding based on non-uniform tool-workpiece interaction: An effect of tool pin size //Journal of Manufacturing Processes, 2023, 86, 85-97.

[3] Sherov K., Sagitov A., Tusupbekova G., Sherov A., Kokayeva G., Kossatbekova D., Abdugaliyeva G., Karsakova N. Experimental Study of Wear Resistance Improvement of Modular Disk Milling Cutter by Preliminary Pre-Processing Method //Designs 2025, 9, 30. https://doi.org/10.3390/designs9020030

[4] Mussayev M., Sherov K., Kassymbabina D., Abdugaliyeva G., Donenbayev B., Kardassinov S., Karsakova N., Tussupova S. Research of wear and increasing wear resistance of the working part of busbar punching tools by surfacing method //Journal of Applied Engineering Science, 2024, Vol. 22, No. 3, 2024, P.654-664. DOI:10.5937/jaes0-51175

[5] Arnolds H., Bonn M. Ultrafast surface vibrational dynamics //Surface Science Reports, 2010, *65*(2), 45-66.

[6] Rao V.S., Rao P.V. Tool deflection compensation in peripheral milling of curved geometries //International Journal of Machine Tools and Manufacture, 2026, *46*(15), 2036-2043.

[7] Li B. A review of tool wear estimation using theoretical analysis and numerical simulation technologies // International Journal of Refractory Metals and Hard Materials, 2012, *35*, 143-151.

[8] Sivaraman V., Prakash S. Recent developments in turning hardened steels–A review // IOP conference series: materials science and engineering, 2017, Vol. 197, No. 1, p. 012009).

[9] Borojević S., Lukić D., Milošević M., Vukman J., Kramar D. (2018). Optimization of process parameters for machining of Al 7075 thin-walled structures //Advances in Production Engineering & Management, 2018, *13*(2), 125-135.

[10] Bogue R. Assembly of 3D micro-components: a review of recent research. *Assembly Automation*, 2011, *31*(4), 309-314.

[11] Zharkevich O.M., Shlyakhov S.V., Nurzhanova O.A., Imasheva K.I. Development and Research of a New Reinforced Design of the Mounting Block //Material and Mechanical Engineering Technology, №1, 2025, P.28-35. DOI 10.52209/2706-977X_2025_1_28

[12] Toshov J., Sherov K., Baratov B., Mussayev M., Baymirzaev B., Esirkepov A., Ismailov G., Abdugaliyeva G., Burieva J. Ways To Optimize The Kinetic Parameters Of Tricone Drill Bits //Material and Mechanical Engineering Technology, №1, 2024, 35-45. DOI 10.52209/2706-977X_2024_1_35

[13] Quintana G., Campa F. J., Ciurana J., de Lacalle L. L. Productivity improvement through chatter-free milling in workshops //Proceedings of the Institution of Mechanical Engineers, Part B: Journal of Engineering Manufacture, 2011, 225(7), 1163-1174.

[14] Juraev M.A., Alikulov D.E., Kardassinov S.M., Tuyboyov O.V. Determination of Critical Depth of Cut for Stable Machining Operations //Material and Mechanical Engineering Technology, №4, 2025, P.3-9. DOI 10.52209/2706-977X_2025_4_3

[15] Said K. A. M., Amin M. A. M. Overview on the response surface methodology (RSM) in extraction processes //Journal of Applied Science & Process Engineering, 2015, *2*(1).

[16] Gupta R., Batra J. L., Lal G. Determination of optimal subdivision of depth of cut in multipass turning with constraints //International Journal of Production Research, 1995, *33*(9), 2555-2565.

[17] Venkatesh V., Swain N., Srinivas G., Kumar, P., Barshilia H. C. Review on the machining characteristics and research prospects of conventional microscale machining operations //Materials and Manufacturing Processes, 2017,*32*(3), 235-262.

[18] Santhosh A. J., Tura A. D., Jiregna I. T., Gemechu W. F., Ashok N., Ponnusamy M. Optimization of CNC turning parameters using face centred CCD approach in RSM and ANN-genetic algorithm for AISI 4340 alloy steel // Results in Engineering, 2021, 11, 100251.

[19] Sousa V. F., Da Silva F. J. G., Pinto G. F., Baptista A., Alexandre R. Characteristics and wear mechanisms of TiAlN-based coatings for machining applications: A comprehensive review //*Metals*, 2021, 11(2), 260.

[20] Henson R. N. Analysis of variance (ANOVA) //Brain mapping, 2015, 1, 477-481.

[21] Stoker P., Tian G., Kim, J. Y. Analysis of variance (ANOVA) //Basic quantitative research methods for urban planners, 2020, 197-219

Information of the authors

Juraev Musurmon Avlaqulovich, c.t.s, Associate professor, Almalyk branch of Tashkent state technical university
e-mail: musurmonjorayev666@gmail.com

Sherov Karibek Tagaevich, d.t.s, Professor, Seifullin Kazakh Agro-Technical Research University
e-mail: k.sherov@kazatu.edu.kz

Tuyboyov Oybek Valijonovich, head of the department at technology transfer office under the Ministry of Higher Education
e-mail: oybektuyboyov85@gmail.com

Kardassinov Sayat Mamyrbaevich, c.t.s., associate professor, Kazakh Automobile and Road Institute
e-mail: sa-yat@yandex.kz

Khan Valery Anatolyevich, c.t.s., associate professor, Seifullin Kazakh Agro-Technical Research University
e-mail: v.khan@kazatu.edu.kz

DOI 10.52209/2706-977X_2026_2_70 **IRSTI 55.21.19** **UDC 621.9**

Optimization of Vibration Treatment and Modification Parameters for 40CrNi3MoV Steel Based on Mathematical Modeling

Tuganbayeva A.A., Issagulov A.Z., Arinova S.K.*, Dostayeva A.M.
Abylkas Saginov Karaganda Technical University, Karaganda, Kazakhstan
*corresponding author

Abstract. The targeted control of the structure and properties of high-strength alloy steels remains one of the key challenges in modern metallurgy. This study investigates the effect of solidification temperature, vibration treatment time, and the content of the complex modifier INSTEEL-7 on the hardness of 40CrNi3MoV steel. To substantiate the temperature parameters of the process, the modeling of phase transformations was performed using the Thermo-Calc software package. Experimental studies were carried out based on a multifactorial experimental design according to V.P. Malyshev's method, involving 25 experimental melts. Based on the experimental results, partial quadratic dependencies were obtained, and a generalized mathematical model was developed to describe the influence of technological factors on Vickers hardness (HV5). It was established that the steel hardness varies within the range of 356-492 HV depending on the combination of process parameters. The rational range of technological regimes was determined: a solidification temperature of 1520-1540 °C, a vibration treatment time of approximately 30 s, and an INSTEEL-7 modifier content of about 0.03 wt.%. The calculated hardness value (~487 HV) demonstrates good agreement with the experimental data, which confirms the adequacy of the developed model. The proposed approach enables the prediction of steel hardness without conducting additional full-scale experiments and can be used to optimize the technological casting parameters of high-strength alloy steels.

Keywords: 40CrNi3MoV steel; thermodynamic modeling; mathematical design of experiments; vibration treatment; modification; hardness prediction

Introduction

Increasing the operational reliability and durability of heavily loaded machine parts is one of the key tasks in modern mechanical engineering. Various approaches are used to solve this problem, including the application of protective coatings [1] and the optimization of modes for restoring worn surfaces by hardfacing [2]. However, the most fundamental way to ensure high mechanical properties of products is the directional formation of an optimal macro- and microstructure of the metal at the stage of its solidification.

High-strength alloy steels, including 40CrNi3MoV, are widely used for manufacturing critical components of heavy-duty equipment [3,4]. Their operational reliability is determined by the microstructure formed during solidification, where the phase composition, the degree of structural heterogeneity, and the characteristics of non-metallic inclusions play a key role in determining hardness, wear resistance, and fracture resistance.

An effective method for controlling the structure is a complex physicochemical treatment of the melt. The application of low-frequency vibration during the solidification process leads to the destruction of the dendritic structure, the intensification of convective flows, and the formation of a fine-grained structure, which is accompanied by a decrease in macrosegregation and an improvement in mechanical properties [5,6]. An additional effect is provided by melt modification: calcium- and barium-containing additives (INSTEEL) promote the formation of dispersed globular oxysulfide inclusions, reducing the stress concentration in the metal matrix [7,8]. It has been established that such modifiers ensure the refining of the melt and the stabilization of inclusions in alloy steels [9-11].

The most promising approach is the combined application of physical and chemical treatments, which provides a synergistic effect manifested in the refinement of the microstructure and the enhancement of mechanical properties [12,13]. Furthermore, structure formation is determined by the combined influence of technological factors, including temperature, treatment duration, and modifier content.

Optimizing these processes solely through empirical methods requires a substantial number of experiments and fails to fully account for the mutual influence of factors [14]. Therefore, the role of mathematical modeling becomes increasingly important. Thermodynamic calculations in software packages such as Thermo-Calc, which are based on Gibbs free energy minimization, enable the prediction of phase equilibria and the parameters of phase transformations [15,16]. The application of the CALPHAD approach allows for the determination of liquidus and solidus temperatures, as well as the phase composition of the alloy at the design stage, thereby justifying the variation range of the temperature factor during experimental design [17].

To quantitatively assess the impact of technological parameters, methods of mathematical design of experiments are applied. The probabilistic-deterministic method based on V.P. Malyshev's methodology significantly reduces the required volume of research while preserving modeling accuracy. This approach relies on constructing regression

dependencies and utilizing M.M. Protodyakonov's generalized function to combine the partial dependencies of factors [18,19], and it has proven highly effective in optimizing metallurgical processes [20,21].

Despite the availability of studies on thermodynamic modeling, vibration treatment, and the use of modifiers, the comprehensive optimization of processing parameters for 40CrNi3MoV steel using a combined approach of thermodynamic calculations and mathematical design of experiments remains insufficiently explored.

The aim of this study is to establish the rational processing parameters for 40CrNi3MoV steel under vibration treatment and INSTEEL-7 modification, based on the combined application of thermodynamic modeling (Thermo-Calc) and Malyshev's method of mathematical design of experiments.

2. Research methods

The object of this study is the high-strength alloy steel 40CrNi3MoV, which belongs to the class of medium-carbon complex-alloy steels containing Cr, Ni, Mo, and V. This combination of elements provides high strength, hardenability, and wear resistance, determining the application of this steel in the manufacturing of critical components for mining, metallurgical, and power equipment [3,4].The operational properties of the steel are dictated by the conditions of structure formation during solidification; therefore, the effectiveness of the technological treatments was evaluated based on the changes in the mechanical characteristics of the cast metal. Vickers hardness (HV5), which is a sensitive indicator of structural and phase transformations, was selected as the primary response. The hardness measurements (Y_{exp}) were performed in accordance with standard procedures [22].To substantiate the temperature parameters of the experiment, solidification modeling was conducted using the Thermo-Calc software package (version 2025b, TCFE13 database), which is based on the CALPHAD method and the principle of Gibbs free energy minimization [15]. The analysis of the phase composition enabled the determination of the liquidus and solidus temperatures, as well as the solidification range of the steel [17]. Based on the obtained data, a temperature variation range of 1480-1560 °C was established and implemented in the experimental design matrix.

Experimental studies were conducted under laboratory conditions using a complex physicochemical treatment on the solidifying melt, which included low-frequency vibration and modification. The complex modifier INSTEEL-7, containing Ca, Ba, rare earth elements, and Ti, was used as a modifying additive, ensuring melt refining and control over the morphology of non-metallic inclusions [7,8].During the experiment, three technological parameters were varied: solidification temperature (X_1), vibration treatment time (X_2), and INSTEEL-7 modifier content (X_3). The experiment was implemented according to a five-level matrix (25 trials), which enabled the determination of the factors' influence on the response-Vickers hardness (Y_{exp}).To quantitatively evaluate the influence of these factors, the probabilistic-deterministic method of mathematical design of experiments according to V.P. Malyshev's methodology was applied. This method allows for a significant reduction in the volume of research while maintaining the reliability of the results [18-20]. To ensure the orthogonality of the design, dummy factors (X_4, X_5) were introduced into the model. The levels of factor variation are presented in Table 1.

Based on the experimental data, partial dependencies of the response on the varied factors were established, and a generalized mathematical model was developed, enabling the prediction of the hardness of 40CrNi3MoV steel under various combinations of technological parameters.

Table 1. Levels of variation for the technological factors.

Factors		Factor levels				
		1	2	3	4	5
X_1	Solidification temperature, °C	1480	1500	1520	1540	1560
X_2	Vibration treatment time, s	0	15	30	45	60
X_3	INSTEEL-7 modifier content, wt.%	0	0,05	0,03	0,02	0,01
X_4	Dummy factor	1	2	3	4	5
X_5	Dummy factor	1	2	3	4	5

Substantiation of the Process Temperature Parameters Based on Modeling

In this study, thermodynamic modeling was utilized to substantiate the temperature parameters of the experiment and was not considered as an independent object of research.

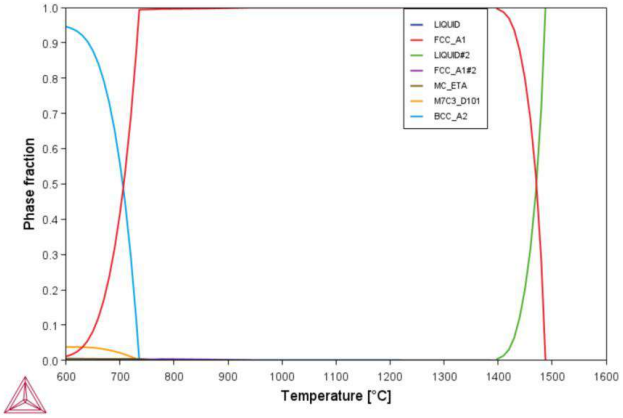

Fig.1 - Calculation of the phase composition of 40CrNi3MoV steel (Thermo-Calc, TCFE13).

The phase composition calculations were performed using the CALPHAD method [15,16], which enabled the determination of the phase transformation temperatures and the solidification behavior of 40CrNi3MoV steel. Figure 1 presents the dependence of the phase composition on temperature. It was established that the liquidus temperature is ~1500 °C, and the completion of solidification (solidus) occurs in the range of ~1420-1440 °C. In the range between the specified temperatures, the system is in the two-phase Liquid + FCC_A1 region, corresponding to the formation of an austenitic dendritic structure.

The technological treatment in this study was applied within the liquid–solid state interval (Liquid + FCC_A1), as vibration treatment is most effective during the nucleation and growth stages of dendrites while maintaining melt mobility. In the fully solidified state, the effect of vibration on structure formation is insignificant; therefore, the temperature range below the solidus was not considered.

Based on the modeling results, a temperature range of 1480-1560 °C was established for use in the experiment. The upper limit corresponds to the superheated liquid state, ensuring high melt fluidity and the active interaction of modifying elements. As the temperature decreases to 1540-1500 °C, the system transitions to the onset of solidification region, where primary austenitic dendrites are formed and the maximum effect of vibration treatment is realized due to the intensification of mass transfer [5,12].

Thus, the selected temperature interval covers the region of solidification nucleation and development, excluding the completely solidified state. The established limits of 1480-1560 °C were adopted as the variation range for the temperature parameter X_1 in the mathematical design of the experiment.

3. Results and discussion

The experimental study of the influence of technological factors on the hardness of 40CrNi3MoV steel was performed based on a multifactorial design of experiments according to V.P. Malyshev's methodology. The varied factors were the melt solidification temperature (X_1), vibration treatment time (X_2), and INSTEEL-7 modifier content (X_3).Each factor was varied at five levels, which enabled the formulation of the experimental design and the execution of 25 experimental melts corresponding to different parameter combinations. Vickers hardness (HV5) was considered as the response. The experimental results are presented in Table 2.

Table 2. Multifactorial experimental matrix and experimental hardness values of 40CrNi3MoV steel.

Trial No.	Temperature, °C	Vibration time, s	INSTEEL-7, wt.%	X4	X5	Experimental result (Y_{exp}), Hardness HV5
1	1480	0	0	1	1	356
2	1480	30	0.03	3	3	402
3	1480	15	0.05	2	2	372
4	1480	60	0.01	5	5	360
5	1480	45	0.02	4	4	386
6	1500	0	0.03	2	5	489
7	1500	30	0.05	5	4	492
8	1500	15	0.01	4	1	488
9	1500	60	0.02	1	3	472
10	1500	45	0	3	2	468
11	1520	0	0.05	4	3	422

Continuation of Table 2

Trial No.	Temperature, °C	Vibration time, s	INSTEEL-7, wt.%	X4	X5	Experimental result (Y_{exp}), Hardness HV5
12	1520	30	0.01	1	2	430
13	1520	15	0.02	3	5	445
14	1520	60	0	2	4	410
15	1520	45	0.03	5	1	440
16	1540	0	0.01	3	4	386
17	1540	30	0.02	2	1	455
18	1540	15	0	5	3	402
19	1540	60	0.03	4	2	462
20	1540	45	0.05	1	5	458
21	1560	0	0.02	5	2	465
22	1560	30	0	4	5	457
23	1560	15	0.03	1	4	474
24	1560	60	0.05	3	1	443
25	1560	45	0.01	2	3	464

An analysis of the obtained data shows that the hardness values vary over a wide range depending on the combination of technological factors. The minimum values correspond to lower solidification temperatures and the absence of an effective modifying treatment, whereas the maximum values are achieved with a rational combination of temperature, vibration time, and modifier content. The obtained hardness range confirms the significant influence of the investigated parameters on the structure formation and mechanical properties of 40CrNi3MoV steel.

To identify the partial regularities of the influence of each factor on hardness, the average response values for the variation levels were calculated. This approach enabled the transition from the matrix of individual experiments to generalized dependencies characterizing the influence of solidification temperature, vibration treatment time, and modifier content on the steel hardness. The average response values according to the factor levels are presented in Table 3.

Table 3. Average hardness values of 40CrNi3MoV steel according to the levels of the varied factors.

Temperature, °C		Vibration time, s		INSTEEL-7 modifier, wt.%	
X_1	$Y_{1\ avg}$	X_2	$Y_{2\ avg}$	X_3	$Y_{3\ avg}$
1480	375	0	404	0	419
1500	429	15	436	0.01	425
1520	481	30	447	0.02	444
1540	465	45	445	0.03	453
1560	460	60	429	0.05	447

The obtained average values were used to construct partial approximating dependencies. It was established that the solidification temperature has a decisive influence on the hardness formation, while vibration treatment and modification additionally intensify the processes of crystal nucleation and growth. Based on the experimental data, partial quadratic dependencies were constructed, describing the influence of each investigated factor on the steel hardness. For the temperature factor, the following dependence was obtained:

$$Y_1 = -0.0334X_1^2 + 102.54X_1 - 78240 \quad (1)$$

The coefficient of determination (R^2):

$$R^2 = 0.9563$$

The approximation is characterized by a high coefficient of determination ($R^2 = 0.9563$), which indicates good agreement between the model and the experimental data. The dependence exhibits an extremal character, pointing to the existence of an optimal solidification temperature range.

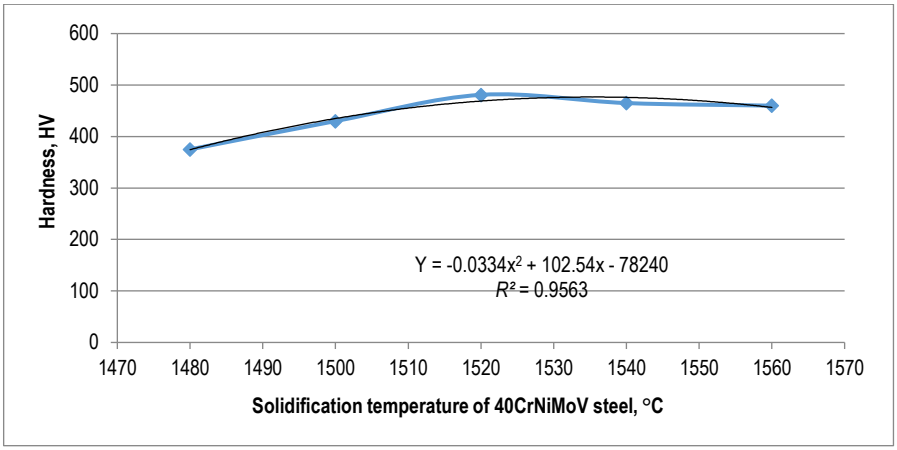

Fig.2 - Dependence of the hardness of 40CrNi3MoV steel on the solidification temperature.

For the vibration treatment time factor, the following dependence was obtained:

$$Y_2 = -0.0346X_2^2 + 2.4695X_2 + 404.83 \quad (2)$$

$$R^2 = 0.995$$

The value of the coefficient of determination ($R^2 = 0.995$) indicates a very high accuracy of the approximation. The presence of a pronounced maximum confirms the existence of a rational vibration treatment duration, at which the greatest structural impact on the melt is achieved.

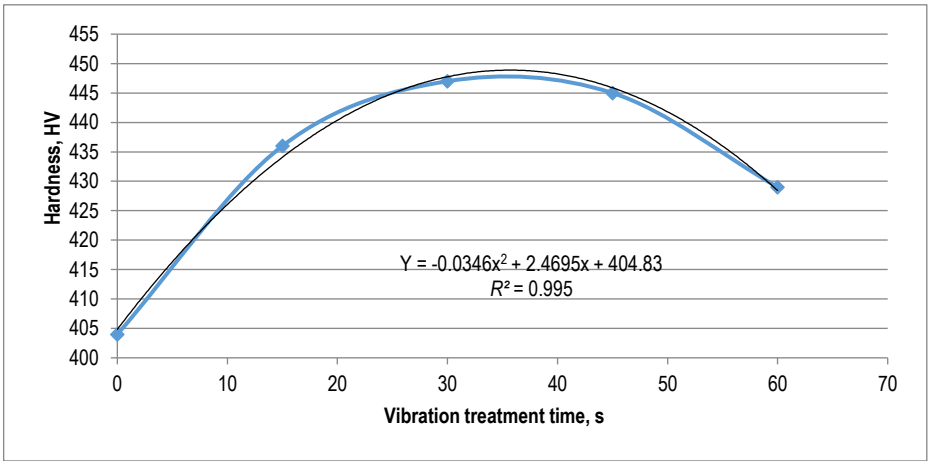

Fig.3 - Effect of vibration treatment time on the hardness of 40CrNi3MoV steel.

For the modifier content factor, the following dependence was obtained:

$$Y_3 = -23969X_3^2 + 1849X_3 + 415.62 \quad (3)$$

$$R^2 = 0.9186$$

The value of the coefficient of determination ($R^2 = 0.9186$) confirms the high adequacy of the model. The parabolic character of the dependence points to the existence of an optimal modifier content, beyond which the effectiveness of the treatment decreases.

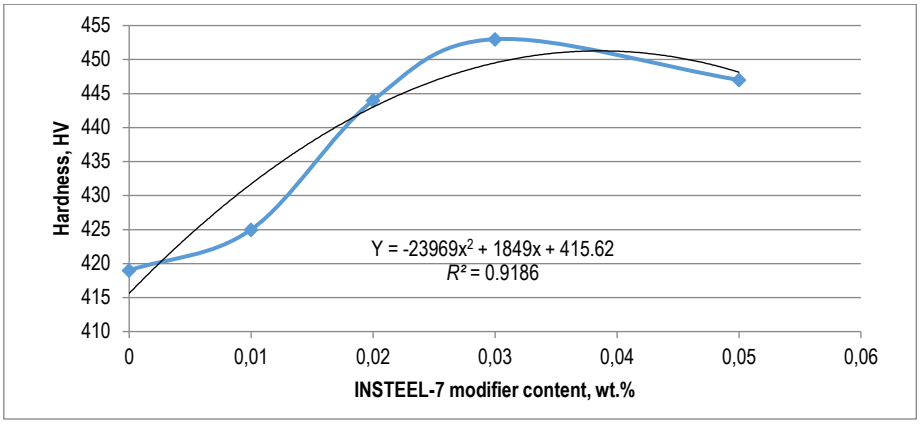

Fig.4 - Dependence of the hardness of 40CrNi3MoV steel on the INSTEEL-7 modifier content.

In general, the obtained dependencies exhibit an extremal character, which indicates the existence of rational values for all the investigated factors at which the maximum hardness of the metal is achieved. The high values of the coefficient of determination confirm the correctness of the approximation and allow the obtained functions to be used for further mathematical modeling.

The decrease in hardness after exceeding the optimal vibration treatment time may be associated with excessive mechanical action on the melt during the final stages of solidification. Prolonged vibration can disturb the stable formation of the solidifying structure and promote gas entrainment, which may lead to the formation of pores and reduce the structural homogeneity of the steel. Similarly, an excessive amount of INSTEEL-7 modifier may decrease the efficiency of modification due to possible coarsening or agglomeration of non-metallic inclusions, reducing their role as effective crystallization centres [23].

For an integral description of the influence of all factors on the steel hardness, the generalized Protodyakonov function was used, allowing the combination of partial dependencies into a single mathematical model:

$$Y = \frac{Y_1 Y_2 Y_3}{Y_{avg}^{m-1}} \tag{4}$$

where Y is the predicted hardness value;

Y_1, Y_2, Y_3 are the partial functions of the factors;

Y_{avg} is the average response value;

m is the number of factors.

In the case under consideration, m = 3 and Y_{avg} = 435.92. Substituting these values yields the final expression of the model, which is applicable for calculating the steel hardness under various combinations of technological parameters within the investigated range.

$$m=3$$

$$Y_{avg} =435.92$$

Substituting these values, we obtain the final expression of the model:

$$Y = \frac{Y_1 Y_2 Y_3}{(435.92)^2}$$

$$(435.92)^2 =190026.25$$

$$Y = (1/190026.25) \times (-0.0334X_1^2 + 102.54X_1 - 78240) \times (-0.0346X_2^2 + 2.4695X_2 + 404.83) \times (-23969X_3^2 + 1849X_3 + 415.62)$$

To determine the rational process parameters, an analytical search for the maximums of the partial functions was performed. Since the dependencies are quadratic functions with a negative coefficient for the squared variable, the maximum is determined by the coordinate of the parabola's vertex:

$$X_{opt} = -\frac{b}{2a} \quad (5)$$

The optimum solidification temperature, determined by the vertex coordinate, is:

$$X_{opt} = -\frac{102.54}{2(-0.0334)} \approx 1535\ ℃$$

which practically corresponds to the experimental level of 1520-1540 °C.

For the optimum vibration treatment time, we obtain:

$$X_{opt} = -\frac{2.4695}{2(-0.0346)} \approx 35\ s$$

Consequently, the optimal vibration treatment duration is approximately 35 s, which practically coincides with the experimental level of 30 s.

For the optimum modifier content, the vertex coordinate is:

$$X_{opt} = -\frac{1849}{2(-23969)} \approx 0.03\ wt.\%$$

The calculation shows that the optimal solidification temperature is approximately 1535 °C, which corresponds to the experimentally established range of 1520-1540 °C. The optimal vibration treatment duration is around 35 s, which agrees with the level of 30 s adopted in the experiment. The optimal modifier content is approximately 0.03 wt.%.

Thus, the rational range of the technological process parameters can be defined as follows:

- solidification temperature: 1520-1540 °C;
- vibration treatment time: approximately 30 s;
- INSTEEL-7 modifier content: approximately 0.03 wt.%.

To verify the adequacy of the developed mathematical model, the rational factor values were substituted: a temperature of 1540 °C, a vibration time of 30 s, and a modifier content of 0.03 wt.%. The calculated hardness value was approximately 487 HV, which is in good agreement with the experimental data.

This confirms the correctness of the constructed model and the possibility of its use for predicting the properties of 40CrNi3MoV steel under varying technological parameters.

Conclusions

1. It was established that the complex physicochemical treatment, including vibration treatment of the melt and modification with the INSTEEL-7 additive, provides a significant change in the structure and hardness of 40CrNi3MoV steel. The hardness variation range was 356-492 HV, which confirms the high sensitivity of the material to the variation of technological parameters.

2. It was determined that the solidification temperature is the dominant factor in the formation of the steel's properties, while vibration treatment and modification perform an intensifying function, affecting the processes of crystal nucleation and growth.

3. Quadratic dependencies of hardness on solidification temperature, vibration treatment time, and modifier content were established. The high values of the coefficient of determination (R^2 = 0.9563-0.995) confirm the adequacy of the approximation and the reliability of the experimental data.

4. A generalized mathematical model based on the Protodyakonov function was developed, allowing the prediction of the steel hardness within the specified parameter range. The calculated value (~487 HV) is in agreement with the experimental data, which confirms the correctness of the model.

5. The rational range of technological regimes ensuring maximum hardness values was established: a temperature of 1520-1540 °C, a vibration treatment time of approximately 30 s, and an INSTEEL-7 modifier content of approximately 0.03 wt.%. The proposed approach allows for a reduction in the volume of experimental research and can be used in the optimization of high-strength steel casting processes.

Funding. This research was funded by the Committee of Science of the Ministry of Science and Higher Education of the Republic of Kazakhstan, Grant No. BR24993020.

References

[1] Zhetessova G., Nikonova T., Gierz L., Berg A., Yurchenko V., Zharkevich O., Alexey K. A Comparative Analysis of the Dynamic Strength Properties of the Long Guides of Intelligent Machines for a New Method of the Thermal Spraying of Polymer Concrete. //Applied Sciences, 2022; 12:10376. DOI: 10.3390/app122010376.

[2] Zharkevich O., Nurzhanova O., Zhunuspekov D., Naboko Ye., Buzauova T., Abdugaliyeva G., Mateshov A., Bessonov A. Determination of Optimal Hardfacing Modes for Recovering Electric Motor Shafts //Tehnički Vjesnik. 2023; 30(3):951-957.
[3] Issagulov A., Kulikov V., Kvon S., Arinova S., Tuganbayeva A. The nanomodifier effect on the structure and properties of 40CrNi3MoV steel //Acta Metallurgica Slovaca. 2025; 31(2):108-112. DOI: 10.36547/ams.31.2.2212.
[4] GOST 4543-2016. Metalloprodukciya iz konstrukcionnoj legirovannoj stali. Tekhnicheskie usloviya [State Standard 4543-2016. Metal products from structural alloy steel. Specifications]. – M.: Standartinform, 2017.
[5] Guo Z., Liu S., Tao Y., Yue S, Ma D., Huang C., Wang M., Jie J., Li T. Effects of mechanical vibration and electromagnetic field on solidification structure and Sn element segregation of Cu-15Ni-8Sn alloy //Materials Science and Technology, 2025. DOI: 10.1177/02670836251349723.
[6] Lyubimova T.P., Parshakova Y.N. Effect of rotational vibrations on directional solidification of high-temperature binary SiGe alloys //International Journal of Heat and Mass Transfer, 2018; 120:714-723. DOI: 10.1016/j.ijheatmasstransfer.2017.12.048.
[7] Shapovalov A.N., Dema R.R., Nefed'ev S.P. Experience of Using Complex Modifiers to Increase Corrosion Resistance of Pipe Steels //Solid State Phenomena, 2021, 316, 369-374. DOI: 10.4028/www.scientific.net/ssp.316.369.
[8] Korovin V.A., Leushin I.O., Balabanov I.P., Savin IA. Increase of resistance of steel moulds using the complex modifier INSTEEL-7 //CIS Iron and Steel Review, 2024; 27, 31-34. DOI: 10.17580/cisisr.2024.01.05.
[9] Tatarko J., Kushnir M.., Markova I, Ivchenko T. Use of complex modifiers for improvement of steel R7 quality //Science and Transport Progress, 2013, 3(45), 67-73. DOI: 10.15802/stp2013/14526.
[10] Zheng J., Liu S., Yang F., Liu L., Peng J., An S. Study on the effect of rare earth Ce on the modification of sulfide inclusions in U71Mn heavy rail steel //Journal of Materials Research and Technology, 2024, 33, 4548-4556. DOI: 10.1016/j.jmrt.2024.10.132.
[11] Suito H., Inoue R. Thermodynamics on Control of Inclusions Composition in Ultra-clean Steels //ISIJ International, 1996, 36(5), 528-536. DOI: 10.2355/isijinternational.36.528.
[12] Kovalyova T., Skvortsov Y., Kvon S, Michot G., Issagulov A., Kulikov V., Skvortsova A. Titanium Carbide and Vibration Effect on the Structure and Mechanical Properties of Medium-Carbon Alloy Steel //Coatings, 2023, 13(7), 1135. DOI: 10.3390/coatings13071135.
[13] Kvon S., Skvortsov Y., Issagulov A., Kulikov V. Enhancement of Carbon Alloy Steel Hardness and Wear Resistance by Vibration and Modification //Metallography, Microstructure, and Analysis, 2025, 14(6), 1243-1260. DOI: 10.1007/s13632-025-01258-3.
[14] Sandeep S., Prakash U., Tewari P.C., Khanduja D. Analysis of Powder Metallurgy Process Parameters for Relative Density of Low Carbon Alloy Steel Using Design of Experiments Tool //Applied Mechanics and Materials, 2014, 592-594, 72-76. DOI: 10.4028/www.scientific.net/amm.592-594.72.
[15] Andersson J-O., Helander T., Höglund L., Shi P., Sundman B. Thermo-Calc & DICTRA, computational tools for materials science. //Calphad, 2002, 26(2), 273-312. DOI: 10.1016/s0364-5916(02)00037-8.
[16] Chen Q., Engström A., Höglund L., Strandlund H., Sundman B. Thermo-Calc Program Interface and Their Applications - Direct Insertion of Thermodynamic and Kinetic Data into Modelling of Materials Processing, Structure and Property //Materials Science Forum, 2005, 475-479, 3145-3148. DOI: 10.4028/www.scientific.net/msf.475-479.3145.
[17] Isagulov A., Akberdin A., Sultangaziyev R., Kim A., Kulikov V., Isagulova D. Diagram of equilibrium phase composition of Fe-C-Si-B system //Metalurgija, 2016, 55(3), 305-308.
[18] Protod'yakonov M.M., Teder R.I. Metodika racional'nogo planirovaniya eksperimentov [Methodology of rational experiment planning]. – M.: Nauka, 1970.
[19] Adler Yu.P., Markova E.V., Granovskiy Yu.V. Planirovanie eksperimenta pri poiske optimal'nyh uslovij [Experiment planning in the search for optimal conditions]. – M.: Nauka, 1976.
[20] Akberdin A.A., Kim A.S., Sultangaziev R.B. Planirovanie chislennogo i fizicheskogo eksperimenta pri modelirovanii tekhnologicheskih processov [Planning of numerical and physical experiments in the modeling of technological processes]. Izvestiya vysshikh uchebnykh zavedeniy. Chernaya metallurgiya [Izvestiya. Ferrous Metallurgy], 2018, 61(9), 737-742. DOI: 10.17073/0368-0797-2018-9-737-742.
[21] Akberdin A.A., Kim A.S., Sultangaziev R.B. Experiment Planning in the Simulation of Industrial Processes //Steel in Translation. 2018, 48(9), 573-577. DOI: 10.3103/s0967091218090024.
[22] GOST 2999-75 (ISO 6507-1). Materialy metallicheskie. Metod izmereniya tverdosti po Vikkersu [State Standard 2999-75 (ISO 6507-1). Metallic materials. Vickers hardness test].
[23] Kovaleva T.V., Isagulov A.Z., Kovalev P.V., Kvon Sv.S., Kulikov V.Yu., Arinova S.K. Structural Anisotropy Parameters' Effect on the Low-Temperature Impact Strength of Alloy Steels in Rolled Products //Metals, 2023, 13(7), 1157. DOI: 10.3390/met13071157.

Information of the authors

Tuganbayeva Assem Adilkhanovna, doctoral student, Abylkas Saginov Karaganda Technical University
e-mail: dicosia0789@gmail.com

Issagulov Aristotel Zeinullinovich, d.t.s., professor, Abylkas Saginov Karaganda Technical University
e-mail: aristotel@kstu.kz

Arinova Sania Kaskataevna, PhD, associate professor, Abylkas Saginov Karaganda Technical University
e-mail: s.arinova@ktu.edu.kz

Dostayeva Ardak Mukhamedievna, PhD, professor, Abylkas Saginov Karaganda Technical University
e-mail: a.dostayeva@ktu.edu.kz

DOI 10.52209/2706-977X_2026_2_78 **IRSTI 55.51.03** **UDC 678.7**

Study of Wear Resistance of Antifriction Materials for Bushings of Lever-Hinge Mechanism of Lifting Installation Brake System

Nurzhanova O.A.[1], Boyko S.B.[2], Berg A.A.[*1], Mukhitova A.E.[1]
[1] Ablykas Saginov Karaganda Technical University, Karaganda, Kazakhstan
[2]Science technology centre Vostoktechnoservis LLP, Ust-Kamenogorsk, Kazakhstan
*corresponding author

Abstract. This article examines the pressing scientific and practical challenge of improving the operational reliability and wear resistance of friction units in lever-hinge mechanisms (LHM) of mine hoist braking systems. The authors provide a detailed analysis of the kinematics and operating characteristics of pin-sleeve friction units using equipment operated at the Kamyshinskaya and Artemyevskaya mines as an example. It is demonstrated that severe operating conditions - high radial loads (80 ÷ 150 kN), alternating pulses, constant vibration, and the presence of abrasive dust - lead to the degradation of protective oxide films, fretting corrosion, and an avalanche-like increase in radial clearances in the hinges. Bushing wear triggers dangerous edge pressures, fatigue stresses in the pin body, and a sharp drop in the mechanical efficiency of the drive. To address this issue, comprehensive comparative tribological tests of various antifriction materials were conducted using a ball-on-disk design on a Microtest automated tribometer under strictly controlled laboratory conditions. The experiments provided a detailed study of the patterns of change in the mass of mating bodies, the dynamics of the friction coefficient over a distance of 100 m, and the geometric parameters of the resulting wear craters for SCh-15 gray cast iron, traditional bronze, grade 45 steel with a MoS_2 solid lubricant coating, and ZhGr3M porous iron-graphite with molybdenum. The quantitative data obtained and the resulting graphical dependencies allow for a scientifically substantiated choice of material for upgrading friction units and transitioning to maintenance-free hinges.

Keywords: friction coefficient, wear time, tribological testing, antifriction materials.

Introducrion.

The articulated lever mechanism of a hoisting system acts as a power transformer, converting the energy of a pneumatic, hydraulic, or spring drive into normal pressure on the rim of the brake pulley [1,2]. The efficiency of force transmission in such systems is critically dependent on the kinematic design: even a 2–3% deviation in the lever geometry results in a significant drop in braking torque [3]. The articulated lever mechanism of a hoisting system brake used at the Kamyshinskaya, Artemyevskaya, and Artemyevskogo mines is shown in Figure 1.

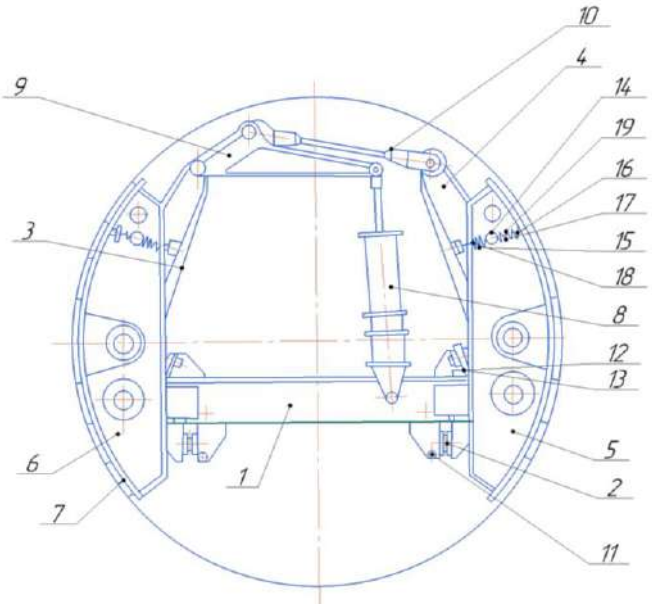

1 - frame; 2 - hinges; 3, 4 - vertical levers; 5, 6 - brake beams; 7 - friction linings; 8 - brake drive; 9 - lever; 10 - rod; 11 - fixing screws; 12 - bracket; 13 - stop screw; 14, 15 - springs; 16 - rod; 17, 18 - bushings; 19 - nuts

Fig. 1. - Lever-hinge mechanism of the lifting unit braking system

The articulated lever mechanism of a hoisting system brake comprises a frame (1), a system of vertical levers (3, 4), brake beams (5, 6) with friction linings (7), and an actuator (8). Braking force is transmitted through a network of hinges (2) and rods (9, 10, 16). During braking, the drive (8) generates a force that is transmitted to the vertical levers via the lever (9) and rod (10). The key element at the pivot points is the connection between the bushing (17, 18) and the pin.

The pin performs a small-radius, reciprocating rotational motion relative to the stationary bushing, pressed into the eye [4]. A radial force F (80-150 kN) is applied perpendicular to the pin axis, causing contact pressure on the inner surface of the bushing. The specific operation of a hoist brake requires frequent starts and stops, which precludes hydrodynamic lubrication. The unit operates under boundary friction conditions.

Bushing wear is the dominant factor determining the reliability of the entire braking system [5]. The bushing, like a friction bearing, operates under oscillatory motion with small rotation angles and high specific pressures, reaching 30-50 MPa. In such conditions, hydrodynamic lubrication is impossible, and the unit operates in boundary friction mode [6]. This leads to gradual compaction of micro-irregularities and adhesive wear of the metal, which is visually manifested as an increase in radial clearance [7]. Even minimal wear of 0.5 mm on one lever arm, passing through the gear ratio system, can translate into an increase in the actuator rod stroke by several centimeters, reducing brake response.

The main physical and chemical problem is fretting corrosion in the pin-bushing assembly [8]. Due to alternating loads and micro-movements caused by vibrations from the operating machine, the protective oxide films on the metal surface are constantly destroyed [9]. The resulting wear products (iron oxides) are highly hard and act as an abrasive, accelerating the degradation of the assembly. In mine hoisting conditions, where coal or rock dust is present in the air, this process occurs in an avalanche-like manner [10]. If the bushing is not sufficiently hard relative to the pin, it fractures, creating an oval-shaped hole, which introduces an irreparable kinematic error in the braking force distribution.

The choice of bushing material determines the overhaul interval for the entire system. The traditional use of bronze (OCS 5-5-5 or BrAZh 9-4) is justified by their antifriction properties; however, under shock loads during emergency braking, they are subject to plastic deformation [11]. This installation uses PA-ZhGr3 iron-graphite (GOST 26802-86).

Geometric distortion of the hinge axis due to bushing wear causes edge pressure. When the bushing wears unevenly, the load is no longer distributed along the entire contact length, concentrating on the ends [12]. This creates a bending moment on the pin, which is not included in the static strength calculations. As a result, fatigue stresses accumulate in the pin body, which can lead to sudden brittle failure [13].

The problem of metal seizure or cold welding in the friction pair occurs when the lifting machine is idle for a long time under load (for example, on a stopper) [14]. Under high pressure, the oil film is squeezed out, causing direct contact between the juvenile surfaces. When attempting to release the brake, metal particles are torn from the bushing surface. To prevent this phenomenon, the application of solid lubricant coatings (molybdenum disulfide) is being introduced into modern design practice. These coatings create a separating layer at the molecular level, ensuring a smooth start-up of the mechanism even after several days of inactivity [15].

The effect of joint clearances on the system's dynamics manifests itself in the generation of shock pulses when the brake is applied [16]. When the drive begins to move, it first eliminates all the play in the worn bushings and only then begins to deform the brake pads. This impact on the lever chain creates peak stresses that are several times higher than the nominal ones. From the perspective of machine theory, wear transforms a rigid kinematic chain into a system with a variable structure and clearances, which is extremely difficult to accurately describe mathematically and can lead to unpredictable system behavior during automatic braking control.

Another important aspect is the method of securing the bushing in the lever body. A traditional press-fitted system can loosen under significant wear and heat, causing the bushing to rotate in its socket [17]. This is a catastrophic failure, as it begins to wear out the lever itself - an expensive cast or forged component.

Ultimately, combating bushing wear in a brake control system (RCS) means maintaining a consistent brake drive efficiency. A well-maintained system with minimal clearances has a mechanical $\eta \approx 0.92\text{-}0.95$, while a worn system loses up to 30% of the drive energy to overcome friction and deformation in the hinges. Modern trends are leading to the development of maintenance-free hinges, where the use of innovative polymers, coatings, and high-precision casting allows the brake system to operate for the entire service life of the machine without bushing replacement, setting the standard for reliability in mining [18].

An additional operational challenge is cold welding or solid-state seizure within the friction pair, which typically occurs during prolonged periods of machine inactivity while remaining under load (e.g., when a hoist is held stationary on a stopper) [19]. Under sustained high contact pressure, the residual boundary lubricant film is completely squeezed out, forcing direct contact between juvenile, chemically active metallic surfaces. Upon subsequent brake release, massive cohesive tearing occurs, stripping material clusters from the bushing surface. While the traditional deployment of copper-based alloys, such as traditional bronze (e.g., OCS 5-5-5 or BrAZh 9-4), provided adequate baseline antifriction

performance, these materials exhibit high susceptibility to permanent plastic deformation when subjected to intense dynamic shock pulses during sudden emergency braking. Conversely, standard porous iron-graphite formulations like PA-ZhGr3 often lack the necessary shear strength and chemical stability to withstand the combination of fretting and abrasive dust infiltration over extended lifecycles.

From the perspective of advanced machine theory, heavy tribological wear fundamentally transitions what was designed as a rigid, predictable kinematic chain into a stochastic system with a variable structure and fluctuating clearances [20]. Such systems are exceptionally difficult to model mathematically, introducing unpredictable dynamic behavior and destabilizing the feedback loops required for automated, high-precision braking control. Additionally, traditional press-fitted bushings frequently suffer from thermal-mechanical loosening due to frictional heating and wear, leading to the catastrophic rotation of the bushing within its housing socket. This turns the wear process inward toward the vertical lever itself-an expensive, structurally vital forged or cast component whose replacement demands extensive downtime [21].

Consequently, the realization of maintenance-free hinge nodes-capable of surviving the entire designated operational lifecycle of a mine hoist without mid-term bushing replacements-stands as a critical objective for modern mining and transport engineering [22]. To achieve this, it is necessary to move away from empirical material selection and instead conduct comprehensive, scientifically rigorous comparative tribological evaluations of advanced self-lubricating composites under strictly controlled boundary states.

The aim of this study is to perform a systematic tribological analysis of the friction and wear kinetics of four candidate materials: SCh-15 gray cast iron, traditional bronze, grade 45 steel with an engineered MoS_2 solid lubricant coating, and a specialized porous iron-graphite composite modified with molybdenum (ZhGr3M). By mapping their friction coefficient dynamics, mass loss profiles, and geometric crater degradation patterns under equivalent boundary constraints, this paper establishes a scientifically substantiated foundation for upgrading critical lever-hinge mechanisms, extending overhaul intervals, and ensuring stable braking drive efficiency.

1. Researh methodology

Tribological studies were conducted using a ball-on-disk friction system on a Microtest tribometer (Microtest, SA, Madrid, Spain, Figure 2) under the following experimental conditions:

- sliding distance – 100 m;
- sliding speed – 150 rpm;
- trajectory radius – 2 mm;
- load – 10 N;
- test temperature – 22.3°C;
- time – 27 min.

Fig. 2. - Microtest tribometer

For the experiment, round specimens were made from the antifriction materials discussed above.

A hardened AISI 52100 stainless steel ball with a diameter of 4 mm and a hardness of 64 HRC was used as an indenter.

Before tribological testing using the ball-on-disk friction scheme (Figure 3), the disc-shaped specimens were subjected to preliminary mechanical treatment and surface preparation.

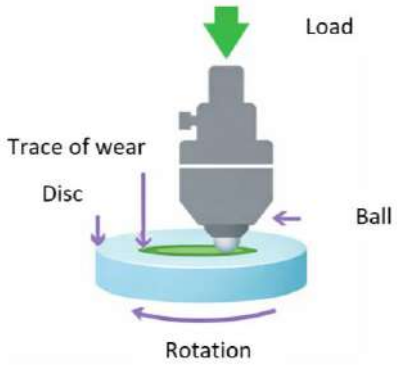

Fig. 3. - Ball-on-disk friction diagram

The specimen working surfaces were successively ground and polished to achieve a uniform mirror surface with minimal roughness, eliminating the influence of macroscopic irregularities on the test results according to the methodology (GOST 23.208–79). After mechanical processing, the specimens were degreased in an ultrasonic bath using ethyl alcohol and dried at room temperature.

The specimen was mounted in the Microtest tribometer disk holder, whose design ensures rigid fixation and prevents its displacement during testing. The specimen was positioned in the holder's mounting socket so that its working surface was strictly perpendicular to the load axis of the counterbody. The center of the specimen was aligned with the tribometer's rotation axis, ensuring the formation of a closed annular friction path of a specified radius.

The specimen was secured using the holder's clamping mechanism (screw or clamp type), ensuring uniform distribution of force across the entire contact area between the specimen and the supporting surface of the holder. The tightening torque of the clamping elements was selected to prevent both sample slippage and deformation, which could lead to distorted measurement results.

After mechanical clamping, the alignment and horizontality of the specimen's working surface relative to the plane of rotation were checked. This was done visually and using the tribometer's indicator equipment. Permissible surface runout deviations did not exceed the values recommended by the equipment manufacturer, ensuring stable contact conditions throughout the entire test cycle.

A counterbody, a standard 6 mm diameter ball made of AISI 52100 (100Cr6) steel, was installed in the upper holder of the tribometer and secured according to the manufacturer's instructions. After installing the counterbody, the ball was preliminarily applied to the specimen surface without load to precisely position the contact zone at the specified radius of the friction path.

Before the main experiment, the system was calibrated using a normal load, after which a specified load of 10 N was applied. Only after contact conditions had stabilized was the specimen rotated at a set sliding speed of 150 rpm. The test temperature was controlled and matched to room temperature (22.3°C).

The degree of wear of the overlay material was assessed by weighing the test specimens before and after testing on an analytical balance (Figure 4).

Fig. 4. - Laboratory scales AS 60/220.R2 PLUS Analytical Balance

Ball weight loss was recorded on a laboratory scale with an accuracy of 0.00001%, and sample weight loss was recorded with an accuracy of 0.001%.

2. Results and Discussion

The resulting dependences of sample weight change on sample and ball mass change for each antifriction material are shown in Figure 5.

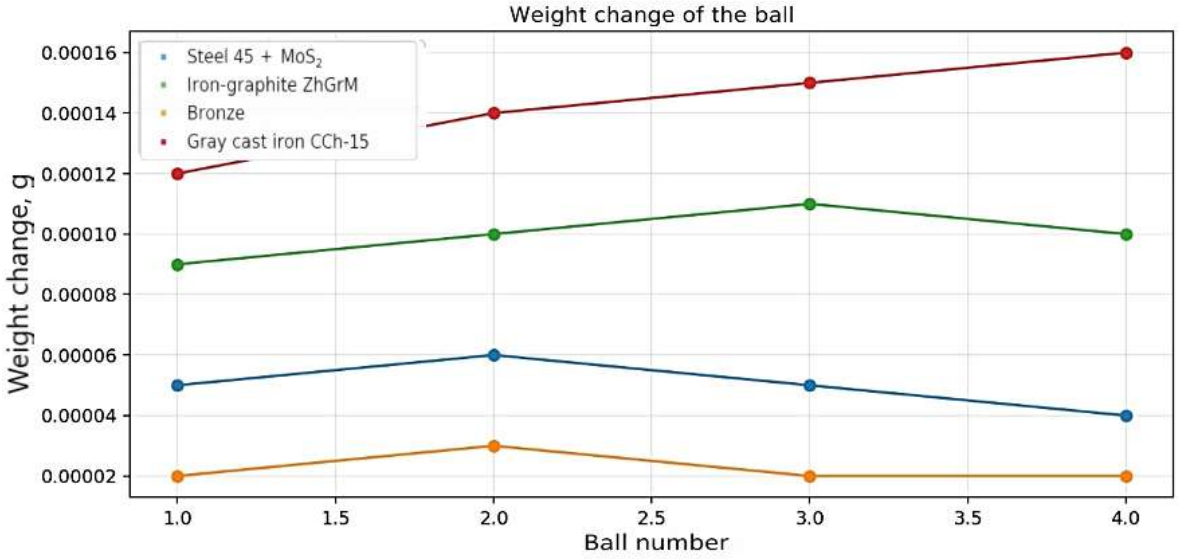

a)

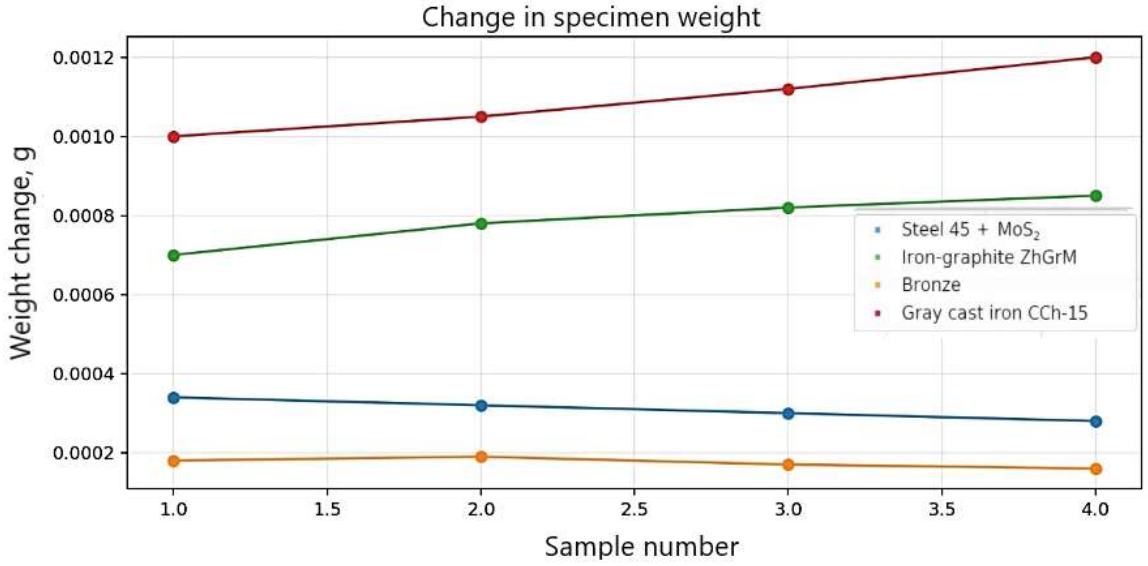

b)

a) change in ball mass for antifriction materials, b) change in sample weight for antifriction materials

Fig.5. - Change in sample and ball mass for each antifriction material

Figure 6 shows the dependence of the friction coefficient on the counterbody travel distance during tribological testing.

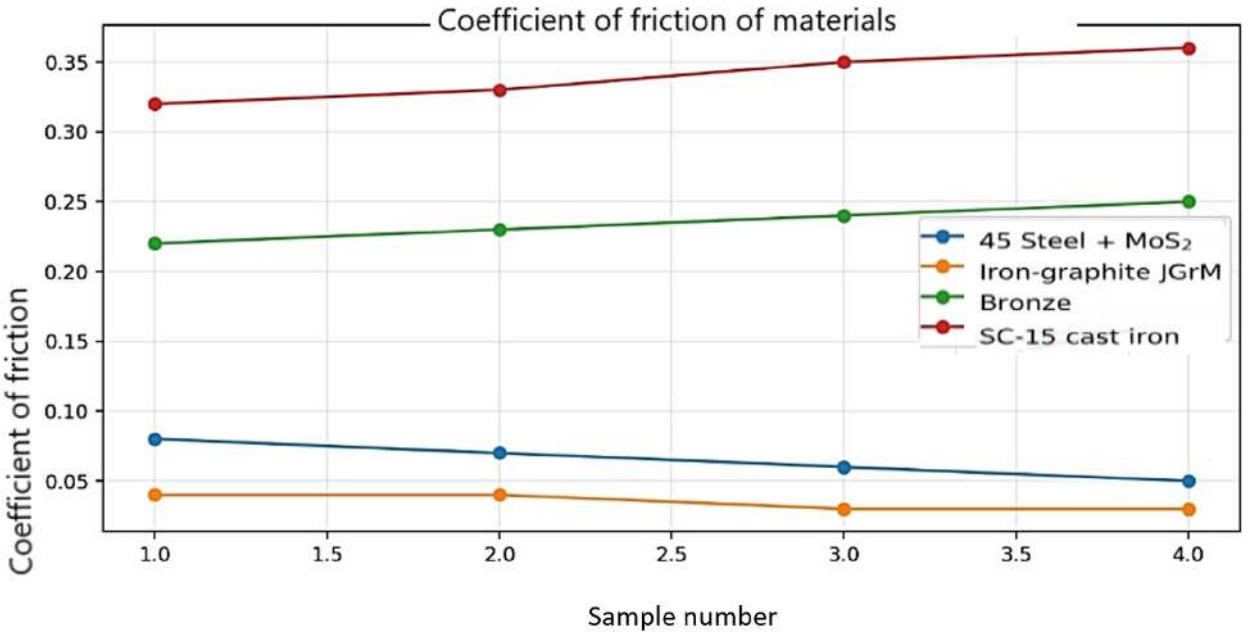

Fig. 6. – Dependence of wear area on wear time

It was found that wear crater area increases linearly with wear time. The largest crater area is observed for the gray cast iron surfacing material, while the smallest crater area is observed for the ZhGr3M iron-graphite with molybdenum.

To evaluate the wear resistance of antifriction materials, the dependence of the friction coefficient on the friction path was determined (Figure 7).

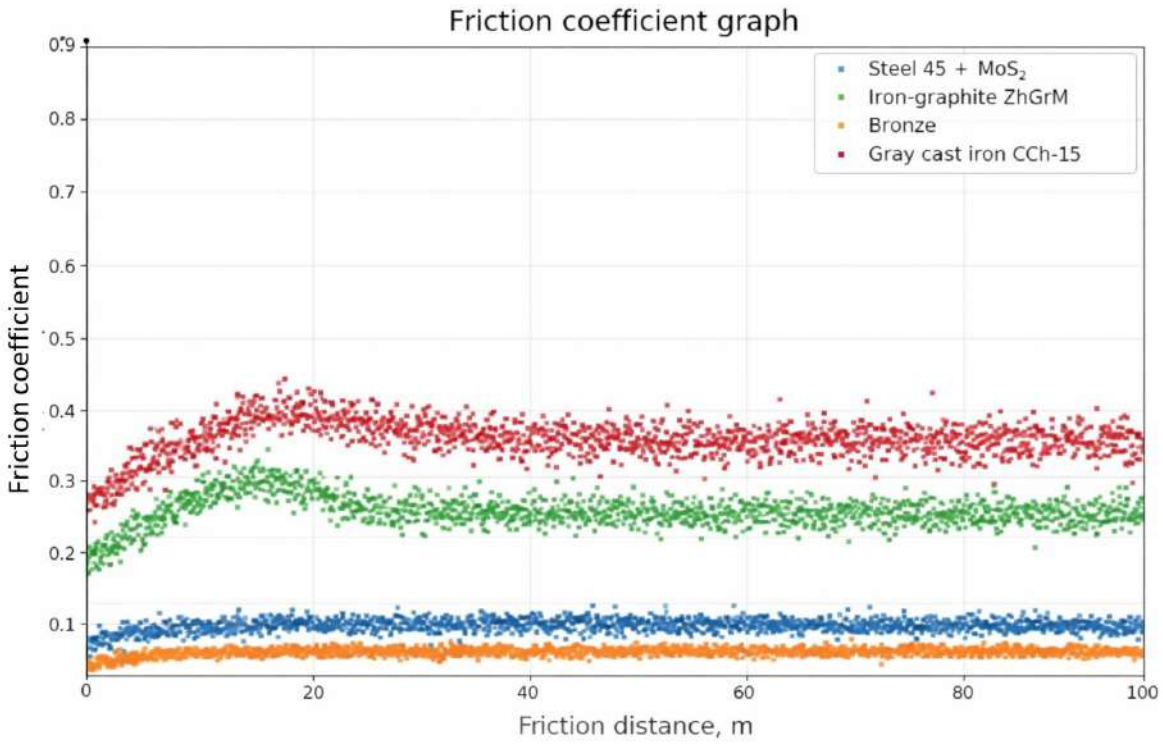

Fig. 7 - Dependence of the friction coefficient on the counterbody travel distance during tribological testing

The friction coefficient over a distance of 100 m was found to be 0.28 to 0.41 for gray cast iron SCh-15; 0.16 to 0.3 for bronze; 0.06 to 0.08 for grade 45 steel coated with MoS_2 and 0.01 to 0.05 for iron-graphite with molybdenum ZhGr3M.

The tribological test results are presented in Table 1.

Table 1. Experimental results

Sample number	Change in the weight of the ball after the experiment, g	Change in sample weight after the experiment, g	Coefficient of friction	Friction path, m
Gray cast iron SCH-15	0,00009	0,00054	0,354312	100
Bronze	0,0001	0,00097	0,265334	100
Steel 45 coated with MoS_2	0,00002	0,00106	0,085334	100
Iron-graphite with molybdenum ZhGR3M	0,0001		0,044052	100

Analyzing the data in Table 1, we can conclude that the most wear-resistant antifriction material is iron-graphite ZhGr3M.

Conclusions

Based on the presented results of tribological tests and analysis of the operation of the lever-hinge mechanism of the braking system of lifting equipment, the following key conclusions can be drawn:

1) The operation of the articulated linkage brake mechanism of the winding machines at the mines studied (Kamyshinskaya and Artemyevskaya) is subject to harsh operating conditions. Due to frequent starts and stops and extreme radial forces (80-150 kN) in the pin-bushing pair, hydrodynamic lubrication is completely impossible. Operating the unit under boundary friction leads to adhesive wear and fretting corrosion activated by mine dust. Even minimal bushing wear (0.5 mm) distorts the lever geometry, causes edge pressure, reduces brake response, and can lead to pin fatigue failure or a loss of up to 30% of the drive energy;

2) Laboratory tests using a Microtest tribometer using a ball-on-disk design allowed us to objectively evaluate the performance of four bushing materials: SCh-15 gray cast iron, traditional bronze, grade 45 steel with a MoS_2 coating, and ZhGr3M iron-graphite with molybdenum;

3) SCh-15 gray cast iron demonstrated the worst results. It had the highest friction coefficient (0.28 to 0.41) and the largest wear crater area. Despite its widespread use, bronze is inferior to modern alternatives (friction coefficient 0.16 to 0.3) and is susceptible to plastic deformation under impact;

4) Steel 45 with a molybdenum disulfide coating demonstrated high friction reduction (0.06 to 0.08), preventing metal seizure during prolonged idle periods under load;

5) Iron-graphite with molybdenum ZhGr3M has been recognized as the most wear-resistant and promising material for brake system bushings. In experiments, it provided a minimal wear crater area and a record-low friction coefficient, ranging from 0.01 to 0.05. This is due to its porous structure and the presence of a solid lubricant, which creates a reliable separating layer at the molecular level;

6) The use of iron-graphite ZhGr3M bushings instead of the standard iron-graphite PA-ZhGr3 or bronze minimizes play in the hinges, eliminates peak dynamic shocks on the lever chain, and stabilizes the brake drive efficiency at ~0.92-0.95. This is an important step toward creating maintenance-free hinge assemblies in mining engineering.

References

[1] Malfunctions of mine hoists / Ed. Bezhok V.R., Gruzutin R.Ya., Kalinin V.G., Chaika B.N. - M.: Nedra, 1991. - 368 p.

[2] Nikonova T., Zhetessova G., Yurchenko V. Mathematical modeling of vibroburnishing of the hole of cylinder // Journal of Applied Engineering Science, 2018, Vol. 16, No. 1. P.5-10

[3] Abdraimov E.S., Abdraimova E.E. Structural features of mechanisms // VII International Conference "Problems of Mechanics of Modern Machines", 2018. - pp. 5 - 10

[4] Dovgyalo V.A. Methods for improving the performance of machines and mechanisms: textbook. - Gomel: BelGUT, 2018. - 374 p.

[5] Ilie F., Cristescu A. C. Experimental Study of the Correlation between the Wear and the Braking System Efficiency of a Vehicle //Appl. Sci. 2023, 13, 8139

[6] Ilyin S.R. Mechanics of Mine Hoisting: a monograph. – D.: NSU, 2014. – 247 p.

[7] Dykha O., Makovkin O., Valchuk I. Adhesive wear of tool steels with functional coatings // Proccedings of International Scientific Conference BALTTRIB, 2024, 1, 64-72
[8] Sikhimbayev M.R., Sherov K. T., Zharkevich O. M., Sherov A.K., Tkacheva Y.O. Experimental studies of stabilization of boring cutter form - building top oscillation //Journal of Vibroengineering, 2012, 14(2), 661–670
[9] Mekhtiev A.D., Yugay V.V. Current state and problems of operation of mine hoists of the Karaganda coal basin // Scientific, analytical and production journal "Mining equipment and electromechanics". - 2011. - No. 6 - pp. 26-29
[10] Kuznetsov N.K. Evaluation of safety braking modes of mine hoists // Bulletin of IrSTU, No. 11 (106), 2015. - pp. 31- 34
[11] Kovaleva T.V., Isagulov A.Z., Kovalev P.V., Kvon Sv.S., Kulikov V.Yu., Arinova S.K. Structural Anisotropy Parameters' Effect on the Low-Temperature Impact Strength of Alloy Steels in Rolled Products//Metals, 2023, 13, 1157. https:// doi.org/10.3390/met13071157
[12] Popescu F.D., Radu S.M., Andras A., Brînas I. Numerical Modeling of Mine Hoist Disc Brake Temperature for Safer Operation //Sustainability 2021, 13, 2874. https:// doi.org/10.3390/su13052874
[13] Zabolotnyi K., Zhupiiev O., Molodchenko A. Development of a model of contact shoe brake-drum interaction in the context of a mine hoisting machine // Min. miner. depos. 2017, 11(4), 38-45
[14] Sherov K. T., Mardonov B.T., Zharkevich, O. M., Mirgorodskiy, Sergey, Gabdyssalyk R, Tussupova S., Smakova N., Akhmedov Kh.I, Imanbaev Y.B Studying the process of tooling cylindrical gears //Journal of Applied Engineering Science, 2020, 18(3), 327–332
[15] Yang C., Tan, J Li F. Research on simulation and test of braking performance of ultra-deep mine hoist // IOP Conf. Series: Earth and Environmental Science 170, 2018, 022020
[16] Li J., Meng G., Xie G., Wang A., Ding J., Zhang W., Wan X. Study on Health Assessment Method of a Braking System of a Mine Hoist // Sensors 2019, 19, 769
[17] Fu H., Zhang H., Zhang L., Niu P., Liu X., Stelmakh O. The loosening mechanism of tin-bronze bushing assembled by interference at connecting rod small end of heavy-duty diesel engines // International Journal of Engine Research, 2024, 26(5)
[18] Agarwal S., Singh S. Evaluation of Dry Sliding Wear Characteristics in Al5052/TiB_2/ZrO_2 Composites Against EN-31 Steel Counterbody //Material and Mechanical Engineering Technology, №4, 2024
[19] Wahab M. A., Dewan M. W., Huggett D. J., Okeil A. M., Liao T. W., Nunes A. C. Challenges in the detection of weld-defects in friction-stir-welding (FSW) //Advances in Materials and Processing Technologies, 2019, DOI: 10.1080/2374068X.2019.1575713
[20] Ardah S., J. Profito F.J., Dini D.A comprehensive review and trends in lubrication modelling, //Advances in Colloid and Interface Science Volume 342, 2025, 103492
[21] Belhocine A., Afzal A. Finite element modeling of thermomechanical problems under the vehicle braking process //Multiscale and Multidisciplinary Modeling, Experiments and Design, 2020, 3(1)
[22] Size K.B., Moyo R., Masethe R., Zvarivadza T., Onifade M. Modernization of Hoisting Operations Through the Design of an Automated Skip Loading System-Enhancing Efficiency and Sustainability //Mining, 2025, 5, 62.

Information of the authors

Nurzhanova Oxana Amangeldyevna, PhD, associate professor, Abylkas Saginov Karaganda Technical University
e-mail: o.nurzhanova@edu.ktu.kz

Boiko Sergey Borisovich, m.t.s., director, Science technology centre Vostoktechnoservis LLP
e-mail: boiko@ntcvts.kz

Berg Alexandra Sergeevna, PhD, senior tutor, Abylkas Saginov Karaganda Technical University
e-mail: a.berg@edu.ktu.kz

Mukhitova Adelia Erzhanovna, assistant, Abylkas Saginov Karaganda Technical University
e-mail: a.mukhitova@edu.ktu.kz

DOI 10.52209/2706-977X_2026_2_86 **IRSTI 55.43.29** **UDC 629.021**

Review of Previous Studies: From Classical Coagulation Theory to Practical Ultrasonic Purification of Exhaust Gases

Kadyrov A.S.[1], Sakhapov R.L.[2], Kukesheva A.B.[1*]
[1]Abylkas Saginov Karaganda Technical University, Karaganda, Kazakhstan
[2]Kazan (Volga region) Federal University, Kazan, Russia
* corresponding author

Abstract. The purpose of this study is to critically review and generalize theoretical and experimental research on ultrasonic coagulation of aerosol and soot particles as a promising approach to reducing the smoke opacity and toxicity of exhaust gases from internal combustion engines. The scope of the work encompasses both classical diffusion-based coagulation theories and contemporary studies of acoustic agglomeration in stationary aerosols, flow channels, and automotive mufflers. The research methodology is based on a systematic analysis and comparison of existing models and experimental results, with an emphasis on their relevance to real exhaust-system operating conditions.
The analysis demonstrates that most diffusion and acoustic coagulation models are formulated under idealized assumptions, such as stationary and isothermal media and negligible turbulence. These assumptions significantly restrict their applicability to real exhaust flows, which are characterized by high temperatures, turbulent and pulsating motion, variable composition, and limited particle residence time. A synthesis of experimental data shows that ultrasonic exposure enhances soot particle growth and promotes their subsequent sedimentation in flowing gases. The effectiveness of ultrasonic purification is determined by several interrelated factors, including turbulence intensity, pressure pulsations, residence time of particles in the active zone, acoustic field configuration, muffler geometry, and the polydisperse structure of soot.
The study also identifies the main shortcomings of existing theoretical and experimental approaches, such as the widespread use of batch-type accumulation chambers, simplified test-bench designs, and the lack of reliable experimental data under high-temperature exhaust conditions. Based on the obtained results, the main conclusions highlight the necessity of optimizing ultrasonic muffler geometry, developing adaptive and multi-frequency acoustic fields, and implementing control algorithms for ultrasonic emitters. The revealed regularities form a scientific basis for the rational design of ultrasonic mufflers and confirm their potential to improve analytical modeling accuracy, reduce experimental workload, and enhance exhaust gas purification efficiency.

Keywords. ultrasonic coagulation, acoustic particle agglomeration, soot (aerosol) particles, flow-through ultrasonic muffler, turbulent pulsating flow

Introduction

Exhaust emissions from motor vehicles are one of the major factors contributing to the development of chronic diseases and the deterioration of urban environmental quality. Prolonged exposure to fine particulate matter, nitrogen oxides, carbon monoxide, and polycyclic hydrocarbons leads to an increased incidence of chronic obstructive pulmonary disease, bronchial asthma, allergic airway reactions, and chronic bronchitis [1]. In addition to respiratory disorders, polluted air elevates the risk of cardiovascular diseases, including arterial hypertension, ischemic heart disease, and cardiac arrhythmias, and also contributes to a higher likelihood of strokes [2, 3].

Particular attention is given to PM2.5 particles and benzopyrene, which are associated with an increased risk of oncological diseases, primarily lung cancer. In recent years, the negative impact of vehicle emissions on cognitive functions has also been demonstrated: long-term exposure to polluted air can lead to reduced attention and impaired memory. Taken together, these factors underscore the urgent need to develop and implement effective solutions aimed at reducing the toxicity of exhaust gases and improving environmental conditions in urban areas.

Along with infrastructural measures, the use of ultrasound is an important and promising area [4]. Ultrasonic exposure leads to coagulation and possible subsequent cavitation of aerosol and soot particles. [5, 6]. This method is considered an effective tool for enhancing the environmental safety of motor vehicles by significantly reducing the concentration of solid particles in exhaust gases [7]

Fundamental concepts of coagulation mechanisms were established in the early 20th century in the works of Albert Einstein and Marian Smoluchowski [8]. However, the classical Einstein–Smoluchowski theory was originally formulated for idealized conditions: stationary, homogeneous, predominantly isothermal systems with Brownian or shear-induced mixing and without any consideration of an organized gas flow.

The gaseous medium in an automotive exhaust system differs fundamentally from the idealized conditions assumed in classical coagulation theory. Exhaust gases have high temperatures, variable composition (a mixture of gaseous components and solid soot particles), and are subject to strong fluctuations in pressure and velocity caused by engine cycles. The flow in the muffler is typically turbulent. Soot particles move within a directed, high-velocity stream,

simultaneously experiencing gas-dynamic forces, viscous drag, gravity, and when ultrasound is applied – acoustic pressure and Bjerknes forces. Under such conditions, classical diffusion-coagulation equations are clearly insufficient: they do not account for the influence of turbulence on effective mixing, the contribution of the acoustic field to the relative motion of particles of different sizes, or the features of flow-through reaction volumes.

To describe the behavior of exhaust gases in an automotive muffler, as well as the processes of particle growth and deposition under the influence of ultrasound, it is necessary to draw upon a broader range of studies. It is essential to consider works that:

- analyze the influence of acoustic forces on particles and the formation of concentration zones;
- investigate coagulation in flow channels and chambers with directed gas streams;
- develop mathematical models of particle motion in mufflers and reaction chambers that incorporate the superposition of gravitational, gas-dynamic, and acoustic forces.

For this reason, the present study finds it appropriate to conduct a targeted review of previous research: from classical models of Brownian and diffusion-induced coagulation to contemporary theoretical and experimental studies on ultrasonic gas cleaning in flow systems and automotive mufflers. Such a review makes it possible, on the one hand, to demonstrate the evolution of understanding of coagulation mechanisms, and, on the other hand, to identify the limitations of existing approaches when applied to exhaust gases of internal combustion engines, thus substantiating the need to account for acoustic, turbulent, and gas-dynamic factors.

The purpose of this study is to conduct a comprehensive analysis of theoretical and experimental research in the field of ultrasonic coagulation of aerosol and soot particles, in order to develop an integrated understanding of particle interaction mechanisms within a flow-through ultrasonic automotive muffler and to identify the key patterns that determine the efficiency of ultrasonic exhaust-gas purification.

To achieve this goal, the following objectives were set:

- to analyze the fundamental coagulation models developed by Einstein and Smoluchowski and to determine the limits of their applicability in real gas-flow conditions;
- to examine modern studies on acoustic coagulation, including the influence of Bjerknes forces, acoustic pressure, standing waves, and orthokinetic mechanisms on particle interactions;
- to analyze research on coagulation in flow systems, including chambers with directed gas streams and mufflers operating under turbulent-flow conditions;
- to identify the main problems and limitations of existing approaches that hinder their direct application in automotive exhaust systems;
- to determine directions for further research aimed at improving the efficiency of ultrasonic coagulation and adapting it to real operating conditions of motor vehicles.

The scientific novelty of the research lies in the systematization of existing studies and the identification of key patterns governing ultrasonic coagulation processes in internal combustion engine exhaust systems. The established dependencies form a scientific basis for the subsequent development of ultrasonic mufflers, enabling a reduction in the volume of experimental work and an increase in the accuracy of analytical models and engineering methodologies.

The practical significance of the study is that the obtained results create prerequisites for the design of an ultrasonic muffler and the justification of optimal operating modes. This will ensure a reduction in smoke opacity and exhaust-gas toxicity, thereby improving the environmental performance of motor vehicles.

1. Materials and Methods

The history of research on ultrasonic coagulation of gas-phase particles originates from the fundamental studies of the 20th century (Figure 1).

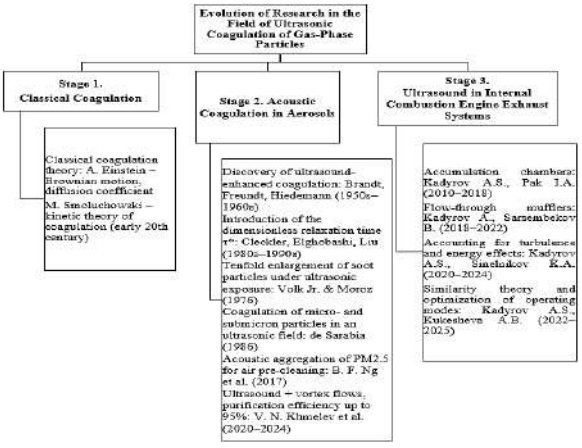

Fig. 1 – Timeline of Research on Ultrasonic Coagulation of Gas-Phase Particles

Figure 2 also presents the geographical distribution of key studies in the field of ultrasonic coagulation of gas-phase particles, which clearly illustrates the evolution of this research area from fundamental physical theories to applied engineering solutions.

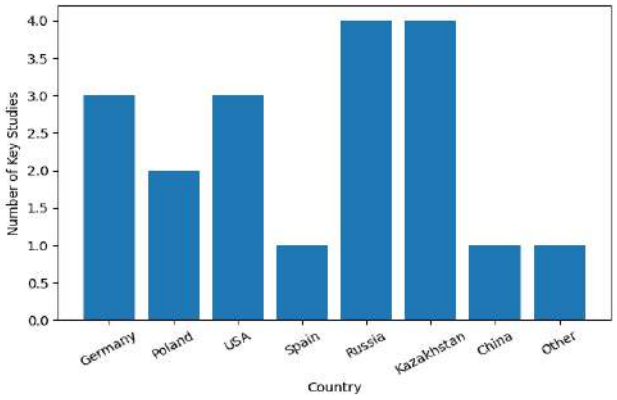

Fig. 2 – Distribution of Ultrasonic Coagulation Research by Countr

Figure 2 was compiled based on publications indexed in the Scopus and Web of Science databases. The literature selection covered the period from 1905 to 2025 and included studies specifically addressing Brownian coagulation, acoustic agglomeration, ultrasonic particle coagulation, aerosol purification, and ultrasonic exhaust gas treatment. Only peer-reviewed journal articles and conference papers directly related to particle coagulation mechanisms were considered.

According to Figure 2 while early theoretical foundations were established in Germany and Poland, recent advances demonstrate a shift toward applied and engineering-oriented research. A significant contribution is provided by Kazakhstan, where ultrasonic coagulation has been adapted to flow-through automotive mufflers with consideration of turbulence, similarity criteria, and real engine operating conditions.

The first concepts of coagulation were formulated by Einstein and Smoluchowski, who examined particle merging in a closed medium without a directed gas flow. Their models were based on Brownian motion and shear fields, which made it possible to describe the probability of particle collisions and aggregate formation.

In the early 20th century, Einstein laid the foundation for describing the Brownian motion of particles by deriving the equation for the diffusion coefficient [9]. The diffusion coefficient characterizes the rate at which particles disperse in a gaseous medium due to their thermal motion: the higher its value, the more intensively the particles move, and the greater the probability of their collision and subsequent interaction [10].

$$D = \frac{k_B T}{6\pi\mu r}, \tag{1}$$

where k_B – Boltzmann constant;

T – absolute temperature;

μ – dynamic viscosity of the gas;

r – particle radius.

Building on Einstein's work, the Polish scientist Marian Smoluchowski developed a quantitative theory of coagulation – the process by which particles collide and merge into larger structures [11]. While Einstein focused on describing the motion of an individual particle, Smoluchowski examined their collective behavior and interactions [12].

For Brownian coagulation, the equation takes the following form:

$$\frac{dN}{dt} = -KN^2, \tag{2}$$

where N is the particle concentration, and the quadratic dependence shows that doubling N increases the coagulation rate by a factor of four;

K is the coagulation constant associated with diffusion, and for spherical particles it is equal to K=8πDr.

Substituting Einstein's expression for D, was obtained [13] :

$$\frac{dN}{dt} = -8\pi\frac{k_B T}{6\pi\mu r} r N^2 = \frac{4}{3}\frac{k_B T}{\mu} N^2, \tag{3}$$

Based on the studies described above, the key principles of coagulation theory were formulated. First, coagulation leads to a reduction in the number of fine particles due to their merging into larger aggregates, which are more easily deposited under external forces. The efficiency of this process decreases with low impurity concentration, small particle radius, increased medium viscosity, and rising temperature, all of which limit collision frequency and the likelihood of adhesion.

Building on the fundamental works of Albert Einstein and Marian Smoluchowski, Brandt, Freundt, and Hiedemann were the first to note that acoustic forces can significantly enhance particle collisions and growth [14]. In their experiments, including studies on the coagulation of tobacco smoke, it was shown that ultrasonic exposure increases the probability of particle interaction severalfold, and the process itself becomes a distinct mechanism of intensified deposition [15]. These studies laid the foundation for the so-called "BFH model," which mathematically described the oscillatory motion of a particle in an acoustic field [16]:

$$m\frac{d^2x}{dt^2} = F_{\text{acous}} + F_{stokes} + F_{\text{grav}}, \quad (4)$$

where F_{acous} – the acoustic radiation force acting on the particle,

$F_{stokes} = -6\pi\mu r dt dx$ – stokes drag force, which depends on the viscosity μ and particle radius r,

$F_{grav} = mg$ – the gravitational force.

These conclusions were later confirmed by more advanced theoretical and computational studies. In the works of Jay Cleckler, Said Elghobashi, and Feng Liu, it was shown that particle motion is governed primarily by the Stokes force. The dimensionless relaxation time parameter they introduced, $\tau^* = \omega\tau$ (where τ is the particle relaxation time and ω is the angular oscillation frequency), made it possible to refine the ranges in which acoustic forces become dominant and lead to substantial aggregation [17].

Experimental confirmation of the effectiveness of acoustic aggregation was obtained in 1976 by Volk Jr. and Moroz [18]. They demonstrated that even under relatively moderate conditions, sound pressure levels of 100–120 dB and a frequency of about 3 kHz, it is possible to achieve nearly a tenfold increase in the diameter of soot particles in an aerosol. This served as important evidence of the practical applicability of acoustic coagulation for gas purification.

In 1986, the studies by de Sarabia advanced this research further by focusing on the dynamic growth of micron- and submicron-sized particles [19]. Their experiments confirmed that an ultrasonic field not only accelerates particle collisions but also consistently increases the average particle radius, which can be quantitatively described using the Smoluchowski equation (2).

The development of practical applications of these ideas was reflected in the work of B. F. Ng and colleagues, who employed acoustic aggregation as a method of pre-treating air to improve the filtration efficiency of fine particulate matter (PM2.5) [20]. Their experiments showed that within just 1–5 seconds of ultrasonic exposure, particle radii increased multiple times, thereby facilitating their subsequent capture by filters.

The most recent and advanced studies belong to V. N. Khmelev and co-authors (2020–2024). The researchers demonstrated that using not only ultrasound but also specially generated vortex flows significantly enhances the agglomeration process. In 2020, they showed that the combination of ultrasound with a swirling flow increases gas-cleaning efficiency from 46% to 85%, while the average particle size (d32) increases by a factor of 4.5 (compared with only 1.6 in a straight flow) [21]. In subsequent experiments (2024), it was proven that in a non-uniform ultrasonic field, agglomeration efficiencies of up to 95% for PM2.5, 92% for PM1.5, and 85% for PM 0.5 can be achieved at a sound pressure of 165 dB and a concentration of 2×10^{-2} g/m 32×10^{-2} g/m^3 [22]. These results provided important confirmation that optimizing the frequency, amplitude, and structure of the acoustic field makes it possible to achieve nearly complete removal of solid impurities from gases.

However, classical models based on these principles did not account for additional factors that arise under real operating conditions. In particular, they overlooked nonlinear effects associated with ultrasonic vibrations, as well as turbulence and gas-flow pulsations that inevitably accompany the operation of an internal combustion engine. For this reason, such approaches proved insufficient for fully describing the processes occurring in ultrasonic mufflers, where particle interactions are governed not only by Brownian or shear-induced coagulation, but also by the combined action of acoustic pressure, Bjerknes forces, gas-dynamic oscillations, and gravitational settling.

In our previous studies [23,24], the coagulation process was investigated using an accumulation-type ultrasonic purification device. The schematic of the accumulation device is shown in Figure 3.

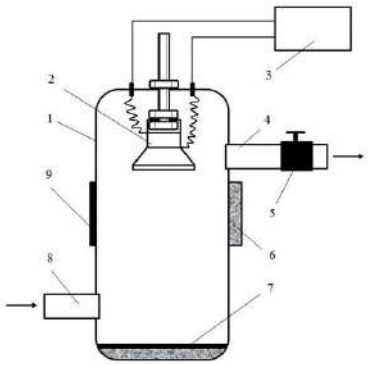

1 – housing; 2 – ultrasonic wave emitter; 3 – ultrasonic vibration generator; 4 – outlet pipe; 5 – valve; 6 – light source; 7 – ultrasonic wave reflector; 8 – inlet pipe; 9 – luxmeter

Fig. 3. – Diagram of the experimental setup for ultrasonic cleaning and treatment of exhaust gases

As part of this study, a mathematical model was developed to describe the coagulation process of soot particles under the influence of ultrasonic waves. This process is governed by two key physical mechanisms:

- orthokinetic coagulation, which arises due to differences in oscillation amplitudes of particles of varying sizes. In an alternating acoustic field, small particles are almost fully entrained by the surrounding gas, while larger and more inertial particles "lag behind." This difference in motion velocities leads to frequent collisions and subsequent merging.

- hydrodynamic coagulation, which becomes significant at high ultrasonic frequencies. This mechanism is determined by a combination of phenomena, including viscous drag forces, Bjerknes forces (interactions between oscillating bodies in a gaseous medium), and acoustic pressure gradients.

The developed mathematical model is based on the principles of kinetic gas theory and describes the dependence of soot mass on its initial quantity, the coagulation coefficient, and the duration of ultrasonic treatment.

The central element of the model is the description of the degree to which a particle is entrained in the acoustic oscillations of the gas medium. This relationship is derived from Newton's second law with consideration of the Stokes drag force and is expressed by the following formula:

$$\frac{U_d}{U_f} = \frac{1}{\left[\left(\frac{4\pi r^2 f}{9\eta}\right)^2+1\right]^{1/2}}, \tag{5}$$

where U_d – amplitude of particle oscillations, m;

U_f – amplitude of gas-medium oscillations, m;

ρ – density of the particle material (soot), kg/m³;

r – particle radius, m;

f – frequency of ultrasonic oscillations, Hz;

η – dynamic viscosity of the gas medium, Pa·s..

From the equation, it follows that the amplitude ratio U_d/U_f approaches 1 for very small particles (small radius r) and approaches 0 for large particles (large radius r) or at high frequencies *f*. This dependence creates the conditions for orthokinetic coagulation: small particles move together with the gas, while larger particles remain almost stationary, which leads to their intensive collisions.

The coagulation process results in a change in the mass distribution of particles within a closed volume. The total mass of the system m remains constant and consists of the mass of the gas m_g and the mass of the suspended soot particles m_c:

$$m=m_g+m_c=\rho V, \tag{6}$$

where ρ is the average density of the mixture and V is the volume.

The decrease in the concentration of fine particles and, consequently, the increase in the mass of soot deposited from the gas phase are described by a first-order kinetic equation:

$$m_c(t)=mc_0(1-e^{-kt}) , \tag{7}$$

where m_{c0} – initial mass of suspended soot particles, kg;

$m_c(t)$ – mass of coagulated (settled) particles at time t, kg;

k – effective coagulation coefficient, s^{-1};

The effective coagulation coefficient closely correlates with the concept of light absorption. The more particles present in a volume, the less light passes through it. For this reason, the following parameters were introduced to quantitatively evaluate the efficiency of coagulation:

- relative illumination ($\alpha i=E/Ei$): the ratio of the light intensity transmitted through the particle-containing medium (E) to the light intensity transmitted through the clean medium (E_i):

- light absorption coefficient ($\beta i=1-\alpha_i$): the fraction of light absorbed by the particles.

Assuming that the absorption coefficient β_i is directly proportional to the particle concentration n, the concentration ratio n_0/n was expressed through measurable optical parameters. This made it possible to calculate the coagulation coefficient k_i directly from the experimental data:

$$k_i = \frac{\ln(\frac{n_0}{n})}{t} \approx \frac{1}{t}\left(\frac{1}{1-\beta_i}\right). \quad (8)$$

To verify the obtained results, experimental studies were conducted using the accumulation device (Figure 3). The results demonstrate that under the influence of ultrasound, the coagulation rate increases by a factor of 3–5, and the gas transparency at the end of the experiment increases almost 2.5 times compared with natural coagulation. Thus, ultrasound not only intensifies the processes of particle growth and deposition but also reduces soot concentration and increases exhaust transparency, confirming the potential of ultrasonic technologies for exhaust-gas purification systems [24].

The authors also proposed several structural variants of the chambers, including vertical and multi-section designs, which provided longer gas residence time and facilitated the formation of standing acoustic waves. However, a limitation of these studies was that the process was considered in a "batch mode." According to this experimental approach, the gas was introduced into a closed volume and treated there for a certain time without continuous flow. In other words, the treatment was performed in a static chamber, and coagulation occurred over a fixed time interval. In this configuration, engine-induced pressure, gas-flow turbulence, and other dynamic factors were not taken into account; therefore, the obtained results have limited applicability to real operating conditions of an ultrasonic muffler.

In our subsequent studies [25], the research was extended to full-scale flow-through ultrasonic mufflers. The authors developed several bench designs, including two-section and all-metal configurations (Figure 4).

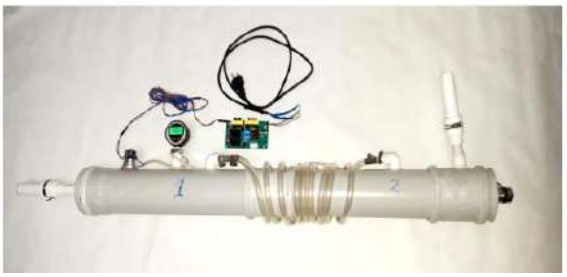

(a) Two-section ultrasonic muffler

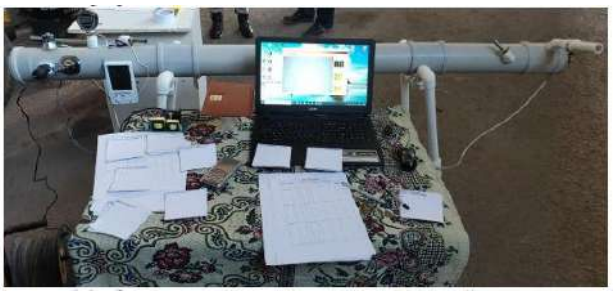

(b) Polypropylene ultrasonic muffler

(c) Metal ultrasonic muffler

Fig. 4 – Experimental ultrasonic mufflers: (a) two-section design; (b) polypropylene design; (c) metal design

The authors also developed a mathematical model describing the motion of a gas particle along the experimental muffler test benches.

In this model, each soot particle is subjected to a superposition of four main forces:

- gravitational force (F_g) directed vertically downward and determined by the particle's mass.

$$F_g=mg, \tag{9}$$

- acoustic radiation force (F_a) – a rises from the pressure gradients in the ultrasonic field (Bjerknes force). This force tends to move particles toward the nodes or antinodes of a standing sound wave, promoting their concentration and deposition.

$$F_a = \pi r^2 pAc\omega cos\omega(t - \frac{n}{c}), \tag{10}$$

where A – amplitude of the acoustic pressure,
ρ – gas density,
c – speed of sound.

- flow drag force (F_D), caused by the pressure of the exhaust gases, which carries the particle along the axis of the muffler:

$$F_D = P\frac{d^2}{4D^2}, \tag{11}$$

where P – exhaust-gas pressure,
d – particle diameter,
D – muffler diameter.

- hydrodynamic drag force (F_c) – the viscous friction force described by Stokes' law, which opposes the motion of the particle relative to the gas:

$$F_c = 6\pi\mu r\frac{dx}{dt}. \tag{12}$$

where μ – dynamic viscosity of the gas,
r – particle radius.

The total equation of motion of a particle, according to Newton's second law, has the form:

$$\frac{md^2x}{dt^2} = \overrightarrow{F_g} + \overrightarrow{F_a} + \overrightarrow{F_D} - \overrightarrow{F_c}, \tag{13}$$

For trajectory analysis, the general equation was decomposed into components along the x-axis (flow direction) and the y-axis (vertical direction, corresponding to particle settling):

- motion along the x-axis:

$$\frac{md^2x}{dt^2} + 6\pi\mu r\frac{dx}{dt} = F_D, \tag{14}$$

- motion along the y-axis::

$$\frac{md^2y}{dt^2} + 6\pi\mu r\frac{dy}{dt} = mg + F_a, \tag{15}$$

These are linear second-order differential equations. Introducing the damping parameter θ=6πμr/m, which characterizes the effect of viscous drag, their analytical solutions were obtained:

$$x(t) = \frac{F_D}{m\theta}t + (x_0 - \frac{F_D}{m\theta^2})e^{-\theta t}, \quad (16)$$

$$y(t) = \frac{mg+F_a}{m\theta}t + (y_0 - \frac{mg+F_a}{m\theta^2})e^{-\theta t}. \quad (17)$$

For soot particles in exhaust gases, the damping parameter θ is small (on the order of 0.02 s^{-1}). This means that the transient process described by the exponential term $e^{-\theta t}$ decays very rapidly. Within fractions of a second, particle motion becomes almost steady. Therefore, the analysis was transitioned to steady-state velocities.

Under steady-state motion, the particle velocities along the x and y axes become constant:

- longitudinal velocity (carryover velocity):

$$\vartheta_x \approx \frac{F_D}{6\pi\mu r} = \frac{Pdr}{6\mu D}, \quad (18)$$

- vertical settling velocity produced by the combined action of gravity and acoustic radiation forces:

$$\vartheta_y = \frac{mg}{6\pi\mu r} = \frac{Pdr}{6\mu D}, \quad (19)$$

Effective particle deposition onto the muffler wall occurs only if the time required for it to traverse the vertical distance ($t_y=D/V_y$) is less than the particle's residence time in the muffler ($t_x=L/V_x$).This leads to the key criterion for deposition efficiency:

$$V_x/V_y>L/D. \quad (20)$$

where L – the length of the muffler,

D – its diameter.

This criterion indicates that, for effective particle capture, the velocity of their transverse displacement (under the action of gravity and acoustic forces) must be sufficiently high compared to the longitudinal flow velocity.

For a macroscopic assessment of the process, a coagulation (deposition) coefficient K was introduced, defined as the ratio of the mass of deposited soot m_c to the total mass of gas m that passed through the engine during time t:

$$K=m_c/m, \quad (21)$$

The mass of gas was expressed through the engine parameters:

$$m=Q\rho\omega t, \quad (22)$$

where Q – the combustion chamber volume,

ρ – the gas density,

ω – the crankshaft rotation frequency.

Taking into account that the gas residence time in the muffler is $t=L/V_x$, the final formula for the coefficient K was obtained:

$$K = \frac{m_c\vartheta_x}{LQ\rho\omega}. \quad (23)$$

Analysis of the obtained equations allows the following conclusions to be drawn. The longitudinal velocity V_x increases with higher exhaust pressure P and larger particle radius r, which accelerates their passage through the muffler. The deposition efficiency decreases with increasing gas viscosity μ and muffler diameter D, as both factors reduce the velocities V_x and V_y.

The acoustic force F_a directly increases the vertical velocity V_y, which is a key factor in improving deposition efficiency according to the criterion $V_y/V_x>D/L$.

The coagulation coefficient K is directly related to the mass of captured soot m_c and the flow velocity V_x. It is inversely proportional to the engine displacement and the rotation frequency, which is logical, since as the gas flow rate increases, capturing the same percentage of particles becomes more challenging.

Thus, the proposed model makes it possible to link microscopic particle-motion parameters (size, density) with macroscopic system characteristics (engine pressure, muffler geometry, ultrasound parameters). It enables prediction and optimization of the performance of ultrasonic exhaust-gas cleaning systems.

According to the above, three types of ultrasonic mufflers were investigated (a two-section design, a polypropylene design, and a metal design), all connected to the exhaust system of a VW Passat B3 vehicle. The experiments were conducted in two modes: without ultrasound and with the activation of ultrasonic emitters (longitudinal, transverse, or their combination). The following performance indicators were measured: the mass of deposited soot (collected on paper sheets) and the concentrations of harmful substances (CO, CH) using gas analyzers.

The experimental studies confirmed the hypothesis that ultrasonic coagulation significantly intensifies the deposition of soot particles in exhaust gases. The greatest effect was observed when using the longitudinal emitter and the combination of emitters. The cleaning efficiency in terms of deposited soot mass increased by more than a factor of two, while the concentration of hydrocarbons (CH) in the exhaust was reduced by nearly half. However, the effect on CO concentration was less pronounced, indicating the need for further investigation.

Overall, the ultrasonic mufflers demonstrated strong potential as an effective method for reducing the toxicity of exhaust gases.

In our later investigations [26], a comprehensive force-balance model was developed, which focused on the balance of forces acting on a particle inside the muffler. A significant innovation was the separation of laminar and turbulent drag components and the introduction of correction factors that allow accurate description of the turbulent regime.

In a turbulent flow, the drag force acting on a particle greatly exceeds the classical Stokes drag force (F_c). To account for this effect, two key corrections are introduced:

- turbulent viscosity (μ_T) – an effective viscosity reflecting the intense momentum exchange in a turbulent flow. It is significantly higher than the molecular viscosity μ;

Composite particle velocity (V_a) – the motion of a particle is determined by the superposition of two velocities: the velocity of the main flow (V) and the particle's oscillation velocity in the ultrasonic field (U_1). Therefore:

$$V_a=V+U_1, \tag{24}$$

Considering these factors, the drag force in a turbulent flow (F_{sT}) can be expressed in terms of the original Stokes drag using correction coefficients:

$$F_{sT},T=F_c(K_1+K_2), \tag{25}$$

where two dimensionless criteria are introduced:

1. Turbulence criterion (K_1)::

$$K_1=\mu_T/\mu, \tag{26}$$

This criterion indicates how many times the effective resistance of the flow exceeds the laminar resistance due to turbulent fluctuations.

Ultrasound intensity criterion (K_2):

$$K_2=U/V, \tag{27}$$

This criterion (an analogue of the Strouhal number) reflects the relative "agitation" of particles by the acoustic field compared to their advection by the main flow. The higher the particle oscillation velocity U relative to the flow velocity V, the more intensive the orthokinetic coagulation becomes.

In addition to the force-based analysis, an energy-based approach was proposed. The total power required for particle transport consists of the power supplied by the engine flow (N_{eng}) and the power introduced by the ultrasonic emitter (N_{US}). To evaluate the relative contribution of the acoustic system, a third dimensionless criterion (the energy criterion) K_3 was introduced:

$$K= N_{US}/ N_{eng}. \tag{28}$$

This parameter can be interpreted as a measure of the energetic "loading" of the purification process. It indicates what fraction of energy is added to the system by ultrasound compared with the energy of the gas flow itself, and indirectly characterizes the intensity of purification.

Thus, the behavior of the complex system was described using three dimensionless criteria (K_1,K_2,K_3), which reflect the degree of turbulence, the relative intensity of the acoustic field, and the energetic contribution of the ultrasonic system.

The proposed dimensionless criteria (K_1,K_2,K_3) make it possible to analyze and compare different operating modes. The model predicts that coagulation efficiency will be maximal under conditions with a high value of criterion K_2 (when U/V is large), which is achieved either by increasing ultrasonic power or by reducing flow velocity.

The authors emphasize that due to the complex nature of wave processes (reflection, interference) and the stochastic character of turbulence, the model does not claim to provide a strictly deterministic description. It formulates general dependencies that require verification through experimental studies.

For the experimental investigations, a flow-through ultrasonic muffler test bench was constructed. It consisted of a steel pipe with a diameter of approximately D≈110 mm and a length of L=1000 mm. Two ultrasonic emitters with a frequency of 40 kHz and a nominal power of 50 W each were integrated into the section and connected to a common 100 W generator. The emitters were oriented to create a longitudinal standing wave inside the section. The scheme of exhaust gas flow in bench was shown in Figure 5.

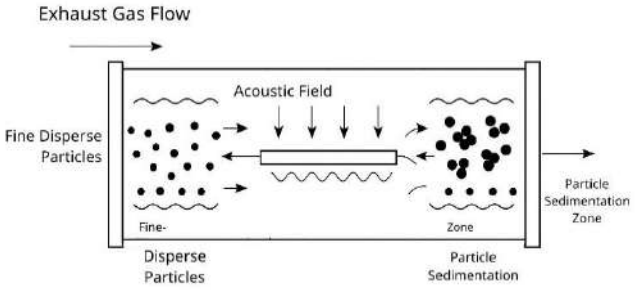

Fig. 5 – Flow ultrasonic muffler stand

Experimental studies were carried out on a Mercedes-Benz ML 2.7 CDI diesel vehicle. All measurements were performed using a certified BOSCH FSA 740 diagnostic system, which includes the BEA 050 gas analyzer for determining O_2, CO_2, HC, and CO concentrations, and the BEA 070 opacity meter for measuring the optical opacity (smoke level) of exhaust gases. The investigations were conducted at three characteristic engine operating modes: idle (750 rpm), low speed (1000 rpm), and medium speed (1400 rpm). For each mode, two measurements were taken: a control measurement (without ultrasound) and a measurement with ultrasonic exposure (with the ultrasonic system activated). The duration of each measurement, including exposure, was 60 seconds.

Measurements of optical opacity showed a significant reduction in smoke level when ultrasound was applied. The maximum effect (a 21.1% reduction in smoke opacity) was observed at medium and low engine speeds. This can be explained by the fact that at lower flow velocities, the particle residence time within the active zone (L = 1 m) is sufficient for effective coagulation (through hydrodynamic and orthokinetic mechanisms) and subsequent gravitational sedimentation onto the bottom of the section. At higher engine speeds, the residence time decreases, resulting in a reduction in deposition efficiency.

A slight but consistent increase in the relative oxygen fraction was also observed in all modes (from 17.34% to 17.36% at 750 rpm). This is attributed to the removal of some of the solid phase (soot) and unburned hydrocarbons from the flow, which shifts the composition of the gas mixture toward a higher relative concentration of O_2. The CO_2 concentration remained practically unchanged.

The influence of ultrasound on hydrocarbons (HC) and carbon monoxide (CO) was found to be strongly dependent on the engine operating mode. A reduction in their concentrations was recorded at idle.

Overall, the experimental investigation confirmed the hypothesis regarding the effectiveness of ultrasonic coagulation for purifying diesel exhaust gases.

First, ultrasonic exposure significantly reduces exhaust smoke opacity (up to 21%), especially at low and medium engine speeds. Second, purification efficiency for toxic gas components (HC and CO) is highest at low speeds, where the particle residence time in the treatment zone is sufficient for their coagulation and sedimentation.

Third, at high engine speeds, the efficiency of the method is limited by the geometry of the experimental section (length L = 1 m), which results in insufficient time for deposition of enlarged particles.

The results are in good agreement with the previously obtained theoretical findings. To further improve the efficiency of the technology, it is necessary to optimize the geometry and length of the reaction chamber, as well as the parameters of the ultrasonic field (power, frequency), taking into account the turbulent nature of the flow.

However, the process of gas purification by ultrasound in a muffler depends on a large number of factors. In our recent study [27], similarity theory was applied to describe the multifactor coagulation process. According to this method, the following key physical parameters governing the process were identified:

- engine operating parameters: engine speed (n), combustion chamber volume (Q);
- ultrasonic parameters: ultrasound frequency (*f*);
- geometric parameters: muffler diameter and length (d, L);
- physical properties of the medium: gas density (ρ), gas viscosity (μ), gas and soot masses (m_g, m_s);
- performance indicators: smoke opacity before (D_1) and after (D_2) ultrasonic treatment.

Based on these parameters, a functional equation was formulated linking the output variable (smoke opacity D_2) with the other parameters. Application of the Buckingham π-theorem made it possible to reduce the large set of variables to four main dimensionless similarity criteria:

- structural-operational criterion (k_1):

$$k_1 = \frac{\pi f L d^2}{30 \omega Q}, \tag{29}$$

This composite parameter links the geometry of the muffler (L, d) with the operating parameters of the system: ultrasonic frequency (*f*), angular engine speed (ω=πn/30), and engine displacement (Q). It characterizes the conditions under which the gas is treated inside the muffler chamber.

- hydrodynamic criterion (k_2):

$$k_2 = Re = \frac{d \vartheta \rho}{\mu}, \tag{30}$$

The Reynolds number – a classical criterion describing the flow regime (laminar or turbulent) and determining the nature of viscous friction forces.

- coagulation criterion (k_3):

$$k_3 = \frac{m_c}{m_g}, \tag{31}$$

which represents the ratio of the mass of deposited soot to the mass of the gas that has passed through the system, directly characterizing the efficiency of particle deposition.

- optimality criterion (k_4):

$$k_4 = \frac{D_2}{D_1}. \tag{32}$$

The ratio of smoke opacity after and before ultrasonic treatment serves as the optimality criterion of the ultrasonic muffler: the lower the value of k_4, the higher the purification efficiency.

This composite parameter links the geometry of the muffler (L, d) with the operating parameters of the system: ultrasonic frequency (*f*), angular engine speed (ω=πn/30), and engine displacement (Q). It characterizes the conditions under which the gas is treated inside the muffler chamber.

The obtained criteria make it possible to determine that maximum process efficiency (minimum k_4) is achieved at a certain optimal ratio between the parameters included in the criteria, in particular, when the ultrasonic frequency f is matched to the angular engine speed ω.

To verify the results, experimental studies were carried out on a full-scale ultrasonic muffler test bench (Figure 3). The muffler was equipped with a set of ultrasonic emitters operating at frequencies of 25, 28, and 40 kHz. Exhaust-gas smoke opacity and the mass of deposited particles were measured at engine speeds of 750, 950, and 1250 rpm.

The experiments demonstrated that activation of the ultrasonic field consistently reduced smoke opacity by 15–20% compared with control measurements. Under optimal conditions, the maximum reduction reached 35%. In addition, it was found that the frequency of 40 kHz was the most effective for coagulating soot particles. At this frequency, the minimum value of the optimality criterion was achieved, $k_4=D_2/D_1\approx0.8–0.85$.

The theoretical hypothesis regarding the presence of an optimal ratio between ultrasonic frequency and shaft rotational speed was also experimentally confirmed. Minimum smoke opacity was observed at $f/\omega\approx402.01$. This indicates that each engine speed corresponds to its own optimal ultrasonic frequency. Additionally, gravimetric analysis showed

that the mass of deposited soot nearly doubled when ultrasound was applied, directly indicating intensification of coagulation and sedimentation processes. It was also determined that the optimal deposition zone length is 0.4 m.

Thus, the practical validity of the proposed approach has been fully confirmed, opening promising prospects for further development and implementation of ultrasonic exhaust-gas purification systems.

2. Results and discussion

Despite significant progress in coagulation theory and the development of ultrasonic technologies, existing models and experimental methods have several limitations that significantly hinder their direct application to automotive exhaust systems (Figure 6).

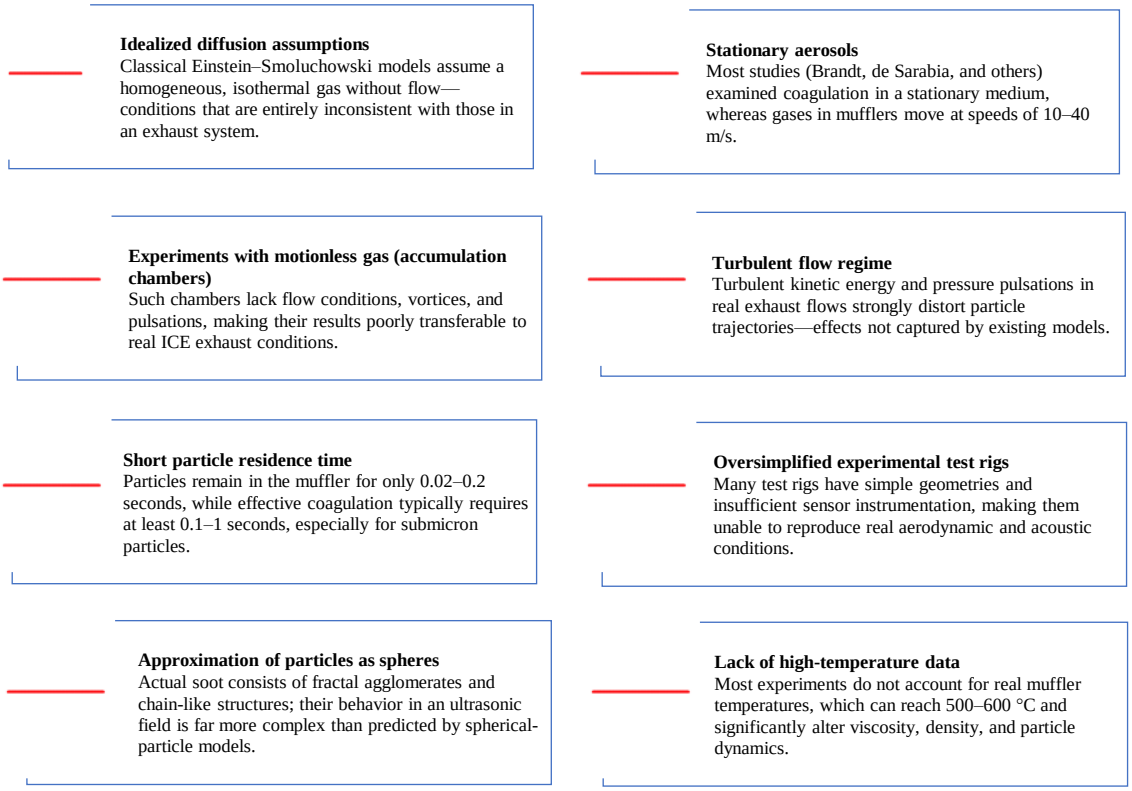

Fig. 6 – Limitations of existing research

First of all, the classical Einstein–Smoluchowski models were developed for idealized conditions: a stationary, isothermal, homogeneous medium without directed gas flow or pressure pulsations. In a real muffler, the temperature ranges from 80 to 600 °C, the flow is high-velocity, pulsating, and turbulent, and the composition of the gas mixture is continuously changing. Under such conditions, classical diffusion coagulation does not reflect the actual mechanisms of particle motion and collision.

Existing acoustic coagulation models also have significant limitations. Numerous studies by Brandt–Freundt–Hiedemann, de Sarabia, Volk Jr. & Moroz were carried out in stationary aerosols and did not account for particle velocity, turbulent diffusion, velocity gradients, or the intermittency of acoustic fields characteristic of automotive mufflers. As a result, it becomes impossible to accurately describe the combined effects of ultrasound, flow velocity, and pressure pulsations.

Another limitation is the “batch-mode” experiments using accumulation chambers, common in early research. In such setups, the gas fills a closed volume and is exposed to ultrasound for a fixed period. However, the absence of flow conditions, vortex structures, and dynamic loads means that the results of these experiments cannot be scaled to real exhaust systems.

A major limitation remains the insufficient treatment of turbulent flow regimes. Diesel and gasoline engines generate complex vortex structures, multiple pulsations, and high turbulent kinetic energy, while most models assume laminar or weakly turbulent flow. Even refined models incorporating turbulent viscosity provide only qualitative descriptions and require adaptation for different vehicle types and engine operating modes.

Additional difficulties arise from the formation of a stable acoustic zone in a flow-through muffler. Sound interference, variable flow velocity, and reflections from walls, perforated inserts, and baffles lead to instability of standing waves, complicating the creation of stable node and antinode zones necessary for effective acoustic aggregation.

A significant limitation is the short residence time of particles in the muffler. At real exhaust-gas velocities, particles pass through the reaction zone in 0.02–0.2 s, whereas ultrasonic coagulation requires 0.1–1.0 s for the formation of stable agglomerates. At high engine speeds, this time decreases even further, reducing the method's effectiveness.

The lack of data on particle behavior at high temperatures also constrains technological development. Most experiments have been conducted under ambient conditions, whereas real exhaust temperatures reach 500–600 °C, causing drastic changes in viscosity, gas density, and particle properties—including their fractal structure and reactivity.

Experimental test rigs used in modern research often do not reproduce the structural complexity of real exhaust systems. Limited length, simplified geometry, and insufficient sensor instrumentation hinder accurate assessment of processes under real operating conditions.

Finally, most mathematical models treat soot particles as spherical objects of uniform diameter, whereas real soot consists of polydisperse fractal agglomerates. This leads to substantial discrepancies between modeled and actual mechanisms of coagulation and sedimentation.

To enhance the efficiency of ultrasonic coagulation in real exhaust systems and to develop practical prototypes of ultrasonic mufflers, a comprehensive set of scientific and engineering directions must be pursued.

An important direction involves optimizing the geometry of the ultrasonic muffler. It is necessary to design flow-slowing zones, expanded reaction chambers, internal baffles, and recirculation sections that increase particle residence time and create conditions for the formation of stable acoustic structures (Figure 7).

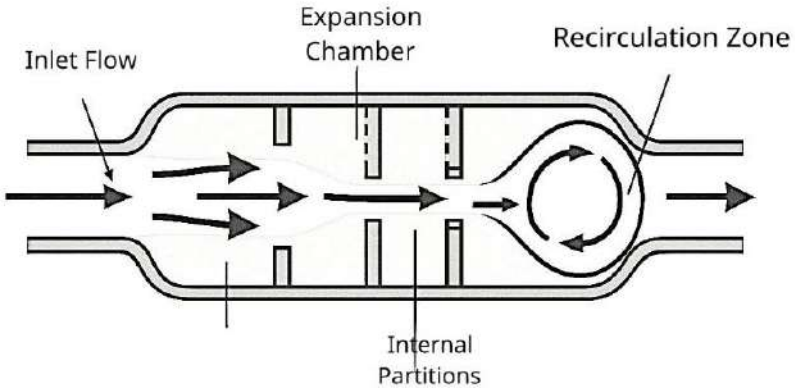

Fig. 7 – Optimization of Ultrasonic Muffler Geometry

Engineering control of the acoustic field is of particular importance. Research is required on the formation of standing waves in turbulent flow, the development of non-uniform (vortical and focused) ultrasonic fields, as well as the creation of resonant chambers and adaptive systems that automatically adjust the ultrasonic frequency to engine speed. Especially promising is the identified pattern of the optimal f/ωf/\omegaf/ω ratio, which enables synchronization of acoustic exposure with the operating mode of the internal combustion engine.

To increase efficiency, multi-frequency ultrasonic systems should be investigated. The polydisperse structure of soot requires the use of multiple frequencies that promote coagulation of both large and submicron particles. Promising approaches include frequency-modulation modes and combinations of low and high frequencies, which enhance orthokinetic and hydrodynamic coagulation mechanisms.

Significant prospects are offered by the development of combined purification systems in which ultrasound operates together with infrared radiation, corona discharge, vortex structures, or catalytic neutralization (Table 1).

Such combined systems can significantly improve the purification of fine particulate matter and toxic components.

A promising direction is the development of control algorithms for ultrasonic emitters, including adaptive power regulation, frequency tuning, and automatic adjustment of operating modes depending on engine load, temperature, and exhaust density.

There is also a need to develop simplified engineering models, nomograms, and diagrams that will enable designers to quickly assess the influence of muffler geometry, ultrasonic frequency, engine speed, and pressure on deposition efficiency.

The final stage of research should involve the creation of an industrial prototype of an ultrasonic muffler, along with the development of design documentation, recommendations for integration into existing vehicles, and modular solutions suitable for different types of transport equipment.

Table 1. Combined Ultrasonic Exhaust-Gas Purification Systems

№	Combination	Primary Mechanism of Action	Key Effects	Expected Outcome
1	Ultrasound + Vortex Flows [28]	Flow swirling creates zones of recirculation and flow deceleration	• Increased particle residence time; • Enhanced orthokinetic coagulation; • Higher collision frequency.	Improved particle deposition efficiency
2	Ultrasound + Infrared Radiation [29]	Thermal activation and partial oxidation of particles	• Breakdown of organic compounds (HC); • Reduced fractality of agglomerates; • Improved settling of enlarged particles.	More complete purification of the mixed (gas + solid particles) phase [30]
3	Ultrasound + Corona Discharge [31]	Charging of soot particles and electrostatic aggregation	• Electrostatic attraction between agglomerates [32] • Combined coagulation and deposition • Reduction of PM concentration [33]	Accelerated agglomeration and effective deposition of submicron particles
4	Ultrasound + Catalytic Neutralization	Vibrational impact and pre-catalyst particle enlargement [34]	• Reduced catalyst clogging • Increased active surface area • Removal of carbon deposits	Improved catalyst performance and reduced CO, HC, and NO_x[35]

Conclusion

The analysis of theoretical and experimental studies in the field of ultrasonic coagulation of aerosol and soot particles has demonstrated that, over recent decades, a substantial scientific foundation has been established. This foundation encompasses both classical diffusion coagulation (Einstein–Smoluchowski) and acoustic aggregation in stationary aerosols and flow-through systems. It has also been shown that the direct application of these models to the exhaust systems of internal combustion engines is limited due to significant discrepancies between real operating conditions and the idealized assumptions of classical theories. High temperature, pulsating turbulent flow, variable chemical composition, and the restricted residence time of particles in the treatment zone necessitate the expansion and modification of existing approaches.

A synthesis of the findings from Brandt–Freundt–Hiedemann, de Sarabia, Volk Jr & Moroz, BF Ng, and others, as well as recent research by V.N. Khmelev and co-authors, has confirmed the fundamental effectiveness of ultrasound as a tool for intensifying particle coagulation and deposition. It has been demonstrated that, with optimal selection of frequency, amplitude, and acoustic field structure, it is possible to achieve a multiple increase in characteristic particle size and substantially enhance gas purification efficiency. However, most of these studies were conducted in stationary aerosols or simplified channels and chambers, which limits their applicability to real engine exhaust systems.

The works by Kadyrov A.S., Pak I.A., Sarsembekov B., Sinelnikov K.A., and Kukesheva A.B. demonstrated the transition from batch-type chambers to full-scale flow-through ultrasonic mufflers and made it possible to link microscopic mechanisms of particle motion and coagulation with macroscopic parameters of the exhaust system. Several dimensionless criteria were introduced and justified, accounting for the influence of muffler geometry, engine operating mode, gas medium properties, ultrasonic intensity, and flow turbulence. Experimental data showed a reduction in smoke opacity by 15–35%, an almost two-fold increase in the mass of deposited soot, and the highest efficiency at a frequency of 40 kHz with optimization of the f/ω ratio in accordance with engine speed. These results confirm the practical feasibility of implementing ultrasonic mufflers in exhaust gas purification systems.

At the same time, a number of key limitations were identified in existing models and experimental methodologies: idealized assumptions of diffusion coagulation, incomplete representation of turbulent flow and pressure pulsations, simplified geometry of experimental setups, insufficient residence time of particles in the treatment zone, and the simplified representation of soot particles as monodisperse spheres. These limitations define the boundaries of applicability for existing solutions and highlight areas that require further investigation.

Based on the conducted review, a comprehensive set of directions for future research was formulated: optimization of ultrasonic muffler geometry (flow deceleration zones, expanded chambers, recirculation regions), development of methods for controlling the acoustic field in turbulent flow, investigation of mult frequency regimes for polydisperse soot, creation of combined systems (ultrasound + vortical flow, infrared irradiation, corona discharge, catalytic neutralization), as well as the development of simplified engineering models and adaptive control algorithms for ultrasonic emitters. The implementation of these directions will enable the transition from laboratory prototypes to industrial-grade ultrasonic mufflers capable of ensuring stable reduction of smoke opacity and exhaust toxicity, thereby improving the environmental performance of motor vehicles.

Thus, the study forms a comprehensive scientific and methodological basis for the further development and refinement of ultrasonic exhaust gas purification systems and serves as a starting point for creating efficient, practically implementable designs of next-generation ultrasonic mufflers.

References

[1] Grigolashvili M., Kadyrova I., Shayakhmetova Y., Beisembayeva M., Muratbekova S., Seryogina A. Circulating microRNAs in various etiopathogenetic subtypes of acute ischemic stroke: A human systematic review study. *Frontiers in Neurology*, Vol. 16, 2025, Article No. 1623597.
[2] Akhmaltdinova L., Kadyrova I., Zhumaliyeva V., Babenko D., Sirota V. Proinflammatory cytokines and colorectal cancer: The impact of the disease stage. *Contemporary Oncology / Współczesna Onkologia*, Vol. 24, Issue 4, 2020, pp. 207–210.
[3] Kadyrova I.A., Mindubaeva F.A., Grjibovski A.M. Prediction of outcomes after stroke: A systematic review. *Human Ecology*, Vol. 22, Issue 10, 2015, pp. 55–64.
[4] Kadyrov A., Warguła Ł., Kukesheva A., Dyssenbaev Y., Kaczmarzyk P., Klapsa W., Wieczorek B. Optimization of vertical ultrasonic attenuator parameters for reducing exhaust gas smoke of compression–ignition engines: Efficient selection of emitter power, number, and spacing. *Applied Sciences*, Vol. 15, Issue 14, 2025, Article No. 7870, pp. 1–19.
[5] Kukesheva A., Kadyrov A., Moldabaev B., Sinelnikov K., Karsakova A., Kyzylbayeva E. Determination of optimal parameters for ultrasonic cleaning of vehicle radiators. *Communications – Scientific Letters of the University of Žilina*, Vol. 27, Issue 3, 2025, pp. B126–B137.
[6] Sakhapov R.L. Method of Cleaning Internal Combustion Engine Radiator Tubes with Ultrasound. // Material and Mechanical Engineering Technology, No. 2, 2024 – p. B18-B24. - DOI 10.52209/2706-977X_2024_2_18
[7] Kabibollayev B.B., Kukesheva A.B., Kadyrov A.S., Kryuchkov E.Y., Karsakova A.Zh., Sinelnikov K.A. Environmental and economic feasibility of implementing electro-impulse mufflers on motor vehicles. *Material and Mechanical Engineering Technology*, Vol. 3, 2025, pp. 99–111. DOI: 10.52209/2706-977X_2025_3_99.
[8] Talbot C., Pattison O. Marian Smoluchowski (on the tenth anniversary of his death). In: *Boris Hessen: Physics and Philosophy in the Soviet Union, 1927–1931: Neglected Debates on Emergence and Reduction*. Cham: Springer, 2021, pp. 61–72.
[9] Liu Z., Jia Y. Two simulation methods of Brownian motion. *Journal of Physics: Conference Series*, Vol. 2012, Issue 1, 2021, Article No. 012015.
[10] Spiechowicz J., Luczka J., Hänggi P. Diffusion coefficient of a Brownian particle in equilibrium and nonequilibrium: Einstein model and beyond. *Entropy*, Vol. 25, Issue 1, 2022, Article No. 42.
[11] Viehland L.A. *Gaseous Ion Mobility, Diffusion, and Reaction*. Cham: Springer International Publishing, 2018, 105 p.
[12] Krajewski W. *Polish Philosophers of Science and Nature in the Twentieth Century*. Leiden: Brill, 2022, 312 p.
[13] Rao B.V. Brownian motion. *Resonance: Journal of Science Education*, Vol. 26, Issue 1, 2021, pp. 1–14.
[14] Brandt H. A study of the speed of sound in porous granular media. *Journal of the Acoustical Society of America*, Vol. 27, 1955, pp. 479–486.
[15] Hiedemann E.A. Metallurgical effects of ultrasonic waves. *Journal of the Acoustical Society of America*, Vol. 26, Issue 5, 1954, pp. 831–842.
[16] González I., Hoffmann T.L., Gallego J.A. Precise measurements of particle entrainment in a standing-wave acoustic field between 20 and 3500 Hz. *Journal of Aerosol Science*, Vol. 31, Issue 12, 2000, pp. 1461–1468.
[17] Cleckler J., Elghobashi S., Liu F. On the motion of inertial particles by sound waves. *Physics of Fluids*, Vol. 24, Issue 3, 2012, Article No. 033301.
[18] Volk M.Jr., Moroz W.J. Sonic agglomeration of aerosol particles. *Water, Air, and Soil Pollution*, Vol. 5, Issue 3, 1976, pp. 319–334.
[19] Gallego-Juárez J.A., Riera-Franco de Sarabia E., Rodríguez-Corral G., Hoffmann T.L., Gálvez-Moraleda J.C., Rodríguez-Maroto J.J., Acha M. Application of acoustic agglomeration to reduce fine particle emissions from coal combustion plants. *Environmental Science and Technology*, Vol. 33, Issue 21, 1999, pp. 3843–3849.
[20] Liu G., Zhang X., Liu P., Lim S.H., Wan M.P., Ng B.F., Lisak G. Enhanced particulate matter removal from flue gas of organic solid waste through acoustic agglomeration. *Separation and Purification Technology*, Vol. 360, 2025, Article No. 131244.
[21] Khmelev V.N., Shalunov A.V., Nesterov V.A. Improving the separation efficiency of particles smaller than 2.5 micrometers by combining ultrasonic agglomeration and swirling flow techniques. *PLoS One*, Vol. 15, Issue 9, 2020, Article No. e0239593.
[22] Khmelev V.N., Shalunov A.V., Nesterov V.A., Terentiev S.A. Influence of acoustic streams on the efficiency of ultrasonic particle agglomeration. *Applied Sciences*, Vol. 14, Issue 2, 2024, Article No. 559.
[23] Pak I., Kadyrov A., Askarov B., Suleyev B., Karsakova A. Developing and studying the method of ultrasonic purification and utilization of internal combustion engine exhaust gases. *Communications – Scientific Letters of the University of Žilina*, Vol. 25, Issue 3, 2023, pp. 245–258.
[24] Pak I. Experimental study of the ultrasonic muffler efficiency for improving the exhaust gas cleaning system of internal combustion engines of automobiles. // Material and Mechanical Engineering Technology, Vol. 6, Issue 2, 2024. - p. 53 – 63
[25] Kadyrov A.S., Sarsembekov B.K., Ganyukov A.A., Zhunusbekova Z.Z., Alikarimov K.N. Experimental research of the coagulation process of exhaust gases under the influence of ultrasound. *Communications – Scientific Letters of the University of Žilina*, Vol. 23, Issue 4, 2021, pp. B288–B298.
[26] Kadyrov A., Sarsembekov B., Ganyukov A., Suyunbaev S., Sinelnikov K. Ultrasonic unit for reducing the toxicity of diesel vehicle exhaust gases. *Communications – Scientific Letters of the University of Žilina*, Vol. 24, Issue 3, 2022, pp. B189–B198.
[27] Kadyrov A., Bembenek M., Sarsembekov B., Kukesheva A., Nurkusheva S. The influence of the frequency of ultrasound on the exhaust gas purification process in a diesel car muffler. *Applied Sciences*, Vol. 14, Issue 12, 2024, pp. 1–19.
[28] Musić M., Ahić-Džokić M., Džemić Z. A new approach to detection of vortices using ultrasound. *Flow Measurement and Instrumentation*, Vol. 42, 2015, pp. 40–46.

[29] Madhavan J., Theerthagiri J., Balaji D., Sunitha S., Choi M.Y., Ashokkumar M. Hybrid advanced oxidation processes involving ultrasound: An overview. *Molecules*, Vol. 24, Issue 18, 2019, Article No. 3341.
[30] Sarsembekov B.K., Kadyrov A.S., Kunayev V.A., Issabayev M.S., Kukesheva A.B. Experimental comparison of methods for cleaning car exhaust gas by exposure using ultrasound and laser radiation. *Material and Mechanical Engineering Technology*, Vol. 6, Issue 3, 2024, pp. 44–54.
[31] Feng C., Zheng Y., Zhang R., Tian E., Zou X., Liu K. Characterizing the pin-to-ring direct-current air corona discharge by its ultrasonic signal and ozone production. *Applied Acoustics*, Vol. 237, 2025, Article No. 110738.
[32] Kukesheva A., Kadyrov A., Kryuchkov Y. Establishing the parameters of the operation mode of the electric pulse automobile muffler. *Journal of Applied Engineering Science*, Vol. 22, Issue 1, 2024, pp. 89–99.
[33] Kadyrov A., Kukesheva A., Kryuchkov E., Pak I., Kurmasheva B., Kabikenov S. Development of calculation methodology for optimizing the operating mode of an electric pulse unit for cleaning exhaust gases. *Communications – Scientific Letters of the University of Žilina*, Vol. 26, Issue 1, 2024, pp. 41–53.
[34] Shi L., Zhang Z., Wang R., Zhou C., Sun C. Study on ultrasound-assisted precipitation for preparing Ni/Al_2O_3 catalyst. *Ultrasonics Sonochemistry*, Vol. 67, 2020, Article No. 105107.
[35] Amaniampong P.N., Jérôme F. Catalysis under ultrasonic irradiation: A sound synergy. *Current Opinion in Green and Sustainable Chemistry*, Vol. 22, 2020, pp. 7–12.

Information of the authors

Kadyrov Adil, d.t.s., research professor, Abylkas Saginov Karaganda Technical University
e-mail: adil.suratovich@mail.ru

Sakhapov Rustem, d.t.s., professor, Kazan (Volga region) Federal University
e-mail: rustem@sakhapov.ru

Kukesheva Aliya, PhD, assistant professor, Abylkas Saginov Karaganda Technical University
e-mail: aliya.kukesheva@bk.ru

DOI 10.52209/2706-977X_2026_2_102 **IRSTI 81.09.81** **UDC 625.84**

Modeling of Design Stresses Caused by Vehicular Loading on Cement Concrete Pavement for Conducting Model Tests

Lukpanov R.[1], Kabdyrova L.[1]*, Karacasu M.[2], Yenkebayev S.[3], Tsygulyov D.[1]
[1]Faculty of Architecture and Construction, L.N. Gumilyov Eurasian National University, Astana, Kazakhstan
[2]Eskisehir Technical University, Eskisehir, Turkey
[3]Technobius, LLP, Astana, Kazakhstan
*corresponding author

Abstract: The article presents the results of calculations of stresses caused by tire pressure on the road surface, which are necessary for modeling design situations on a scale. Calculations of actual stresses were performed based on the standard characteristics of tires, the permissible load capacity of motor vehicles, and the potentially variable air pressure in the tire. The latter has a particular influence on the change in the contour area of the contact patch. The calculation of model stresses for the model wheel was performed based on the law of dynamic similarity from the condition of the scale ratio of the actual contact area to the model area, taking into account the elastic properties of the model wheel rubber (determined by laboratory tests). The results of the study are presented as the minimum and maximum values of actual and model stresses by category (types according to main characteristics) of motor vehicles. According to the results, stresses were obtained from the model wheel depending on the type of motor vehicle (described in detail in the article), which range from 0.5 kg/cm² (bicycles) to 12.4 kg/cm² (trucks and buses). The proposed calculation method will allow simulating the calculated stresses from motor vehicle wheels for any model tests on a scale with a high degree of correspondence (to actual stresses).

Keywords: road surface, icing, contact patch, modeling, abrasion.

Introduction

Road construction plays a key role in the development of infrastructure, the economy, and society as a whole. To ensure the sustainable socio-economic development of a country, it is necessary not only to build new roads but also to maintain them in proper condition. The scope of road maintenance work directly depends on the climatic characteristics of the region. In areas with a variable climate, the urgent task is to prevent road surface icing in winter. In modern road construction practice, cement concrete and asphalt concrete pavements are widely used [1]. Concrete roads have a number of undeniable advantages over asphalt concrete roads, including increased durability, high strength, and resistance to frost heaving of the base. However, one of the significant disadvantages of concrete roads is their tendency to ice up at low temperatures, which negatively affects traffic safety during the cold season [2].

The most common method of preventing icing in domestic practice is to treat roads with sand or other abrasive materials, but this approach has its drawbacks, both in terms of effectiveness and appearance [3]. First, the effect of sand is short-lived, especially in heavy traffic. Second, flying sand particles, along with dirt and ice, contaminate vehicles and impair visibility, which increases the likelihood of accidents. Salt or other chemicals (sodium chloride, calcium chloride with or without corrosion inhibitors, potassium acetate, and agricultural products) are also often used worldwide for deicing [4]. Unlike sand, the use of salt has many negative consequences. In addition to the aforementioned disadvantages, such as low efficiency and pollution, salt impairs traction, as melting ice creates a wet road with poor characteristics. When dissolved in water, salt releases active ions through hydrolysis and has a destructive effect on road surfaces and cars, causing corrosion. The issue of chloride concentrations in water after de-icing treatment and their impact on the environment has been actively discussed in the European Parliament since 2006 [5].

The problem of icing on concrete roads remains significant, and its solution may lie in the use of impregnations that do not require regular maintenance but effectively reduce or completely prevent ice formation [6]. In addition to technological characteristics, the economic feasibility of such compositions is becoming an important aspect [7].

The technological solution for preventing icing proposed in the article stands out among existing solutions not only for its design features, but also for its composition, if considered as a hydrophobic agent. The production of the ice-repellent composition is planned to be based on keratin-containing substances obtained from livestock waste, with the addition of water-soluble polymers. In general, the use of polymer components in building materials science is of great importance [8]. In our case, the polymer component acts as a shielding hydrophobic layer. Since concrete is a hydrophilic material that absorbs water, a greater effect will be achieved by using a concentrate of the impregnating composition in water. That is, the water that tends to penetrate the concrete structure will carry with it the suspended mixture of the polymer component of the impregnating composition. This will ensure that the porous surface structure of the concrete is enveloped, creating a layer of tension difference that prevents ice and concrete from becoming a single monolith (as a result, the ice breaks even with minor mechanical impact) [8].

The aim of the general study is to develop an impregnating composition that helps reduce the adhesive resistance of ice crust to concrete roads. However, this article presents part of the study related to the method of calculating and analyzing the design stresses from motor vehicle wheels when modeling design situations on a scale. The results presented may be of interest not so much in terms of the quantitative data obtained, but in terms of the method used to convert real vehicle stresses into model stresses, and the factors and laws that were used for this purpose. Qualitative modeling of design situations, including design loading diagrams, will primarily affect the quality of the results obtained.

To model samples to scale, similarity laws are typically used, which ensure correct comparison of results between the model and the real object [9]. A distinction is made between geometric similarity, which is based on the fact that the model and the real object must have the same geometric shapes but differ in scale [10]. Kinematic similarity is based on the proportionality of velocity, acceleration, and displacement of points in the model and the real object [11]. In dynamic similarity, in order to maintain the equality of forces between the model and the real object, it is necessary to observe the proportionality between all types of forces, and in physical similarity, the materials of the model and the real object must have the same dimensionless parameters characterizing their behavior [12-13]. In our case, the law of dynamic similarity was also used, but the results of the ratios of the forces acting from the wheel load were corrected relative to the contact area values, taking into account the elastic properties of the model wheel rubber, and are described further in the methodology and research results section.

1. Materials and methods

The anti-icing impregnating composition investigated in the broader research project is based on keratin containing agricultural waste and polymer components. Since the present study focuses on stress modeling and scaling procedures, only information relevant to the wear resistance testing program is presented.

The need to recalculate normal stresses on concrete roads caused by motor vehicles was due to model tests of the wear resistance of the impregnating composition. Since the tests were large-scale, high-quality modeling of design situations with adjustments to design schemes and loads was a priority task of the study. The quality of the simulation of the calculation schemes determines the quality of the results of subsequent tests on the wear resistance of the ice-repellent coating, which were performed using equipment designed to assess the abrasion of concrete – an abrasion circle (Figure 1). The tests are large-scale, therefore, the wheel load was calculated using the dynamic similarity method based on the real stress transmitted from the car wheel to the concrete road surface.

In this case, it is not the scale of the actual and model wheels that is important, but the ratio of the contact patch sizes under load, which depends on the tire pressure and the elasticity of the model wheel. However, stresses are directly related to scaling, since their values are a guideline for selecting loads for a scale model wheel (see results, Table 2 - Calculation of normal loads on a model wheel). For this purpose, motor vehicles were conditionally divided into 5 categories according to their load capacity: A1 - bicycles; A2 - motorcycles (mopeds); A3 – passenger cars; A4 - light trucks and buses with particularly low capacity; A5 - trucks and buses.

A – General view of the test

B – Model wheel of a motor vehicle

Fig. 1.- Wear resistance testing of the impregnating composition on an abrasion wheel

The contour area of the contact patch is calculated using the formula for the area of an ellipse [1]. The use of this method is attractive because the parameters of the universal tire characteristic — coefficients c_1 (m²/kN) and c_2 (1/m), determined by calculation from the linear graph of the universal tire characteristic, constructed in the coordinate system (XOY), where x=f/($p_w - p_0$) and y=f²/G_k, together with the coefficient p_0 (kPa), determined by the tire's ply count n, are constant for each tire. They allow the calculation of the normal deflection of the tire, the linear dimensions of the tire tread contact patch—width b_k and length a_k and the contour area of the contact patch on a flat, rigid surface F_k for any combination of normal load on the tire G_k and internal tire air pressure p_w, [1].

$$S_t = \frac{\pi}{4}\frac{20.5}{11.9+\left|\frac{D}{B}-\frac{|n-9|}{2}-3\right|} \times \sqrt{D \times \left(\frac{D}{2}-r_s\right)-\left(\frac{D}{2}-r_s\right)^2} \times 2\sqrt{2 \times \frac{B+(D-d)/2}{2.5} \times \left(\frac{D}{2}-r_s\right)-\left(\frac{D}{2}-r_s\right)^2} \qquad (1)$$

Where, S_t - is the contour area of the contact patch, m2; D - is the outer diameter of the tire, m; B - is the width of the tire profile, m; n - is the tire ply ratio; r_s - is the static radius of the tire, m; d - is the nominal rim diameter, m.

The tire characteristics used to determine the contour area of the contact patch for each type of transport were taken from standards and are summarized in Table 1 [15-19].

Table 1. Tire characteristics

Category	Tire width (d), mm	Tire pressure, MPa	Maximum permissible load (F) for single and twin wheels, kN		Linear load F/d, kN/m
			S	D	
A1 (GOST 4750)	28-59	0.19-0.40	0.29-0.85		4.99-21.02
A2 (GOST 5652)	67-180	0.15-0.35	0.98-3.29		11.62-29.88
A3 (GOST 52900)	140-206	0.17-0.21	2.6-5.7		18-56-29-69
A4 (GOST 4754)	154-218	0.20-0.59	4.2-14.2		27.06-62.37
A5 (GOST 5513)	213-425	0.73-0.90	13.34-50.52	12.26-35.80	57.56-125.77

According to the requirements, the pressure deviation from the standard value is within ±2-5%, but in the calculations, a higher value of ±15% was used, which will significantly increase the stress range and will not contradict the real operating conditions of vehicles. When the pressure decreases, the static radius will decrease and the static deflection will increase, therefore the contact patch will increase. Conversely, when the pressure increases, the contact patch will increase, and consequently, the stress transmitted by the wheel will also increase. Thus, voltage range calculations will be performed at maximum (ρ_{max}), standard (ρ_{St}) and minimum (ρ_{min}) tire pressures.

To simulate actual stresses in model tests, the law of dynamic similarity was used based on the scale ratio of the actual contact area to the model area. To determine the model contact area, we will use the results of loading the model wheel rubber with specified loads (see the results section below).

The tests consist of measuring the vertical deformation of the rubber sample under normal compression (Figure 2). The lateral relative deformations were determined under the assumption of constant volume (although, strictly speaking, this condition is not fully satisfied for real rubber materials) and by adopting an average Poisson's ratio for rubber of 0.5. However, since rubber is generally considered a nearly incompressible material with a Poisson's ratio close to 0.5, this assumption is acceptable for engineering estimation of the contact area and the corresponding stresses. To determine the test program (maximum load during testing), preliminary calculations were performed to estimate the expected range of loads acting on the model wheel.

The tests were performed using a certified and calibrated DMA device (Mettler Toledo), which allows a static load to be applied to the sample, followed by measurement of its deformation. The tests were performed at a standard temperature of 22°C and humidity of 50% (constant throughout the entire test period). Vertical deformations were recorded by the device in automatic mode, and horizontal deformations were recorded using a certified and calibrated digital caliper (Sylva System) with a measurement accuracy of 0.01 mm. The loading rate was irrelevant, as the aim of the study was to apply a stepwise load to the rubber sample and then record its volumetric deformation.

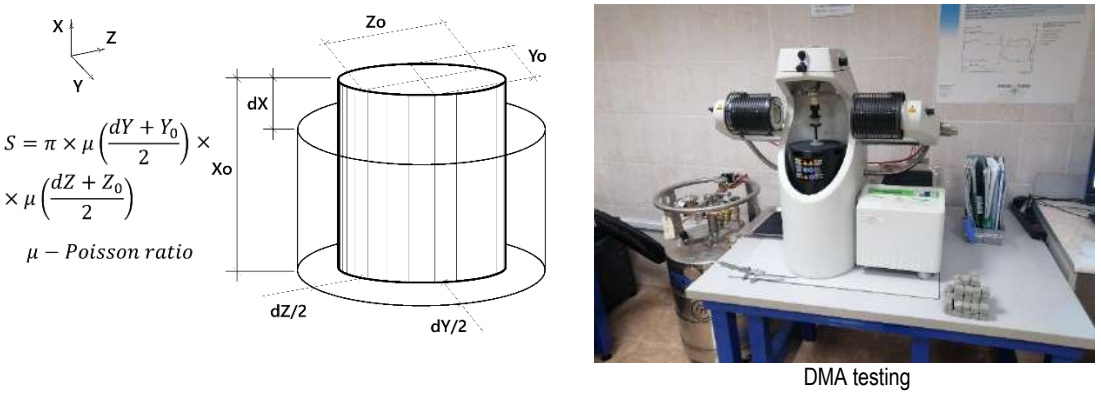

Fig. 2.- Testing of a rubber model wheel

2. Results and discussion

As mentioned earlier, tire pressure will have a significant impact on the stress transmitted by the wheel. Based on the previously agreed tire pressure criteria, Figures 3-5 show the results of calculations of stress ranges at maximum (ρ_{max}), standard (ρ_{St}), and minimum (ρ_{min}) tire pressures.

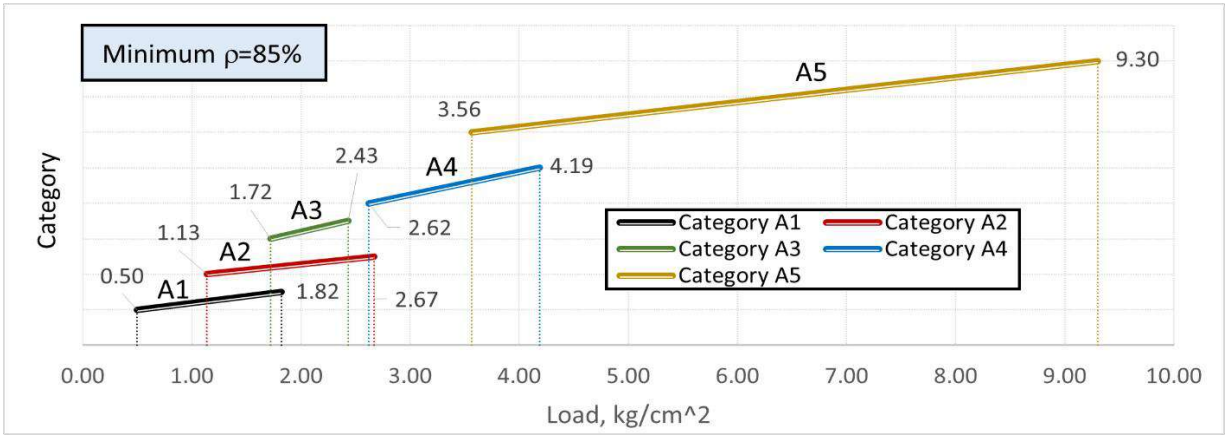

Fig 3. - Voltage range at minimum tire pressure

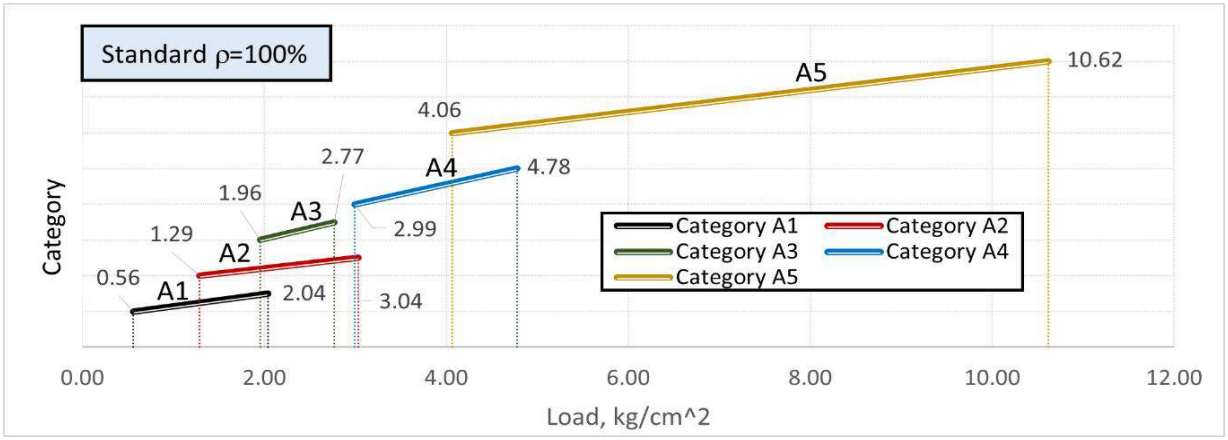

Fig 4. - Voltage range at standard tire pressure

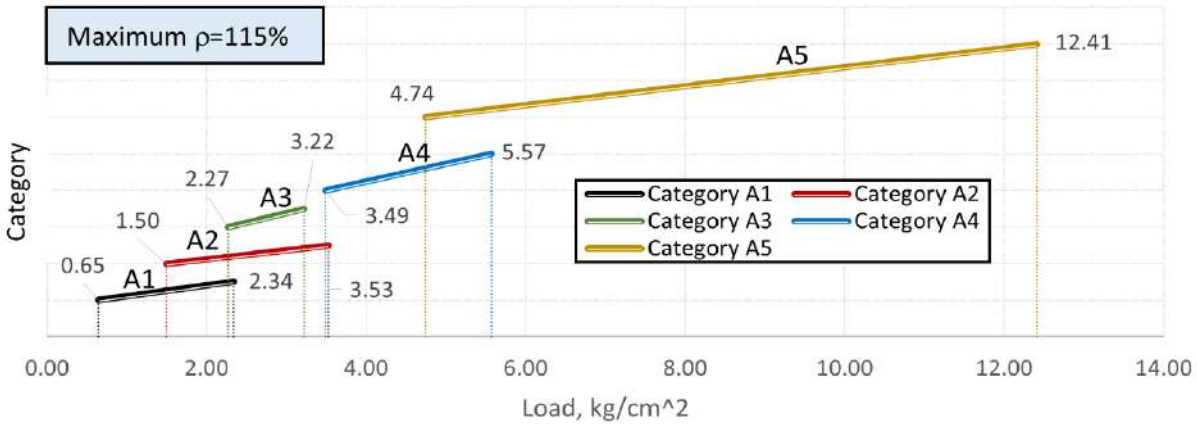

Fig 5. - Voltage range at maximum tire pressure

According to the calculation results for category A1, the decrease in normal stress at minimum tire pressures relative to the standard tire pressure $\left(100 \times \frac{\rho_{min}}{\rho_{st}} - 100\right)$, ranges from -10.8 to 11.3%, while the increase in normal stress at maximum tire pressures relative to the standard tire pressure $\left(100 \times \frac{\rho_{max}}{\rho_{st}} - 100\right)$, ranges from 28.6 to 30.2%. For category A2, the decrease in normal stress is 12.1% (both at maximum and minimum load), and the increase varies from 32.1 to 32.2%. For category A3, the decrease in normal stress varies from 12.0 to 12.2%, and the increase varies from 32.0 to 32.6%. For category A4, the decrease in normal stress is 12.3% (for both cases), and the increase varies from 33.0 to 33.1%. For category A5, the decrease in normal tension varies from 12.3 to 12.4%, and the increase varies from 33.0 to 33.4%. Overall, it was found that the decrease and increase in normal tension for all categories of motor vehicles are very similar, i.e., they do not depend significantly on the load capacity by tire width. Thus, regardless of the category of motor vehicle, it can be concluded that: when tire pressure is reduced by 15% from the standard, the stress from the motor vehicle wheel on the road surface is reduced from the standard stress by 12.0±0.32% (0.32 – confidence interval); when the tire pressure is increased by 15% from the standard, the stress from the wheel increases from the standard by 32.0±0.94% (0.94 – confidence interval).

Figure 6 shows the results of compression tests on model wheel rubber: Figure 6A shows measurements of vertical deformation of the rubber along the X-axis; Figure 6B shows calculations of horizontal deformation along the Y-axis (along the wheel), based on a Poisson's ratio of 0.5; Figure 6C shows the calculations of horizontal deformation along the Z axis (across the wheel), based on a Poisson's ratio of 0.5; Figure 6D shows the calculations of changes in the contact patch contour; Figure 6E shows changes in normal stress from the applied load.

According to the measurement results, the maximum relative deformations at the maximum wheel load of 20 kg were: along the X-axis – 0.14%, along the Y- and Z-axes – 0.07%.

At the same time, attenuation of the deformation processes of the model wheel is observed when the maximum test load is applied, and the deformation values of the penultimate and last stages remain unchanged (at least within the hundredths range). The maximum increase in contact area is 15% of the initial area (without load), which corresponds to the maximum normal stress equal to $\sigma = \frac{20\ \text{kg}}{1.348\ \text{cm}^2} = 14.8\text{kg/cm}^2$. To determine the exact values of the model wheel loads, we will use interpolation based on the previously determined maximum and minimum wheel load values (Figures 3-6).

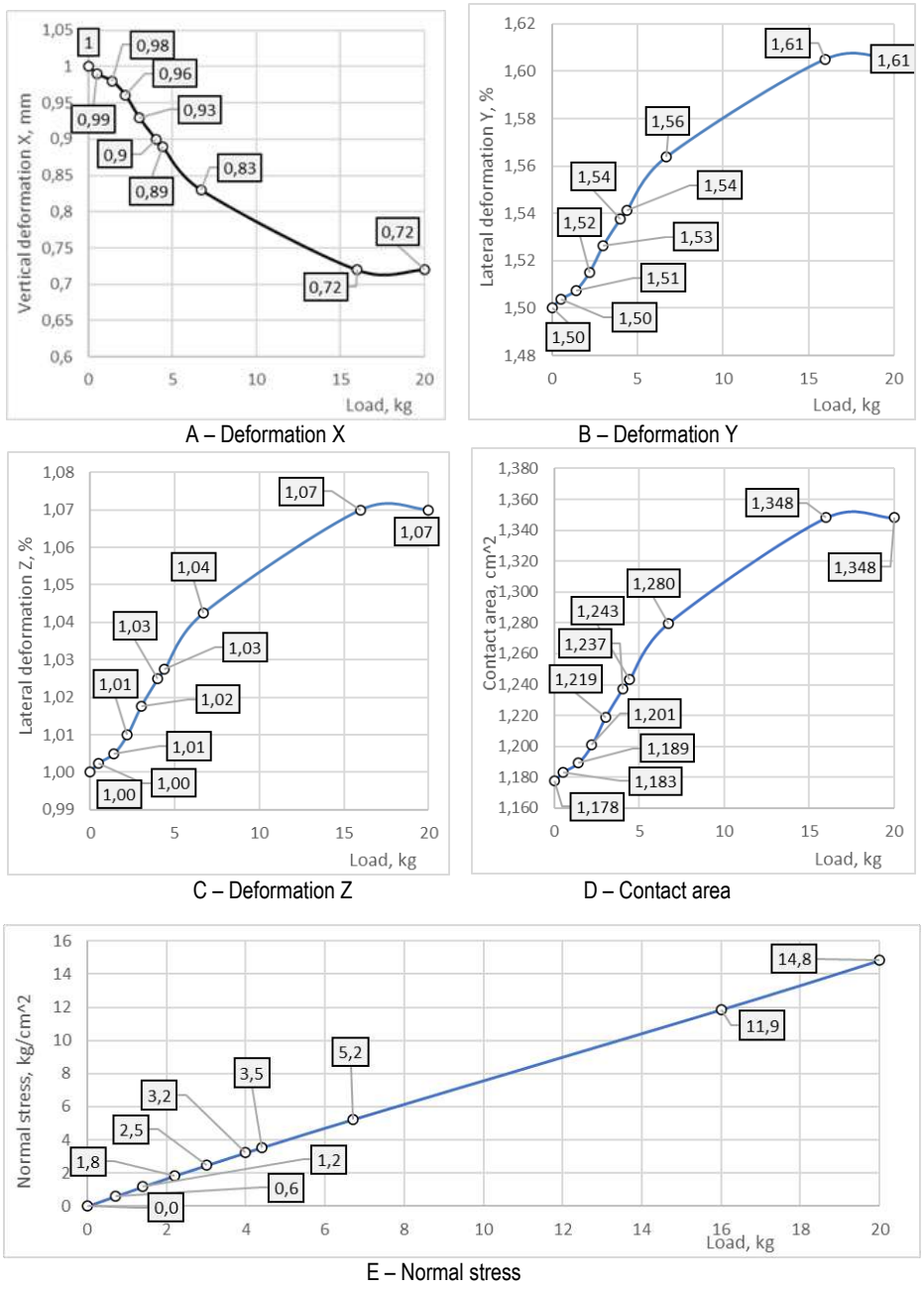

A – Deformation X

B – Deformation Y

C – Deformation Z

D – Contact area

E – Normal stress

Fig. 6.- Results of compression tests on a model wheel

Table 2 shows the results of calculations of the minimum and maximum normal loads on the model wheel, taking into account the deformation of the model wheel, based on the previously determined stresses of the actual vehicle. As a check, the stresses on the actual wheel correspond to the loads on the model wheel.

Table 2. Calculation of normal loads on a model wheel

Category		Tension of the full-size wheel, kg/cm^2 (Figures 3-5)	Model wheel load, kg (calculated by interpolation of values in Figure 6)	Contact area of the model wheel, cm^2 (calculated by interpolation of the values in Figure 6)	Model wheel tension, kg/cm^2 Check = $\frac{\text{column (3)}}{\text{column (4)}}$
1		2	3	4	5
A1	Min	0.50 (0.049)	0.56 (5.49)	1.13	0.50 (0.049)
	Max	1.13 (0.111)	1.36 (13.34)	1.20	1.13 (0.111)
A2	Min	1.72 (0.169)	1.84 (18.04)	1.07	1.72 (0.169)
	Max	2.62 (0.260)	2.82 (27.65)	1.08	2.62 (0.260)

Continuation of Table 2

1	2	3	4	5	
A3	Min	2.34 (0.230)	2.60 (25.50)	1.11	2.34 (0.230)
	Max	3.56 (0.349)	4.42 (43.35)	1.24	3.56 (0.349)
A4	Min	3.22 (0.317)	3.59 (35.21)	1.11	3.22 (0.317)
	Max	3.53 (0.346)	3.82 (37.46)	1.08	3.53 (0.346)
A5	Min	5.57 (0.546)	5.90 (57.86)	1.06	5.57 (0.546)
	Max	12.40 (1.22)	16.40 (160.83)	1.32	12.40 (1.22)

The results of calculations and measurements will be used for further research into the abrasion resistance of the impregnating composition when simulating the movement of loaded vehicles of different categories. The research results will allow simulating calculated situations taking into account the maximum stress (at maximum tire pressure of vehicles with maximum load capacity values within their category) and minimum stress (at minimum tire pressure for vehicles with minimum load capacity within their category). Thus, we will obtain the maximum and minimum service life of the impregnating composition, taking into account the intensity of use of a particular type of vehicle.

Conclusion

1. Statistical studies of vehicle types were conducted based on key characteristics, followed by their classification into categories, within which they were differentiated according to tire technical characteristics. Within each category of motor vehicles, the standard loads from motor vehicles on the road surface were graded, and the minimum and maximum stresses transmitted by the wheel were determined. At the same time, the maximum and minimum stresses (depending on the standard load capacity and tire contact patch) were further divided into minimum and maximum values depending on the tire pressure (Figures 3-5).

2. The obtained samples (maximum and minimum stress values) were used to calculate the stresses of the model wheel, taking into account the deformation properties of the rubber model wheel. For this purpose, the model wheel was loaded on a press with the vertical deformation of the sample fixed. The calculation results (Figure 6, Table 2) are presented as loads on the model wheel necessary to reproduce the normal stresses of the model wheel on a model road surface identical to the actual one.

3. The proposed method for adjusting wheel loads for large-scale testing allows for more accurate calculation of large-scale design load situations on road surfaces by motor vehicles, taking into account standard loads, corresponding contact patch areas, and the elastic properties of the model wheel. The results obtained have a high degree of reliability, as evidenced by statistical indicators with a confidence interval not exceeding 1.0%.

Acknowledgments

This research was/is funded by the Scientific Committee of the Ministry of Science and Higher Education of the Republic of Kazakhstan (grant No. AR26197579 «Development of the composition and production technology of an anti-icing reagent for concrete roads based on latex emulsion and agricultural waste»).

References

[1] Saleh M., Ahmed N., Moghaddam T. B., & Hashemian L. Towards a high-performance asphalt concrete for extreme climatic conditions using asphaltenes and polyethylene terephthalate fibres //Construction and Building Materials, Vol. 420, 2024, 135573. https://www.sciencedirect.com/science/article/abs/pii/S0950061824007141

[2] Kydyrbay N., Adotey E., Zhazitov M., Suiindik Z., Toktarbay Z., Nuraje N., Toktarbaiuly O. Enhancing road durability and safety: a study on silica-based superhydrophobic coating for cement surfaces in road construction //Engineered Science, Vol. 30, 2024, 1221. https://www.espublisher.com/journals/articledetails/1221/

[3] Lukpanov R. E., Dyussembinov D. S., Yenkebayev S. B., Tsygulyov D.V. Impregnation composition to increase the ice-phobic properties of concrete roads //Retrieved from www.scopus.com, Vol.173, 2022, pp.305-311. https://doi:10.1007/978-3-030-81289-8_39

[4] Mudiyono R., Haidar A. D., Fredy A. Analysis of Environmentally Friendly Concrete (Green Concrete) Using Coal Fly Ash as a Substitute Material for Portland Cement in Road Pavement // IOP Conference Series: Earth and Environmental Science,Vol. 1321, No. 1, 2024, p. 012043. IOP Publishing. https://www.mdpi.com/1996-1944/17/13/3162 https://doi.org/10.21122/2227-1031-2016-15-2-87-94

[5] Pshembaev M. K., Kovalev Ya. N., Yaglov V. N., Girinsky V. V. Methods of combating winter slipperiness //Science and Technology, Vol.19, No.3, 2020, pp.230-240. https://doi:10.21122/2227-1031-2020-19-3-230-240

[6] Lukpanov R. E., Dyussembinov D. S., Yenkebayev S. B., Tsygulyov, D. V. Impregnation composition to increase the ice-phobic properties of concrete roads. Springer International Publishing //Lecture Notes in Civil Engineering Digital Technologies in Construction Engineering, Vol.173, 2022, pp.305-311. https://doi:10.1007/978-3-030-81289-8_39

[7] Ma H., Yang R., Qian S. Research on asphalt concrete pavement deicing technology //Journal of Southeast University (English Edition). Vol.30, No. 3, 2014, pp. 336–342. https://DOI:10.3969/j.issn.1003-7985.2014.03.015

[8] Pshembaev M. K., Kovalev Ya. N., Shevchuk L. I. Stresses in cement-concrete pavement caused by thermal shock //Science and Technology, Vol.15, No.2, 2016, pp.87-94. https://doi.org/10.21122/2227-1031-2016-15-2-87-94

[9] Lukpanov R., Tsygulyov D., Zhantlessova Z., Altynbekova A., Yenkebayev S., & Kozhahmet M. Selection of equivalent material for soil testing using piles on a scale model testing apparatus //Geomate Journal. Vol. 26, No.117, 2024, Pp.11-18. https://geomatejournal.com/geomate/article/view/4167
[10]Vorobiev V. S., & Apfelbaum E. M. Generalized similarity laws based on some consequences of the Van der Waals equation. //High Temperature Thermophysics, Vol. 54, No.2, 2016, pp. 186-196. https://doi.org/10.7868/S0040364416020253
[11] Loginova M. E., Movsumzade E. M., Fattakhov M. M., Akhtyamov E. K., & Chetvertnev S. S. Development of similarity theories for physicochemical processes. History and pedagogy of natural sciences. No.4, 2022, Pp. 39-42. https://doi.org/10.24412/2226-2296-2022-4-39-42
[12] Barabanov E. A. Kinematic similarity of linear differential systems with a multiplier parameter at the derivative. Journal of Mathematical Sciences //Proceedings of the IG Petrovsky Seminar. Vol. 210, 2015, Pp. 135-147. https://doi.org/10.1007/s10958-015-2552-9
[13]Lukpanov R. E., Yenkebayeva A. S., Tsygulyov D. V., Sabitov Y. Y., & Dyussembinov D. S. Assessment of ash-storage coolector stability using geosynthetic reinforcement elements by tray testing and numerical modeling //News of the National Academy of Sciences of the Republic of Kazakhstan. Series of Geology and Technical Sciences, Vol.3, No.453, 2022, pp. 212-225. https://doi:10.32014/2022.2518-170X.191
[14] Interstate standard GOST 5652 - Pneumatic tires for motorcycles, motorcycles, scooters and mopeds. Technical specifications. 2023, pp. 1-16. https://internet-law.ru/gosts/gost/11351/
[15] Interstate standard GOST 52900 - Pneumatic tires for passenger cars and trailers. Technical specifications. 2023, pp. 1-23. https://internet-law.ru/gosts/gost/47531/
[16] Interstate standard GOST 4754 - Pneumatic tires for passenger cars, trailers, light trucks and buses of small capacity. Technical specifications. 2023, pp. 1-33. https://internet-law.ru/gosts/gost/7152
[17] Interstate standard GOST 5513 - Pneumatic tires for trucks, trailers, buses and trolleybuses. Technical specifications. 2023, pp. 1-22. https://internet-law.ru/gosts/gost/46320/
[18] Interstate standard GOST 4750 - Pneumatic tires for bicycles. Technical specifications. 2023, pp. 1-14. https://internet-law.ru/gosts/gost/11205/

Information of the authors

Lukpanov Rauan Ermagambetovich, PhD, professor, L.N. Gumilyov Eurasian National University
e-mail: rauan_82@mail.ru

Kabdyrova Lyailya Temirzhanovna, Doctoral student at L.N.Gumilyov Eurasian National University
leila_0781@mail.ru

Karacasu Murat, PhD, professor, Eskisehir Technical University
muratk@ogu.edu.tr

Yenkebayev Serik Beisengalievich, PhD., associate professor, Technobius LLP
Yenkebayev-serik@mail.ru

Tsygulyov Denis Vladimirovich, Candidate of Technical Sciences, associate professor, L.N. Gumilyov Eurasian National University, denis_72@mail.ru

DOI 10.52209/2706-977X_2026_2_110 **IRSTI 81.09.81** **UDC 625.84**

Quantitative Activation-Energy and Boundary-Layer Analysis of Pressure-Dependent Hydrogen and Nitrogen Desorption in Vacuum-Refined Low-Carbon Steel

Imamverdi B.*
Department of Mechanical Engineering, Baku Engineering University, Baku, Azerbaijan
*corresponding author

Abstract. A recently proposed thermodynamic–kinetic framework established that, during industrial vacuum refining of low-carbon steel, the removal of dissolved gases shifts from reaction control to diffusion control as the chamber pressure is lowered [13]. The present work converts that qualitative picture into a quantitative one. Re-analysing the same industrial dataset acquired at Baku Steel Company, apparent activation energies for hydrogen and nitrogen desorption are extracted as explicit functions of the vacuum-pressure regime, a liquid-side boundary-layer model is introduced to locate the pressure at which transport becomes rate-limiting, and a time-resolved description of the activation barrier is developed to quantify the efficiency penalty of an unstable vacuum. The analysis yields hydrogen barriers that fall from roughly 44 to 31 kJ/mol and nitrogen barriers from roughly 168 to 139 kJ/mol as the pressure is reduced from above 5 mbar to below 2 mbar, places the reaction-to-diffusion crossover near 3–5 mbar, and links the comparatively high nitrogen barrier to surface-active residual elements. Together these results provide quantitative targets for vacuum-treatment practice that the earlier qualitative framework could not supply.

Keywords: activation energy; vacuum refining; mass transfer; boundary layer; reaction-to-diffusion transition; low-carbon steel.

Introduction

Vacuum degassing is central to the production of clean low-carbon steel, because dissolved hydrogen and nitrogen reduce ductility, promote internal cracking and degrade downstream performance. Lowering the partial pressure of these species above the melt is the thermodynamic lever that drives them out of solution, and the governing gas–metal equilibria are well documented in classical steelmaking theory [1,2,4].

In earlier work the present author proposed a unified thermodynamic–kinetic framework for this system and showed, using plant data from Baku Steel Company, that the controlling mechanism changes from reaction-limited to diffusion-limited as the vacuum deepens [13]. That study, however, treated the activation barriers only qualitatively: it established that hydrogen desorbs more readily than nitrogen and that barriers decrease with pressure, but it did not assign numerical activation energies to specific pressure regimes, did not specify the transport conditions under which the diffusion limit takes over, and did not describe how an unstable vacuum perturbs the barrier in time.

The present paper addresses precisely these three open points. Building on the same experimental basis, it (i) extracts apparent activation energies for hydrogen and nitrogen as explicit functions of the pressure regime; (ii) introduces a liquid-side boundary-layer and mass-transfer treatment that makes the diffusion-controlled boundary condition quantitative and locates the reaction-to-diffusion crossover; and (iii) develops a time-resolved barrier model that quantifies the efficiency loss caused by vacuum instability. The aim is to convert the qualitative framework of [13] into a set of quantitative, transferable criteria for process design [3,5,6].

1. Materials and Methods

1.1 Experimental basis and dataset

The quantitative analysis presented here does not rely on new heats. It re-uses the industrial dataset already reported in [13] - dissolved-gas decay curves, continuously logged vacuum-pressure profiles and immersion-thermocouple temperature records for 40–60 ton low-carbon steel heats treated in the vacuum-degassing (VD) ladle at Baku Steel Company - now examined for a different purpose, namely the extraction of quantitative activation barriers and transport-controlled desorption criteria. The facility uses porous-plug argon stirring (8–16 m^3/h) and multi-stage mechanical pumping capable of reaching 1–2 mbar, with melt temperatures held at 1580–1620 °C. The nominal composition and initial dissolved-gas levels of the treated heats are summarised in Table 1; these ranges define the material window to which the present quantitative results apply.

Table 1. Nominal chemical composition and initial dissolved-gas ranges of the low-carbon steel heats treated in the 40–60 ton VD ladle

Element / parameter	Nominal range (low-carbon heats)
Carbon, C	0.04–0.12 wt%
Manganese, Mn	0.30–0.80 wt%
Silicon, Si	0.10–0.30 wt%
Phosphorus, P (max)	≤ 0.020 wt%
Sulphur, S (max)	≤ 0.015 wt%
Initial dissolved oxygen, $[O]_0$	250–550 ppm
Initial hydrogen, $[H]_0$	4.0–7.0 ppm
Initial nitrogen, $[N]_0$	40–90 ppm

1.2 Activation-energy extraction

For each heat, first-order rate constants for hydrogen and nitrogen removal were obtained from exponential fits of the corresponding concentration–time curves. Plotting ln k against 1/T over the 1580–1620 °C window (1853–1893 K) gives the Arrhenius lines of Figure 1, whose slopes yield the apparent activation energies [4,7,8]. Crucially for the present analysis, the rate constants were grouped by the recorded pressure regime — above 5 mbar, 3–5 mbar and below 2 mbar — so that a distinct barrier could be assigned to each regime rather than a single global value.

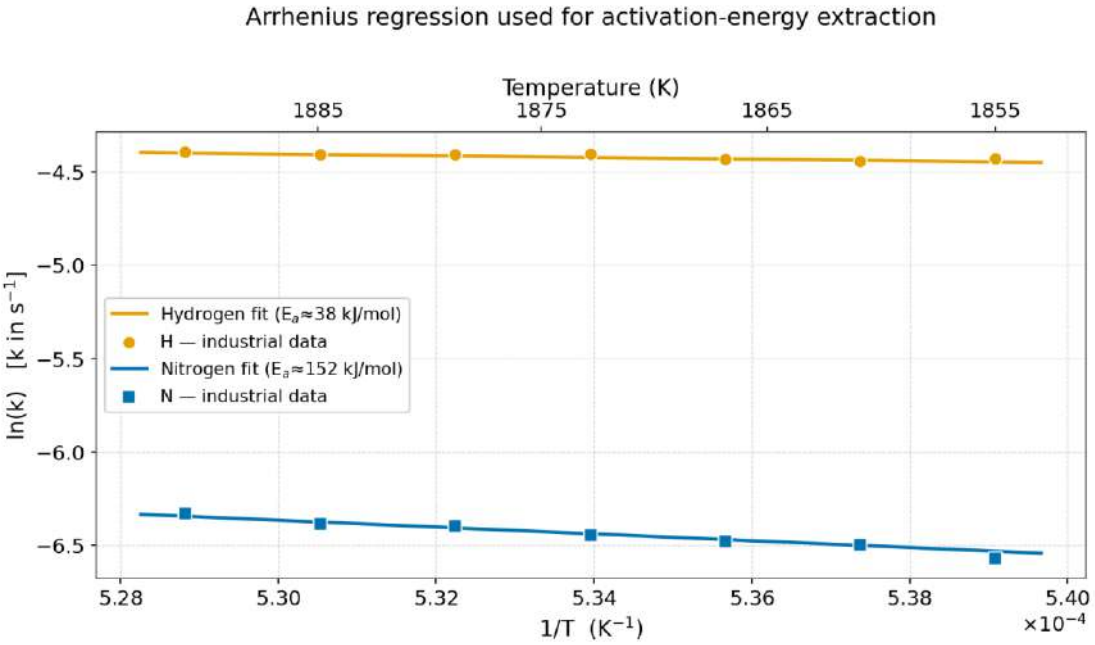

Fig. 1. – Arrhenius regression of ln k versus 1/T for hydrogen and nitrogen desorption, used to extract the apparent activation energies. Points are the industrial data; lines are the per-species fits.

1.3 Boundary-layer and mass-transfer model

The pressure at which desorption ceases to be limited by the interfacial reaction and becomes limited by liquid-phase transport is set by the conditions in a thin boundary layer at the gas–metal interface. The melt bulk is taken as well mixed by argon stirring, so that composition gradients are confined to this layer; the interfacial gas content is assumed to obey Sieverts-type equilibrium; and, because the mean free path is large and pumping is fast at sub-mbar pressure, gas-phase resistance is neglected. The liquid-side mass-transfer coefficient follows from the layer thickness as $k_L = D/\delta$. Using diffusivities of dissolved hydrogen and nitrogen in liquid iron of about $D_H \approx 1.1 \times 10^{-7}$ m^2/s and $D_N \approx 1.0 \times 10^{-8}$ m^2/s, and an effective layer thickness $\delta \approx 0.3$ mm typical of vigorous stirring, k_L falls in the range $2–4 \times 10^{-4}$ m/s [9,11]. Comparing this transport rate with the interfacial reaction rate inferred from the fitted constants identifies the pressure at which control passes from reaction to diffusion.

1.4 Time-resolved barrier model

To examine the role of vacuum stability, the $\Delta p/\Delta t$ classification of [13] - stable (≤ 0.5 mbar/s), semi-stable (0.5–1.5 mbar/s) and unstable (> 1.5 mbar/s) - was combined with the pressure dependence of the barrier obtained above. Treating

the instantaneous barrier as a function of the instantaneous pressure allows it to be propagated in time for a representative fluctuating pressure signal and compared against the stable case.

2. Results and Discussion

2.1 Quantified activation energies

The Arrhenius regression confirms that both gases follow Arrhenius behaviour but with markedly different barriers and - the new result - that each pressure regime carries its own barrier (Table 2, Figure 2). The apparent hydrogen barrier falls from about 44 kJ/mol above 5 mbar to about 38 kJ/mol at 3–5 mbar and about 31 kJ/mol below 2 mbar. Nitrogen, held back by a stronger triple bond and a slower interfacial dissociation step, lies far higher, declining from about 168 to 152 to 139 kJ/mol over the same regimes [5,6]. The roughly four-fold gap between the two explains the routine industrial observation that hydrogen is stripped well before nitrogen, while the downward trend with pressure shows that deepening the vacuum lowers the thermal demand of desorption rather than merely improving the driving force.

Table 2. Apparent activation energies for hydrogen and nitrogen desorption obtained for three vacuum-pressure regimes over the 1580–1620 °C operating window.

Vacuum-pressure regime	E_a (H), kJ/mol	E_a (N), kJ/mol
p > 5 mbar	44	168
3–5 mbar	38	152
p < 2 mbar	31	139

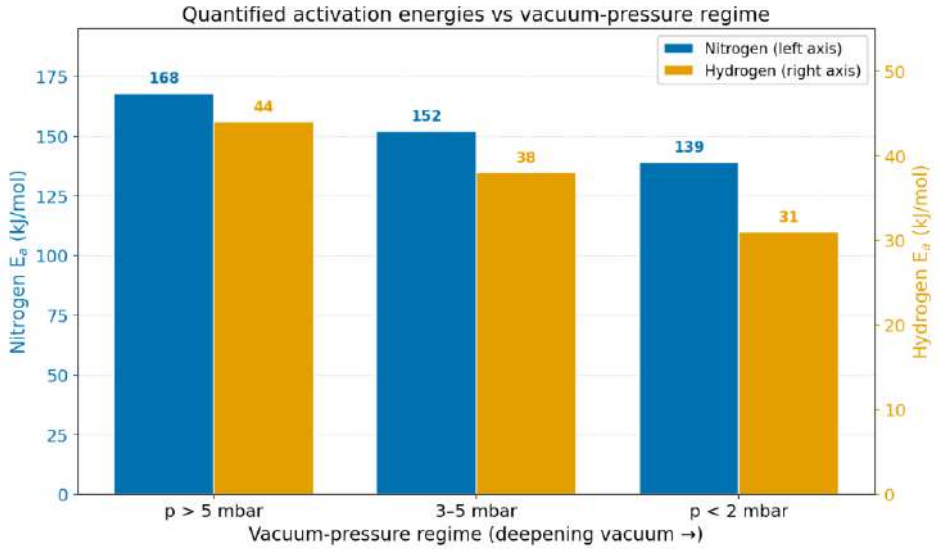

Fig. 2. – Apparent activation energies of hydrogen and nitrogen plotted against the vacuum-pressure regime (note the separate left and right scales). Both barriers decrease as the vacuum deepens, with nitrogen remaining several times higher than hydrogen.

2.2 Influence of alloying and residual elements on the nitrogen barrier

The size of the nitrogen barrier is set not only by pressure but by the chemistry of the interface. Surface-active species — chiefly the residual oxygen and sulphur present before deep deoxidation, together with the manganese and silicon of these low-carbon grades — adsorb at the gas–metal boundary and impede the nitrogen adsorption–dissociation step, raising its apparent barrier above the clean-interface value. Hydrogen, which dissolves and diffuses atomically, is largely indifferent to these species, so its barrier depends far more weakly on melt chemistry. As oxygen and sulphur are removed during treatment, the nitrogen barrier should ease, amplifying the pressure-driven reduction noted in Section 3.1. This coupling between residual chemistry and the kinetic barrier was not resolved in the earlier framework [13] and is one of the new contributions of the present analysis.

2.3 Transition-state position and the reaction-to-diffusion crossover

Representing desorption along a normalised coordinate $\xi \in [0,1]$, with $\xi = 0$ the dissolved atom and $\xi = 1$ the gaseous molecule, the transition state lies at the position ξ^* that maximises the free-energy profile, $\xi^* = \text{argmax}\, G(\xi)$. Lowering the pressure makes the overall reaction more exergonic; by the Leffler–Hammond relation $\alpha = \partial\Delta G^{\ddagger}/\partial\Delta G_{rxn}$ this draws the transition state to smaller ξ^* - earlier along the path and closer to the metal surface - as shown in Figure 3 [2,4]. The boundary-layer model of Section 2.3 fixes the physical meaning of this shift: above roughly 5 mbar the fitted interfacial

rate is slower than the transport rate k_L, so the interfacial step controls; below roughly 2 mbar transport through the liquid layer is slower, so diffusion controls; the crossover falls in the 3–5 mbar band. The quantitative location of this crossover, absent from the earlier framework, provides a concrete pressure target for operating in the fast, diffusion-limited regime.

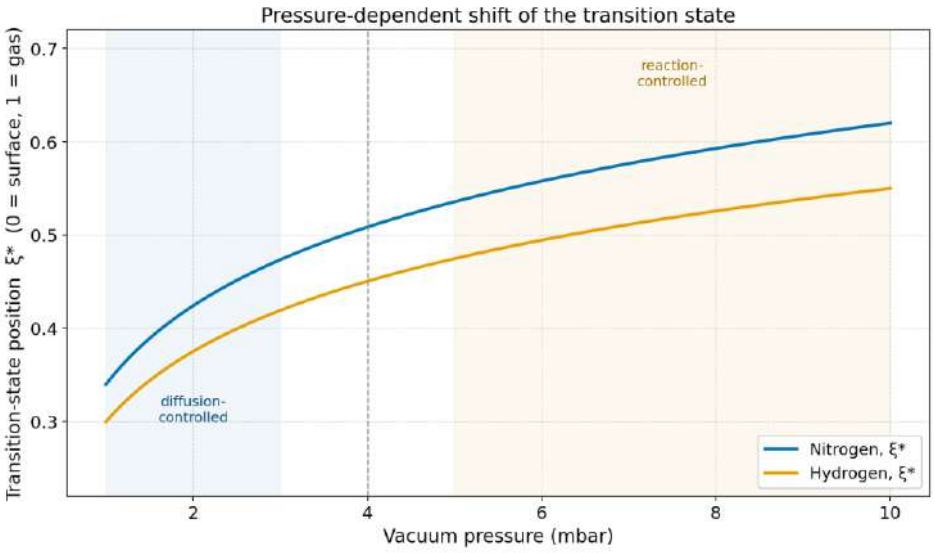

Fig. 3. – Modelled transition-state position ξ* as a function of vacuum pressure for hydrogen and nitrogen. As the pressure falls, ξ* shifts toward the surface (smaller values); the shaded bands indicate the reaction-controlled and diffusion-controlled regimes identified by the boundary-layer model.

2.4 Barrier fluctuation under an unstable vacuum

Propagating the barrier in time shows why vacuum stability matters as much as absolute pressure. Under unstable operation ($\Delta p/\Delta t > 1.5$ mbar/s) the modelled barrier swings by tens of kJ/mol about its mean, repeatedly climbing back toward the high-pressure value and intermittently choking desorption; under stable operation (≤ 0.5 mbar/s) it remains low and almost flat (Figure 4) [10,12]. The time-averaged barrier under fluctuation therefore exceeds the value implied by the mean pressure alone, which accounts quantitatively for the loss of efficiency observed when a pumping system cannot maintain a smooth pressure decay — a behaviour described only qualitatively before.

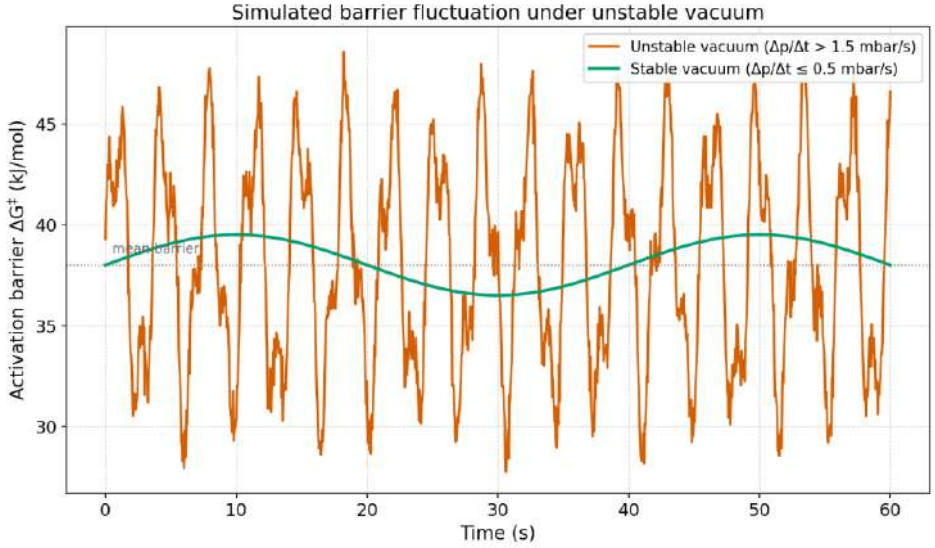

Fig. 4. – Simulated time evolution of the hydrogen desorption barrier under unstable and stable vacuum. Rapid pressure fluctuations periodically raise the barrier toward its high-pressure value, intermittently suppressing desorption.

2.5 Relation to prior work and the literature

The present results are consistent with the established framework [13] and with the broader literature: hydrogen is removed faster than nitrogen because of its lower barrier [3,5]; reducing pressure increases spontaneity and lowers gas solubility [1,2]; and deep vacuum makes diffusion the controlling step [7,11]. What is added here is quantitative -

numerical barriers for each regime, a transport criterion that locates the controlling-mechanism crossover, and a time-resolved measure of the cost of vacuum instability - rather than a restatement of the qualitative mechanism.

Conclusion

This work places the previously established, qualitative thermodynamic–kinetic picture of vacuum refining [13] on a quantitative footing. Re-analysing the same Baku Steel Company dataset, it assigns explicit activation energies to hydrogen (≈ 44 → 31 kJ/mol) and nitrogen (≈ 168 → 139 kJ/mol) across the >5, 3–5 and <2 mbar regimes; introduces a liquid-side boundary-layer model that places the reaction-to-diffusion crossover near 3–5 mbar; attributes the high nitrogen barrier to surface-active residual elements; and quantifies, through a time-resolved barrier, the efficiency penalty of an unstable vacuum. The practical implication is that both a sufficiently deep vacuum (below about 2 mbar) and a stable pressure decay are required to operate in the fast, diffusion-limited regime, and that nitrogen removal in particular benefits from prior removal of surface-active oxygen and sulphur. Replacing the representative values used here with the corresponding measured plant figures would turn these criteria into directly applicable operating set-points.

Acknowledgments

This research is funded by the Azerbaijan Science Foundation – Grant № AEF-MCG-2023 1(43)-13(01)1-M-01.

Conflict of Interests

The author declares there is no conflict of interests related to the publication of this article.

References

[1] Fruehan R. J. The Making, Shaping and Treating of Steel: Steelmaking and Refining. AISE Steel Foundation, Pittsburgh, 1998.
[2] Turkdogan E. T. Fundamentals of Steelmaking. The Institute of Materials, London, 1996.
[3] Li J., Wang Z. Thermodynamic analysis and modeling of vacuum degassing processes in steel refining //Metallurgical and Materials Transactions B, 53(4), 1125–1140, 2022.
[4] Hidayat T., Hayes, P., Jak E. Fundamentals of gas–metal reactions in iron and steelmaking //Metallurgical and Materials Transactions B, 2018, 49(2), 563–585
[5] Zhang L., Thomas, B. G. State of the art in evaluation and control of steel cleanliness //ISIJ International, 2003, 43(3), 271–291
[6] Ghosh A., Chatterjee A. Ironmaking and Steelmaking: Theory and Practice //PHI Learning, New Delhi, 2018.
[7] Wang Y., Zhang, G. Bubble growth and floating behavior during the degassing process of molten steel (N_2–H_2 system) // ISIJ International, 2020, 60(3), 875–883,
[8] Chen W., He Y. Volume of fluid simulation of single argon bubble dynamics in liquid steel under vacuum conditions //Journal of Materials Research and Technology, 2024, 26, 456–469,
[9] Li M., Yang S., Chen X. Mass transfer kinetics during vacuum degassing of molten steel: A theoretical review // Ironmaking & Steelmaking, 48(7), 802–814, 2021.
[10] Gudov A. G., et al. Metal degassing in a vacuum chamber of circulating vacuum degasser // Steel in Translation, 52(12), 920–924, 2023.
[11] Dai B., Li M., Yang Y., et al. Efficient hydrogen removal from H-supersaturated liquid steel in a vacuum degasser with various gas injection modes //Metals, 2023, 13(7), 1229
[12] Konar B., Quintana N., Sharma M. Modeling and optimization of vacuum degassing in electric steelmaking route // Processes, 2025, 13(8), 2368,
[13] Behbudlu I. A. Investigation of Reaction Mechanisms During Vacuum Processing of Low-Carbon Steels // Herald of the Azerbaijan Engineering Academy, 2026, Vol. 18 https://doi.org/10.52171/herald.433

Information of the author

Imamverdi Ali Behbudlu, Doctorate Student, Department of Mechanical Engineering, Faculty of Engineering, Baku Engineering University
e-mail: behbudlu.imamverdi@gmail.com

DOI 10.52209/2706-977X_2026_2_115 IRSTI 62.20.35 UDC 621.43.03

Mathematical Modeling of the Economic Effectiveness of Repurposed Automotive Engine Swap Kits for Diesel Generator Units

Aimukhanov D.S. [1], Mehtiev A.D. [1], Wargula L.[2], Sembaev N.S.[3], Aimukhanov S.M.[3]
[1,2] Abylkas Saginov Karaganda Technical University», Karaganda, Kazakhstan
[2] Poznan Polytechnic University, Poland, Poznań
[3] Toraigyrov University, Pavlodar, Kazakhstan

Abstract. The article employs an integrated scientific research method, including systems, kinematic, and comparative analysis, as well as techno-economic modeling. A methodology is proposed for evaluating the economic efficiency of utilizing automotive «swap kits» (complete engine assemblies including auxiliary systems and attachments) and manual transmissions for subsequent operation in stationary machinery drives, using diesel generators as a primary example. An efficiency criterion is introduced based on a comparison of the levelized cost per engine hour, fuel consumption, and total lifecycle savings. The role of gearboxes in the drive design is substantiated. The developed mathematical model, which accounts for capital expenditures, differences in specific fuel consumption, and residual engine life, enables the justification of techno-economic advantages and efficiency conditions. The results of the study are recommended as an engineering methodology for the rapid assessment of swap project efficiency in stationary machinery drive systems.

Keywords: mathematical model, swap kit, diesel generator, residual engine life, specific fuel consumption, economic efficiency, manual transmission gear.

Introduction

Currently, in the territory of the EAEU countries, the practice of upgrading commercial passenger and freight vehicles – in particular, the Gazelle, Ford, and Mercedes-Benz families – has seen increasing adoption of a method whereby the factory engine and associated components are replaced with complete power units that are used but exhibit high reliability and remaining service life. Units from brands such as Toyota, Mercedes-Benz, and Nissan, which are widely available and known for their reliability on the secondary market, are used as donors. Such kits are commonly referred to as «swap kits» [1].

The accumulated experience with swap kits in road transport opens prospects for their use in stationary machines, for example, as drives for diesel generators.

The alternative is the use of «swap kits» – power units removed from decommissioned vehicles but retaining significant remaining service life. Restoring the operability of stationary machines that have exhausted their service life by this method represents a promising direction for resource conservation. The practice of repurposing (converting) automotive internal combustion engines (ICEs) for use as part of stationary equipment creates favorable conditions for reducing vehicle recycling levels and achieving substantial material savings [2-4].

The economic feasibility of replacing standard industrial drives with automotive equivalents (“swap kits”) is determined by the following factors:

– Component cost. The expenses for acquiring components for repurposing a stationary machine drive are 3-5 times lower than the cost of a new industrial engine of equivalent power. A price analysis shows that the cost of a new 100 kW industrial diesel engine ranges from €8,000 to €12,000. At the same time, the cost of a contract (used but operational) automotive engine with comparable parameters and confirmed remaining service life varies between €1,500 and €2,500 [5];

– Logistics and availability. A significant reduction in transportation and logistics costs is achieved due to the well-developed network of vehicle dismantling enterprises (auto recyclers) and the wide availability of spare parts on the secondary market. This minimizes the time required to locate and deliver the necessary units [1]. The broad standardization and prevalence of service and repair facilities for automotive engines ensure high availability of both new and used spare parts, simplifying subsequent maintenance;

– Reduced downtime. The use of localized and easily accessible automotive units makes it possible to drastically shorten the time required to restore stationary machines. While waiting for delivery of a new industrial engine can take 3 to 6 months, the acquisition, delivery, and installation of an automotive equivalent typically takes 1 to 2 weeks, which is critical for reducing forced equipment downtime [1];

– Restoration cost. A comparative cost analysis demonstrates that the cost of repurposing and installing an automotive engine is 40–60% lower than the cost of overhauling a failed industrial engine. This effect is achieved due to the lower price of the original donor unit and the lower labor intensity of preparatory work [5-7];

– Utilization of remaining service life. Conversion enables the effective transfer of unused remaining service life of components from transport operating conditions to stationary operation. As noted in the technical literature [10], after 150-250 thousand km of mileage, the mechanical parts of an automotive engine retain up to 70-80% of their original

service life. In the gentle operating mode of a stationary installation (e.g., a standby generator), this potential can be realized over many years, effectively extending the product's life cycle [8];

– Application area. The operation of stationary machines restored by installing automotive ICEs becomes particularly relevant in hard-to-reach and less developed regions. Such units are optimal for use as temporary sources of mechanical energy or electric power generation during peak load periods, seasonal work, emergency power outages, and in road construction. Their low cost and rapid installation make them an ideal solution for local tasks where the use of expensive industrial equipment is economically unjustified;

Restoration by repairing or replacing the standard engines of stationary machines, such as diesel generators [9], often requires significant capital investment. The alternative is the use of «swap kits» – power units removed from decommissioned vehicles but retaining substantial remaining service life. This approach is being actively developed in the modernization of commercial vehicles.

The presence of a manual transmission (MT) or robotic transmission as part of such a kit makes it possible to optimize the internal combustion engine's operating mode with respect to the rotational speed of the loaded actuator shaft, bringing the engine into the zone of minimum specific fuel consumption. The aim of this work was to develop a mathematical model enabling a quantitative assessment of the feasibility of such an approach.

1. Materials and Methods

Within the framework of this study, a comprehensive methodological apparatus integrating engineering, technical, and economic approaches was applied to assess the feasibility of using automotive swap kits in stationary machine drives. The main research methods include:

1. Method of technical-economic modeling and system analysis. The methodological approach of this work is system analysis of the resource and cost aspects of the life cycle of power units. On this basis, a rigorous formalization of the cost structure was performed: capital investments (acquisition, adaptation, installation) and operating expenses (fuel consumption) were differentiated and structured for two competing scenarios – implementation of a swap project versus conventional overhaul (or replacement) of the standard industrial engine. This made it possible to develop a comprehensive technical-economic model describing system behavior under real operating conditions;
2. Method of comparative economic efficiency and cost normalization. To ensure objective comparability of power units with significantly different useful lifetimes (remaining service life), the method of normalizing costs to a common baseline – the cost per operating hour – was applied. This step allowed correct comparison of heterogeneous capital and fuel costs, eliminating distortions arising from differences in initial cost and projected durability of the components;
3. Analytical mathematical modeling. Based on the identified economic indicators, a system of mathematical equations was developed. The outcome of the analytical synthesis was the derivation of a final functional relationship serving as the main payback criterion. The developed model (Equation 23) mathematically relates three key independent variables: the difference in capital investments, the delta of specific fuel consumption, and the available remaining service life of the donor engine [11, 12];
4. Kinematic analysis and optimization of operating modes for systems with discrete states. To substantiate the achievement of fuel efficiency, an approach accounting for the influence of gear ratios of the mechanical transmission was applied. The presence of a manual transmission (MT) is considered as a tool for matching the external speed characteristic of the automotive engine with the required synchronous speed of the generator. It was demonstrated by calculation that selecting the optimal gear allows the power unit to be purposefully operated in the zone of maximum torque and minimum specific fuel consumption;
5. Computational experiment and parametric visualization. To verify the developed analytical model and determine the domains of economic feasibility, a computational experiment was implemented using programming methods (Python). The numerical solution of the obtained mathematical relationships enabled the construction of contour plots and clear visualization of the multidimensional parameter space. This ensured precise determination of the break-even boundary and identification of zones generating net savings as a function of variable operating parameters.

Initial hypothesis is the assumption is that lower capital costs due to the use of a recycled swap kit, together with improved fuel efficiency through selection of the MT gear ratio, can compensate for the lower remaining service life of such a unit compared to a standard overhauled engine.

The study was performed in the following sequence:

– capital and fuel components were identified for the two compared options – the swap project and the alternative (overhaul / new engine);

– costs were normalized to a common indicator: the cost per operating hour was introduced, allowing correct comparison of options with different projected service lives (L_{rem} и L_{alt});

– efficiency criteria were developed: the total net savings (TS) over the entire service period of the swap unit is calculated as the difference between the normalized costs of the alternative and the project, multiplied by the remaining service life;

– based on the initial data of the experimental sample and using linear programming together with the scientific computing libraries NumPy and Matplotlib, a functional relationship was constructed to solve the mathematical model.

The proposed approach made it possible to quantitatively evaluate the influence of three key factors (capital costs, difference in specific fuel consumption, remaining service life) on the overall efficiency. The development of a mathematical model is justified because without formalized relationships it is impossible to reliably compare options with heterogeneous cost structures and service lives, nor to account for the nonlinear nature of specific fuel consumption [14] as a function of crankshaft rotational speed. The outcome of applying the integrated method is Equation (23), which can be used as an engineering technique for rapid assessment of swap projects.

2. Results and discussion

Equations of capital costs and fuel efficiency.

The economic efficiency of manufacturing a drive based on a swap kit is determined by comparison with the alternative (overhaul of the standard engine or purchase of a new one). The main criterion is the net savings over the projected operating period.

Let us represent the capital costs for the two options as follows [2, 15]:

– Costs for implementing the swap project:

$$I_{swap} = C_{swap.eng} + C_{adapt} + C_{gen} + C_{frame} + C_{other}, \text{(m.u.)} \quad (1)$$

– Costs for the alternative option (overhaul of the standard engine):

$$I_{alt} = C_{repair} \, (C_{new}), \text{(m.u.)} \quad (2)$$

where C_{swap} – cost of the swap kit (engine with MT and all auxiliary systems);

C_{adapt} – costs for adapting the engine, clutch, MT, and connecting the MT – alternator assembly;

C_{gen} – cost of repairing or restoring the alternator, if required (or the cost of a new alternator for manufacturing a stationary machine);

C_{frame} – cost of manufacturing the frame and mountings;

C_{other} – other costs (repurposing of engine auxiliary systems, calibration of the ECU, instrument panel, wiring, fuel system piping);

C_{repair} – cost of overhauling the standard engine;

C_{new} – cost of a new standard equivalent engine;

I_{swap} – total costs for manufacturing a diesel generator based on a swap kit, monetary units;

I_{alt} – costs for the alternative solution (overhaul or a new standard engine), monetary units.

To ensure a valid comparison, both options must be normalized to a common output power. Considering that the required power at the output shaft of the swap engine $N_{eng.req}$ must account for a power reserve of at least 15%, the maximum load power N_{req} and the generator efficiency η_{gen}, we obtain the following expression:

$$N_{eng.req} = \frac{1{,}15 \times N_{req}}{\eta_{gen}}, \quad (3)$$

where $N_{eng.req}$ – Required engine power including generator efficiency and safety margin (kW);

N_{req} – Required electrical power at the generator output (kW) at $N_{req} = N_{gen} \times \eta_{gen}$;

N_{gen} – Rated output power of the generator (kW);

η_{gen} – generator efficiency (typically 0,85 – 0,95).

The derived relationship allows for the use of either the maximum load power or the initial rated generator power in the calculations. The expressions for determining the theoretical volumetric fuel consumption were established in [3] by Kolchin A.L. and Demidov V.P. The volumetric flow rate for a swap engine equipped with a manual transmission is defined as follows:

$$V_{swap} = \frac{g_{swap} \times N_{eng.req}}{1000 \times \rho_{fuel}}, \text{(l/h)} \quad (4)$$

For the standard engine:

$$V_{alt} = \frac{g_{alt} \times N_{n.gen}}{1000 \times \rho_{fuel}}, \text{(l/h)} \quad (5)$$

where V_{alt} – volumetric fuel consumption of the standard engine (l/h);

V_{swap} – volumetric fuel consumption of the swap engine at the optimal MT gear (if any) (l/h);

g_{alt} – brake specific fuel consumption (BSFC) of the standard engine at power $N_{n.gen}$ (g/kWh);

g_{swap} – brake specific fuel consumption (BSFC) of the swap engine (with or without MT) at the required power (g/kWh);
$N_{n.gen}$ – rated power of the stock engine at the generator operating speed n_{gen}.
MT efficiency $\eta_{swap.gear}$ is not taken into account, $\eta_{swap.gear}$ =1 in the calculation due to its negligible value.

The rotational speed of the generator rotor (n_{gen}) for an industrial frequency of 50 Hz is typically 1500 or 3000 rpm. The presence of an MT makes it possible to vary the rotational speed of the engine crankshaft (n_{eng}) at a fixed n_{gen}:

$$n_{swap} = n_{gen} \times i_{gear} \tag{6}$$

By selecting the gear ratio i_{gear}, we can control the engine torque reserve M_{swap}. For the required power $N_{eng.req}$, the following relation holds:

$$N_{eng.req} = \frac{M_{swap} \times n_{swap}}{9550} \tag{7}$$

Selecting the optimal gear allows the engine to be loaded in the high – torque zone, which corresponds to minimum specific fuel consumption $g_{swap} = f(M_{swap}, n_{swap})$ [13].

In the calculations, it is assumed that the efficiency η_{gear} of a two – shaft or three – shaft MT is close to unity and is neglected, since any possible power loss during downshifting is compensated by an increase in torque.

In the operating mode with an MT, for a given required power $N_{eng.req}$ and a fixed generator speed n_{gen}, a gear ratio i_{gear} is selected to achieve a speed n_{swap} at which the torque M_{swap} will be greater than the torque required by the generator. In this zone, the specific fuel consumption g_{swap} will be minimal for the power $N_{eng.req}$.

The method for determining the theoretical specific, mass (volumetric) fuel consumption of an engine equipped with a manual transmission is based on the classic work by A.I. Kolchin and V.P. Demidov, «Calculation of Automotive and Tractor Engines» [3]. Their approach is particularly valuable because it allows for the analytical calculation of engine performance indicators in the absence of a complete BSFC map (efficiency map). Given the nominal data from the technical specifications $N_{eng.req}$ and g_{swap}, the calculations were performed using Leiderman's formula [2, 3].

As the reference drive for the swap project, a 4D68T engine with a VAZ-2107 5-speed MT was adopted. Based on known methods for determining operational characteristics and reference data, the specific fuel consumption at the MT gears is determined taking into account the constant rotational speed of the output shaft synchronized with the stationary machine (diesel generator).

Based on the calculation results required for the preliminary selection of an engine with MT for use as a diesel generator, the specific fuel consumption at various gears is determined (Fig. 1):

– On the 2nd gear (i_{gear} = 2,1) – operation is possible but not efficient. The engine rotates at 3150 rpm, which increases wear, noise, and specific fuel consumption (241 g/kWh).

– On the 3rd gear (i_{gear} = 1,36) – the most efficient option. When using this gear, to rotate the generator shaft at 1500 rpm, the 4D68T engine must be accelerated to 2040 rpm. At this speed, the 4D68T operates at its peak fuel efficiency (224 g/kWh), which is better than the nameplate data of the D-246.1 (226 g/kWh).

– On the 4th gear (i_{gear} = 1,0). When operating in direct drive, the engine will run at 1500 rpm. At low speeds, the 4D68T turbodiesel does not develop sufficient turbocharger pressure or torque, resulting in an increase in specific fuel consumption to 248 g/kWh. This is 10% worse than that of the D-246.1.

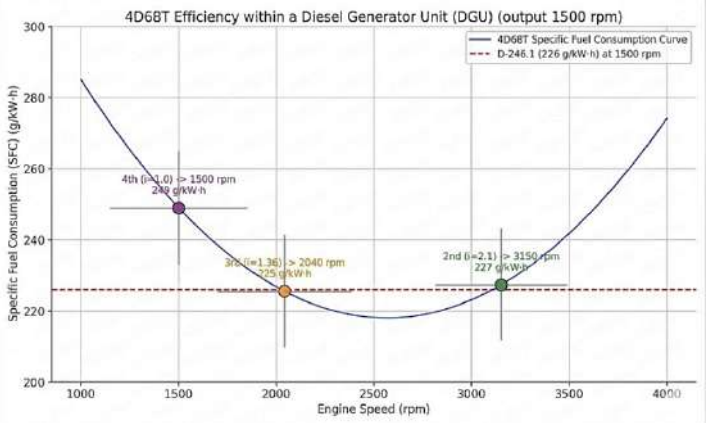

Fig. 1 – Specific fuel consumption curves for various gears of the swap kit (4D68T engine with VAZ-2107 5-speed MT) and for the standard D-246.1 engine with direct drive

The region between the 2nd and 3rd gears, situated below the red dashed reference line of the D-246.1, represents the theoretical reduction in specific fuel consumption (SFC).

Consequently, the aforementioned methodology enables the selection of an engine-MT (manual transmission) combination with gear ratios (i_{gear}) optimized for the swap project. This approach ensures that the engine's crankshaft speed is minimized while still delivering the required torque (M_{swap}). This effectively shifts the engine's operating point into a zone characterized by high torque and low specific fuel consumption.

To evaluate the fuel efficiency of the swap project relative to the stock engine, the total fuel savings can be calculated for the projected remaining service life (L_{rem}) of the replacement engine [16].

Annual fuel savings ($S_{fuel.annual}$, monetary units/year):

$$S_{fuel.annual} = (V_{alt} - V_{swap}) \times T_{op} \times P_{fuel} \tag{8}$$

Substituting the fuel consumption formulas:

$$S_{fuel.annual} = \frac{((g_{alt} \times N_{n.gen}) - (g_{swap} \times N_{eng.req})) \times T_{op} \times P_{fuel}}{1000 \times \rho_{fuel}} \tag{9}$$

Total fuel savings over the entire remaining engine service life (Total Fuel Saving, monetary units):

$$S_{fuel.total} = \frac{(g_{alt} \times N_{n.gen} - g_{swap} \times N_{eng.req}) \times L_{rem} \times P_{fuel}}{1000 \times \rho_{fuel}} \tag{10}$$

where:

L_{rem} is the projected remaining service life of the swap engine (in operating hours);

T_{op} is the average annual operating time (hours/year), assuming $T_{op} = L_{rem}$ /n years;

L_{alt} is the projected service life of the stock engine (in operating hours) following an overhaul or major rebuild;

P_{fuel} is the diesel fuel price (monetary units per liter);

ρ_{fuel} is the diesel fuel density (typically assumed to be ~0,84 kg/L);

$S_{fuel.annual}$ is the annual fuel cost savings.

Normalizing costs to a single indicator. To compare options with different service lives, it is necessary to normalize costs per operating hour, accounting for both capital expenditures (CAPEX) and fuel expenses.

The normalized hourly cost for the swap unit ($C_{swap.hourly}$) is defined as follows:

$$C_{swap.hourly} = \frac{I_{swap}}{L_{rem}} + V_{swap} \times P_{fuel} \tag{11}$$

or

$$C_{swap.hourly} = \frac{I_{swap}}{L_{rem}} + \frac{g_{swap} \times N_{eng.req} \times P_{fuel}}{1000 \times \rho_{fuel}} \tag{12}$$

where I_{swap} / L_{rem} is the hourly depreciation of the fabrication (swap) cost;

$V_{swap} \times P_{fuel}$ is the fuel cost per operating hour;

$g_{swap} \times N_{eng.req} \times P_{fuel} / 1000 \times \rho_{fuel}$ is the fuel cost per operating hour, based on the reference specific fuel consumption (SFC) at a given swap engine power output.

The levelized hourly cost for the stock engine $C_{alt.hourly}$ with a projected post-overhaul service life L_{alt} is:

$$C_{alt.houtly} = \frac{I_{alt}}{L_{alt}} + V_{alt} \times P_{fuel} \tag{13}$$

or

$$C_{alt.hourly} = \frac{I_{alt}}{L_{alt}} + \frac{g_{alt} \times N_{n.gen} \times P_{fuel}}{1000 \times \rho_{fuel}} \tag{14}$$

A project is considered absolutely cost-effective if the hourly operating cost of the swap powertrain is lower than that of the alternative:

$$C_{swap.hourly} \leq C_{alt.hourly} \tag{15}$$

Based on the above, the condition is defined as follows:

$$\frac{I_{swap}}{L_{rem}} + V_{swap} \times P_{fuel} \leq \frac{I_{alt}}{L_{alt}} + V_{alt} \times P_{fuel} \quad (16)$$

The hourly savings for the swap project engine compared to the stock engine have been determined:
Hourly savings (S_{hour}):

$$S_{hour} = C_{alt.hourly} - C_{swap.hourly} \quad (17)$$

$$S_{hour} = \left(\frac{I_{alt}}{L_{alt}} + V_{alt} \times P_{fuel}\right) - \left(\frac{I_{swap}}{L_{rem}} + V_{swap} \times P_{fuel}\right) \quad (18)$$

Hence, the total net savings (TS) over the entire remaining service life of the swap unit (L_{rem}) are calculated as the difference in normalized costs multiplied by the engine's resource:

$$TS = S_{hour} \times L_{rem} \quad (19)$$

$$TS = \left(\left(\frac{I_{alt}}{L_{alt}} + V_{alt} \times P_{fuel}\right) - \left(\frac{I_{swap}}{L_{rem}} + V_{swap} \times P_{fuel}\right)\right) \times L_{rem} \quad (20)$$

$$TS = \frac{I_{alt} \times L_{rem}}{L_{alt}} + (V_{alt} \times P_{fuel} \times L_{rem}) - I_{swap} - (V_{swap} \times P_{fuel} \times L_{rem}) \quad (21)$$

By substituting equations (4) and (5) into (22) and performing the necessary algebraic transformations, we obtain the final efficiency equation:

$$TS = \left(I_{alt} \times \frac{L_{rem}}{L_{alt}}\right) - I_{swap} + (P_{fuel} \times L_{rem} \times (V_{alt} - V_{swap})) \quad (22)$$

The mathematical efficiency model based on the remaining service life, incorporating the known specific fuel consumption at the selected engine power output, is presented as follows:

$$TS = \left(I_{alt} \times \frac{L_{rem}}{L_{alt}}\right) + \frac{P_{fuel} \times L_{rem} \times (g_{alt} \times N_{n.gen} - g_{swap} \times N_{eng.req})}{1000 \times \rho_{fuel}} - I_{swap} \quad (23)$$

The payback criteria are defined as follows:

If $TS > 0$: The project is economically viable and yields net savings in monetary units over the projected remaining service life.

If $TS = 0$: The project reaches the break-even point; the investment is recovered, but no additional savings are generated.

If $TS < 0$: The project is unprofitable; an overhaul of the stock engine is the preferred alternative.

To verify the viability of the developed functional relationship, baseline data from both the selected engine swap kit and the original engine were utilized.

For instance, the capital expenditures for a 4D68T swap engine (paired with a VAZ-2107 7-speed manual transmission) with a required power output of $N_{eng.req}$ = 33 kW and a predicted residual life L_{rem} of at least 3500 hours amounted to I_{swap} = 1779 m.u. In comparison, the restoration costs for the original D-246.1 engine with a power output of $N_{n.gen}$ = 42 kW and a service life L_{alt} = 10000 hours amounted to I_{alt} = 2500 m.u. Given a diesel fuel cost of P_{fuel} = 0.7 m.u. and fuel savings from the swap project totaling ΔV = 900 g/h.

By implementing the mathematical model's programmed code – incorporating the known volumetric (mass) fuel consumption rates V_{alt} and V_{swap} as defined by Equation (22), and the specific fuel consumption g_{alt} и g_{swap} derived from Equation (23) – and inputting the required variables, the efficiency (payback) graph for the selected swap project was obtained (Fig. 2).

On the graph, the ordinate (Y-axis) represents the net savings index TS. The X-axis represents the residual service life of the swap engine, L_{rem} (measured in engine hours).

The graph originates in the negative zone at – 1779 m.u, which corresponds to the initial capital investment for the purchase and installation of the swap kit I_{swap}.

The curve intersects the x-axis at approximately 1900 operating hours. This is the break-even point – a critical metric indicating that once this runtime is reached, the project has fully recovered the installation costs through fuel savings and depreciation advantages.

At the calculated milestone of 3500 hours, the graph reaches a value of +1690,12 m.u. This represents the net savings realized by the equipment owner beyond the initial costs of the swap project.

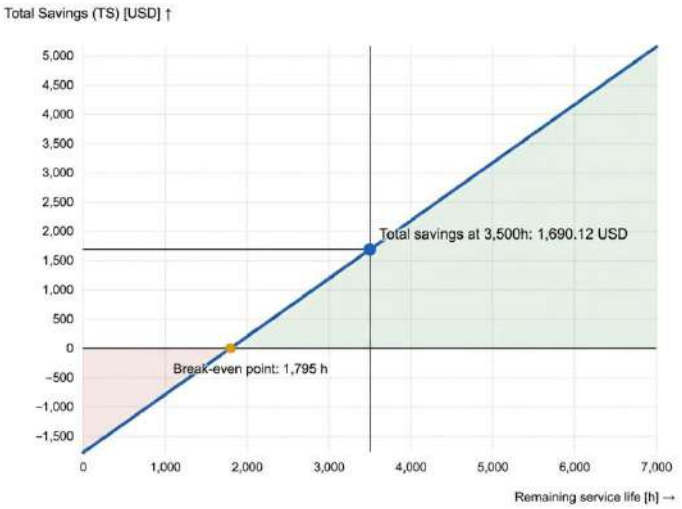

Fig. 2. – Economic efficiency of the project with a swap kit cost of 1779 m. units and a target operating time of 3500 hours, based on the 4D68T engine and the VAZ-2107 5-speed manual transmission

The fuel consumption reduction parameter ΔV = 900 g/h is the determining factor of efficiency and directly influences the geometry of the graph. Fuel economy dictates the steepness (gradient) of the line. The greater the difference in specific fuel consumption between the stock and swap engines, the steeper the upward slope of the graph. In this model, every gram of fuel saved acts to increase the angle of inclination, accelerating the transition out of the loss zone.

Due to the significant difference in consumption (900 g/h), the savings on fuel and lubricants quickly offset the initial investment. With lower fuel economy, the break-even point would shift to the right (e.g., toward 5000-6000 hours), thereby increasing the project's financial risks.

Conclusions

Based on the results of the study, the following conclusions have been formulated:

1. Capital Expenditures I_{swap} and I_{alt}. It is demonstrated that the low cost of a swap kit is a necessary but not sufficient condition for economic viability.
2. Operational Savings ΔV or Δg. The model mathematically substantiates the role of the manual transmission (MT) as a tool for optimizing operating modes and reducing fuel consumption, as confirmed by the $g = f(M, n)$ dependencies across various MT gears. It was established that high fuel efficiency of the swap kit is a critical factor that compensates for its lower residual service life compared to a new industrial engine.
3. Residual Service Life L_{rem}.. The inclusion of this parameter via the levelized hourly cost formulas (13 and 14) prevents errors when comparing projects with different amortization periods or lifespans.
4. Kinematic Analysis. The analysis confirmed that by selecting the optimal gear ratio (in this specific case, 3rd gear), the automotive engine is shifted into the range of maximum torque and minimum specific fuel consumption. This effectively mitigates the negative effects of operating in regimes that were not originally designed for stationary machinery.
5. Hypothesis Confirmation. The hypothesis that utilizing used automotive units is an effective resource-saving tool has been confirmed. This approach allows for a 3-to-5-fold reduction in initial capital investment and significantly shortens equipment downtime under conditions of limited access to new imported components.

The practical significance of the model lies in its ability to determine the boundary conditions under which a swap project becomes more profitable than traditional overhaul or repair.

Equation (23) indicates that the project generates a positive economic effect even with higher specific adaptation costs, provided that the difference in hourly fuel consumption and residual life is large enough to offset these expenses. Thus, the proposed model serves as a tool for techno-economic justification when designing drives for stationary machinery using secondary automotive resources.

The study provides an accessible engineering methodology for a rapid assessment of swap project feasibility based on current market prices for units and fuel. These results are recommended for implementation at enterprises

operating small-scale power systems in remote regions and as a foundation for further research into the rational reuse of automotive industry resources.

References

[1] Warguła Ł., Kadirov A., Aimukhanov D., et al. Ecological Paradox in the Reuse of Internal Combustion Engines from Scrapped Vehicles for Electric Power Generation – Circular Economy Potential Versus Emission Certification Barriers // Sustainability, 2025, Vol. 17, No. 23. – P. 10435. – DOI: 10.3390/su172310435
[2] Aimukhano, D.S., Kadyrov A.S., Warguła L., Aimukhanov S.M. Investigation of drive configurations based on power units of recycled vehicles // Science and Technology of Kazakhstan, 2025, No. 2, P. 372 – 385. – DOI: 10.48081/RRUQ5726
[3] Kolchin A.I., Demidov V.P. Calculation of automobile and tractor engines: textbook. – 4th ed. – Moscow: Vysshaya shkola, 2008. – 496 p
[4] Grigoryev M.A., Ponomarev Yu.K., Davydov V.V., Shishkov V.V. Diesel engines for electric generating units and power plants: a textbook. – Moscow: MPEI Publishing House, 2007. – 212 p.
[5] Ovchinnikov A.V. Price aspects of using contract engines in industry // Ekonomika mashinostroeniya, 2022., No. 4, 14 – 19
[6] Karpov, A.N., Egorov, V.I., Fomin, D.S., Smirnov, P.A. Methodology for assessing the residual life of internal combustion engines // Repair, Reconditioning, Modernization, 2022, No. 3, P. 28 – 34
[7] Sokolov V.A., Nikitin E.P. Assessment of the residual life of automotive and tractor engines after long-term operation // Engine Building, 2021, No. 4, P. 44 – 50
[8] Kuznetsov E.S., Voronov V.P., Boldin A.P. Technical operation of vehicles: textbook for universities. – 5th ed. – Moscow: Transport, 2017. – 413 p.
[9] Diesel generator sets for data centers: what is happening on the Russian market: survey results [Electronic resource] // IKSMEDIA.RU: portal. – Moscow, 2025. – August 15. – URL: https://stat.iksmedia.ru/news/6061559-DGU-dlya-CZODov-chto-proisxodit.html
[10] Golovin S.I., Revyakin M.M., Zhosan A.A. On the issue of assessing operating conditions and predicting the residual life of internal combustion engines // Bulletin of the Orel State Agrarian University, 2024, Vol. 21, No. 5, P. 62–71.
[11] Nuretdinov D.I., Barykin A.Yu., Galiev R.M., Ayukin Z.A. Development of a mathematical model for assessing the residual life of an automobile engine // Scientific and Technical Bulletin of the Volga Region, 2020, No. 2, P. 75 – 77
[12] Sevostyanov A.L., Golovin S.I., Bulavintsev R.A. Development of a software product for assessing the residual life of internal combustion engines based on the chemmotological indicator of engine oil // Bulletin of Altai State Agricultural University, 2025, No. 9 (251), P. 85–95. – DOI: 10.53083/1996-4277-2025-251-9-85-95
[13] Heywood, J.B. Internal Combustion Engine Fundamentals. – 2nd ed. – New York: McGraw-Hill Education, 2018. – 1056 p. – ISBN 978-1260116106
[14] Harris C.R., Millman K.J., van der Walt, S.J. et al. Array programming with NumPy // Nature, 2020, Vol. 585, P. 357 – 362. – DOI: 10.1038/s41586-020-2649-2
[15] Diesel Generator Global Market Report 2026 [Electronic resource] / The Business Research Company. – 2026. – URL: https://www.thebusinessresearchcompany.com/report/diesel-generator-global-market-report
[16] Makhyoun M.N. Economic Analysis of Automotive-Derived Engine-Generator Sets as Energy Conversion Systems at Small Landfills [Electronic resource] / M.N. Makhyoun; Appalachian State University. – Boone, NC, 2011. – 91 p. – URL: https://libres.uncg.edu/asu/listing.aspx?id=5919

Information of the authors

Aimukhanov Damir Sapargalievich, doctoral student, Abylkas Saginov Karaganda Technical University
e-mail: adspavlodar@gmail.com

Mehtiyev Ali Javanshirovich, c.t.s., professor, Abylkas Saginov Karaganda Technical University
e-mail: barton.kz@mail.ru

Wargula Lukasz, professor, Poznan Polytechnic University
e-mail: lukasz.wargula@put.poznan.pl

Sembayev Nurbulat Sakenovich, c.t.s., associate Professor, Toraigyrov University
e-mail: n.sembaev@mail.ru

Aimukhanov Sapargali Mukhidenovich, c.a.s., professor, Toraigyrov University
e-mail: ads-pavl@mail.ru